



Hans-Peter Daxer, BSc

The behaviour of anchored structures affected by the failure of ground anchors

MASTER'S THESIS

to achieve the university degree of
Diplom-Ingenieur

Master's degree programme:
Geotechnical and Hydraulic Engineering

submitted to

Graz University of Technology

Supervisor

Assoc. Prof. Dipl.-Ing. Dr.techn., Franz Tschuchnigg

Institute of Soil Mechanics, Foundation Engineering and Computational Geotechnics

Dipl.- Dipl.-Ing. Dr.techn. Matthias Rebhan, BSc., Baumeister

Graz, September 2020

AFFIDAVIT

I declare that I have authored this thesis independently, that I have not used other than the declared sources/resources, and that I have explicitly indicated all material which has been quoted either literally or by content from the sources used. The text document uploaded to TUGRAZonline is identical to the present master's thesis.

Date, Signature

Acknowledgment

Since many people have contributed to the successful completion of my studies and to the realisation of this master's thesis as its final step, I am using this opportunity to say 'Thank you.'

First and foremost, I wish to express my deepest gratitude to Assoc. Prof. Dipl.-Ing. Dr.techn. Franz Tschuchnigg for his enthusiastic, motivating and patient supervision throughout the entire challenging process of this thesis.

Special thanks to Dipl.- Dipl.-Ing. Dr.techn. Matthias Rebhan for assigning me this worthwhile topic and for his practical, kind and time-consuming support.

I also would like to give special regards to Univ.-Prof. Dipl.-Ing. Dr.techn. Roman Marte, who was able to inspire me with his interactive and passionate teaching approach to geotechnical engineering.

To all my friends, many thanks for accompanying me over the past years and decades and for all the memorable moments we have shared together.

Finally, my deepest gratitude and appreciation belong to my family for their unparalleled love and support. I owe sincere thanks to my parents, without whose help and compassion I would not have been able to walk this path.

Kurzfassung

In den vergangenen Jahrzehnten haben Verpressanker im Bereich der Geotechnik breiten Anklang gefunden. Solche Anker werden verwendet, um Stützkonstruktionen zu sichern, Böschungen zu stabilisieren, Auftrieb zu verhindern und eine Reihe weiterer Verbesserungen zu ermöglichen. Obwohl der Entwurfsprozess für Verpressanker durch den Eurocode 7 (Austrian Standards Institute, 2009) geregelt ist, wird die Standsicherheit von verankerten Bauwerken durch das Versagen dieser Anker, sei es aufgrund von Korrosion oder anderen Versagensmechanismen, regelmäßig negativ beeinflusst. Dennoch wird die Bemessungssituation eines „Ankerversagens“ in der Praxis häufig vernachlässigt, beispielsweise weil sich beim Versagen von Verpressankern komplexe und unzureichend untersuchte dreidimensionale (3D) Spannungszustände einstellen. Da 3D-Berechnungen zeitaufwändig sowie ressourcenintensiv sind (und sich somit für praktische Zwecke oft als ungeeignet erweisen), wird in der vorliegenden Masterarbeit untersucht, ob diese 3D-Effekte in 2D-Berechnungen realistisch reproduziert werden können. Um dieses Ergebnis zu erreichen, wurden numerische Studien, sowohl in 2D als auch in 3D, mit Hilfe der Finiten-Elemente-Software PLAXIS, Version 2018.01, durchgeführt.

Anhand einer mehrfach rückverankerten Stützkonstruktion konnte gezeigt werden, wie sich das reihenweise Versagen von Verpressankern in 2D bzw. ein individueller Ankerausfall in 3D auf die Gesamtstandsicherheit, das Tragwerk selbst und auf umliegende Anker auswirken. Zu diesem Zweck wurden numerische Studien mit verschiedenen konstitutiven Modellen, variierender Kohäsion und unterschiedlicher Diskretisierung der Verankerungslänge durchgeführt. Dabei wurde besonderes Augenmerk auf eine übersichtliche Darstellung von Sicherheitsfaktoren, Versagensmechanismen, Schnittkraftverläufen in den Betonbauteilen, Verschiebungen sowie Ankerkräften gelegt.

In Übereinstimmung mit Zhao et al. (2018) deuten Auswertungen der 2D-Analysen darauf hin, dass insbesondere Ankerversagen nahe des Wandfußes sowie an der Oberseite der Stützkonstruktion als kritisch angesehen werden können. Während für das Versagen nahe des Wandfußes eine signifikante Abnahme des Sicherheitsfaktors festgestellt werden konnte, wurden die Schnittkräfte durch das Versagen im Bereich der Wandsohle bzw. durch das Versagen an der Oberseite der Stützkonstruktion negativ beeinflusst. Diese Biegemomente und Querkräfte, teilweise auch Verschiebungen, werden jedoch bei 2D-Berechnungen im Vergleich zu 3D-Analysen signifikant unterschätzt.

Es wird daher der Schluss gezogen, dass weitere numerische Studien zum Versagen von Verpressankern nicht ausschließlich aus einem 2D-Blickwinkel betrachtet werden sollten, sondern ein 3D-Aspekt zu berücksichtigen ist.

Abstract

In recent decades, ground anchors have gained wide acceptance in the field of geotechnical engineering. Such anchors are used to support retaining structures, stabilise slopes, prevent uplift and enable a number of other improvements. Although the design process for ground anchors is regulated by Eurocode 7 (Austrian Standards Institute, 2009), the stability of anchored structures is negatively affected by the failure of these anchors, whether because of corrosion or other failure mechanisms, regularly. Nevertheless, the design situation regarding ground anchor failure is often neglected in practise, for example because complex and inadequately investigated three-dimensional (3D) stress states occur when ground anchors fail. Since 3D calculations are time-consuming and resource-intensive (and thus often unsuitable for practical purposes), the present master's thesis determines whether these 3D effects can be realistically reproduced in 2D calculations. To achieve this outcome, numerical studies, both in 2D and in 3D, were conducted using the Finite Element Software PLAXIS, Version 2018.01.

By means of a multiple-anchored retaining wall it was possible to show how row-wise ground anchor failure in 2D and individual ground anchor failure in 3D respectively affect the overall stability, the structure itself and the surrounding anchors. For this purpose, numerical studies with different constitutive models, varying cohesion and varied discretisation of the fixed anchor length were conducted. Special emphasis was placed on a clear presentation of safety factors, failure mechanisms, internal forces within the concrete components, displacements and anchor forces.

In agreement with Zhao et al. (2018), evaluations of the 2D analyses indicate that anchor failure close to the wall base and at the top of the retaining wall can be considered especially critical. While a significant decrease in the safety factor could be identified for failure near the wall base, internal forces were negatively affected by failure close to the wall base and failure at the top of the retaining structure, respectively. However, these bending moments and shear forces, partially also displacements, are significantly underestimated by 2D calculations compared to 3D analyses.

It is therefore concluded that further numerical studies on ground anchor failure should not be examined from solely a 2D point of view, but rather a 3D aspect is to be considered.

Table of contents

| | | |
|----------|---|-----------|
| 1 | Introduction | 1 |
| 2 | Anchorage and anchored structures | 2 |
| 2.1 | General | 2 |
| 2.2 | Classification of anchors | 3 |
| 2.3 | Ground anchors | 8 |
| 2.3.1 | Development of ground anchors | 8 |
| 2.3.2 | Standards for design, execution and testing | 9 |
| 2.3.3 | Anchor assembly and parts | 9 |
| 2.3.4 | Construction process | 13 |
| 2.3.5 | Bearing capacity | 14 |
| 2.3.6 | Design | 16 |
| 2.3.7 | Testing procedure | 20 |
| 2.3.8 | Applications | 25 |
| 2.4 | Modes of failure | 32 |
| 2.4.1 | Structural failure of the tendon or the anchor head | 32 |
| 2.4.2 | Corrosion | 33 |
| 2.4.3 | Failure at the interface between the grout body and the ground | 35 |
| 2.4.4 | Failure of the bond between the steel tendon and the grout body | 35 |
| 2.4.5 | Loss of anchor force by creep and relaxation | 36 |
| 2.4.6 | Failure of the ground mass | 36 |
| 3 | Verification methods for the failure of ground anchors | 37 |
| 3.1 | Standards and guidelines | 37 |
| 3.2 | Corroded Anchor Structure Stability/Reliability (CAS_Stab-R) Software for Hydraulic Structures | 38 |
| 3.2.1 | Remaining anchor life computation | 38 |
| 4 | Finite element analyses using PLAXIS 2D | 42 |
| 4.1 | Retaining wall Egger | 42 |
| 4.2 | PLAXIS 2D model | 44 |
| 4.3 | Results | 50 |

| | | |
|----------|--|------------|
| 5 | Finite element analyses using PLAXIS 3D | 98 |
| 5.1 | PLAXIS 3D model | 98 |
| 5.2 | Results | 100 |
| 6 | Conclusion | 121 |
| 7 | Bibliography | 123 |
| 8 | Appendix | 128 |
| 8.1 | <i>MC</i> _R _{inter} =0.9_Geogrid_AnchorPre-stressed in 2D | 128 |
| 8.2 | <i>MC</i> _R _{inter} =0.9_ <i>EB</i> _Constant_AnchorPre-stressed in 2D | 138 |
| 8.3 | <i>MC</i> _R _{inter} =0.9_ <i>EB</i> _Linear_AnchorPre-stressed in 2D | 141 |
| 8.4 | <i>HSS</i> _R _{inter} =0.9_Geogrid_AnchorPre-stressed in 2D | 147 |
| 8.5 | <i>HSS</i> _R _{inter} =0.9_ <i>EB</i> _Linear_AnchorPre-stressed in 2D | 151 |
| 8.6 | <i>MC</i> _R _{inter} =1_Geogrid_AnchorPre-stressed in 3D | 154 |
| 8.7 | <i>MC</i> _R _{inter} =0.9_ <i>EB</i> _Constant_AnchorPre-stressed in 3D | 161 |
| 8.8 | <i>MC</i> _R _{inter} =0.9_ <i>EB</i> _Linear_AnchorPre-stressed in 3D | 169 |
| 8.9 | <i>MC</i> _R _{inter} =1_VolumeElements_AnchorPre-stressed in 3D | 174 |
| 8.10 | <i>MC</i> _R _{inter} =1_Geogrid_AnchorNon-Pre-stressed | 182 |
| 8.10.1 | Tendon in 3D modelled with plate elements | 182 |
| 8.10.2 | Tendon in 2D/3D modelled with plate elements | 185 |
| 8.10.3 | Tendon in 3D modelled with plate and geogrid elements | 188 |

List of figures

| | | |
|----------|--|----|
| Fig. 1: | Strutted building pit (Markl and Bahr, 2018)..... | 2 |
| Fig. 2: | Anchored building pit with heavy construction machinery (Hechendorfer and Haag, 2018) | 2 |
| Fig. 3: | Various applications of anchors (adapted from Schmidt <i>et al.</i> , 2017) | 2 |
| Fig. 4: | Difference between ground anchors and soil nails regarding load- transfer mechanism (adapted from Schmidt <i>et al.</i> , 2017) | 4 |
| Fig. 5: | Spring system prior to and during the pre-stressing of the anchor (Adam <i>et al.</i> , 2017)..... | 5 |
| Fig. 6: | Spring system after pre-stressing and fixing the anchor (Adam <i>et al.</i> , 2017)..... | 5 |
| Fig. 7: | Relationship between forces and deflections of pre-stressed anchors in several loading stages (Adam <i>et al.</i> , 2017) | 6 |
| Fig. 8: | Bracing triangle 1 (adapted from Adam <i>et al.</i> , 2017)..... | 7 |
| Fig. 9: | Bracing triangle 2 (adapted from Adam <i>et al.</i> , 2017)..... | 7 |
| Fig. 10: | Secant pile wall for ‘Bayerischer Rundfunk’ in Munich (Ostermayer, 1993) | 8 |
| Fig. 11: | Dead man anchorage (Kolymbas, 2019) | 8 |
| Fig. 12: | Schematic representation of a ground anchor (acc. to Austrian Standards Institute, 2015b)..... | 9 |
| Fig. 13: | Various types of anchor heads (Ostermayer, 1982) | 10 |
| Fig. 14: | Schematic representation of a single bar anchor (adapted from DSI Underground GmbH, 2019b) | 10 |
| Fig. 15: | Schematic representation of a strand anchor (adapted from DSI Underground GmbH, 2019a)..... | 11 |
| Fig. 16: | Construction process of ground anchors (BAUER Spezialtiefbau GmbH, 2013) | 13 |
| Fig. 17: | Ultimate bearing capacity of anchors for coarse-grained soils (Ostermayer <i>et al.</i> , 2003)..... | 14 |
| Fig. 18: | Ultimate sleeve friction of post-grouted anchors for fine-grained soils (Ostermayer <i>et al.</i> , 2003)..... | 15 |
| Fig. 19: | Ultimate sleeve friction of non-post-grouted anchors for fine- grained soils (Ostermayer <i>et al.</i> , 2003)..... | 15 |
| Fig. 20: | Failure at the lower failure plane (Deutsche Gesellschaft für Geotechnik e.V., 2012)..... | 17 |

| | | |
|----------|--|----|
| Fig. 21: | Acting forces on trapezoidal soil body and polygon of forces (Deutsche Gesellschaft für Geotechnik e.V., 2012)..... | 17 |
| Fig. 22: | Loss of overall capacity for a single anchored wall (Deutsche Gesellschaft für Geotechnik e.V., 2012)..... | 18 |
| Fig. 23: | Examples of single and double corrosion protection for a bar anchor (Austrian Standards Institute, 2015b)..... | 19 |
| Fig. 24: | Different types of test methods; left: Test method 1; centre: Test method 2; right: Test method 3 (adapted from Schmidt <i>et al.</i> , 2017)..... | 20 |
| Fig. 25: | Creep rate (Möller, 2016)..... | 24 |
| Fig. 26: | Cross section of deep excavation for GLC building at ETH Zurich (Hechendorfer and Haag, 2018)..... | 25 |
| Fig. 27: | Deep excavation for GLC building at ETH Zurich 1 (Hechendorfer and Haag, 2018)..... | 26 |
| Fig. 28: | Deep excavation for GLC building at ETH Zurich 2 (Hechendorfer and Haag, 2018)..... | 26 |
| Fig. 29: | Cross section of deep excavation for Coop (Ducksch and Ammann, 2018)..... | 27 |
| Fig. 30: | Analytical and numerical model of deep excavation for Coop (Ducksch and Ammann, 2018)..... | 27 |
| Fig. 31: | Deep excavation for Coop (Ducksch and Ammann, 2018)..... | 27 |
| Fig. 32: | Cross section of the RW Rötteln (Wichter and Meiniger, 2000)..... | 28 |
| Fig. 33: | RW Rötteln (Wichter and Meiniger, 2000)..... | 28 |
| Fig. 34: | Landslide and stabilization measures below the Hochmoselbrücke (Katzenbach and Bergmann, 2018)..... | 29 |
| Fig. 35: | Uplift prevention (Wichter and Meiniger, 2000)..... | 29 |
| Fig. 36: | Strengthening of the dam body at the Edertalsperre (Wichter and Meiniger, 2000)..... | 30 |
| Fig. 37: | Foundation of tensile force at the Neckarbrücke 1 (Wichter and Meiniger, 2000)..... | 30 |
| Fig. 38: | Foundation of tensile force at the Neckarbrücke 2 (Wichter and Meiniger, 2000)..... | 31 |
| Fig. 39: | Stress-strain curve for pre-stressing steel (adapted from Xanthakos, 1991)..... | 32 |
| Fig. 40: | General corrosion, localised corrosion and corrosion cracking (Fédération Internationale de la Précontrainte, 1986)..... | 33 |
| Fig. 41: | Intergranular and transgranular cracks (Wichter and Meiniger, 2000)..... | 34 |

| | | |
|----------|---|----|
| Fig. 42: | Distribution of skin friction along the grout body in gravelly sand (Scheele, 1982) | 35 |
| Fig. 43: | Schematic representation of the tendon-grout interface (Xanthakos, 1991)..... | 36 |
| Fig. 44: | Loading capacity as a function of the minimum corroded wire area (Haskins <i>et al.</i> , 2016)..... | 39 |
| Fig. 45: | Loading capacity as a function of the minimum corroded wire short axis diameter (Haskins <i>et al.</i> , 2016) | 39 |
| Fig. 46: | Corrosion effect on a wire (Warren <i>et al.</i> , 2017)..... | 40 |
| Fig. 47: | <i>RW Egger</i> (adapted from 3G Gruppe Geotechnik Graz ZT GmbH, 2017) | 42 |
| Fig. 48: | Front view and cross section of analysis profile QP-E (3G Gruppe Geotechnik Graz ZT GmbH, 2017)..... | 43 |
| Fig. 49: | Model dimensions ‘Final’ | 44 |
| Fig. 50: | Model dimensions; left: ‘Small’; right: ‘Big’ | 44 |
| Fig. 51: | <i>EB</i> interaction with soil (Brinkgreve <i>et al.</i> , 2018b)..... | 47 |
| Fig. 52: | Mesh discretisation for model ‘Final’; left: Geogrid; right: <i>EB</i> | 48 |
| Fig. 53: | Mesh discretisation; left: Model ‘Small’; right: Model ‘Big’ | 48 |
| Fig. 54: | Representation of selected calculation phases..... | 49 |
| Fig. 55: | <i>FoS</i> after ϕ -c reduction Plastic nil step for $c = 0.1$ kPa..... | 50 |
| Fig. 56: | Incremental deviatoric strains and plastic points after as well as τ_{rel} before/after ϕ -c reduction Plastic nil step for $c = 0.1$ kPa; left: ‘Small’; centre: ‘Final’; right: ‘Big’ | 51 |
| Fig. 57: | <i>FoS</i> after ϕ -c reduction Plastic nil step for $c = 1$ kPa..... | 52 |
| Fig. 58: | Incremental deviatoric strains and plastic points after as well as τ_{rel} before/after ϕ -c reduction Plastic nil step for $c = 1$ kPa; left: ‘Small’; centre: ‘Final’; right: ‘Big’ | 52 |
| Fig. 59: | <i>FoS</i> after ϕ -c reduction Plastic nil step for $c = 3$ kPa..... | 53 |
| Fig. 60: | Incremental deviatoric strains and plastic points after as well as τ_{rel} before/after ϕ -c reduction Plastic nil step for $c = 3$ kPa; left: ‘Small’; centre: ‘Final’; right: ‘Big’ | 53 |
| Fig. 61: | <i>FoS</i> after ϕ -c reduction Plastic nil step for $c = 5$ kPa..... | 54 |
| Fig. 62: | Incremental deviatoric strains and plastic points after as well as τ_{rel} before/after ϕ -c reduction Plastic nil step for $c = 5$ kPa; left: ‘Small’; centre: ‘Final’; right: ‘Big’ | 54 |
| Fig. 63: | <i>FoS</i> after ϕ -c reduction Initial phase and Plastic nil step for $c = 0.1$ kPa | 56 |

| | | |
|----------|--|----|
| Fig. 64: | Incremental deviatoric strains and plastic points after ϕ -c reduction for $c = 0.1$ kPa; left: Initial phase; right: Plastic nil step..... | 56 |
| Fig. 65: | FoS after ϕ -c reduction Initial phase and Plastic nil step for $c = 5$ kPa | 57 |
| Fig. 66: | Incremental deviatoric strains and plastic points after ϕ -c reduction for $c = 5$ kPa; left: Initial phase; right: Plastic nil step..... | 57 |
| Fig. 67: | FoS after ϕ -c reduction Construction fill | 58 |
| Fig. 68: | Incremental deviatoric strains and plastic points after as well as τ_{rel} before/after ϕ -c reduction Construction fill; left: $c = 0.1$ kPa; right: $c = 5$ kPa | 59 |
| Fig. 69: | BMs M_{min}/M_{max} after Construction fill..... | 60 |
| Fig. 70: | SFs Q_{min}/Q_{max} after Construction fill | 60 |
| Fig. 71: | Horizontal displacements u_x after Construction fill | 61 |
| Fig. 72: | Total displacements $ u $ after Construction fill | 61 |
| Fig. 73: | Evolution of anchor forces over calculation phases for $c = 0.1$ kPa | 62 |
| Fig. 74: | FoS after ϕ -c reduction Construction fill and Failure cases for $c = 0.1$ kPa | 63 |
| Fig. 75: | Incremental deviatoric strains and plastic points after as well as τ_{rel} before/after ϕ -c reduction Failure cases for $c = 0.1$ kPa; left: Failure anchor row 1; centre left: Failure anchor row 3; centre right: Failure anchor row 3+4; right: Failure anchor row 2+3 | 64 |
| Fig. 76: | FoS after ϕ -c reduction Construction fill and Failure cases for $c = 5$ kPa | 65 |
| Fig. 77: | Incremental deviatoric strains and plastic points after as well as τ_{rel} before/after ϕ -c reduction Failure cases for $c = 5$ kPa; left: Failure anchor row 1; centre left: Failure anchor row 3; centre right: Failure anchor row 3+4; right: Failure anchor row 2+3 | 65 |
| Fig. 78: | BMs M_{actual} after Construction fill and Failure cases for $c = 0.1$ kPa | 66 |
| Fig. 79: | BMs : Ratio M_{min} | 66 |
| Fig. 80: | SFs Q_{actual} after Construction fill and Failure cases for $c = 0.1$ kPa | 67 |
| Fig. 81: | SFs : Ratio Q_{min} | 68 |
| Fig. 82: | SFs : Ratio Q_{max} | 68 |
| Fig. 83: | Horizontal displacements u_x after Construction fill and Failure cases for $c = 0.1$ kPa | 69 |
| Fig. 84: | Horizontal displacements: Ratio $u_{x,max}$ | 70 |

| | | |
|-----------|--|----|
| Fig. 85: | Total displacements $ u $ after Construction fill and anchor Failure cases for $c = 0.1$ kPa | 70 |
| Fig. 86: | Total displacements: Ratio $ u _{\max}$ | 71 |
| Fig. 87: | Anchor forces after Construction fill and Failure cases for $c = 0.1$ kPa | 72 |
| Fig. 88: | FoS after ϕ -c reduction Construction fill and Failure cases for $c = 0.1$ kPa; EBs with constant skin resistance | 74 |
| Fig. 89: | Incremental deviatoric strains and plastic points after as well as τ_{rel} before/after ϕ -c reduction Failure cases for $c = 0.1$ kPa; EBs with constant skin resistance; left: Failure anchor row 1; centre left: Failure anchor row 3; centre right: Failure anchor row 3+4; right: Failure anchor row 2+3 | 74 |
| Fig. 90: | FoS after ϕ -c reduction Construction fill and Failure cases for $c = 0.1$ kPa; EBs with linear skin resistance | 75 |
| Fig. 91: | FoS after ϕ -c reduction Construction fill and Failure cases for $c = 5$ kPa; EBs with constant skin resistance | 76 |
| Fig. 92: | Incremental deviatoric strains and plastic points after as well as τ_{rel} before/after ϕ -c reduction Failure cases for $c = 5$ kPa; EBs with constant skin resistance; left: Failure anchor row 1; centre left: Failure anchor row 3; centre right: Failure anchor row 3+4; right: Failure anchor row 2+3 | 76 |
| Fig. 93: | FoS after ϕ -c reduction Construction fill and Failure cases for $c = 5$ kPa; EBs with linear skin resistance | 77 |
| Fig. 94: | Incremental deviatoric strains and plastic points after as well as τ_{rel} before/after ϕ -c reduction Failure cases for $c = 5$ kPa; EBs with linear skin resistance; left: Failure anchor row 1; centre left: Failure anchor row 3; centre right: Failure anchor row 3+4; right: Failure anchor row 2+3 | 77 |
| Fig. 95: | BM_s M_{actual} after Construction fill and Failure cases for $c = 0.1$ kPa; EBs with constant skin resistance | 78 |
| Fig. 96: | BM_s M_{actual} after Construction fill and Failure cases for $c = 0.1$ kPa; EBs with linear skin resistance | 79 |
| Fig. 97: | BM_s : Ratio M_{\min} ; EBs with constant skin resistance | 79 |
| Fig. 98: | BM_s : Ratio M_{\min} | 80 |
| Fig. 99: | SFs Q_{actual} after Construction fill and Failure cases for $c = 0.1$ kPa; EBs with constant skin resistance | 81 |
| Fig. 100: | SFs Q_{actual} after Construction fill and Failure cases for $c = 0.1$ kPa; EBs with linear skin resistance | 81 |
| Fig. 101: | SFs : Ratio Q_{\min} ; EBs with constant skin resistance | 82 |

| | | |
|-----------|---|----|
| Fig. 102: | <i>SFs</i> : Ratio Q_{\max} ; <i>EBs</i> with constant skin resistance..... | 82 |
| Fig. 103: | Horizontal displacements u_x after Construction fill and Failure cases for $c = 0.1$ kPa; <i>EBs</i> with constant skin resistance | 83 |
| Fig. 104: | Horizontal displacements u_x after Construction fill and Failure cases for $c = 0.1$ kPa; <i>EBs</i> with linear skin resistance..... | 84 |
| Fig. 105: | Horizontal displacements: Ratio $u_{x,\max}$; <i>EBs</i> with constant skin resistance | 84 |
| Fig. 106: | Total displacements $ u $ after Construction fill and Failure cases for $c = 0.1$ kPa; <i>EBs</i> with constant skin resistance | 85 |
| Fig. 107: | Total displacements $ u $ after Construction fill and Failure cases for $c = 0.1$ kPa; <i>EBs</i> with linear skin resistance..... | 86 |
| Fig. 108: | Total displacements: Ratio $ u _{\max}$; <i>EBs</i> with constant skin resistance | 86 |
| Fig. 109: | Anchor forces after Construction fill and Failure cases for $c = 0.1$ kPa; <i>EBs</i> with constant skin resistance..... | 87 |
| Fig. 110: | Anchor forces after Construction fill and Failure cases for $c = 0.1$ kPa; <i>EBs</i> with linear skin resistance..... | 88 |
| Fig. 111: | <i>FoS</i> after ϕ - c reduction Construction fill and Failure cases for $c = 0.1$ kPa; <i>HSS</i> model; <i>EBs</i> with constant skin resistance | 91 |
| Fig. 112: | <i>FoS</i> after ϕ - c reduction Construction fill and Failure cases for $c = 0.1$ kPa; <i>HSS</i> model; <i>EBs</i> with linear skin resistance..... | 91 |
| Fig. 113: | Incremental deviatoric strains and plastic points after as well as τ_{rel} before/after ϕ - c reduction anchor failure for $c = 0.1$ kPa; <i>HSS</i> model; <i>EBs</i> with linear skin resistance; left: Failure anchor row 1; centre left: Failure anchor row 3; centre right: Failure anchor row 3+4; right: Failure anchor row 2+3 | 92 |
| Fig. 114: | <i>BMs</i> M_{actual} after Construction fill and Failure cases for $c = 0.1$ kPa; <i>HSS</i> model; <i>EBs</i> with constant skin resistance | 93 |
| Fig. 115: | <i>SFs</i> Q_{actual} after Construction fill and Failure cases for $c = 0.1$ kPa; <i>HSS</i> model; <i>EBs</i> with constant skin resistance..... | 93 |
| Fig. 116: | Horizontal displacements u_x after Construction fill and Failure cases for $c = 0.1$ kPa; <i>HSS</i> model; <i>EBs</i> with constant skin resistance | 94 |
| Fig. 117: | Total displacements $ u $ after Construction fill and Failure cases for $c = 0.1$ kPa; <i>HSS</i> model; <i>EBs</i> with constant skin resistance | 95 |
| Fig. 118: | Anchor forces after Construction fill and Failure cases for $c = 0.1$ kPa; <i>HSS</i> model; <i>EBs</i> with constant skin resistance | 96 |
| Fig. 119: | Model dimensions ‘Final’ with discretised anchor grid in 3D..... | 98 |

| | |
|---|-----|
| Fig. 120: Mesh discretisation for model ‘Final’ in 3D; top left: Geogrid; top right: <i>EB</i> ; bottom left: <i>VE</i> | 99 |
| Fig. 121: <i>FoS</i> after ϕ -c reduction Plastic nil step for $c = 0.1$ kPa; 2D vs. 3D | 101 |
| Fig. 122: Incremental deviatoric strains and plastic points after as well as τ_{rel} before/after ϕ -c reduction Plastic nil step for model dimensions ‘Final’ with $c = 0.1$ kPa; left: 2D; right: 3D at $y = 10$ m..... | 101 |
| Fig. 123: <i>FoS</i> after ϕ -c reduction Plastic nil step for $c = 1$ kPa; 2D vs. 3D | 102 |
| Fig. 124: Incremental deviatoric strains and plastic points after as well as τ_{rel} before/after ϕ -c reduction Plastic nil step for model dimensions ‘Final’ with $c = 1$ kPa; left: 2D; right: 3D at $y = 10$ m..... | 102 |
| Fig. 125: <i>FoS</i> after ϕ -c reduction Plastic nil step for $c = 5$ kPa; 2D vs. 3D | 103 |
| Fig. 126: Incremental deviatoric strains and plastic points after as well as τ_{rel} before/after ϕ -c reduction Plastic nil step for model dimensions ‘Final’ with $c = 5$ kPa; left: 2D; right: 3D at $y = 10$ m..... | 103 |
| Fig. 127: <i>FoS</i> after ϕ -c reduction Construction fill; 2D vs. 3D | 104 |
| Fig. 128: Incremental deviatoric strains and plastic points after as well as τ_{rel} before/after ϕ -c reduction Construction fill for model dimensions ‘Final’ with $c = 5$ kPa; left: 2D; right: 3D at $y = 10$ m . | 105 |
| Fig. 129: <i>FoS</i> after ϕ -c reduction Construction fill and Failure cases for $c = 0.1$ kPa; 2D vs. 3D..... | 106 |
| Fig. 130: <i>FoS</i> after ϕ -c reduction Construction fill and Failure cases for $c = 5$ kPa; 2D vs. 3D | 106 |
| Fig. 131: Incremental deviatoric strains and plastic points after as well as τ_{rel} before/after ϕ -c reduction Failure cases for $c = 5$ kPa at $y = 10$ m; left: Failure anchor 5; centre left: Failure anchor 7; centre: Failure anchor 7+8; centre right: Failure anchor 6+7; right: Failure anchor 8+12 | 107 |
| Fig. 132: <i>BMs</i> $M_{22,actual}$ after Construction fill and single anchor failure cases for $c = 0.1$ kPa; 2D vs. 3D at $y = 7.50$ m..... | 108 |
| Fig. 133: <i>BMs</i> $M_{22,actual}$ after Construction fill for $c = 0.1$ kPa; 2D vs. 3D at $y = 7.50/10$ m..... | 108 |
| Fig. 134: <i>SFs</i> $Q_{23,actual}$ after Construction fill and single anchor failure cases for $c = 0.1$ kPa; 2D vs. 3D at $y = 7.50$ m..... | 109 |
| Fig. 135: <i>SFs</i> $Q_{23,actual}$ after Construction fill for $c = 0.1$ kPa; 2D vs. 3D at $y = 7.50/10$ m..... | 109 |
| Fig. 136: Horizontal displacements u_x after Construction fill and Failure cases for $c = 0.1$ kPa; 2D vs. 3D at $y = 7.50$ m | 110 |

| | |
|--|-----|
| Fig. 137: Total displacements $ u $ after Construction fill and Failure cases for $c = 0.1$ kPa; 2D vs. 3D at $y = 7.50$ m | 111 |
| Fig. 138: BMs $M_{22,actual}$ after Construction fill and double anchor failure cases for $c = 0.1$ kPa; EBs with linear skin resistance; 2D vs. 3D at $y = 7.50$ m..... | 112 |
| Fig. 139: BMs $M_{22,actual}$ after Construction fill for $c = 0.1$ kPa; EBs with linear skin resistance; 2D vs. 3D at $y = 7.50/10$ m..... | 112 |
| Fig. 140: SFs $Q_{23,actual}$ after Construction fill and double anchor failure cases for $c = 0.1$ kPa; EBs with linear skin resistance; 2D vs. 3D at $y = 7.50$ m | 113 |
| Fig. 141: SFs $Q_{23,actual}$ after Construction fill for $c = 0.1$ kPa; EBs with linear skin resistance; 2D vs. 3D at $y = 7.50/10$ m..... | 113 |
| Fig. 142: Horizontal displacements u_x after Construction fill and Failure cases for $c = 0.1$ kPa; EBs with linear skin resistance; 2D vs. 3D at $y = 7.50$ m..... | 114 |
| Fig. 143: Total displacements $ u $ after Construction fill and Failure cases for $c = 0.1$ kPa; EBs with linear skin resistance; 2D vs. 3D at $y = 7.50$ m | 115 |
| Fig. 144: BMs $M_{22,actual}$ after Construction fill and single anchor failure cases for $c = 0.1$ kPa; VEs 3D at $y = 2.50$ m vs. EBs with constant skin resistance 2D | 116 |
| Fig. 145: BMs $M_{22,actual}$ after Construction fill and double anchor failure cases for $c = 0.1$ kPa; VEs 3D at $y = 2.50$ m vs. EBs with constant skin resistance 3D at $y = 7.50$ m | 116 |
| Fig. 146: BMs $M_{22,actual}$ after Construction fill for $c = 0.1$ kPa; VEs 3D at $y = 2.50/5$ m vs. EBs with constant skin resistance 3D at $y = 7.50/10$ m | 117 |
| Fig. 147: SFs $Q_{23,actual}$ after Construction fill and single anchor failure cases for $c = 0.1$ kPa; VEs 3D at $y = 2.50$ m vs. EBs with constant skin resistance 3D at $y = 7.50$ m | 118 |
| Fig. 148: SFs $Q_{23,actual}$ after Construction fill and double anchor failure cases for $c = 0.1$ kPa; VEs 3D at $y = 2.50$ m vs. EBs with constant skin resistance 3D at $y = 7.50$ m | 118 |
| Fig. 149: SFs $Q_{23,actual}$ after Construction fill for $c = 0.1$ kPa; VEs 3D at $y = 2.50/5$ m vs. EBs with constant skin resistance 3D at $y = 7.50/10$ m | 119 |
| Fig. 150: Horizontal displacements u_x after Construction fill and Failure cases for $c = 0.1$ kPa; VEs 3D at $y = 2.50$ m vs. EBs with constant skin resistance 2D..... | 120 |

| | |
|--|-----|
| Fig. 151: Total displacements $ u $ after Construction fill and Failure cases for $c = 0.1$ kPa; VEs 3D at $y = 2.50$ m vs. EBs with constant skin resistance 2D..... | 120 |
| Fig. 152: FoS after ϕ -c reduction Pre-stressing anchor 1 | 128 |
| Fig. 153: FoS after ϕ -c reduction Pre-stressing anchor 2 | 128 |
| Fig. 154: FoS after ϕ -c reduction Pre-stressing anchor 3 | 129 |
| Fig. 155: FoS after ϕ -c reduction Pre-stressing anchor 1, 2 and 3 for $c = 0.1$ kPa | 129 |
| Fig. 156: Incremental deviatoric strains and plastic points after as well as τ_{rel} before/after ϕ -c reduction Pre-stressing anchor 3; left: $c = 0.1$ kPa; right: $c = 5$ kPa | 130 |
| Fig. 157: BM_s M_{min}/M_{max} after Pre-stressing anchor 3..... | 131 |
| Fig. 158: SFs Q_{min}/Q_{max} after Pre-stressing anchor 3 | 131 |
| Fig. 159: Horizontal displacements u_x after Pre-stressing anchor 3..... | 132 |
| Fig. 160: Total displacements $ u $ after Pre-stressing anchor 3 | 132 |
| Fig. 161: Evolution of BM_s over calculation phases for $c = 0.1$ kPa..... | 133 |
| Fig. 162: Evolution of anchor forces over calculation phases for $c = 5$ kPa ... | 134 |
| Fig. 163: FoS after ϕ -c reduction Construction fill and Failure cases for $c = 1$ kPa | 134 |
| Fig. 164: FoS after ϕ -c reduction Construction fill and Failure cases for $c = 3$ kPa | 135 |
| Fig. 165: BM_s M_{actual} after Construction fill and Failure cases for $c = 5$ kPa .. | 135 |
| Fig. 166: SFs Q_{actual} after Construction fill and Failure cases for $c = 5$ kPa | 136 |
| Fig. 167: Horizontal displacements u_x after Construction fill and Failure cases for $c = 5$ kPa | 136 |
| Fig. 168: Total displacements $ u $ after Construction fill and Failure cases for $c = 5$ kPa | 137 |
| Fig. 169: Anchor forces after Construction fill and Failure cases for $c = 5$ kPa | 137 |
| Fig. 170: FoS after ϕ -c reduction Pre-stressing anchor 1; EBs with constant skin resistance..... | 138 |
| Fig. 171: FoS after ϕ -c reduction Pre-stressing anchor 2; EBs with constant skin resistance..... | 138 |
| Fig. 172: FoS after ϕ -c reduction Pre-stressing anchor 3; EBs with constant skin resistance..... | 139 |
| Fig. 173: FoS after ϕ -c reduction Construction fill; EBs with constant skin resistance..... | 139 |

| | |
|---|-----|
| Fig. 174: <i>FoS</i> after ϕ - c reduction Construction fill and Failure cases for $c = 1$ kPa; <i>EBs</i> with constant skin resistance..... | 140 |
| Fig. 175: <i>FoS</i> after ϕ - c reduction Construction fill and Failure cases for $c = 3$ kPa; <i>EBs</i> with constant skin resistance..... | 140 |
| Fig. 176: <i>FoS</i> after ϕ - c reduction Pre-stressing anchor 1; <i>EBs</i> with linear skin resistance..... | 141 |
| Fig. 177: <i>FoS</i> after ϕ - c reduction Pre-stressing anchor 2; <i>EBs</i> with linear skin resistance..... | 141 |
| Fig. 178: <i>FoS</i> after ϕ - c reduction Pre-stressing anchor 3; <i>EBs</i> with linear skin resistance..... | 142 |
| Fig. 179: <i>FoS</i> after ϕ - c reduction Construction fill; <i>EBs</i> with linear skin resistance | 142 |
| Fig. 180: <i>FoS</i> after ϕ - c reduction Construction fill and Failure cases for $c = 1$ kPa; <i>EBs</i> with linear skin resistance..... | 143 |
| Fig. 181: <i>FoS</i> after ϕ - c reduction Construction fill and Failure cases for $c = 3$ kPa; <i>EBs</i> with linear skin resistance..... | 143 |
| Fig. 182: <i>BMs</i> : Ratio M_{\min} ; <i>EBs</i> with linear skin resistance | 144 |
| Fig. 183: <i>SFs</i> : Ratio Q_{\min} ; <i>EBs</i> with linear skin resistance | 144 |
| Fig. 184: <i>SFs</i> : Ratio Q_{\max} ; <i>EBs</i> with linear skin resistance..... | 145 |
| Fig. 185: Horizontal displacements: Ratio $u_{x,\max}$; <i>EBs</i> with linear skin resistance | 145 |
| Fig. 186: Total displacements: Ratio $ u _{\max}$; <i>EBs</i> with linear skin resistance... | 146 |
| Fig. 187: <i>FoS</i> after ϕ - c reduction during construction of the <i>RW</i> for $c = 0.1$ kPa; <i>HSS</i> model..... | 147 |
| Fig. 188: <i>FoS</i> after ϕ - c reduction Construction fill and Failure cases for $c = 0.1$ kPa; <i>HSS</i> model..... | 147 |
| Fig. 189: <i>BMs</i> M_{actual} after Construction fill and Failure cases for $c = 0.1$ kPa; <i>HSS</i> model..... | 148 |
| Fig. 190: <i>SFs</i> Q_{actual} after Construction fill and Failure cases for $c = 0.1$ kPa; <i>HSS</i> model | 148 |
| Fig. 191: Horizontal displacements u_x after Construction fill and Failure cases for $c = 0.1$ kPa; <i>HSS</i> model..... | 149 |
| Fig. 192: Total displacements $ u $ after Construction fill and Failure cases for $c = 0.1$ kPa; <i>HSS</i> model..... | 149 |
| Fig. 193: Anchor forces after Construction fill and Failure cases for $c = 0.1$ kPa; <i>HSS</i> model..... | 150 |
| Fig. 194: <i>BMs</i> M_{actual} after Construction fill and Failure cases for $c = 0.1$ kPa; <i>HSS</i> model; <i>EBs</i> with linear skin resistance..... | 151 |

| | | |
|-----------|---|-----|
| Fig. 195: | <i>SFs</i> Q_{actual} after Construction fill and Failure cases for $c = 0.1$ kPa; <i>HSS</i> model; <i>EBs</i> with linear skin resistance | 151 |
| Fig. 196: | Horizontal displacements u_x after Construction fill and Failure cases for $c = 0.1$ kPa; <i>HSS</i> model; <i>EBs</i> with linear skin resistance.. | 152 |
| Fig. 197: | Total displacements $ u $ after Construction fill and Failure cases for $c = 0.1$ kPa; <i>HSS</i> model; <i>EBs</i> with linear skin resistance..... | 152 |
| Fig. 198: | Anchor forces after Construction fill and Failure cases for $c = 0.1$ kPa; <i>HSS</i> model; <i>EBs</i> with linear skin resistance | 153 |
| Fig. 199: | <i>BM</i> s $M_{11,\text{actual}}$ after Construction fill and single anchor failure cases for $c = 0.1$ kPa; 2D vs. 3D at $y = 7.50$ m..... | 154 |
| Fig. 200: | <i>BM</i> s $M_{11,\text{actual}}$ after Construction fill and double anchor failure cases for $c = 0.1$ kPa; 2D vs. 3D at $y = 7.50$ m | 154 |
| Fig. 201: | <i>BM</i> s $M_{22,\text{actual}}$ after Construction fill and double anchor failure cases for $c = 0.1$ kPa; 2D vs. 3D at $y = 7.50$ m | 155 |
| Fig. 202: | <i>BM</i> s $M_{22,\text{actual}}$ after Failure anchor 5 for $c = 0.1$ kPa; 2D vs. 3D at $y = 7.50/10$ m..... | 155 |
| Fig. 203: | Top view of <i>BM</i> s $M_{11,\text{actual}}/M_{22,\text{actual}}$ after Construction fill for $c = 0.1$ kPa; top: Horizontal cross section at level of anchor row 2; bottom: Horizontal cross section between anchor row 2 and anchor row 3 | 156 |
| Fig. 204: | <i>SFs</i> $Q_{13,\text{actual}}$ after Construction fill and single anchor failure cases for $c = 0.1$ kPa; 2D vs. 3D at $y = 7.50$ m..... | 157 |
| Fig. 205: | <i>SFs</i> $Q_{13,\text{actual}}$ after Construction fill and double anchor failure cases for $c = 0.1$ kPa; 2D vs. 3D at $y = 7.50$ m..... | 157 |
| Fig. 206: | <i>SFs</i> $Q_{23,\text{actual}}$ after Construction fill and double anchor failure cases for $c = 0.1$ kPa; 2D vs. 3D at $y = 7.50$ m..... | 158 |
| Fig. 207: | <i>SFs</i> $Q_{23,\text{actual}}$ after Failure anchor 5 for $c = 0.1$ kPa; 2D vs. 3D at $y = 7.50/10$ m..... | 158 |
| Fig. 208: | Horizontal displacements u_x after Construction fill for $c = 0.1$ kPa; 2D vs. 3D at $y = 7.50/10$ m..... | 159 |
| Fig. 209: | Horizontal displacements u_x after Failure anchor 5 for $c = 0.1$ kPa; 2D vs. 3D at $y = 7.50/10$ m..... | 159 |
| Fig. 210: | Total displacements $ u $ after Construction fill for $c = 0.1$ kPa; 2D vs. 3D at $y = 7.50/10$ m | 160 |
| Fig. 211: | Total displacements $ u $ after Failure anchor 5 for $c = 0.1$ kPa; 2D vs. 3D at $y = 7.50/10$ m | 160 |
| Fig. 212: | <i>FoS</i> after ϕ - c reduction Construction fill and Failure cases for $c = 0.1$ kPa; <i>EBs</i> with constant skin resistance; 2D vs. 3D | 161 |

| | |
|--|-----|
| Fig. 213: <i>FoS</i> after ϕ - <i>c</i> reduction Construction fill and Failure cases for $c = 5$ kPa; <i>EBs</i> with constant skin resistance; 2D vs. 3D | 161 |
| Fig. 214: <i>BMs</i> $M_{11,actual}$ after Construction fill and single anchor failure cases for $c = 0.1$ kPa; <i>EBs</i> with constant skin resistance; 2D vs. 3D at $y = 7.50$ m..... | 162 |
| Fig. 215: <i>BMs</i> $M_{11,actual}$ after Construction fill and double anchor failure cases for $c = 0.1$ kPa; <i>EBs</i> with constant skin resistance; 2D vs. 3D at $y = 7.50$ m..... | 162 |
| Fig. 216: <i>BMs</i> $M_{22,actual}$ after Construction fill and single anchor failure cases for $c = 0.1$ kPa; <i>EBs</i> with constant skin resistance; 2D vs. 3D at $y = 7.50$ m..... | 163 |
| Fig. 217: <i>BMs</i> $M_{22,actual}$ after Construction fill and double anchor failure cases for $c = 0.1$ kPa; <i>EBs</i> with constant skin resistance; 2D vs. 3D at $y = 7.50$ m..... | 163 |
| Fig. 218: <i>BMs</i> $M_{22,actual}$ after Construction fill for $c = 0.1$ kPa; <i>EBs</i> with constant skin resistance; 2D vs. 3D at $y = 7.50/10$ m | 164 |
| Fig. 219: <i>SFs</i> $Q_{13,actual}$ after Construction fill and single anchor failure cases for $c = 0.1$ kPa; <i>EBs</i> with constant skin resistance; 2D vs. 3D at $y = 7.50$ m..... | 164 |
| Fig. 220: <i>SFs</i> $Q_{13,actual}$ after Construction fill and double anchor failure cases for $c = 0.1$ kPa; <i>EBs</i> with constant skin resistance; 2D vs. 3D at $y = 7.50$ m..... | 165 |
| Fig. 221: <i>SFs</i> $Q_{23,actual}$ after Construction fill and single anchor failure cases for $c = 0.1$ kPa; <i>EBs</i> with constant skin resistance; 2D vs. 3D at $y = 7.50$ m..... | 165 |
| Fig. 222: <i>SFs</i> $Q_{23,actual}$ after Construction fill and double anchor failure cases for $c = 0.1$ kPa; <i>EBs</i> with constant skin resistance; 2D vs. 3D at $y = 7.50$ m..... | 166 |
| Fig. 223: <i>SFs</i> $Q_{23,actual}$ after Construction fill for $c = 0.1$ kPa; <i>EBs</i> with constant skin resistance; 2D vs. 3D at $y = 7.50/10$ m | 166 |
| Fig. 224: Horizontal displacements u_x after Construction fill and Failure cases for $c = 0.1$ kPa; <i>EBs</i> with constant skin resistance; 2D vs. 3D at $y = 7.50$ m..... | 167 |
| Fig. 225: Horizontal displacements u_x after Construction fill for $c = 0.1$ kPa; <i>EBs</i> with constant skin resistance; 2D vs. 3D at $y = 7.50/10$ m..... | 167 |
| Fig. 226: Total displacements $ u $ after Construction fill and Failure cases for $c = 0.1$ kPa; <i>EBs</i> with constant skin resistance; 2D vs. 3D at $y = 7.50$ m | 168 |
| Fig. 227: Total displacements $ u $ after Construction fill for $c = 0.1$ kPa; <i>EBs</i> with constant skin resistance; 2D vs. 3D at $y = 7.50/10$ m | 168 |

| | | |
|-----------|---|-----|
| Fig. 228: | <i>FoS</i> after ϕ - <i>c</i> reduction Construction fill and Failure cases for $c = 0.1$ kPa; <i>EBs</i> with linear skin resistance; 2D vs. 3D | 169 |
| Fig. 229: | <i>FoS</i> after ϕ - <i>c</i> reduction Construction fill and Failure cases for $c = 5$ kPa; <i>EBs</i> with linear skin resistance; 2D vs. 3D..... | 169 |
| Fig. 230: | <i>BMs</i> $M_{11,actual}$ after Construction fill and single anchor failure cases for $c = 0.1$ kPa; <i>EBs</i> with linear skin resistance; 2D vs. 3D at $y = 7.50$ m | 170 |
| Fig. 231: | <i>BMs</i> $M_{11,actual}$ after Construction fill and double anchor failure cases for $c = 0.1$ kPa; <i>EBs</i> with linear skin resistance; 2D vs. 3D at $y = 7.50$ m | 170 |
| Fig. 232: | <i>BMs</i> $M_{22,actual}$ after Construction fill and single anchor failure cases for $c = 0.1$ kPa; <i>EBs</i> with linear skin resistance; 2D vs. 3D at $y = 7.50$ m | 171 |
| Fig. 233: | <i>SFs</i> $Q_{13,actual}$ after Construction fill and single anchor failure cases for $c = 0.1$ kPa; <i>EBs</i> with linear skin resistance; 2D vs. 3D at $y = 7.50$ m | 171 |
| Fig. 234: | <i>SFs</i> $Q_{13,actual}$ after Construction fill and double anchor failure cases for $c = 0.1$ kPa; <i>EBs</i> with linear skin resistance; 2D vs. 3D at $y = 7.50$ m | 172 |
| Fig. 235: | <i>SFs</i> $Q_{23,actual}$ after Construction fill and single anchor failure cases for $c = 0.1$ kPa; <i>EBs</i> with linear skin resistance; 2D vs. 3D at $y = 7.50$ m | 172 |
| Fig. 236: | Horizontal displacements u_x after Construction fill for $c = 0.1$ kPa; <i>EBs</i> with linear skin resistance; 2D vs. 3D at $y = 7.50/10$ m | 173 |
| Fig. 237: | Total displacements $ u $ after Construction fill for $c = 0.1$ kPa; <i>EBs</i> with linear skin resistance; 2D vs. 3D at $y = 7.50/10$ m..... | 173 |
| Fig. 238: | Modelling sequence for grout body discretised by means of <i>Ves</i> | 174 |
| Fig. 239: | <i>FoS</i> after ϕ - <i>c</i> reduction Construction fill and Failure cases for $c = 0.1$ kPa; <i>VEs</i> 3D vs. <i>EBs</i> with constant skin resistance 3D | 175 |
| Fig. 240: | <i>BMs</i> $M_{11,actual}$ after Construction fill and single anchor failure cases for $c = 0.1$ kPa; <i>VEs</i> 3D at $y = 2.50$ m vs. <i>EBs</i> with constant skin resistance 3D at $y = 7.50$ m | 175 |
| Fig. 241: | <i>BMs</i> $M_{11,actual}$ after Construction fill and double anchor failure cases for $c = 0.1$ kPa; <i>VEs</i> 3D at $y = 2.50$ m vs. <i>EBs</i> with constant skin resistance 3D at $y = 7.50$ m..... | 176 |
| Fig. 242: | <i>BMs</i> $M_{22,actual}$ after Construction fill and single anchor failure cases for $c = 0.1$ kPa; <i>VEs</i> 3D at $y = 2.50$ m vs. <i>EBs</i> with constant skin resistance 2D..... | 176 |

| | | |
|-----------|---|-----|
| Fig. 243: | <i>BMs</i> $M_{22,actual}$ after Construction fill and single anchor failure cases for $c = 0.1$ kPa; <i>VEs</i> 3D at $y = 2.50$ m vs. <i>EBs</i> with constant skin resistance 3D at $y = 7.50$ m | 177 |
| Fig. 244: | <i>SFs</i> $Q_{13,actual}$ after Construction fill and single anchor failure cases for $c = 0.1$ kPa; <i>VEs</i> 3D at $y = 2.50$ m vs. <i>EBs</i> with constant skin resistance 3D at $y = 7.50$ m | 177 |
| Fig. 245: | <i>SFs</i> $Q_{13,actual}$ after Construction fill and double anchor failure cases for $c = 0.1$ kPa; <i>VEs</i> 3D at $y = 2.50$ m vs. <i>EBs</i> with constant skin resistance 3D at $y = 7.50$ m | 178 |
| Fig. 246: | <i>SFs</i> $Q_{23,actual}$ after Construction fill and single anchor failure cases for $c = 0.1$ kPa; <i>VEs</i> 3D at $y = 2.50$ m vs. <i>EBs</i> with constant skin resistance 2D | 178 |
| Fig. 247: | <i>SFs</i> $Q_{23,actual}$ after Construction fill and double anchor failure cases for $c = 0.1$ kPa; <i>VEs</i> 3D at $y = 2.50$ m vs. <i>EBs</i> with constant skin resistance 2D | 179 |
| Fig. 248: | Horizontal displacements u_x after Construction fill and Failure cases for $c = 0.1$ kPa; <i>VEs</i> 3D at $y = 2.50$ m vs. <i>EBs</i> with constant skin resistance 3D at $y = 7.50$ m | 179 |
| Fig. 249: | Horizontal displacements u_x after Construction fill for $c = 0.1$ kPa; <i>VEs</i> 3D at $y = 2.50/5$ m vs. <i>EBs</i> with constant skin resistance 3D at $y = 7.50/10$ m..... | 180 |
| Fig. 250: | Total displacements $ u $ after Construction fill and Failure cases for $c = 0.1$ kPa; <i>VEs</i> 3D at $y = 2.50$ m vs. <i>EBs</i> with constant skin resistance 3D at $y = 7.50$ m | 180 |
| Fig. 251: | Total displacements $ u $ after Construction fill for $c = 0.1$ kPa; <i>VEs</i> 3D at $y = 2.50/5$ m vs. <i>EBs</i> with constant skin resistance 3D at $y = 7.50/10$ m..... | 181 |
| Fig. 252: | <i>BMs</i> $M_{22,actual}$ after Construction fill and single row failure cases for $c = 0.1$ kPa; 2D vs. 3D (Plate) at $y = 7.50$ m..... | 182 |
| Fig. 253: | <i>BMs</i> $M_{22,actual}$ after Construction fill and double row failure cases for $c = 0.1$ kPa; 2D vs. 3D (Plate) at $y = 7.50$ m..... | 182 |
| Fig. 254: | <i>SFs</i> $Q_{23,actual}$ after Construction fill and single row failure cases for $c = 0.1$ kPa; 2D vs. 3D (Plate) at $y = 7.50$ m..... | 183 |
| Fig. 255: | <i>SFs</i> $Q_{23,actual}$ after Construction fill and double row failure cases for $c = 0.1$ kPa; 2D vs. 3D (Plate) at $y = 7.50$ m..... | 183 |
| Fig. 256: | Horizontal displacements u_x after Construction fill and Failure cases for $c = 0.1$ kPa; 2D vs. 3D (Plate) at $y = 7.50$ m | 184 |
| Fig. 257: | Total displacements $ u $ after Construction fill and Failure cases for $c = 0.1$ kPa; 2D vs. 3D (Plate) at $y = 7.50$ m..... | 184 |

| | |
|--|-----|
| Fig. 258: <i>BMs</i> $M_{22,actual}$ after Construction fill and single row failure cases for $c = 0.1$ kPa; 2D (Plate) vs. 3D (Plate) at $y = 7.50$ m | 185 |
| Fig. 259: <i>BMs</i> $M_{22,actual}$ after Construction fill and double row failure cases for $c = 0.1$ kPa; 2D (Plate) vs. 3D (Plate) at $y = 7.50$ m | 185 |
| Fig. 260: <i>SFs</i> $Q_{23,actual}$ after Construction fill and single row failure cases for $c = 0.1$ kPa; 2D (Plate) vs. 3D (Plate) at $y = 7.50$ m | 186 |
| Fig. 261: <i>SFs</i> $Q_{23,actual}$ after Construction fill and double row failure cases for $c = 0.1$ kPa; 2D (Plate) vs. 3D (Plate) at $y = 7.50$ m | 186 |
| Fig. 262: Horizontal displacements u_x after Construction fill and Failure cases for $c = 0.1$ kPa; 2D (Plate) vs. 3D (Plate) at $y = 7.50$ m | 187 |
| Fig. 263: Total displacements $ u $ after Construction fill and Failure cases for $c = 0.1$ kPa; 2D (Plate) vs. 3D (Plate) at $y = 7.50$ m | 187 |
| Fig. 264: <i>BMs</i> $M_{22,actual}$ after Construction fill and single row failure cases for $c = 0.1$ kPa; 3D (Plate) at 7.50 m vs. 3D (Geogrid) at $y = 7.50$ m | 188 |
| Fig. 265: <i>BMs</i> $M_{22,actual}$ after Construction fill and double row failure cases for $c = 0.1$ kPa; 3D (Plate) at 7.50 m vs. 3D (Geogrid) at $y = 7.50$ m | 188 |
| Fig. 266: <i>SFs</i> $Q_{23,actual}$ after Construction fill and single row failure cases for $c = 0.1$ kPa; 3D (Plate) at 7.50 m vs. 3D (Geogrid) at $y = 7.50$ m ... | 189 |
| Fig. 267: <i>SFs</i> $Q_{23,actual}$ after Construction fill and double row failure cases for $c = 0.1$ kPa; 3D (Plate) at 7.50 m vs. 3D (Geogrid) at $y = 7.50$ m | 189 |
| Fig. 268: Horizontal displacements u_x after Construction fill and Failure cases for $c = 0.1$ kPa; 3D (Plate) at 7.50 m vs. 3D (Geogrid) at $y = 7.50$ m | 190 |
| Fig. 269: Total displacements $ u $ after Construction fill and Failure cases for $c = 0.1$ kPa; 3D (Plate) at 7.50 m vs. 3D (Geogrid) at $y = 7.50$ m ... | 190 |

List of tables

| | | |
|----------|--|----|
| Tab. 1: | Characteristics of anchorages (acc. to Austrian Standards Institute, 2013)..... | 4 |
| Tab. 2: | Standards for design, execution and testing | 9 |
| Tab. 3: | Specifications for Dywidag bar anchors (acc. to DSI Underground GmbH, 2019c) | 11 |
| Tab. 4: | Specifications for Dywidag strand anchors (acc. to DSI Underground GmbH, 2019c)..... | 12 |
| Tab. 5: | Loading sequence for investigation tests (Austrian Standards Institute, 2019)..... | 22 |
| Tab. 6: | Loading sequence for suitability tests (Austrian Standards Institute, 2019)..... | 22 |
| Tab. 7: | Loading sequence for acceptance tests (Austrian Standards Institute, 2019)..... | 23 |
| Tab. 8: | Recommended ground parameters (acc. to 3G Gruppe Geotechnik Graz ZT GmbH, 2017) | 43 |
| Tab. 9: | Parameters of soil and fill for the <i>MC</i> model | 45 |
| Tab. 10: | Parameters of soil and fill for the <i>HSS</i> model | 45 |
| Tab. 11: | Parameters of wall modelled with plate elements | 46 |
| Tab. 12: | Parameters of tendon modelled with node-to-node anchors | 46 |
| Tab. 13: | Parameters of grout body modelled with geogrid and <i>EB</i> elements | 47 |
| Tab. 14: | Calculation phases for model with pre-stressing of the anchors | 48 |
| Tab. 15: | <i>FoS</i> after φ -c reduction Plastic nil step for different model dimensions with varying cohesion | 55 |
| Tab. 16: | <i>FoS</i> after φ -c reduction in the Initial phase and Plastic nil step for model dimensions ‘Final’, with varying cohesion..... | 58 |
| Tab. 17: | Results of calculation phase Construction fill | 63 |
| Tab. 18: | Results of the calculation phases Construction fill and Failure cases..... | 73 |
| Tab. 19: | Results of the calculation phases Construction fill and Failure cases; <i>EBs</i> with constant skin resistance | 89 |
| Tab. 20: | Results of the calculation phases Construction fill and Failure cases; <i>EBs</i> with linear skin resistance..... | 90 |
| Tab. 21: | Results of the calculation phases Construction fill and Failure cases; <i>HSS</i> model with $c = 0.1$ kPa..... | 97 |

| | | |
|----------|---|-----|
| Tab. 22: | Parameters of wall modelled with plate elements in 3D | 98 |
| Tab. 23: | Parameters of grout body modelled with <i>VEs</i> in 3D | 99 |
| Tab. 24: | Failure cases for 3D <i>FEAs</i> | 100 |

List of symbols and abbreviations

Small letters

| | | |
|--------------|-------------------------|---|
| d_c | [mm] | Diameter of the most corroded wire in the seven-wired strand assembly |
| d_{LOL} | [mm] | Diameter of the corroded wire in the seven-wired strand assembly which provides stability for the lock-off load |
| d_p | [mm] | Diameter of the smallest pristine wire in the seven-wired strand assembly |
| f_{el} | [kN/m ²] | Transition from elastic to elastoplastic behaviour |
| f_{pk} | [kN/m ²] | Characteristic stress value of the ultimate tensile strength of the tendon |
| $f_{p,0.1k}$ | [kN/m ²] | Characteristic value of the stress in the tendon which leads to 0.1% remaining elongation |
| $f_{t,0.2k}$ | [kN/m ²] | Characteristic value of the stress in the tendon which leads to 0.2% remaining elongation |
| k_s | [mm] | Creep rate |
| s_a | [mm] | Displacement of the anchor head at the time t_a |
| s_b | [mm] | Displacement of the anchor head at the time t_b |
| t_a | [min] | Start of the respective time interval |
| t_b | [min] | End of the respective time interval |
| x | [mm ² or mm] | Minimum corroded wire area in Eq. 17 or minimum corroded wire short axis diameter in Eq. 18 |
| y | [kN] | Reduced loading capacity of corroded strand tendon |

Capital letters

| | | |
|----------|----------------------|---|
| A | [mm ²] | Area of the corroded wire in the seven-wired strand assembly which provides stability for the lock-off load |
| A_C | [mm ²] | Area of the most corroded wire in the seven-wired strand assembly |
| A_t | [m ²] | Area of the tendon |
| C_B | [kN/m] | Stiffness of spring representing the ground |
| C_S | [kN/m] | Stiffness of spring representing the anchor |
| E_t | [kN/m ²] | Elastic modulus of the tendon |
| $F_z(x)$ | [kN] | Tensile force along the tendon |
| L_A | [m] | Anchor length |

| | | |
|--------------|-----------|--|
| L_{app} | [m] | Apparent free tendon length |
| L_e | [m] | External length of tendon |
| L_{fixed} | [m] | Fixed anchor length |
| L_{free} | [m] | Free anchor length |
| L_{tb} | [m] | Tendon-bond length |
| L_{tf} | [m] | Tendon-free length |
| P_0 | [kN] | Lock-off load |
| P_a | [kN] | Datum load |
| P_B | [kN] | Pre-stressing force of the spring representing the ground |
| $P_{B,Z}$ | [kN] | $P_B - Z_B$ |
| P_d | [kN] | Design value of the anchor load |
| P_k | [kN] | Characteristic value of the anchor load |
| P_P | [kN] | Proof load |
| P_S | [kN] | Pre-stressing force of the spring representing the anchor |
| $P_{S,Z}$ | [kN] | $P_S + Z_S$ |
| R | [mm/year] | User supplied corrosion rate |
| $R_{a;d}$ | [kN] | Design value of the pull-out resistance |
| $R_{a;k}$ | [kN] | Characteristic value of the pull-out resistance |
| R_{pk} | [kN] | Characteristic value of the ultimate tensile strength of the tendon |
| $R_{p,0.1k}$ | [kN] | Characteristic value of the force in the tendon which leads to 0.1% remaining elongation |
| $R_{t,0.2k}$ | [kN] | Characteristic value of the force in the tendon which leads to 0.2% remaining elongation |
| $R_{t;d}$ | [kN] | Design value of the structural resistance of the tendon |
| $T(x)$ | [kN] | Shear force along the grout body |
| Z | [kN] | External tensile force applied to the coupled spring system |
| Z_B | [kN] | Amount of Z taken by the ground |
| Z_{gr} | [kN] | Magnitude of Z where pre-stressing force within the ground is lost |
| Z_S | [kN] | Amount of Z taken by the anchor |

Small greek letters

| | | |
|---------------|-----|---|
| γ_a | [-] | Partial safety factor for the pull-out resistance |
| γ_E | [-] | Partial safety factor for the effect of an action |
| γ_s | [-] | Partial safety factor for the tendon |
| δ_B | [m] | Compression of the spring representing the ground before the lock-off |
| δ_S | [m] | Elongation of the spring representing the anchor before the lock-off |
| δ_{SZ} | [m] | Deformation of coupled spring system after the lock-off |
| η | [-] | Factor depending on the consequence class |
| τ_{rel} | [-] | Relative shear stresses |

Capital greek letters

| | | |
|-----------------|------|-----------------------------------|
| ΔP_f | [kN] | Friction loss |
| ΔS_{el} | [m] | Elastic contraction of the tendon |

Abbreviations

| | | |
|------|--------|--|
| BM | | Bending moment |
| EB | | Embedded beam |
| ERDC | | U.S. Army Engineer Research and Development Center |
| FEA | | Finite element analysis |
| FM | | Failure mechanism |
| FoS | | Factor of safety |
| GEO | | Geotechnical failure |
| HSS | | Hardening soil small |
| LOS | [year] | Length of service |
| MC | | Mohr-Coulomb |
| NDT | | Non-destructive test |
| PUP | | Probability of unsatisfactory performance |
| RAL | [year] | Remaining anchor life |
| RW | | Retaining wall |
| SCC | | Stress corrosion cracking |

| | | |
|-----|--------|--------------------|
| SF | | Shear force |
| STR | | Structural failure |
| TTF | [year] | Time-to-failure |
| VE | | Volume element |

1 Introduction

Anchorage technology has revolutionised geotechnical engineering and become integral to the field. Through the development of ground anchors, it was suddenly possible to transfer high tensile forces into the subsoil. This discovery resulted in intensive studies on ground anchors and the rapid advancement of the technology. Until the early 60s, ground anchors had been mainly used for temporary support measures. Afterwards, corrosion protection systems were developed, offering the possibility of permanent force transmission. Nowadays, Eurocode 7 (Austrian Standards Institute, 2009) regulates the design process for ground anchors. Nevertheless, corrosion and other causes of failure are essential for those permanent anchors.

Although Eurocode 7 (Austrian Standards Institute, 2009) defines a special design situation which should consider the consequences of individual ground anchor failure, there are no clear regulations on how the loss of anchors or, for example, a corrosion related decrease of their pre-stressing force should be dealt with during the design process. This lack is most likely because complex 3D stress states are involved when ground anchors fail. Because 3D finite element analyses (*FEAs*) are time-consuming and resource-intensive, and therefore often unsuitable for practical purposes, this thesis determines whether 3D effects can be realistically reproduced by 2D *FEAs*. Previous research has often been limited to an investigation of the failure of struts (e.g. Pong *et al.*, 2012; Zhang *et al.*, 2018), whereas Zhao *et al.* (2018) conducted numerical studies concerning ground anchor failure for a deep excavation retained by anchored pile walls.

After a brief introduction and the general classification of anchorages, chapter 2 of this thesis focuses on the theoretical background regarding ground anchors. Possible failure modes are discussed before chapter 3 gives an overview on present standards and guidelines concerning ground anchor failure. In addition, a software product is presented – namely, CAS_Stab-R (Warren *et al.*, 2017), which is able to predict the remaining anchor life (*RAL*) in terms of corrosion.

Chapter 4 covers 2D *FEAs*, which were conducted using PLAXIS 2D (Brinkgreve *et al.*, 2018b), on the behaviour of an anchored retaining wall (*RW*) affected by row-wise ground anchor failure. By means of a multiple-anchored *RW* in Salzburg, it is shown how ground anchor failure affects the overall stability of the structure, the *RW* itself and the surrounding anchors.

Last, before the final conclusion is drawn in chapter 6, the influence of individual ground anchor failure is investigated in chapter 5, aiming to validate the results from 2D calculations by means of 3D *FEAs*. For this purpose, PLAXIS 3D (Brinkgreve *et al.*, 2018a) was used to simulate the failure of individual tension members, whereby all results are compared to those obtained from 2D *FEAs*.

2 Anchorages and anchored structures

2.1 General

Today's state-of-the-art anchorage technology enables the construction of civil engineering structures, which would have a completely different design without the utilisation of anchors. Until the early 60s, high lateral earth pressure acting on deep excavations or retaining structures (see Fig. 2) was absorbed by using the dead load of the structure or additional struts (see Fig. 1). This approach led to an uneconomical design and in case of installed struts, the use of heavy construction machinery has often been limited. Such deficiencies could be remedied by the development of anchors (Wichter and Meiniger, 2018).



Fig. 1: Strutted building pit (Markl and Bahr, 2018)



Fig. 2: Anchored building pit with heavy construction machinery (Hechendorfer and Haag, 2018)

Therefore, anchoring has become an integral part in geotechnical engineering. Besides the support of retaining structures, anchors are used for slope stabilisation measures, uplift prevention, mitigation of safety risks caused by sliding and tilting, foundation of tensile forces and many other areas of application (see Fig. 3).

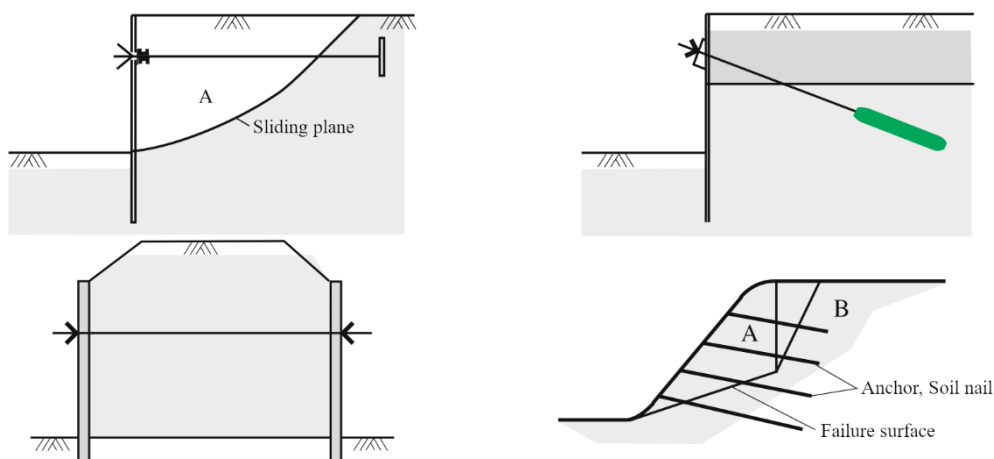


Fig. 3: Various applications of anchors (adapted from Schmidt *et al.*, 2017)

An anchor is a tension-resistant connection. Along the direction of the anchor, this connection allows two points to be fixed in their spatial position relative to each other. While at least one of those two points (i.e. the anchor head) is located on a free surface, the second point is embedded within a soil/rock body or other structural elements (e.g. Fig. 3 bottom left). Thus, unstable zones can be anchored into stable or sound zones, where the load is transferred to the subsurface (Schmidt *et al.*, 2017).

2.2 Classification of anchors

Anchorages can be classified according to various aspects, such as soil type, design life and anchorage type. The latter, a fundamental differentiation, is regulated by the national appendix of Eurocode 7 (Austrian Standards Institute, 2013). In general, a differentiation between following three anchorage types can be made:

- **Ground anchors**

Ground anchors are pre-stressed or non-pre-stressed construction elements with a tendon-free length according to ÖNORM EN 1537 (Austrian Standards Institute, 2015b).

- **Injection piles**

Injection piles are grouted micro piles according to ÖNORM EN 14199 (Austrian Standards Institute, 2016) or grouted displacement piles according to ÖNORM EN 12699 (Austrian Standards Institute, 2015a). Used as anchorage, injection piles work under tensile stress and act as a single tendon.

- **Soil nails**

Soil nails are rod-shaped construction elements according to ÖNORM EN 14490 (Austrian Standards Institute, 2010). Used as soil reinforcement, they form a composite body with the surrounding soil. The key parameter relating to soil nails is the spacing between them. To ensure a monolithic bearing behaviour, the spacing must be small enough. The horizontal distance between soil nails is usually around 1.50 m in loose soil. Soil nails always act collectively.

The main difference between ground anchors and injection piles or soil nails is the bond length of the tendon as shown in Fig. 4. While ground anchors have an apparent tendon-free length (i.e. the bond length is confined), injection piles and soil nails are grouted over the entire length of the tendon (Dausch and Zimbelmann, 2012).

Fig. 4 shows the load-transfer mechanism of ground anchors and soil nails, where $F_z(x)$ specifies the tensile force along the tendon and $T(x)$ the shear force (SF) along the grout body. The figure highlights the significant difference between the SF distributions. While an anchor (see Fig. 4 left) transfers the SF over the confined bond length of the tendon, a soil nail (see Fig. 4 right) transfers the SF over its entire length.

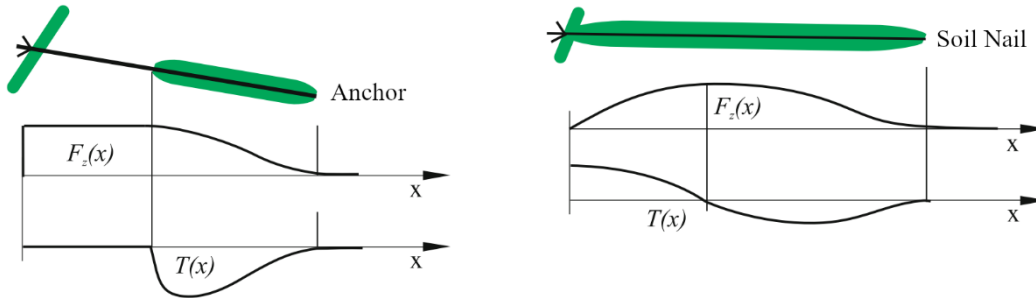


Fig. 4: Difference between ground anchors and soil nails regarding load-transfer mechanism (adapted from Schmidt *et al.*, 2017)

Tab. 1: Characteristics of anchorages (acc. to Austrian Standards Institute, 2013)

| Characteristic | Ground anchors | Injection piles | Soil nails |
|------------------------|----------------|----------------------------------|---|
| Standard of execution | ÖNORM EN 1537 | ÖNORM EN 14199 ÖNORM EN 12699 | ÖNORM EN 14490 |
| Mechanism | Individually | Individually | Collectively |
| Pre-stressing possible | Yes | No | No |
| Number of tests n | 100% | $\geq 3\%$, $n \geq 3$ | CC 1 and CC 2: $\geq 2\%$, $n \geq 2$ CC 3: $\geq 3\%$, $n \geq 5$ |

- **Pre-stressed and non-pre-stressed tendon**

As shown in Tab. 1, tendons of anchors can either be pre-stressed or non-pre-stressed. Pre-stressed anchors, also called active anchors, apply an initial active force on the anchored structure (Xanthakos, 1991). By pre-stressing the tendons, deformations, which are required for the activation of an anchor, are imposed on the system.

Adam et al. (2017) described the ground-anchor interaction as a coupled spring system. This description illustrates the individual phases, pre-stressing and external loading of the system, in an understandable manner and shows how the stiffness ratio between anchor and surrounding subsoil influences the load distribution.

A spring, representing the tendon of the anchor (C_S), is idealised as linear elastic. This idealisation also holds for the spring representing the ground (C_B). Before the pre-stressing process, where no interlock between anchor head and substructure is present, both springs act individually and in a decoupled manner. While the system is being pre-stressed, a tensile force P_S is applied to the tendon. Equilibrium of forces leads to the same magnitude of force P_B , though compressive force, within the ground (Adam et al., 2017).

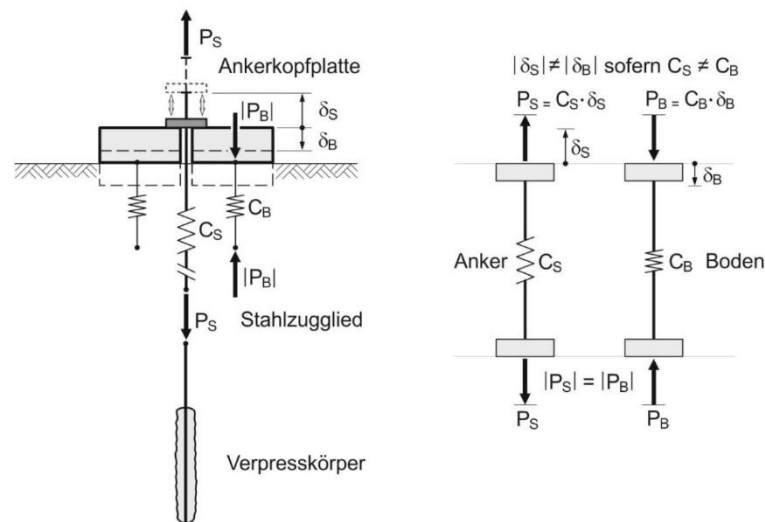


Fig. 5: Spring system prior to and during the pre-stressing of the anchor (Adam et al., 2017)

After pre-stressing and lock-off, the system is coupled and deformations are equal for both springs (i.e. anchor and ground). The stiffness ratio determines how external loads are shared between both springs. Usually, the ground is stiffer than the anchor, and therefore takes more load (Adam et al., 2017).

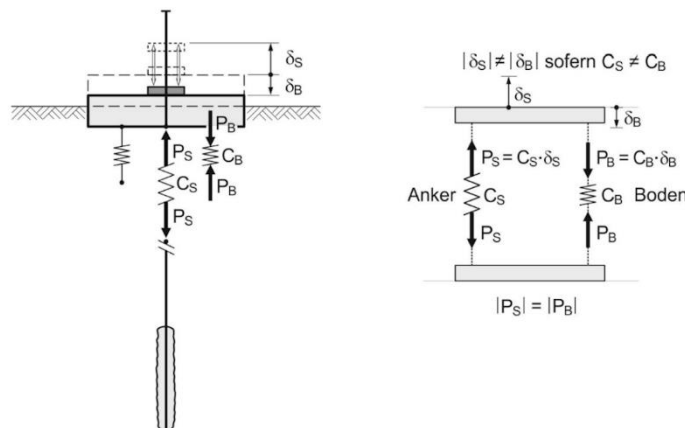


Fig. 6: Spring system after pre-stressing and fixing the anchor (Adam et al., 2017)

For different reasons, the loading situation changes after the pre-stressing process. Adam et al. (2017) described this process by adding an external tensile force Z . This force is shared between the anchor Z_S and the ground Z_B , separated depending on the stiffness ratio. If the external force is raised until $Z \geq Z_{gr}$, the pre-stressing force within the ground is lost and the whole load is carried by the anchor.

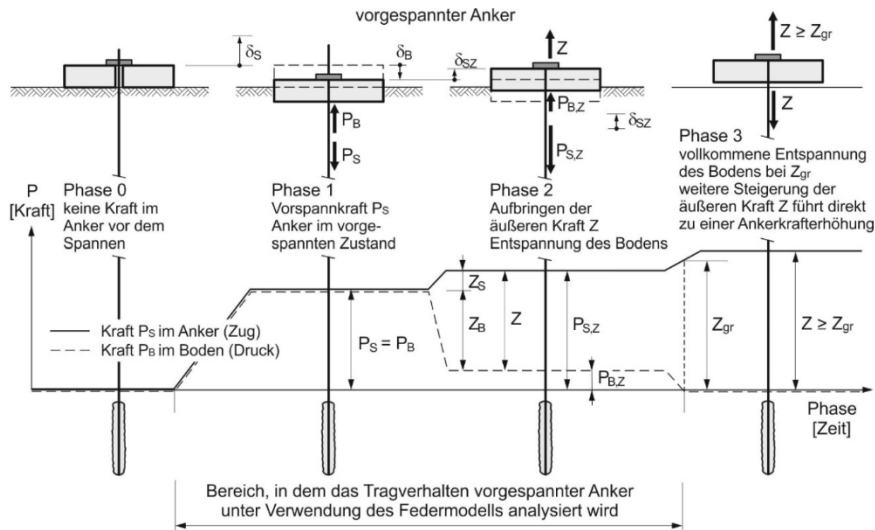


Fig. 7: Relationship between forces and deflections of pre-stressed anchors in several loading stages (Adam et al., 2017)

A graphical representation of the whole process is given in the form of a bracing triangle (see Fig. 8 and Fig. 9), which is well known from structural steel engineering (e.g. Verein Deutscher Ingenieure, 2003). Between Points A and B, the pre-stressing force is applied to the decoupled system. While the anchor undergoes an elongation δ_s , the ground is compressed by δ_B . The gradients of the straight lines represent the spring stiffnesses C_S and C_B . At this point, the absolute value of the anchor force P_S equals the force P_B within the ground. From Point B to Point D/D', the tensile force Z is applied to the coupled spring system. Depending on the stiffness ratio between anchor and the ground, P_S is raised to Point D', while P_B is reduced to Point D. If the external force Z is raised to Point C/C', the pre-stressing force within the ground is lost and the whole load is taken by the anchor (Adam et al., 2017).

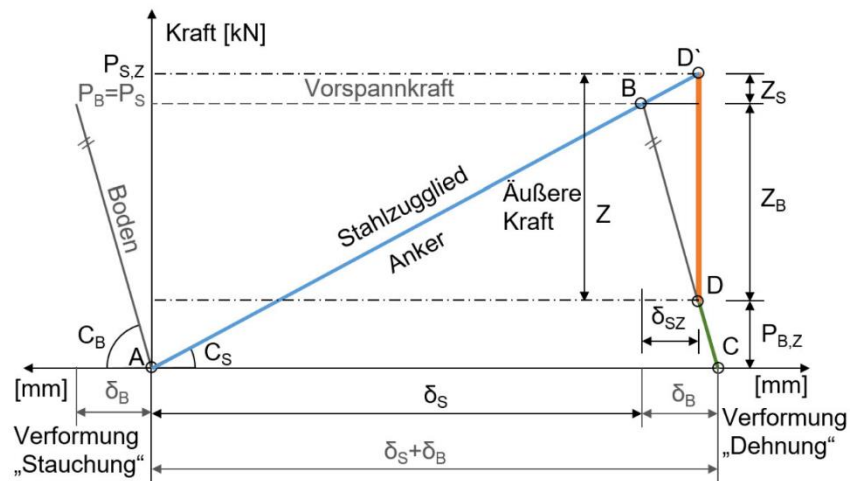


Fig. 8: Bracing triangle 1 (adapted from Adam *et al.*, 2017)

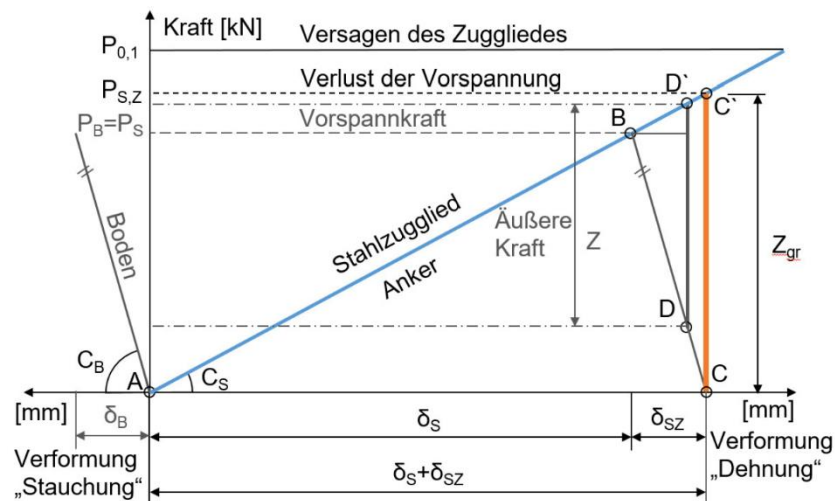


Fig. 9: Bracing triangle 2 (adapted from Adam *et al.*, 2017)

Non-pre-stressed anchors, also referred to as passive or dead anchors, do not apply any initial force to the structure. They become effective if the anchored structure (e.g. soil nail wall) is subjected to deformations or movements (Kolymbas, 2019).

• Temporary and permanent anchorages

Depending on the duration of force transmission into the subsoil, Eurocode 7 (Austrian Standards Institute, 2009) specifies two categories:

- Permanent anchorage: Design life ≥ 2 years
- Temporary anchorage: Design life < 2 years

The difference between those two categories is mainly the type of corrosion protection of the anchorage system (Dausch and Zimbelmann, 2012). Possibly temporary anchors must be used for a longer period than two years. In this case, so-called semi-permanent anchors can be applied. They show a higher level of corrosion protection, mainly at the anchor head, compared to temporary anchors (Wichter and Meiniger, 2018).

2.3 Ground anchors

2.3.1 Development of ground anchors

The first application of pre-stressed ground anchors dates to 1935, when the height of the Cheurfas dam in Algeria was raised. Anchors with a length of 60 m and a working load of 10 MN were installed. Until then, the usage of anchors was limited to bedrock. It seemed impossible to transfer tensile forces, as well as loads significantly smaller than 10 MN, into soil (Ostermayer, 1993).

Executed differently than originally designed, the first ground anchors in ‘loose’ soil were used in 1958. The excavation support for ‘Bayerischer Rundfunk’ in Munich was designed as secant pile wall, the first one in Germany at that time (see Fig. 10). Anchors, which should replace struts inside the building pit, were planned to be dead man anchors with anchorage plates and shafts (see Fig. 11). During drilling operations, many of the anchorage shafts were missed. When withdrawing the drilling rods, resistance in the order of the planned anchor loads was noticed. As a result of this misfortune, cement was injected in a confined section of the boreholes to mobilise and increase the resistance of the subsoil. Approximately five days later, pull-out tests confirmed the proper load-capacity of the newly developed ground anchors (Ostermayer, 1993).

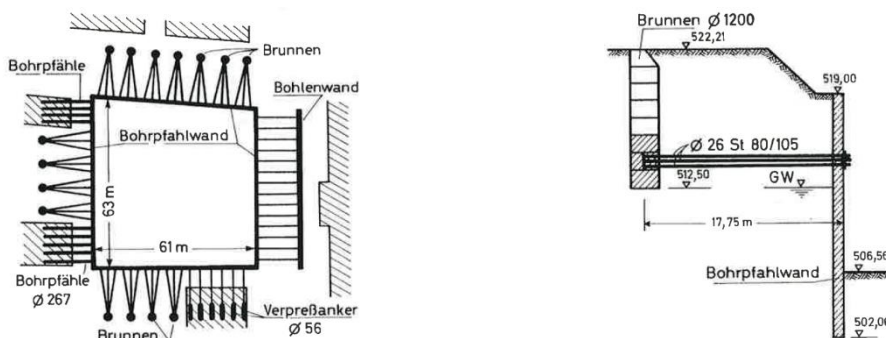


Fig. 10: Secant pile wall for ‘Bayerischer Rundfunk’ in Munich (Ostermayer, 1993)

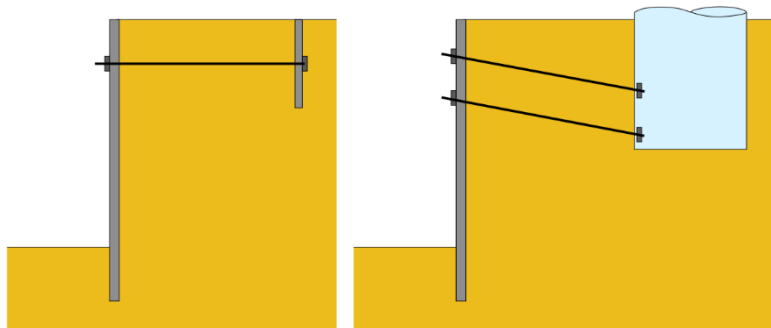


Fig. 11: Dead man anchorage (Kolymbas, 2019)

Until the mid-60s, ground anchors were mainly used as temporary anchors. Since then, corrosion protection systems, which enabled a long term usage, were developed (Wichter and Meiniger, 2018).

2.3.2 Standards for design, execution and testing

There are different regulations and design guidelines for ground anchors and anchored structures. Tab. 2 shows the current (Austrian) standards for design, execution and testing of ground anchors.

Tab. 2: Standards for design, execution and testing

| Standard | Title |
|---------------------------|--|
| ÖNORM EN 1997-1:2009 | Eurocode 7: Geotechnical design Part 1: General rules |
| ÖNORM B 1997-1-1:2013 | National appendix to ÖNORM EN 1997-1 |
| ÖNORM EN 1537:2015 | Execution of special geotechnical works – Ground anchors |
| ÖNORM EN ISO 22477-5:2019 | Geotechnical investigation and testing – Testing of geotechnical structures Part 5: Testing of grouted anchors |

It should be noted that a more recent version of Eurocode 7 (Austrian Standards Institute, 2014) has been published. However, the implementation of the standard is postponed by a clause in the national foreword until the national appendix of Eurocode 7 (Austrian Standards Institute, 2013) is updated to the recent version. Until then, the version of 2009 should be applied.

2.3.3 Anchor assembly and parts

In general, ground anchors consist of three main parts as shown in Fig. 12:

- Anchor head
- Steel tendon, divided into free anchor length and fixed anchor length
- Grout body

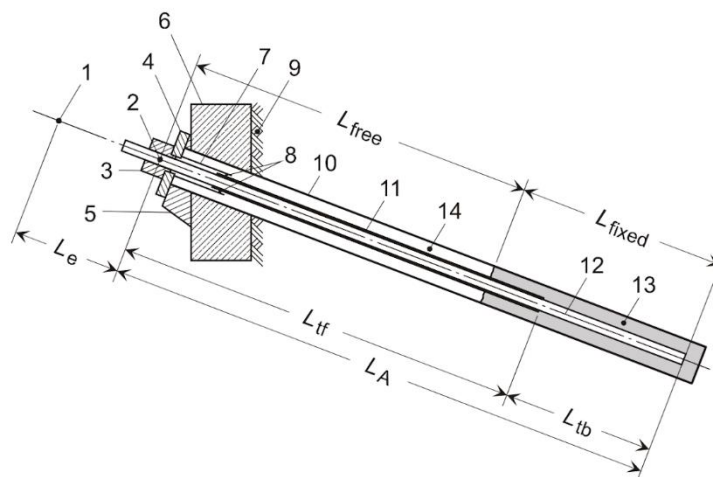


Fig. 12: Schematic representation of a ground anchor (acc. to Austrian Standards Institute, 2015b)

- **Anchor head**

The anchor head is responsible for the transmission of the anchor force into the substructure. To ensure this transmission, an interlock between tendon and substructure is required. The design of this interlock depends on the nature of the used tendon. Bar anchors are usually fixed with nuts (e.g. Fig. 13 a & b). In this case, the regulation of the anchor force, re-stressing or de-stressing of the tendon, is relatively simple. Moreover, slippage during the installation process is low or nearly non-existent. Strand anchors, on the contrary, are fixed with gripping wedges (e.g. Fig. 13 c & d). Gripping wedges produce small notches in the anchor strands. Those notches are not allowed to be within the free anchor length, thus complicating the process of force regulation, especially the de-stressing procedure. Furthermore, gripping wedges can show significant slippage (Wichter and Meiniger, 2018).

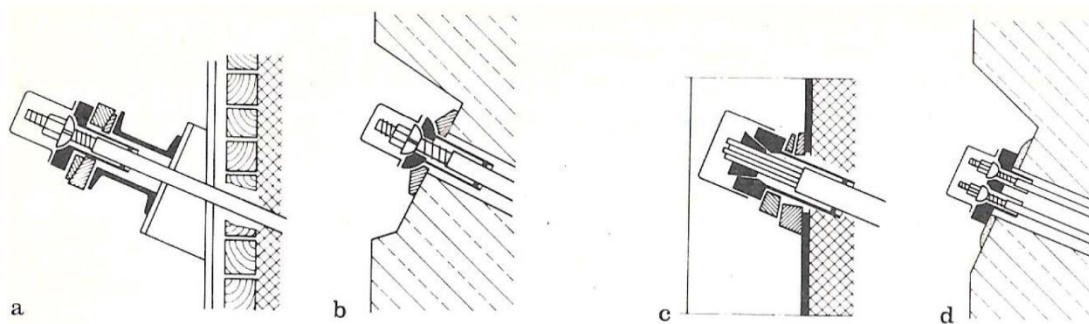


Fig. 13: Various types of anchor heads (Ostermayer, 1982)

- **Steel tendon**

Usually, tendons for ground anchors are made from approved pre-stressing steel. In some cases (e.g. low loads), structural steel (GEWI) can be a proper solution (Wichter and Meiniger, 2018). A distinction is made between bar tendons and strand tendons, used singly or in groups (Xanthakos, 1991).

- Single bar anchors (see Fig. 14)

Single bar anchors consist of a single threaded bar. The full-length thread enables cutting and coupling at any point. Moreover, the thread ensures a high shear bond between the tendon and grout body (Wichter and Meiniger, 2018).

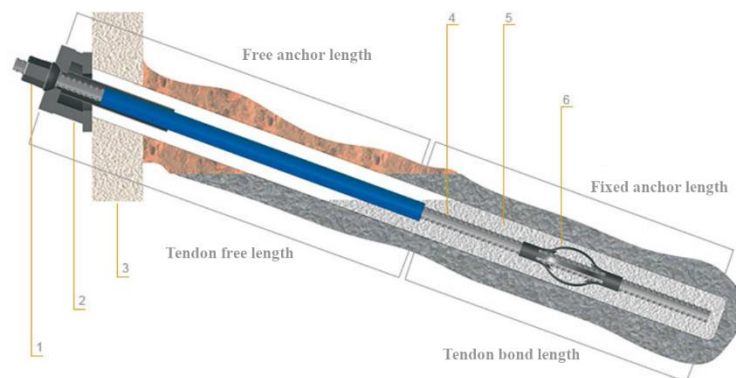


Fig. 14: Schematic representation of a single bar anchor (adapted from DSI Underground GmbH, 2019b)

Tab. 3: Specifications for Dywidag bar anchors (acc. to DSI Underground GmbH, 2019c)

| Steel | Diameter [mm] | Area [mm ²] | Ultimate load F_{pk} [kN] |
|------------------------------------|---------------|-------------------------|-----------------------------|
| Pre-stressing steel Y1050H | 26.5 | 552 | 580 |
| | 32 | 804 | 845 |
| | 36 | 1018 | 1070 |
| GEWI® threaded steel B500B | 32 | 804 | 442 |
| | 40 | 1257 | 691 |
| GEWI® Plus-threaded steel S670/800 | 18 | 254 | 204 |
| | 22 | 380 | 304 |
| | 25 | 491 | 393 |
| | 28 | 616 | 493 |
| | 30 | 707 | 565 |
| | 35 | 962 | 770 |
| | 43 | 1452 | 1162 |

- Multiple bar anchors

Multiple bar anchors (e.g. Fig. 13 d) consist of three to 12 single bar tendons. They have been installed in many existing structures but are no longer used (Wichter and Meiniger, 2018).

- Strand anchors (see Fig. 15)

A strand consists of seven wires, with the six outer wires wrapped around the central king wire in a helical form. The diameter of the central wire is slightly larger than the diameter of the outer wires. Several strands, usually between two and 12, form the tendon of an anchor (Wichter and Meiniger, 2018).

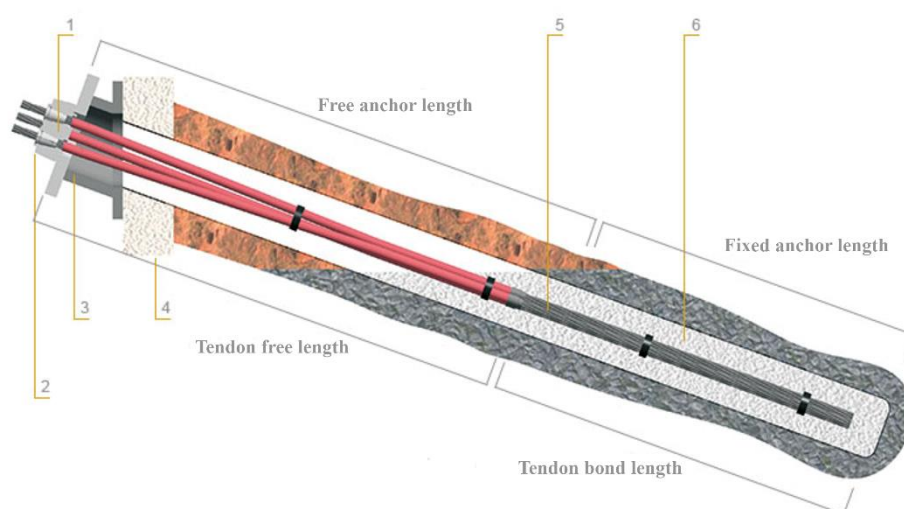


Fig. 15: Schematic representation of a strand anchor (adapted from DSI Underground GmbH, 2019a)

Tab. 4: Specifications for Dywidag strand anchors (acc. to DSI Underground GmbH, 2019c)

| Steel | Number of strands | Area [mm ²] | Ultimate load F_{pk} [kN] | |
|--|-------------------|-------------------------|-----------------------------|-------------------|
| | | | Standard Y 1770 | High grade Y 1860 |
| Pre-stressing steel, strands 140 mm ² Ø15.3 mm (0,6") | 1 | 140 | 248 | 260 |
| | 2 | 280 | 496 | 521 |
| | 3 | 420 | 743 | 781 |
| | 4 | 560 | 991 | 1042 |
| | 8 | 1120 | 1982 | 2083 |
| | 12 | 1680 | 2974 | 3125 |
| Steel | Number of strands | Area [mm ²] | Ultimate load F_{pk} [kN] | |
| | | | Standard Y 1770 | High grade Y 1860 |
| Pre-stressing steel, strands 150 mm ² Ø15.7 mm (0,62") | 1 | 150 | 266 | 279 |
| | 2 | 300 | 531 | 558 |
| | 3 | 450 | 797 | 837 |
| | 4 | 600 | 1062 | 1116 |
| | 8 | 1200 | 2124 | 2232 |
| | 12 | 1800 | 3186 | 3348 |

- Free anchor length

The section between the anchor head and the beginning of the grout body is called free anchor length. This portion of the anchor is isolated from the surrounding soil and therefore is free to elongate. Because of its free mobility, no load transfer into the soil body is assumed within the free anchor length (Xanthakos, 1991).

Under practical conditions, a small amount of the anchor force is transferred within the free anchor length by friction. The amount of friction within the system depends on the straightness of the borehole and has to be determined and limited in the testing procedure (Marte, 2018).

- Fixed anchor length

The design length of the grout body is referred to as the fixed anchor length. Along the fixed anchor length, the applied tensile force is transferred from the tendon into the subsoil (Xanthakos, 1991).

- Grout body

Normally, the cylindrical grout body is cement based and has a length between four and eight meters. Much longer grout bodies are not appropriate, as the bearing capacity is just marginally increased above eight meters. In contrast to grout bodies longer than eight meters, post-grouting can significantly improve the bearing capacity (Wichter and Meiniger, 2018). Besides its capacity of load transmission, the grout body serves as protection against corrosion (Xanthakos, 1991).

2.3.4 Construction process

The construction process comprises several execution steps, which are schematically illustrated in Fig. 16.

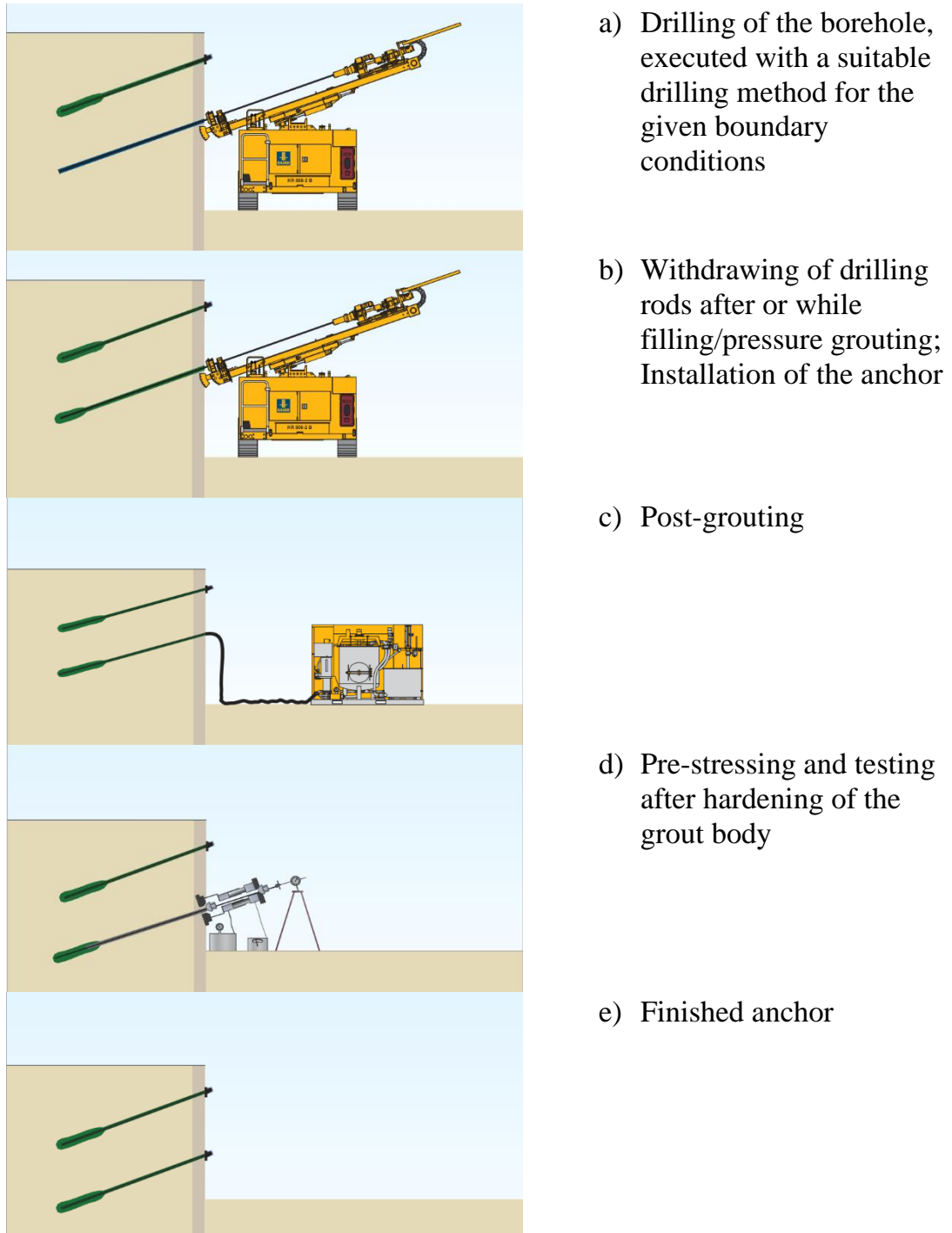


Fig. 16: Construction process of ground anchors (BAUER Spezialtiefbau GmbH, 2013)

2.3.5 Bearing capacity

The bearing capacity of ground anchors is governed by two main factors. On the one side, the bearing capacity of the steel tendon, also referred to as inner bearing capacity, has a major impact. The inner bearing capacity depends on the tensile strength and the area of the steel tendon. Furthermore, the transferable shear stress between grout body and subsoil, or outer bearing capacity, are of major importance. Because the outer bearing capacity is influenced by several factors, its determination appears to be far more complex. Both factors have to be verified within the anchor design (Wichter and Meiniger, 2018).

The transferable shear stress between grout body and soil is limited by the maximum pull-out resistance $R_{a;k}$. Schmidt et al. (2017) propose the following typical values for the characteristic pull-out resistance:

- 1 MN for fine-grained soils
- 1.5 MN for coarse-grained soil
- 10 MN for rock

To estimate the pull-out resistance of ground anchors, nomograms provided by Ostermayer (2003) are useful. While Fig. 17 to Fig. 19 can be used for a preliminary design, the actual bearing capacity has to be determined by suitability and acceptance tests according to ÖNORM EN ISO 22477-5 (Austrian Standards Institute, 2019) (Wichter and Meiniger, 2018).

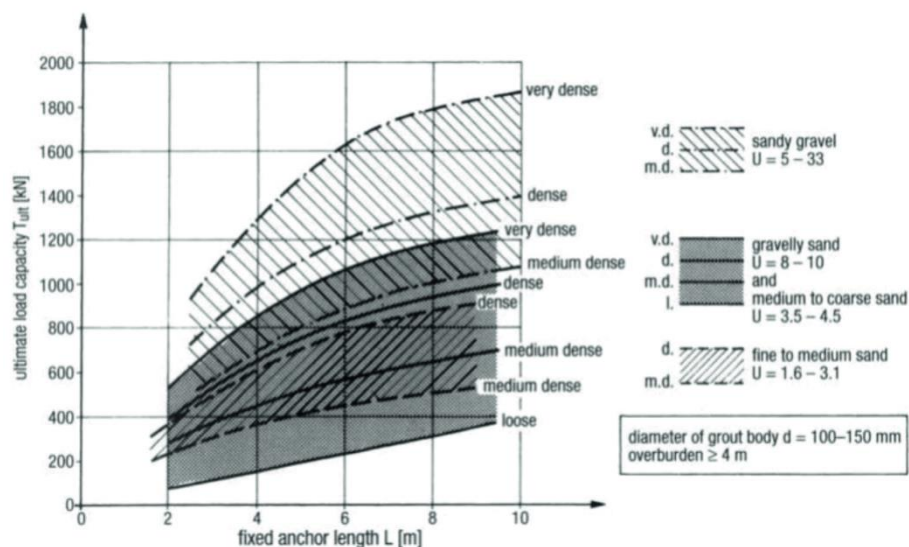


Fig. 17: Ultimate bearing capacity of anchors for coarse-grained soils (Ostermayer et al., 2003)

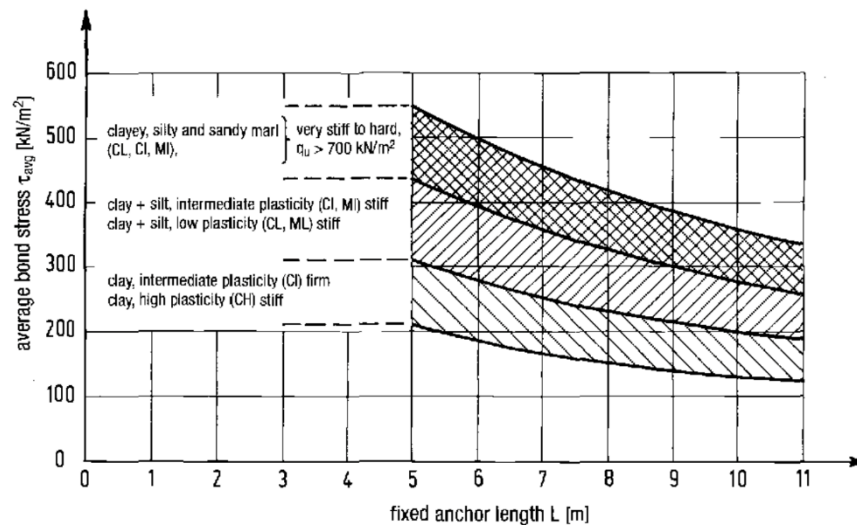


Fig. 18: Ultimate sleeve friction of post-grouted anchors for fine-grained soils (Ostermayer *et al.*, 2003)

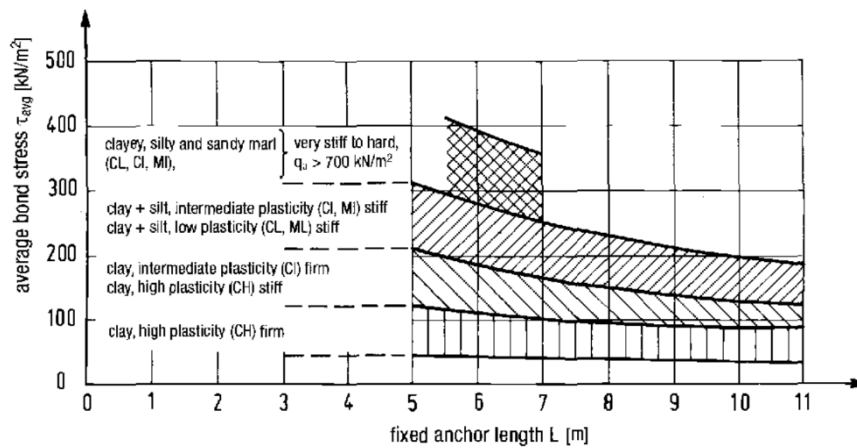


Fig. 19: Ultimate sleeve friction of non-post-grouted anchors for fine-grained soils (Ostermayer *et al.*, 2003)

To apply Fig. 17 to Fig. 19 in practical terms, a minimum overburden of 4 m must be assured. Anchors with an embedment depth of more than 4 m below the ground surface basically show no shallow ground mass failure. A comparison of Fig. 17 with Fig. 18 and Fig. 19 reveals that the diameter within the usual range between 100 mm and 150 mm does not significantly affect the bearing capacity in coarse-grained soils, whereas the bearing capacity in fine-grained soils rises as the diameter is increased. It must be noted that the bearing capacity is not proportional to the fixed anchor length, and as already discussed in section 2.3.3, the figures also support the statement that grout bodies much longer than eight meters are uneconomical because of the marginal increase of the bearing capacity (Schmidt *et al.*, 2017).

2.3.6 Design

2.3.6.1 Limit states

According to Eurocode 7 (Austrian Standards Institute, 2009) following limit states, acting individually or in combination, shall be considered:

- *‘structural failure of the tendon or anchor head, caused by the applied stresses;’*
- *‘distortion or corrosion of the anchor head;’*
- *‘for grouted anchors, failure at the interface between the body of grout and the ground;’*
- *‘for grouted anchors, failure of the bond between the steel tendon and the grout;’*
- *‘for deadman anchorages, failure by insufficient resistance of the deadman;’*
- *‘loss of anchorage force by excessive displacements of the anchor head or by creep and relaxation;’*
- *‘failure or excessive deformation of parts of the structure due to the applied anchorage force;’*
- *‘loss of overall stability of the retained ground and the retaining structure;’*
- *‘interaction of groups of anchorages with the ground and adjoining structures;’*

Some of those limit states have already been verified by the general technical approval provided by manufacturers (e.g. ANP - Systems GmbH, 2018; DSI Underground Austria GmbH, 2019). Section 2.3.6.2 gives an overview of which verifications must be made during the design process.

2.3.6.2 Verifications

Under the rules of Eurocode 7 (Austrian Standards Institute, 2009), the following ultimate limit states have to be verified by calculation and testing procedures:

- **Structural failure of the tendon (STR)**

$$R_{t;d} \geq R_{a;d} \geq P_d \quad (1)$$

$$R_{p,0.1k} = A_t * f_{p,0.1k} \dots \text{for pre-stressing steel} \quad (2)$$

$$R_{t,0.2k} = A_t * f_{t,0.2k} \dots \text{for reinforcement steel} \quad (3)$$

$$R_{t;d} = \frac{R_{p,0.1k}}{\gamma_s * \eta} \dots \text{for pre-stressing steel} \quad (4)$$

$$R_{t;d} = \frac{R_{t,0.2k}}{\gamma_s * \eta} \dots \text{for reinforcement steel} \quad (5)$$

- **Failure at the interface between grout body and ground (GEO)**

$$P_d = (P_k * \gamma_E) \leq R_{a;d} \quad (6)$$

$$R_{a;d} = \frac{R_{a;k}}{\gamma_a} \quad (7)$$

- **Failure at the lower failure plane (GEO)**

Anchored structures with insufficient anchor length can fail at the lower failure plane (see Fig. 20). It is assumed, that the anchor forms a composite body with the wall and the enclosed subsoil. This body fails along an upward-curved failure plane and rotates around a deep point (Adam and Waibel, 2012; Deutsche Gesellschaft für Geotechnik e.V., 2012).

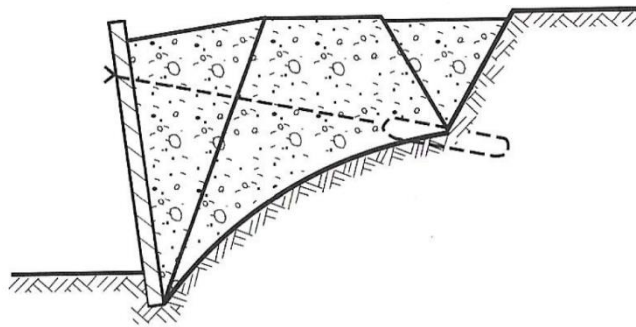


Fig. 20: Failure at the lower failure plane (Deutsche Gesellschaft für Geotechnik e.V., 2012)

EAB (Deutsche Gesellschaft für Geotechnik e.V., 2012) recommends using the method proposed by Kranz (1953) for verification. That method replaces the upward-curved failure plane by a planar failure plane. All acting forces on the trapezoidal soil body (see Fig. 21 left) are presented in the polygon of forces (see Fig. 21 right). This polygon of forces results in the anchor force which would cause the trapezoidal soil body to fail (Adam and Waibel, 2012).

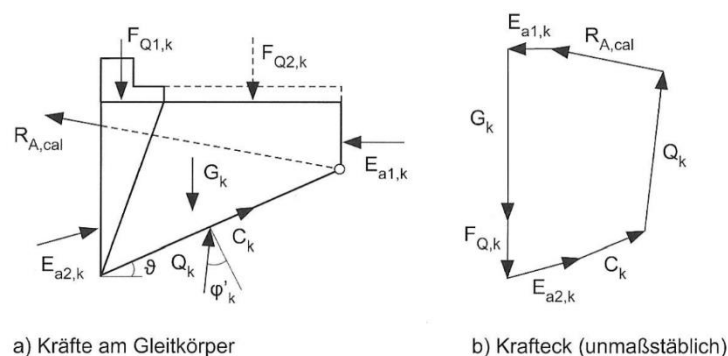


Fig. 21: Acting forces on trapezoidal soil body and polygon of forces (Deutsche Gesellschaft für Geotechnik e.V., 2012)

- **Loss of overall stability (*GEO*)**

The overall stability (see Fig. 22) of anchored structures must be examined. However, because EAB (Deutsche Gesellschaft für Geotechnik e.V., 2012) restricts such verification to exceptional cases, it is not further elaborated in this thesis.



Fig. 22: Loss of overall capacity for a single anchored wall (Deutsche Gesellschaft für Geotechnik e.V., 2012)

2.3.6.3 Corrosion protection

Ground anchors are often used in environments where individual components are exposed to water, de-icing salts or other de-icing agents as well as other chemical and biological substances. Therefore, insufficiently protected steel components are vulnerable to corrosion. The design life of permanent anchors must, nevertheless, correspond to the design life of steel and concrete structures. Hence, permanent anchors must be appropriately protected to fulfil their requirement of remaining sustainable between 80 and 100 years (Burtscher *et al.*, 2017; Wichter and Meiniger, 2000).

Corrosion protection measures for ground anchors are regulated by EN 1537 (Austrian Standards Institute, 2015b). In agreement with EN 1537 (Austrian Standards Institute, 2015b), the general technical approvals (e.g. ANP - Systems GmbH, 2018; DSI Underground Austria GmbH, 2019) for ground anchors specify the corrosion protection requirements for anchor head, free anchor length and fixed anchor length. EN 1537 (Austrian Standards Institute, 2015b) differentiates between corrosion protection systems for temporary and permanent anchors. For permanent anchors, EN 1537 (Austrian Standards Institute, 2015b) states, ‘*The minimum corrosion protection surrounding the tendon of the anchor shall be a single continuous layer of corrosion preventive material which does not degrade during the designed service life of the anchor*’ (Austrian Standards Institute, 2015b).

To ensure a single continuous protection layer, two types of preventive systems are mentioned in EN 1537 (Austrian Standards Institute, 2015b):

- **Single corrosion protection (see Fig. 23 left)**

Single corrosion protection systems consist of a single continuous barrier. If the barrier fails, no further protection is guaranteed. Therefore, single corrosion protection systems are mainly used for temporary anchors. In the case of permanent anchors, the integrity of the single barrier must be verified (e.g. by electrical resistance measurements) (Austrian Standards Institute, 2015b; Marte, 2018).

- **Double corrosion protection (see Fig. 23 right)**

Double corrosion protection systems consist of two continuous barriers and are usually used for permanent anchors. If one of the two barriers fails, the tendon is still protected by a continuous barrier. Therefore, a verification of the integrity is not required (Austrian Standards Institute, 2015b; Marte, 2018).

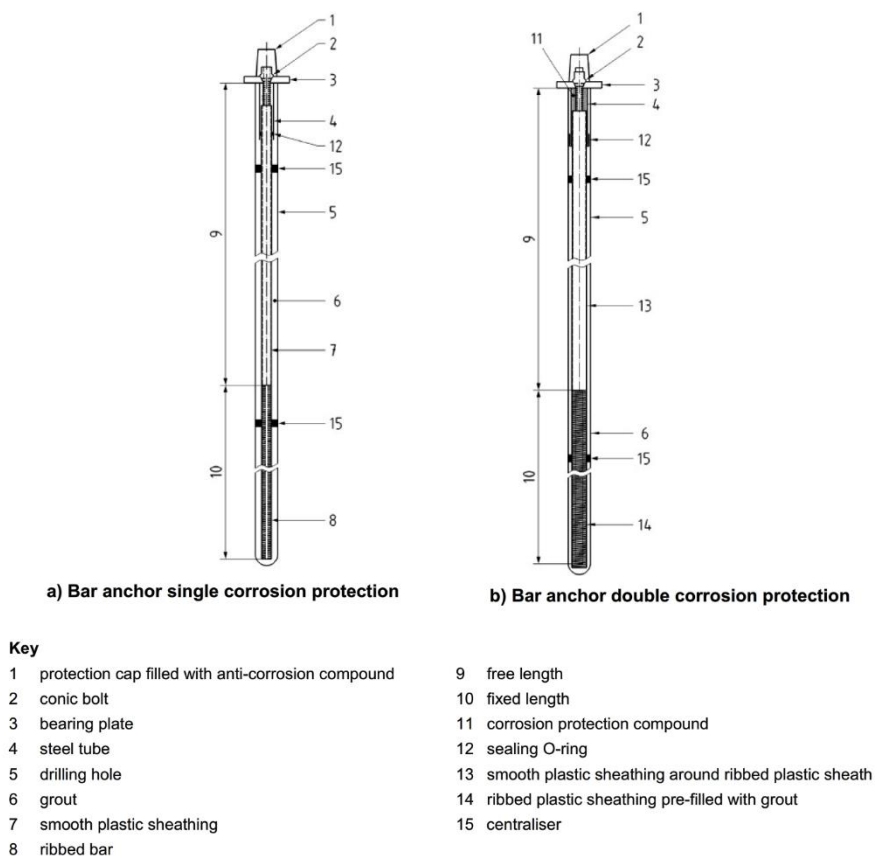


Fig. 23: Examples of single and double corrosion protection for a bar anchor (Austrian Standards Institute, 2015b)

2.3.7 Testing procedure

To ensure the usability of preliminary anchor system designs, different tests have to be performed (Schmidt *et al.*, 2017). Testing of anchors is executed according to ÖNORM EN ISO 22477-5 (Austrian Standards Institute, 2019), which differentiates between three types of anchor tests:

- Investigation test (see section 2.3.7.3)
- Suitability test (see section 2.3.7.4)
- Acceptance test (see section 2.3.7.5)

2.3.7.1 Methods of load application

ÖNORM EN ISO 22477-5 (Austrian Standards Institute, 2019) describes three different methods of load application. A clause in the national foreword defines Test Method 1 for Austria.

- **Test method 1 (see Fig. 24 left)**

'The anchor is loaded stepwise by one or more load cycles increasing from the datum load to the proof load. At each load step the displacement of the tendon end shall be measured during a fixed time period.' (Austrian Standards Institute, 2019)

- **Test method 2 (see Fig. 24 centre)**

'The anchor is loaded stepwise by load cycles increasing from a datum load to the proof load. At each load step the load loss in the anchor shall be measured during a fixed time period.' (Austrian Standards Institute, 2019)

- **Test method 3 (see Fig. 24 right)**

'The anchor is loaded in incremental steps from a datum load to a maximum load. The displacement of the tendon end is measured under maintained load at each loading step.' (Austrian Standards Institute, 2019)

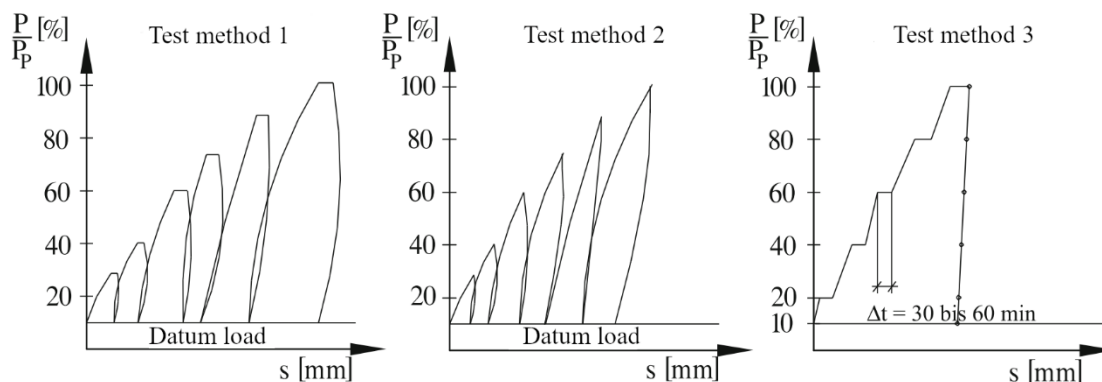


Fig. 24: Different types of test methods; left: Test method 1; centre: Test method 2; right: Test method 3 (adapted from Schmidt *et al.*, 2017)

2.3.7.2 Proof load

The proof load P_p must be defined during the design process. ÖNORM B 1997-1-1:2013 (Austrian Standards Institute, 2013) defines following requirements for all three test types:

$$P_p = P_d * \gamma_a \quad (8)$$

$$P_p \leq 0.80 * R_{pk} \quad (9)$$

$$P_p \leq 0.90 * R_{p,0.1k} \dots \text{for pre-stressing steel} \quad (10)$$

$$P_p \leq 0.90 * R_{t,0.2k} \dots \text{for reinforcement steel} \quad (11)$$

2.3.7.3 Investigation test

Investigation tests are required if no experiences on the load-bearing behaviour have been gained under comparable subsoil conditions. The tests must be executed on sacrificial anchors (i.e. prior to the installation of production anchors), which in contrast to production anchors are not involved in the support of the anchored structure. Therefore, sacrificial anchors are just installed for testing purposes. These anchors are loaded until failure occurs (i.e. a creep rate k_s of 2 mm is exceeded) or limit loads are reached (i.e. $P_p = 0.80 * R_{pk}$ or $P_p = 0.90 * R_{p,0.1k}$) (Schmidt *et al.*, 2017).

Results of such investigation tests are among others (Möller, 2016):

- Pull-out resistance
- Critical creep load
- Creep behaviour until failure
- Load-loss for serviceability limit state
- Apparent tendon-free length

Tab. 5 shows the loading sequence for investigation tests. In order to reach the proof load, the loading of the anchor should be done in at least six cycles. The minimum observation period for each cycle is dependent on the grain size of the predominant subsoil. Subsequently, the unloading of the anchor down to the datum load should be done in the same cycles, in which the observation period should not be less than 1 min (Austrian Standards Institute, 2019).

Tab. 5: Loading sequence for investigation tests (Austrian Standards Institute, 2019)

| Cycle | Maximum load | Minimum observation period at maximum load for each cycle [min] | |
|-------|--------------|---|-----------|
| | | Coarse soil and rock | Fine soil |
| 0 | P_a | 1 | 1 |
| 1 | $0.40 P_p$ | 15 | 15 |
| 2 | $0.55 P_p$ | 15 | 15 |
| 3 | $0.70 P_p$ | 30 | 60 |
| 4 | $0.80 P_p$ | 30 | 60 |
| 5 | $0.90 P_p$ | 30 | 60 |
| 6 | $1.00 P_p$ | 60 | 180 |

2.3.7.4 Suitability test

If no investigation tests are performed, suitability tests should provide characteristics of the anchor design for particular subsoil conditions. At least three tests, under identical conditions as the production anchors will be constructed, should be carried out. For temporary anchors, where suitability tests were performed in comparable conditions on the same anchor types, suitability tests are not necessary (Schmidt *et al.*, 2017).

Results of these suitability tests are as follows (Möller, 2016):

- Ability to resist the proof load
- Observance of acceptable creep rate and load-loss behaviour at proof load
- Apparent tendon-free length

The loading sequence for suitability tests, which can be seen in Tab. 6, requires a minimum of five loading cycles. In addition to the grain size, the minimum observation period also depends on the design life of the anchors. Again, the unloading of the anchor should be done in the same cycles, with a minimum observation period of 1 min (Austrian Standards Institute, 2019).

Tab. 6: Loading sequence for suitability tests (Austrian Standards Institute, 2019)

| Cycle | Maximum load | Minimum observation period at maximum load for each cycle [min] | | | |
|-------|--------------|---|-----------|----------------------|-----------|
| | | Temporary anchor | | Permanent anchor | |
| | | Coarse soil and rock | Fine soil | Coarse soil and rock | Fine soil |
| 0 | P_a | 1 | 1 | 1 | 1 |
| 1 | $0.40 P_p$ | 1 | 1 | 15 | 15 |
| 2 | $0.55 P_p$ | 1 | 1 | 15 | 15 |
| 3 | $0.70 P_p$ | 5 | 10 | 30 | 60 |
| 4 | $0.85 P_p$ | 5 | 10 | 30 | 60 |
| 5 | $1.00 P_p$ | 30 | 60 | 60 | 180 |

2.3.7.5 Acceptance test

The load-bearing capacity and behaviour of each production anchor has to be tested and checked (Möller, 2016).

Results are as follows (Möller, 2016):

- Ability to resist the proof load
- Apparent tendon-free length
- Creep rate of the anchor in the serviceability limit state

Tab. 7 shows that acceptance tests should be executed in a minimum of five loading cycles. Each cycle should be observed for at least 1 min, whereas the proof load needs to be maintained for a longer period. After unloading in the same cycles with a minimum observation period of 1 min, the anchor is loaded up to P_0 and locked off (Austrian Standards Institute, 2019).

Tab. 7: Loading sequence for acceptance tests (Austrian Standards Institute, 2019)

| Cycle | Maximum load | Minimum duration of observation period [min] | |
|-------|--------------|---|-----------|
| | | Coarse soil and rock | Fine soil |
| 0 | P_a | 1 | 1 |
| 1 | $0.40 P_p$ | 1 | 1 |
| 2 | $0.55 P_p$ | 1 | 1 |
| 3 | $0.70 P_p$ | 1 | 1 |
| 4 | $0.85 P_p$ | 1 | 1 |
| 5 | $1.00 P_p$ | 5 | 15 |

2.3.7.6 Acceptance criteria

- **System friction**

As mentioned in section 2.3.3, depending on the straightness of the borehole, a small amount of the anchor force is transferred within the free anchor length by friction. This amount should be limited to 5% of the proof load (Marte, 2018).

$$\Delta P_f \leq 0.05 * P_p \quad (12)$$

- **Creep rate**

The time-displacement behaviour under constant load is described by the creep rate k_s . For time-displacement curves with a logarithmic representation of time, the creep rate plots as a gradient of the straight line (see Fig. 25) at the end of a load cycle. The creep rate is defined by following formula and is limited to 2 mm.

$$k_s = \frac{(s_b - s_a)}{\log\left(\frac{t_b}{t_a}\right)} \quad (13)$$

$$k_s \leq 2 \text{ mm} \quad (14)$$

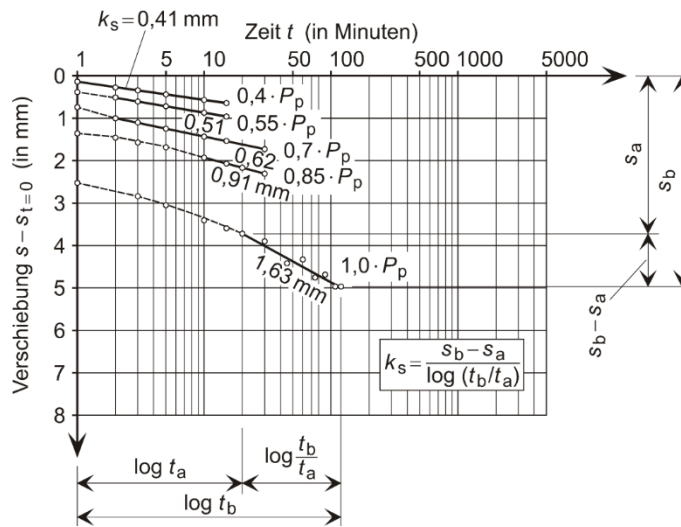


Fig. 25: Creep rate (Möller, 2016)

- **Control of apparent tendon-free length**

Resulting from limitations in the construction procedure, deviations from the designed free tendon length to the apparent tendon-free length are inevitable. The apparent tendon-free length has to be determined according to Eq. 15. Its limits (i.e. lower and upper bound) are given by Eq. 16.

$$L_{app} = \frac{A_t \cdot E_t \cdot \Delta s_{el}}{P_p - P_a - \Delta P_f} \quad (15)$$

$$0.80 \cdot L_{tf} + L_e \leq L_{app} \leq L_{tf} + L_e + 0.50 \cdot L_{tb} \quad (16)$$

2.3.8 Applications

This section focuses on typical areas of application in which ground anchors are utilised. By means of selected examples, this section shows where and for which purposes ground anchors can be used. Some of the selected examples show extreme situations with a large number of anchor rows. Therefore, the following examples should not be considered as daily routine in the field of geotechnical engineering.

- **Deep excavation for the GLC building at ETH Zurich (see Fig. 26 to Fig. 28)**

Currently, the new GLC building for the ETH Zurich is built. After the demolition of the existing building in June, 2015, ground engineering works started in the second quarter of 2016. To realise the project, an excavation with a depth of 25 m measured at the hillside was necessary. The excavation support was designed as bored soldier pile wall. Those soldier piles were stiffened with 25 cm of concrete and tied back with up to nine rows of anchors (Hechendorfer and Haag, 2018).

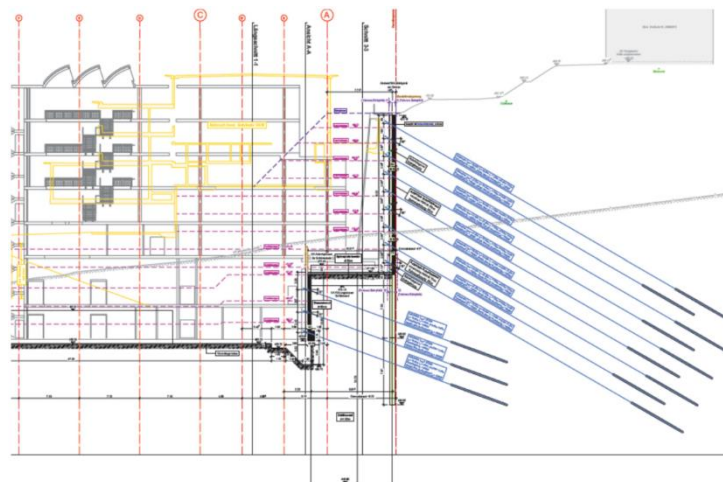


Fig. 26: Cross section of deep excavation for GLC building at ETH Zurich (Hechendorfer and Haag, 2018)



Fig. 27: Deep excavation for GLC building at ETH Zurich 1 (Hechendorfer and Haag, 2018)



Fig. 28: Deep excavation for GLC building at ETH Zurich 2 (Hechendorfer and Haag, 2018)

- **Deep excavation for service provider Coop in Switzerland (see Fig. 29 to Fig. 31)**

In the canton of Aargau in Switzerland, a new logistics centre for Coop was built between 2012 and 2016. A vertical excavation with a depth of 30 m was executed. This excavation support was planned as soldier pile wall. Partially, this soldier pile wall was supported by eight rows of anchors. For the whole project, around 900 anchors were installed (Ducksch and Ammann, 2018).

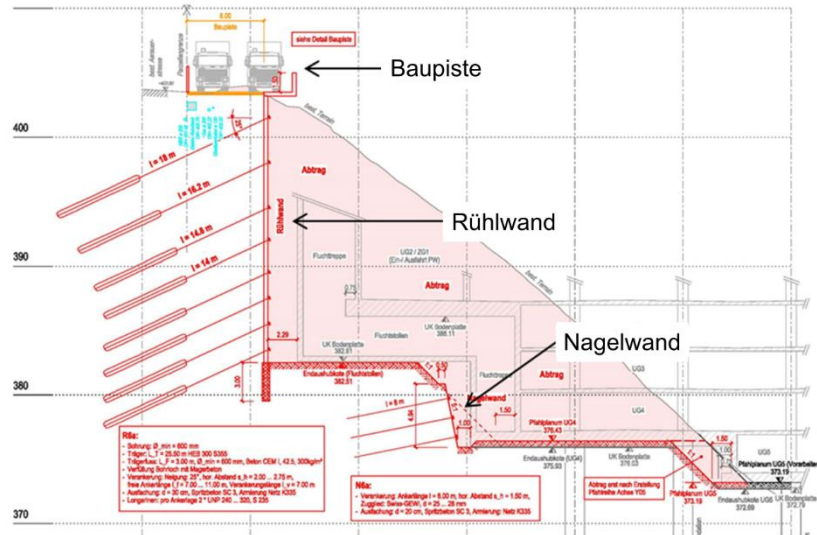


Fig. 29: Cross section of deep excavation for Coop (Ducksch and Ammann, 2018)

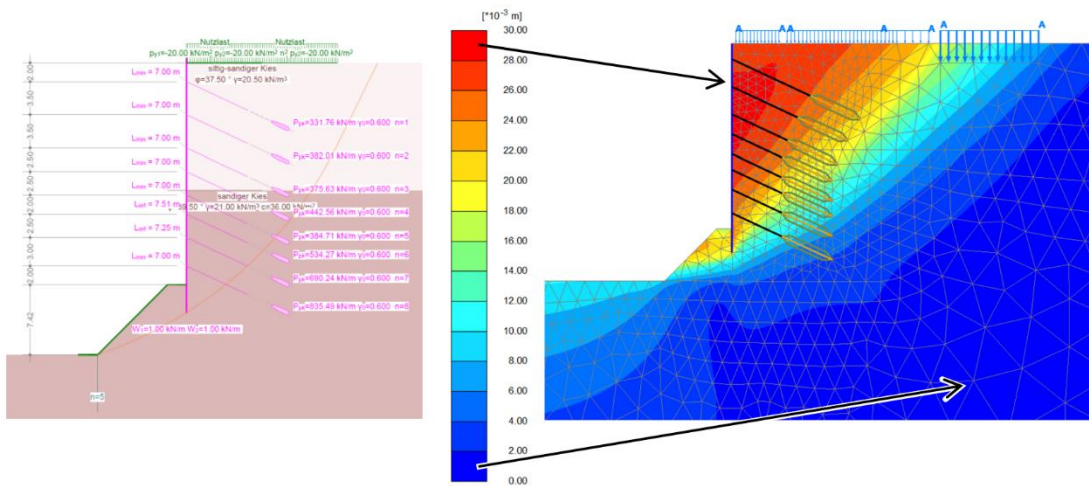


Fig. 30: Analytical and numerical model of deep excavation for Coop (Ducksch and Ammann, 2018)



Fig. 31: Deep excavation for Coop (Ducksch and Ammann, 2018)

- **RW Rötteln (see Fig. 32 and Fig. 33)**

The reconstruction works at the Bundesautobahn A 98 in Lörrach, Germany, required a 300 m long and partially 25 m deep slope cut. Up to five rows of reinforced concrete panels were stabilised with two to three rows of ground anchors for each panel. In total, around 1000 single bar anchors with a length between 9 m and 37 m were planned. However, during construction, excessive displacements occurred, resulting in a significant increase of the anchor forces. This misfortune led to the installation of 250 additional anchors as well as an additional drainage at the distal end of the grout body (Wichter and Meiniger, 2000).

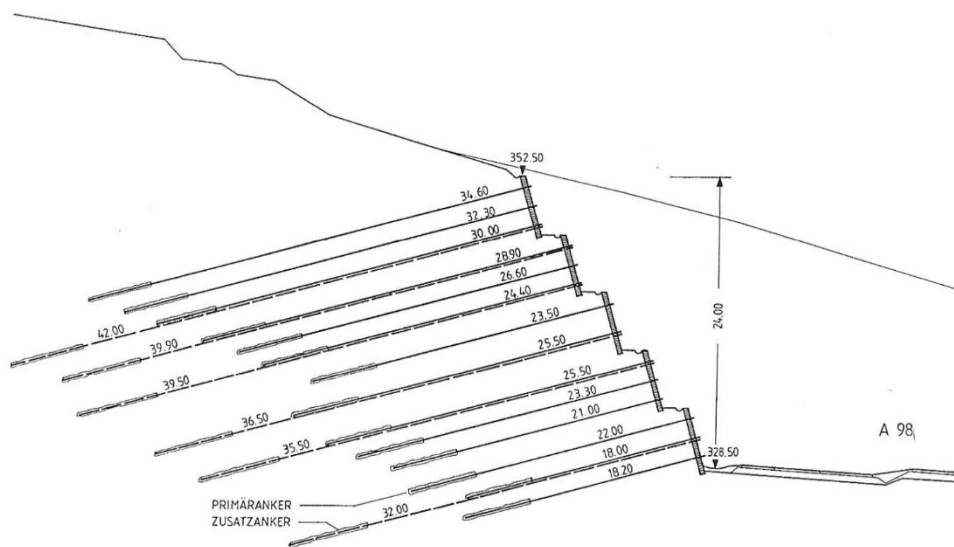


Fig. 32: Cross section of the RW Rötteln (Wichter and Meiniger, 2000)

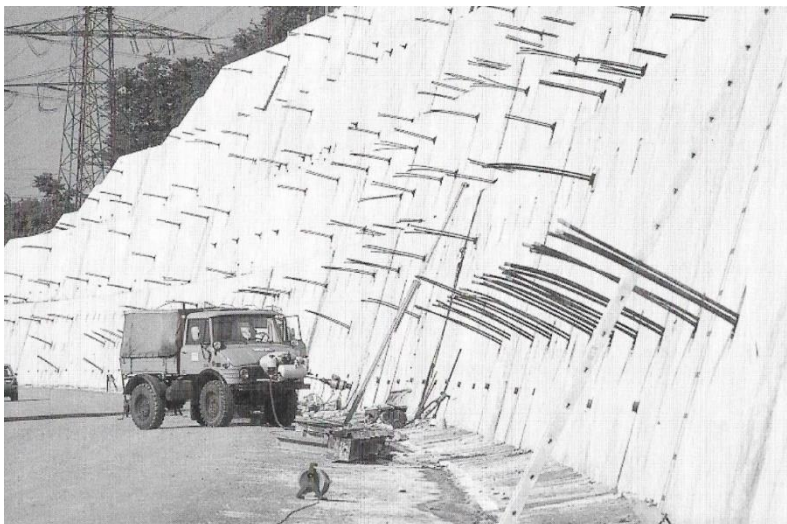


Fig. 33: RW Rötteln (Wichter and Meiniger, 2000)

- **Slope stabilization for construction of the Hochmoselbrücke (see Fig. 34)**

In the framework of the observational method according to Eurocode 7 (Austrian Standards Institute, 2009) at the Hochmoselbrücke in Germany, displacements of approximately 3.60 cm at the inclinometer head were measured between May, 2000, and November, 2017. The sliding plane was detected at a depth of 22 m, passing almost parallel to the ground inclination of approximately 25°. A total of six anchoring shafts with a diameter of 6.60 m and a depth of 45 m were arranged in two rows. Each of the two shaft rows were anchored with 60 pieces of high capacity, permanent anchors (Katzenbach and Bergmann, 2018).

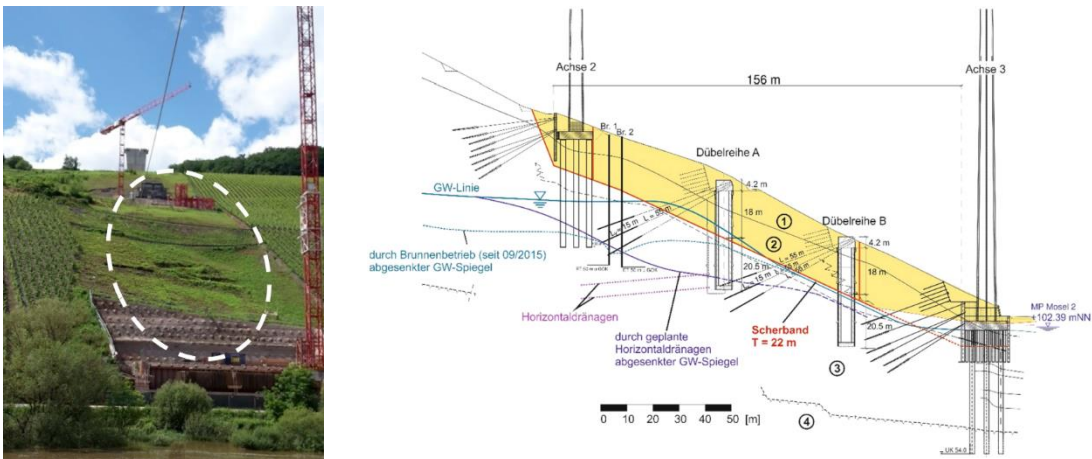


Fig. 34: Landslide and stabilization measures below the Hochmoselbrücke (Katzenbach and Bergmann, 2018)

- **Uplift prevention (see Fig. 35)**

Permanent ground anchors are often used to prevent uplift problems for basins with low self-weight. Because of the pre-stressing process, ground anchors offer the advantage of permanent compressive stresses below the basin bottom. Depending on the filling of the basin, alternating stresses may occur when passive systems like injection piles are utilised (Wichter and Meiniger, 2000).

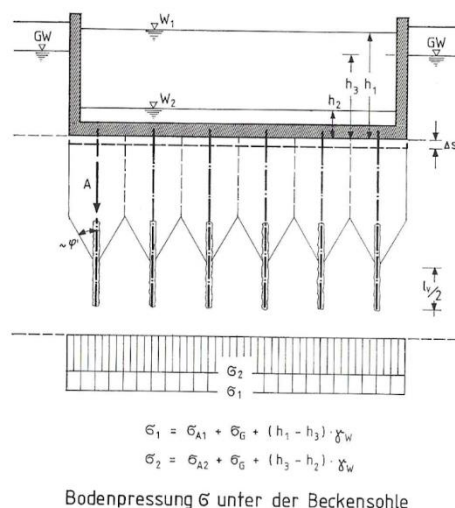


Fig. 35: Uplift prevention (Wichter and Meiniger, 2000)

- **Improving safety by preventing sliding and tilting of the Edertalsperre (see Fig. 36)**

The review of the Edertalsperre in Germany found that it lacked the required self-weight at a magnitude of 2,000 kN/m to meet its requirements concerning flood protection. A total of 104 high capacity ground anchors were installed down from the dam crest. Each anchor was composed of 34 strands, with a working load of around 4,500 kN (Wichter and Meiniger, 2000).

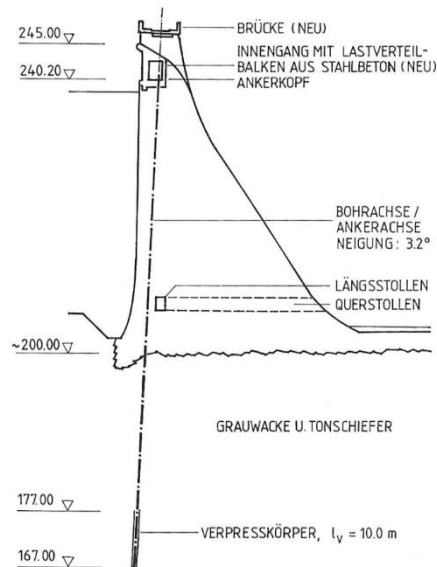


Fig. 36: Strengthening of the dam body at the Edertalsperre (Wichter and Meiniger, 2000)

- **Foundation of tensile forces at the Neckarbrücke (see Fig. 37 and Fig. 38)**

Suspension bridges require the transmission of rope forces into the subsoil. In practice, ground anchors are often utilised for the foundation of tensile forces. Fig. 37 and Fig. 38 show the foundation of the rope force at the Neckarbrücke in Stuttgart-Hofen, Germany (Wichter and Meiniger, 2000).

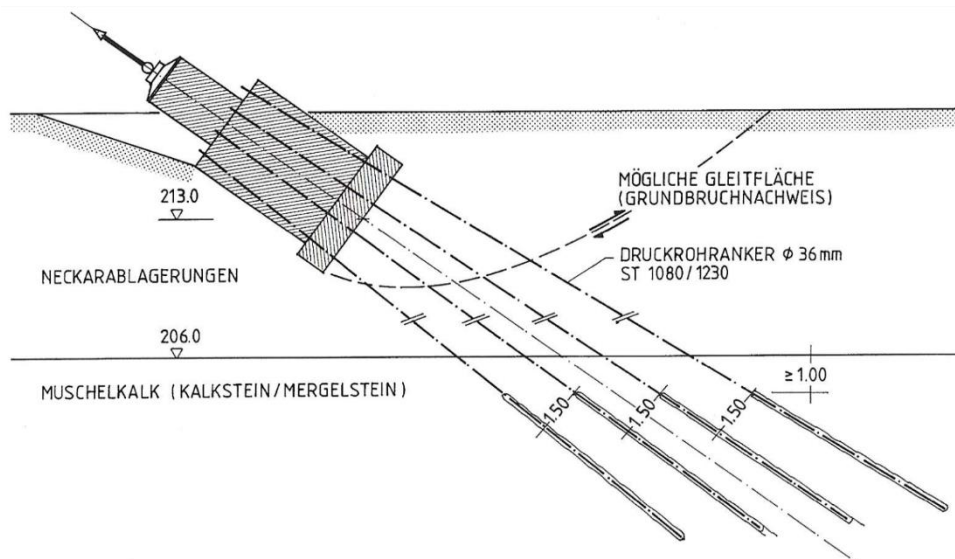


Fig. 37: Foundation of tensile force at the Neckarbrücke 1 (Wichter and Meiniger, 2000)

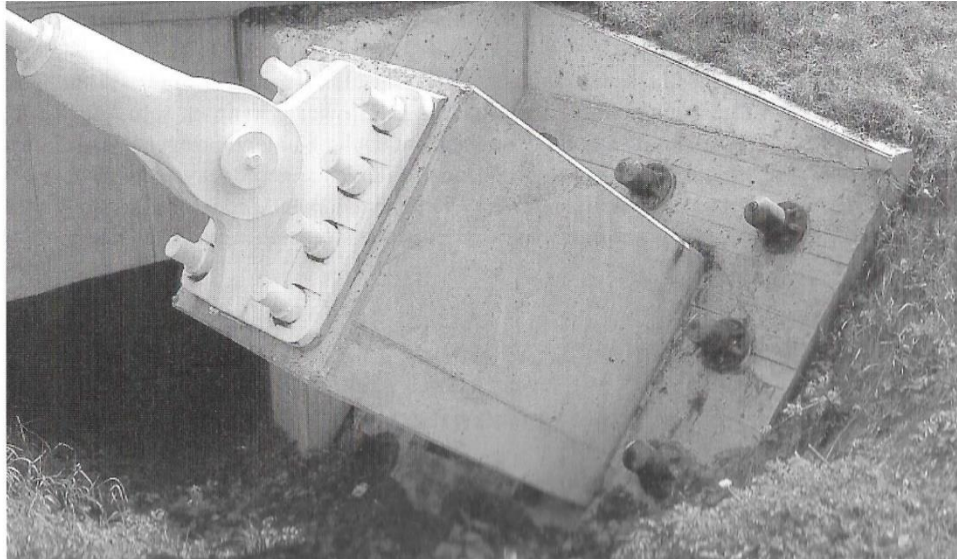


Fig. 38: Foundation of tensile force at the Neckarbrücke 2 (Wichter and Meiniger, 2000)

2.4 Modes of failure

If a single anchor fails, the anchored structure lacks support and must transfer the anchor load from the failed anchor to other anchors or structural elements. In other words, a rearrangement of forces (or loads) must occur within the structure. This can cause single anchors or anchor parts, such as the anchor tendon, to be overstressed, causing them to fail as well. Moreover, depending on the structure, cracks or deformations may appear as a result of the load redistribution. To take protective measures, such ductile behaviour would be desirable. If the rearrangement of forces occurs without visible signs, a series of reactions and the collapse of the structure might be the consequence (Hanel and Prehn, 2006).

As shown in section 2.3.6.2, a distinction between the failure of the ground anchor itself (*STR*) and failure of the retained ground (*GEO*) is made. It should be noted that structural failure of ground anchors may lead to geotechnical failure and vice versa.

2.4.1 Structural failure of the tendon or the anchor head

If tensile stresses within the tendon exceed the material strength, failure by excessive yielding followed by sectioning is inevitable. Fig. 39 shows a typical stress-strain curve for pre-stressing steel. Though no clear yield point is observed, the stress-strain curve indicates the three characteristic points f_{pk} , $f_{p,0.1k}$ and f_{el} . The ultimate tensile strength or characteristic strength is given by f_{pk} . Since there is no explicit yield point, yielding is defined by $f_{p,0.1k}$. This point corresponds to the characteristic stress value in the tendon, lead to 0.1% remaining elongation. As already seen in section 2.3.6.2, allowable working loads are determined from $f_{p,0.1k}$. The third point f_{el} defines the transition from elastic to plastic behaviour and is defined by E_t , the constant elastic modulus of the tendon in the linear portion of the stress-strain curve (Xanthakos, 1991).

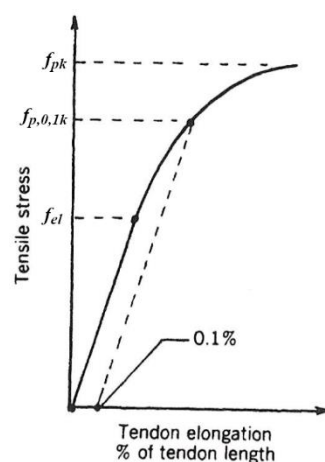


Fig. 39: Stress-strain curve for pre-stressing steel (adapted from Xanthakos, 1991)

2.4.2 Corrosion

2.4.2.1 General

ÖNORM EN ISO 8044 (Austrian Standards Institute, 2015c) defines corrosion as follows:

'Physicochemical interaction between a metal and its environment that results in changes in the properties of the metal, and which may lead to significant impairment of the function of the metal, the environment, or the technical system, of which these form a part.' (Austrian Standards Institute, 2015c)

Most metals are extracted from their naturally occurring ores under high energy input by extracting oxides. The refined metal remains in a high-energy, thermodynamically unstable condition. Corrosion (i.e. the formation of oxides) is the reversal of this extraction process. By releasing the amount of energy necessary for the extraction of the oxides, the metal strives for a low-energy, thermodynamically stable condition (Fédération Internationale de la Précontrainte, 1986; Nürnberger, 1995).

Besides the metal, the presence of corrosive substances, such as molten salts, liquid metals and water or aqueous solutions is necessary for this reversal reaction to occur. The interaction between metal and the corrosive substance defines if and to what degree corrosion takes place. Therefore, the vulnerability of a metal to corrosion is always related to a special corrosive substance (Nürnberger, 1995).

2.4.2.2 Types of corrosion

Corrosion can be classified into three groups according its effect on the metal:

- General corrosion
- Localised corrosion
- Corrosion cracking

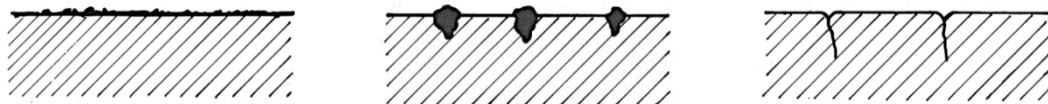


Fig. 40: General corrosion, localised corrosion and corrosion cracking (Fédération Internationale de la Précontrainte, 1986)

- **General corrosion**

General corrosion is characterised by a uniform attack of the surface exposed to corrosion. The loss in mass (e.g. the areal loss or the reduction of the thickness) can be used to describe the degree of damage. Usually, general corrosion can be seen less critical than localised corrosion and is of minor importance for ground anchors (Nürnberger, 1995; Wichter and Meiniger, 2000).

- **Localised corrosion**

Even though the loss in mass may be small, localised corrosion can have severe consequences. In contrast to general corrosion, faster and deeper penetration of corrosion as well as more rapid failure should be expected (Fédération Internationale de la Précontrainte, 1986; Nürnberger, 1995).

Local types of corrosion, which do not need mechanical stresses to occur and are of importance for ground anchors, are as follows:

- Pitting corrosion
- Crevice corrosion
- Bimetallic corrosion
- Stray current corrosion

A local type of corrosion, which does need mechanical stresses to occur and is of importance for ground anchors, is as follows:

- Fretting corrosion

- **Corrosion cracking**

Corrosion on cracks is the most hazardous form of corrosion. If anchorage failure occurs as a result of corrosion, mechanical tensile stresses are usually the key factors. This phenomenon is referred to as stress corrosion cracking (SCC). Such cracks can either develop in an intergranular or transgranular manner (see Fig. 41) (Wichter and Meiniger, 2000).

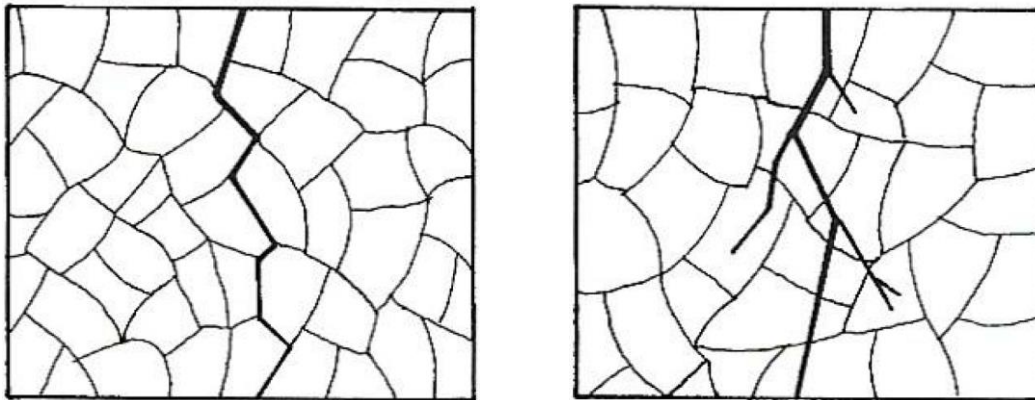


Fig. 41: Intergranular and transgranular cracks (Wichter and Meiniger, 2000)

A special type of *SCC* is stress corrosion cracking induced by hydrogen. In the case of a corrosion attack on pre-stressing steel, such cracking is the main cause of failure. Atomic hydrogen migrates into the metal lattice, forms molecules and builds up internal pressure. As a result of this process, the steel embrittles and subsequently may fail (Wichter and Meiniger, 2000; Fédération Internationale de la Précontrainte, 1986).

2.4.3 Failure at the interface between the grout body and the ground

Ground anchors mobilise skin friction between the grout body and the surrounding ground. This bond mainly depends on the confining stress around the grout body, the nature of their interface (i.e. adhesion) and the mobilised skin friction between the grout body and the ground. Fig. 42 shows the distribution of skin friction along the grout body for dense and medium-packed gravelly sand. When loaded, the proximal end of the bond zone elongates and transfers load to the ground. As the resistance of this portion is mobilised, the shear stress shifts to the distal end of the grout body. Once the stress reaches the end of the bond zone and the ultimate grout-ground bond is exceeded, pull-out failure of the anchor occurs (Sabatini *et al.*, 1999).

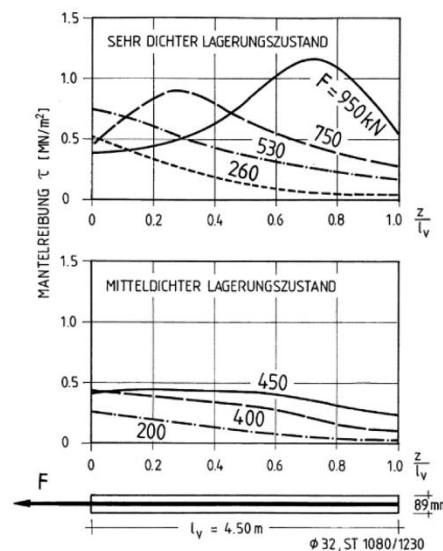


Fig. 42: Distribution of skin friction along the grout body in gravelly sand (Scheele, 1982)

2.4.4 Failure of the bond between the steel tendon and the grout body

If anchors are constructed within ground of sound quality, the tendon-grout interface may govern the bearing capacity. Fig. 43 shows an enlarged schematic representation of this interface. Three types of bond mechanisms – namely, adhesion, friction and mechanical interlock are present. Adhesion is the physical attraction at an interface attaching the microscopically rough steel to the surrounding grout. Depending on the confining stress, the surface finish and the magnitude of slip, friction develops as movement occurs. Finally, mechanical interlock is generated between protrusions of the tendon and the surrounding grout (Jarred and Haberfield, 1997; Xanthakos, 1991).

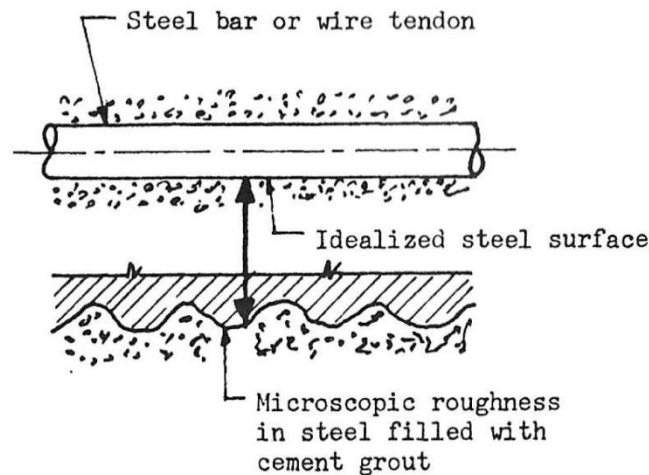


Fig. 43: Schematic representation of the tendon-grout interface (Xanthakos, 1991)

2.4.5 Loss of anchor force by creep and relaxation

Creep describes the time-dependent displacement behaviour under constant static loading. Because of long-term static loading, displacements of an anchor may change with time, involving a reduction of the anchor force. Associated with ground anchors, creep is represented by both creep in the soil and in the anchor components (i.e. creep of the grout, steel relaxation, partial debonding of the steel-grout interface and creep of the tendon connections with the wall and the anchorage) (Xanthakos, 1991).

As already seen in section 2.3.7.6, the creep behaviour of ground anchors is defined and limited by the creep rate k_s (Austrian Standards Institute, 2015b).

Relaxation is the decrease of stress over time under constant strain. Hence, while a tendon is kept under constant strain, the anchor force decreases. The relaxation behaviour of steel mainly depends on the manufacture procedure, the temperature and the time (Xanthakos, 1991).

2.4.6 Failure of the ground mass

The ground mass adjacent to ground anchors must have sufficient resistance to withstand the anchor forces. Ground mass failure for shallow anchors is characterised by uplift of the soil mass in front of the grout body, followed by pull-out of the bond zone. The failure surface corresponds to a passive earth pressure failure. For anchors embedded more than 4 m below the ground surface, failure of the ground mass is of minor importance (Brady *et al.*, 1997; Sabatini *et al.*, 1999).

3 Verification methods for the failure of ground anchors

3.1 Standards and guidelines

Eurocode 7 (Austrian Standards Institute, 2009) defines a special design situation which should consider *'the consequences of the failure of any anchorage'* (Austrian Standards Institute, 2009). In practice, however, this design situation is not clearly outlined and therefore barely examined.

Technical Reference 26:2010 (Spring Singapore, 2010) requires the design of a deep excavation or a retaining structure to be structurally safe at each stage of the construction, even when an individual structural element fails. If a structural element fails, the load from the failed element will be redistributed to the remaining structural elements. Therefore, the structure itself, as well as the remaining structural elements, should have enough capacity to redistribute and absorb the load from the failed element without causing overall failure. In fact, this load redistribution represents a 3D problem. Nevertheless, the conventional analysis approach for deep excavations and retaining structures is a 2D plane strain analysis, where a whole layer of failed structural elements (in a row) is removed. This 2D plane strain analysis is restricted to a force redistribution in a vertical direction only, usually leading to more conservative designs (Pong *et al.*, 2012; Spring Singapore, 2010).

Clause 3.7.4 of Technical Reference 26:2010 (Spring Singapore, 2010) is commonly known as 'one-strut failure', but as outlined below, it is also valid for ground anchors or any other structural elements. Clause 3.7.4 states the following:

'The design for deep excavations should accommodate possible failure of any individual strut, tie rod, ground anchor, structural member or connection at each stage of the construction works. The wall and remaining supporting members, including walings and connections, should be capable of redistributing the load from the failed member. The remaining structural system and wall should continue to be safe without causing any danger to surrounding adjacent structures and properties.' (Spring Singapore, 2010)

Similar to clause 3.7.4 of Technical Reference 26:2010 (Spring Singapore, 2010), BS 8002:1994 (British Standards Institution, 1994) mentions the following in clause 4.5.2.2.1:

'The design should also accommodate the possible failure of an individual strut, tie rod or anchor. The wall and walings should be capable of redistributing the load from the failed tie rod or anchor.' (British Standards Institution, 1994)

3.2 Corroded Anchor Structure Stability/Reliability (CAS_Stab-R) Software for Hydraulic Structures

The U.S. Army Corps of Engineers operates and maintains a large number of hydraulic structures. Many of those structures have been retrofitted with post-tensioned strand anchors over the past four decades to improve their serviceability and stability. Because of inappropriate corrosion mitigation procedures during the anchor installation, older retrofits have been exposed to corrosion. Therefore, the U.S. Army Engineer Research and Development Center (*ERDC*) created a software product, CAS_Stab-R (Warren *et al.*, 2017), with the ability to predict the remaining anchor life (*RAL*) regarding corrosion. Additionally, CAS_Stab-R (Warren *et al.*, 2017) is able to determine the probability of unsatisfactory performance (*PUP*) for hydraulic structures in terms of sliding, but that feature is not further elaborated in this thesis (Warren *et al.*, 2017).

3.2.1 Remaining anchor life computation

In 2013, a series of pull-test experiments for seven-wired strand tendons were carried out at *ERDC*. The results, which were published by Ebeling *et al.* (2016) and Haskins *et al.* (2016), provided the statistical relationships between the reduced loading capacity to the reduced cross-section area of the smallest wire in the assembly and the minimum short axis diameter of the most corroded wire, for various degrees of corrosion (Warren *et al.*, 2017).

Fig. 44 shows a scatter plot of the loading capacity as a function of the minimum cross-sectional wire area. The blue line in Fig. 44 represents the graph of the function given in Eq. 17, where y specifies the loading capacity [kN] and x the minimum wire area [mm²]. R^2 , which can be seen in Fig. 44, represents a measure of error (Haskins *et al.*, 2016).

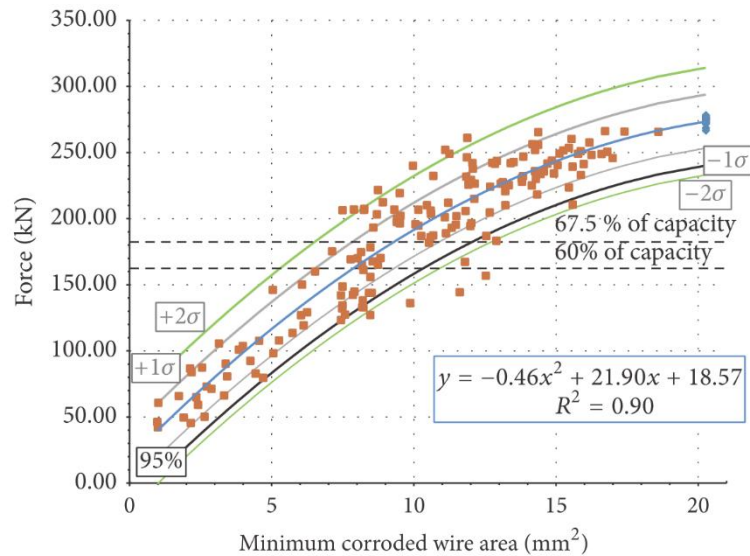


Fig. 44: Loading capacity as a function of the minimum corroded wire area (Haskins *et al.*, 2016)

$$y = -0.4605 * x^2 + 21.901 * x + 18.574 \quad (17)$$

Fig. 45, again, shows the scatter plot but relates the capacity to the short axis diameter of the most corroded wire. The mean estimation function is given by Eq. 18 and is graphically plotted as the blue line in Fig. 45. In Eq. 18, y is again the capacity [kN], whereas x is the minimum diameter [mm] (Haskins *et al.*, 2016).

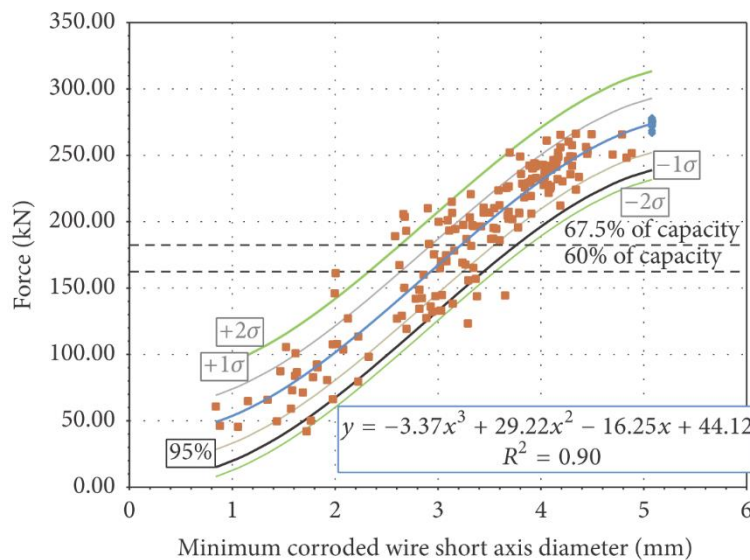


Fig. 45: Loading capacity as a function of the minimum corroded wire short axis diameter (Haskins *et al.*, 2016)

$$y = -3.3709 * x^3 + 29.217 * x^2 - 16.247 * x + 44.12 \quad (18)$$

CAS_Stab-R (Warren *et al.*, 2017) provides both options for predicting the reduced loading capacity; either Eq. 17 or Eq. 18 can be utilised.

If an anchor tendon is exposed to corrosion, the loading capacity of the tendon will decrease because of material loss (see Fig. 46). When the loading capacity of the tendon is lower than the lock-off load, the tendon will fail. That statement implies that the anchor force does not increase after lock-off. Therefore, the lifetime of the tendon is affected by the lock-off load and the corrosion rate. To determine the degree of corrosion, CAS_Stab-R (Warren *et al.*, 2017) provides the user three input options: corrosion rate, oxygenation level and non-destructive test (*NDT*) corroded wire cross sectional area (Warren *et al.*, 2017).

- **Calculation with corroded wire area curve and time-to-failure (*TTF*) computation**

If Eq. 17 is used for the prediction of the reduced loading capacity, the diameter of the corroded wire d_C is computed according to Eq. 19, where d_P is the diameter of the pristine wire, R the user supplied corrosion rate and the length of service (*LOS*) of the tendon. From the corroded diameter, the corroded area of the wire A_C is calculated (see Eq. 20). In the next step, A_C is substituted for x in Eq. 17 to obtain the reduced loading capacity of the seven-wired strand (Warren *et al.*, 2017).

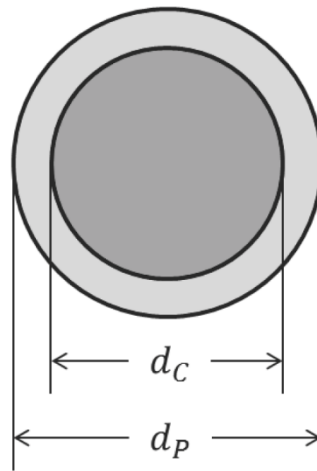


Fig. 46: Corrosion effect on a wire (Warren *et al.*, 2017)

$$d_C = d_P - 2 * R * LOS \quad (19)$$

$$A_C = \frac{d_C^2 * \pi}{4} \quad (20)$$

By assigning the lock-off load to y in Eq. 17 and solving for x , the wire area A , which provides stability for the lock-off load, is determined. From this area A , the wire diameter d_{LOL} , which provides stability for the lock-off load, is computed (see Eq. 21). Utilizing Eq. 22, the TTF is obtained (Warren *et al.*, 2017).

$$d_{LOL} = \sqrt{\frac{4 * A}{\pi}} \quad (21)$$

$$TTF = \frac{(d_C - d_{LOL})}{R} \quad (22)$$

- **Calculation with corroded short axis diameter curve and TTF computation**

As shown in Eq. 19, the diameter of the corroded wire d_C is computed. The corroded diameter d_C is substituted for x in Eq. 18 to obtain the reduced loading capacity of the seven-wired strand (Warren *et al.*, 2017).

By assigning the lock-off load to y in Eq. 18 and solving for x , the corroded wire diameter d_{LOL} , which provides stability for the lock-off load, is computed. Then, the TTF is again calculated by utilising Eq. 22 (Warren *et al.*, 2017).

To summarise, in one of its main functions, CAS_Stab-R (Warren *et al.*, 2017) provides a probabilistic estimate of the RAL for strand tendons regarding corrosion. Based on statistical correlations, the following input parameters result in the TTF (Warren *et al.*, 2017):

- Lock-off load applied to the tendon at installation
- Amount of time the tendon has been in service
- Method to determine corroded wire size and corresponding corrosion rate
 - Corrosion rate
 - Oxygenation level
 - NDT corroded wire cross sectional area
- Method to determine the reduced loading capacity
 - Minimum corroded wire area
 - Minimum corroded short axis diameter
- Distribution information for the variables (lock-off load and corrosion rate)

4 Finite element analyses using PLAXIS 2D

The primary aim of this chapter is to investigate the behaviour of an anchored *RW* affected by row-wise failure of ground anchors in 2D analyses. By means of a multiple-anchored *RW* in Salzburg, this chapter shows how ground anchor failures affect the overall stability of the structure, the *RW* itself and the surrounding anchors. For this purpose, special emphasis is placed on the factor of safety (*FoS*), bending moments (*BMs*) and *SFs* within the concrete components (i.e. within the *RW*), displacements and anchor forces. Besides the studies related to row-wise ground anchor failure, a study is presented comprising different model dimensions. All *FEAs* shown in this chapter were conducted with PLAXIS 2D, Version 2018.01 (Brinkgreve *et al.*, 2018b).

4.1 Retaining wall Egger

In order to examine the effects of ground anchor failure, the anchored *RW* Egger was selected for the *FEAs*. The *RW* is located between km 50.60 and km 50.90 on the A10 Tauernautobahn in Salzburg. In total, the wall extends over a length of approximately 235 m, and the wall height ranges between approximately 7 m to 22 m. The structure itself is composed of 40-cm- and 50-cm-thick concrete panels, behind which there is 10 cm of shotcrete. A cross-sectional view of the *RW* shows an inclination of 4:1, which corresponds to around 76° . Depending on the varying height, one to seven rows of ground anchors were installed to ensure the stability of the structure. Parallel to the motorway, a 3-m-wide forest path passes behind the top of the wall, to which the initial ground surface connects with an inclination of approximately 37° to 40° (3G Gruppe Geotechnik Graz ZT GmbH, 2017).

Fig. 47 shows an image of the *RW*, taken from the traffic lane Villach. The red marking, which can be seen on the left-hand side of the figure, corresponds to the area chosen to analyse.



Fig. 47: *RW* Egger (adapted from 3G Gruppe Geotechnik Graz ZT GmbH, 2017)

The front view and cross section of the analysis profile QP-E can be observed in Fig. 48. Four rows of ground anchors are installed over the retained height of around 13 m in this portion of the wall. Though water was found at the wall base in drainages and as leakage on the wall surface, geotechnical investigations could not detect a continuous groundwater table. Moreover, the following four ground layers were identified by the investigations (3G Gruppe Geotechnik Graz ZT GmbH, 2017):

- Homogenous layer A – Hangschutt: Thickness between 0.50 m and 3.30 m
- Homogenous layer B – Weathered rock, softened: Thickness between 5.00 m and 15.00 m
- Homogenous layer C – Compact rock
- Cataclastic fault zones

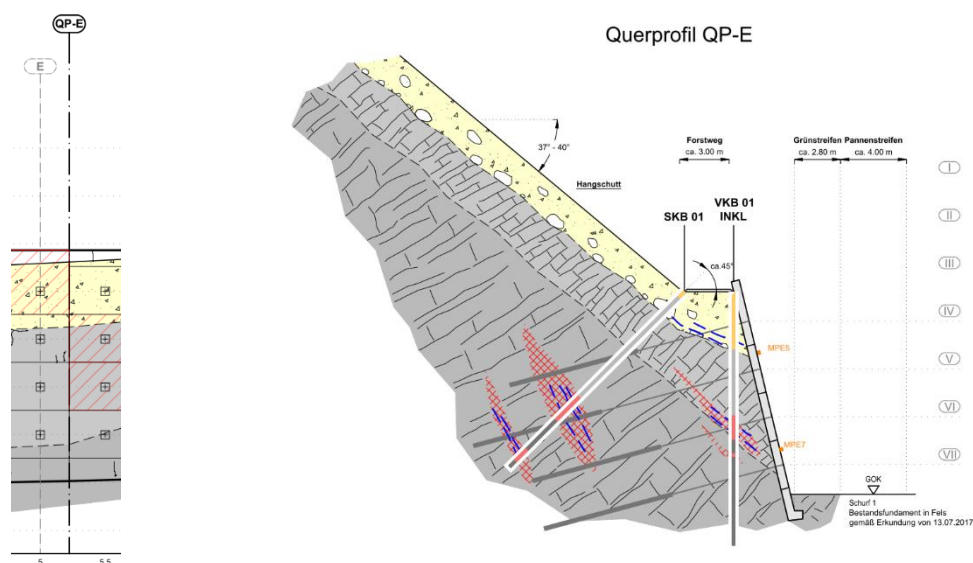


Fig. 48: Front view and cross section of analysis profile QP-E (3G Gruppe Geotechnik Graz ZT GmbH, 2017)

Because of the gradual transition between Hangschutt and weathered rock, the geotechnical report (3G Gruppe Geotechnik Graz ZT GmbH, 2017) recommended a subsoil model with two layers, in which the upper 6 m are composed of Hangschutt, with compact rock beneath. The suggested ground parameters are given in Tab. 8.

Tab. 8: Recommended ground parameters (acc. to 3G Gruppe Geotechnik Graz ZT GmbH, 2017)

| Homogenous layer | ϕ [°] | c [kPa] | E [kPa] | γ [kN/m ³] |
|------------------|------------|---------|---------------|-------------------------------|
| A: Hangschutt | 35 | 0 | 70000 | 21 |
| C: Compact rock | 40 | 40 | 150000/500000 | 24 |

4.2 PLAXIS 2D model

Regarding the geology and geometry, some simplifications were made. Given that an initial ground surface with an inclination of 40° would have needed high strength parameters to be stable, the initial slope was modelled at 30° inclined towards the horizontal. Additionally, the subsoil was modelled as one single homogenous ground layer. The parameters for this layer have been varied. Groundwater, for reasons mentioned in section 4.1, was not considered.

The model dimensions of geometry 'Final' can be seen in Fig. 49. Four rows of ground anchors are installed, inclined 14° towards the horizontal, over the retained height of 13.39 m, which is excavated in five steps. Concerning initial conditions, a study of the model size was conducted. Therefore, Fig. 50 shows two additional model dimensions, namely 'Small' and 'Big.' The dashed lines in Fig. 50 represent geometry 'Final', compared to which the left and top boundaries were adapted, while the right and the bottom boundaries were kept fixed.

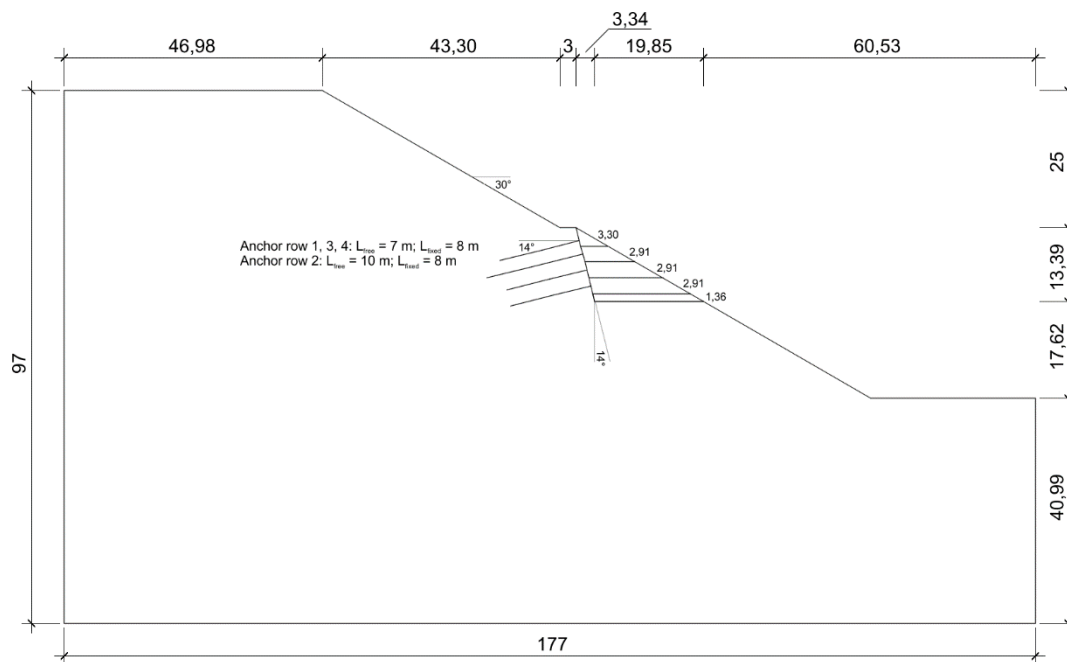


Fig. 49: Model dimensions 'Final'

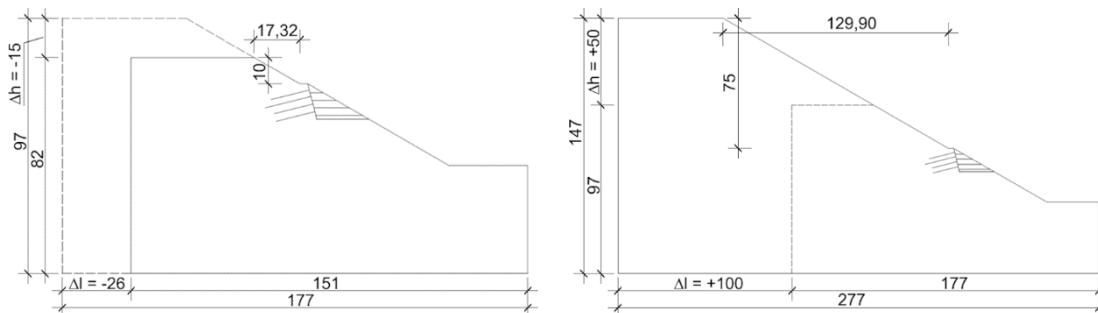


Fig. 50: Model dimensions; left: 'Small'; right: 'Big'

When modelling the homogenous ground layer, the main emphasis was placed on the Mohr-Coulomb (*MC*) model. This model describes the soil by means of linear elastic perfectly plastic behaviour. Tab. 9 shows the parameters of the materials representing soil and fill, the latter describing the re-fill material after the last excavation stage over a predefined height. To compare results and identify the influence of the constitutive model, *FEAs* were also conducted with the Hardening soil small (*HSS*) model seen in Tab. 10. More details on the *HSS* model can be found in Benz (2007).

Tab. 9: Parameters of soil and fill for the *MC* model

| | Soil | Fill |
|--|-------------|-----------|
| Material model | <i>MC</i> | <i>MC</i> |
| Drainage type | Drained | Drained |
| $\gamma_{\text{unsat}} = \gamma_{\text{sat}}$ [kN/m ³] | 20 | 21 |
| E' [kN/m ²] | 20000 | 60000 |
| ν' [-] | 0.30 | 0.30 |
| c'_{ref} [kN/m ²] | 0.10/1/3/5 | 0.10 |
| ϕ' [°] | 38 | 40 |
| ψ [°] | 8 | 10 |
| R_{inter} [-] | 0.70/0.90/1 | 0.90 |
| K_0 determination | Automatic | Automatic |

Tab. 10: Parameters of soil and fill for the *HSS* model

| | Soil | Fill |
|--|------------|------------|
| Material model | <i>HSS</i> | <i>HSS</i> |
| Drainage type | Drained | Drained |
| $\gamma_{\text{unsat}} = \gamma_{\text{sat}}$ [kN/m ³] | 20 | 21 |
| E_{50}^{ref} [kN/m ²] | 20000 | 80000 |
| $E_{\text{oed}}^{\text{ref}}$ [kN/m ²] | 20000 | 80000 |
| $E_{\text{ur}}^{\text{ref}}$ [kN/m ²] | 60000 | 240000 |
| Power m [-] | 0.50 | 0.50 |
| c'_{ref} [kN/m ²] | 0.10/5 | 0.10 |
| ϕ' [°] | 38 | 40 |
| ψ [°] | 8 | 10 |
| $\gamma_{0.7}$ [-] | 0.00015 | 0.00010 |
| G_0^{ref} [kN/m ²] | 75000 | 300000 |
| ν'_{ur} [-] | 0.20 | 0.20 |
| p_{ref} [kN/m ²] | 100 | 100 |
| K_0^{nc} | 0.384339 | 0.357212 |
| R_{inter} [-] | 0.90 | 0.90 |
| K_0 determination | Automatic | Automatic |
| OCR [-] | 1 | 1 |

The wall itself was modelled by means of elastic plate elements. For these plate elements, which are actually beam elements, an equivalent thickness, based on the bending stiffness EI and axial stiffness EA , is calculated (Brinkgreve *et al.*, 2018b). Parameters which lead to an equivalent thickness of 0.50 m can be observed in Tab. 11.

Tab. 11: Parameters of wall modelled with plate elements

| | Wall |
|--|-------------|
| Material type | Elastic |
| Isotropic | Yes |
| EA_1 [kN/m] | 15000000 |
| EI [kNm²/m] | 312500 |
| w [kN/m/m] | 10 |
| ν [-] | 0.20 |
| Prevent punching | No |

To account for the free anchor length, PLAXIS 2D (Brinkgreve *et al.*, 2018b) offers structural elements with constant axial stiffness EA – namely, node-to-node anchors. Input parameters from Tab. 12 were calculated based on a seven-wired strand assembly with an area of 1050 mm².

Tab. 12: Parameters of tendon modelled with node-to-node anchors

| | Tendon |
|--|---------------|
| Material type | Elastic |
| EA [kN] | 220500 |
| L_{spacing} [m] | 5 |

Regarding discretisation of the fixed anchor length, *FEAs* comprised geogrids and embedded beams (*EBs*). The parameters for both options can be seen in Tab. 13. Additionally, the *EB* alternative was calculated with constant and linear distribution of the skin resistance.

Geogrids in PLAXIS 2D (Brinkgreve *et al.*, 2018b) are line elements with axial stiffness EA but without bending stiffness EI ; such geogrids can only sustain tensile forces. As with plate elements, special interface elements are necessary around geogrids to account for the soil-structure interaction.

In PLAXIS 2D (Brinkgreve *et al.*, 2018b), *EBs* are line elements which are not included in the mesh but rather are superimposed on the mesh (see Fig. 51). *EBs* are a simplified approach to account for 3D effects in a 2D plane strain model. Implemented interfaces connect the continuous underlying mesh and the overlying *EB* in the out-of-plane direction. Therefore, no additional interfaces, such as for plates or geogrids, are needed.

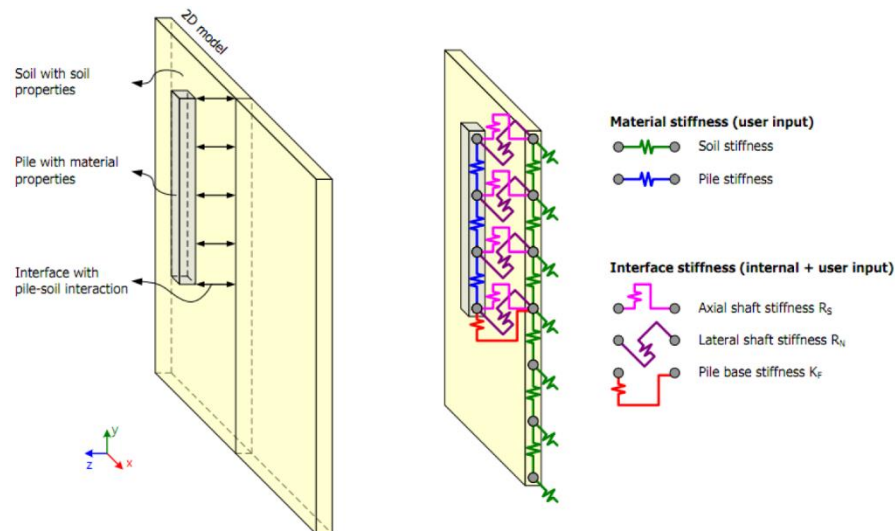


Fig. 51: *EB* interaction with soil (Brinkgreve *et al.*, 2018b)

Tab. 13: Parameters of grout body modelled with geogrid and *EB* elements

| | Grout (Geogrid) | Grout (<i>EB</i>) |
|--|------------------------|--------------------------|
| Material type | Elastic | Elastic |
| Isotropic | Yes | - |
| EA_1 [kN/m] | 85000 | - |
| E [kN/m²] | - | 16500000 |
| γ [kN/m³] | - | 4 |
| Beam type | - | Predefined |
| Predefined beam type | - | Massive circular beam |
| Diameter [m] | - | 0.178 |
| L_{spacing} [m] | - | 5 |
| Axial skin resistance | - | Linear |
| $T_{\text{skin, start, max}}$ [kN/m] | - | 700/0 |
| $T_{\text{skin, end, max}}$ [kN/m] | - | 700/1400 |
| Lateral skin resistance | - | Unlimited |
| F_{max} [kN] | - | 0 |

Fig. 52 portrays the mesh discretisation of geometry ‘Final’, whereby the fixed anchor length is modelled with geogrids and *EBs*. Solely 15-noded triangular elements were used for the mesh generation. In addition, the mesh coarseness was mainly adapted in the area of the anchors and in the area close to the slope, where the failure mechanism (*FM*) was to be expected.

The mesh discretisation of the additional dimensions ‘Small’ and ‘Big’ can be seen in Fig. 53.

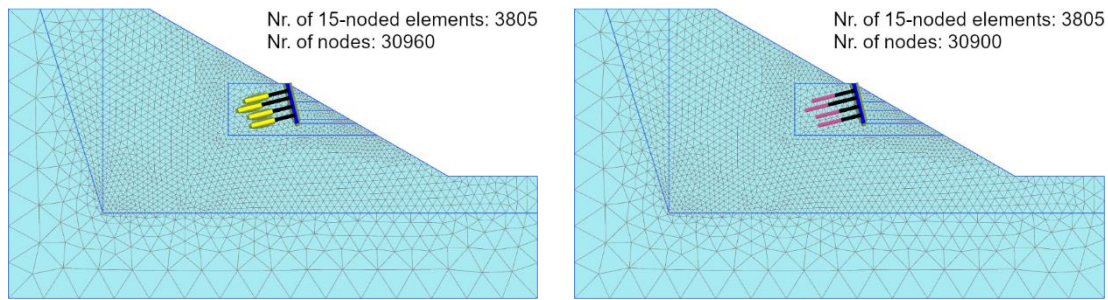


Fig. 52: Mesh discretisation for model 'Final'; left: Geogrid; right: *EB*

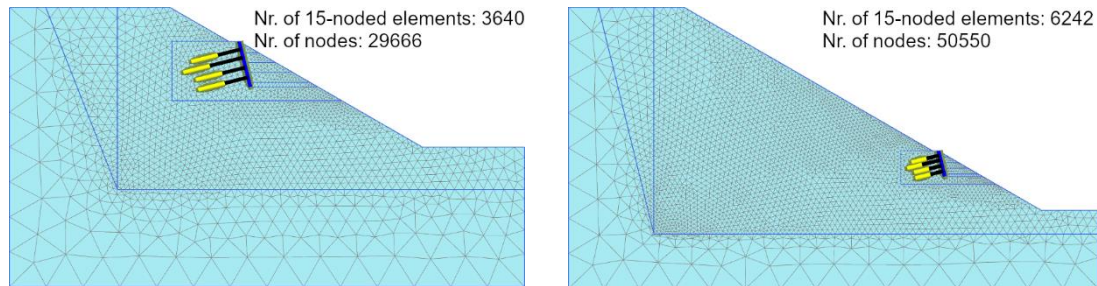


Fig. 53: Mesh discretisation; left: Model 'Small'; right: Model 'Big'

One *FEA* comprised 25 calculation phases, which are presented in Tab. 14. Because of the non-horizontal ground conditions, the Initial phase was calculated by means of gravity-loading. A Plastic nil step was introduced following the Initial phase. It should be noted that the option 'Arc-length control type' was deactivated during the Plastic nil step. Following the Plastic nil step, displacements were set to zero. Excavation, installation of the wall and installation of one anchor row were modelled in a single phase, followed by the pre-stressing procedure, during which a force of 800 kN was applied to each anchor. Furthermore, the whole construction procedure was investigated without pre-stressing of the anchors (i.e. phases which include pre-stressing of the anchors were simply deleted). To simulate the failure of a whole ground anchor row, free and fixed anchor length were deactivated during the associated calculation phase.

Tab. 14: Calculation phases for model with pre-stressing of the anchors

| ID | Stage | Start from phase |
|----|------------------------------------|------------------------------------|
| 0 | Initial phase | - |
| 1 | Plastic nil step | Initial phase |
| 2 | Exc. + Inst. wall + Inst. anchor 1 | Plastic nil step |
| 3 | Pre-stressing anchor 1 | Exc. + Inst. wall + Inst. anchor 1 |
| 4 | Exc. + Inst. wall + Inst. anchor 2 | Pre-stressing anchor 1 |
| 5 | Pre-stressing anchor 2 | Exc. + Inst. wall + Inst. anchor 2 |
| 6 | Exc. + Inst. wall + Inst. anchor 3 | Pre-stressing anchor 2 |
| 7 | Pre-stressing anchor 3 | Exc. + Inst. wall + Inst. anchor 3 |
| 8 | Exc. + Inst. wall + Inst. anchor 4 | Pre-stressing anchor 3 |
| 9 | Pre-stressing anchor 4 | Exc. + Inst. wall + Inst. anchor 4 |
| 10 | Excavation + Installation wall 5 | Pre-stressing anchor 4 |
| 11 | Construction fill | Excavation + Installation wall 5 |
| 12 | Safety Plastic nil step | Plastic nil step |

| ID | Stage | Start from phase |
|----|-------------------------------|------------------------|
| 13 | Safety Pre-stressing anchor 1 | Pre-stressing anchor 1 |
| 14 | Safety Pre-stressing anchor 2 | Pre-stressing anchor 2 |
| 15 | Safety Pre-stressing anchor 3 | Pre-stressing anchor 3 |
| 16 | Safety Construction fill | Construction fill |
| 17 | Failure anchor row 1 | Construction fill |
| 18 | Failure anchor row 3 | Construction fill |
| 19 | Failure anchor row 3+4 | Construction fill |
| 20 | Failure anchor row 2+3 | Construction fill |
| 21 | Safety Failure anchor row 1 | Failure anchor row 1 |
| 22 | Safety Failure anchor row 3 | Failure anchor row 3 |
| 23 | Safety Failure anchor row 3+4 | Failure anchor row 3+4 |
| 24 | Safety Failure anchor row 2+3 | Failure anchor row 2+3 |

Some representative calculation phases from Tab. 14 are schematically visualised in Fig. 54, showing the fixed anchor length modelled by means of geogrid elements.

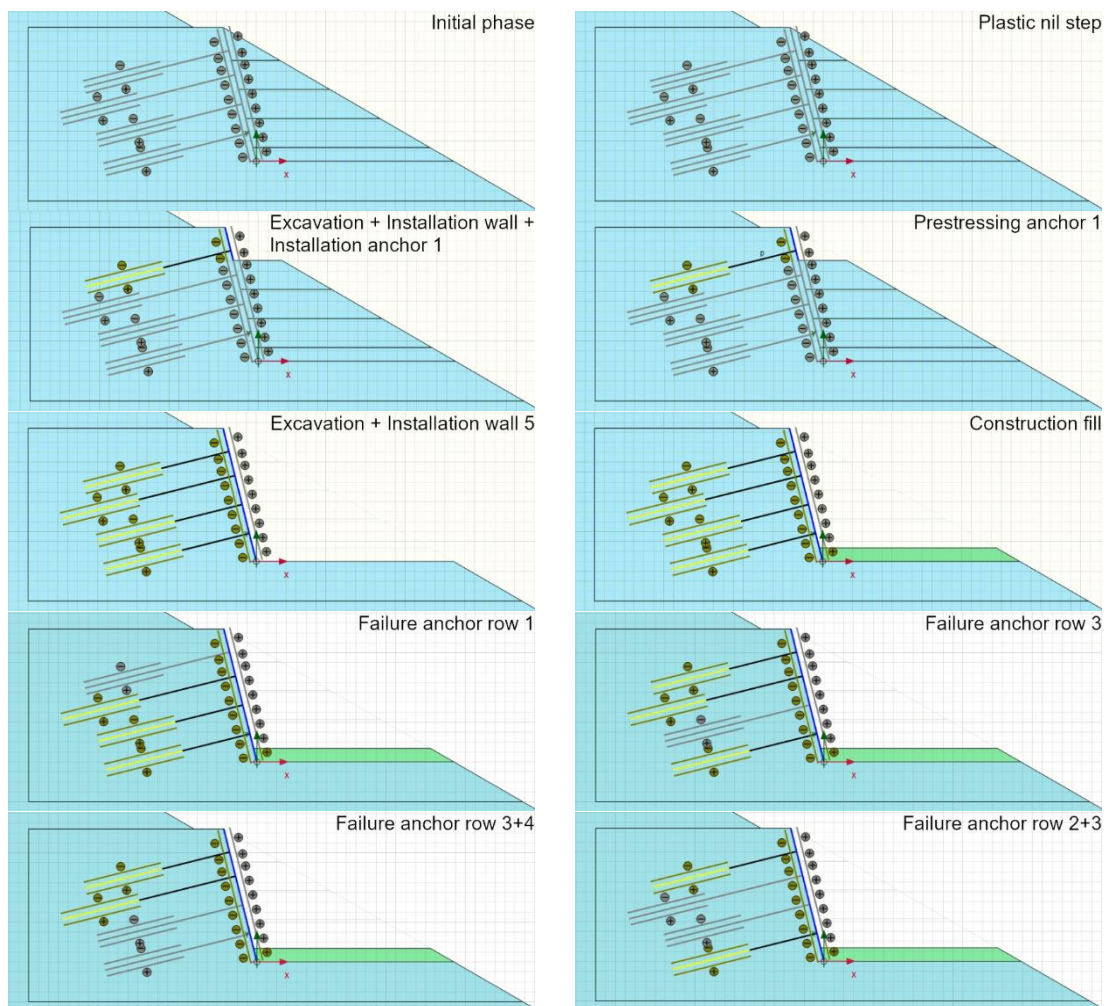


Fig. 54: Representation of selected calculation phases

4.3 Results

Fig. 55 to Fig. 62 depict the results of the study on different model dimensions concerning initial conditions with varying cohesion. These results represent *FEAs* conducted with the *MC* model, where the *FoS* values are evaluated after the calculation phase Plastic nil step.

The *FoS* for the parameter set with a cohesion of 0.1 kPa can be seen in Fig. 55. Corresponding to comparable *FMs*, which are visualised in Fig. 56 by the incremental deviatoric strains, plastic points and relative shear stresses, the dimensions ‘Small’ and ‘Final’ exhibit a similar *FoS* of 1.31 and 1.30, respectively. Model ‘Big’ shows the lowest *FoS*, which also applies to all other variations of the cohesion, at a magnitude of 1.28.

Details on incremental deviatoric strains, plastic points and relative shear stresses can be found in Brinkgreve et al. (2018b).

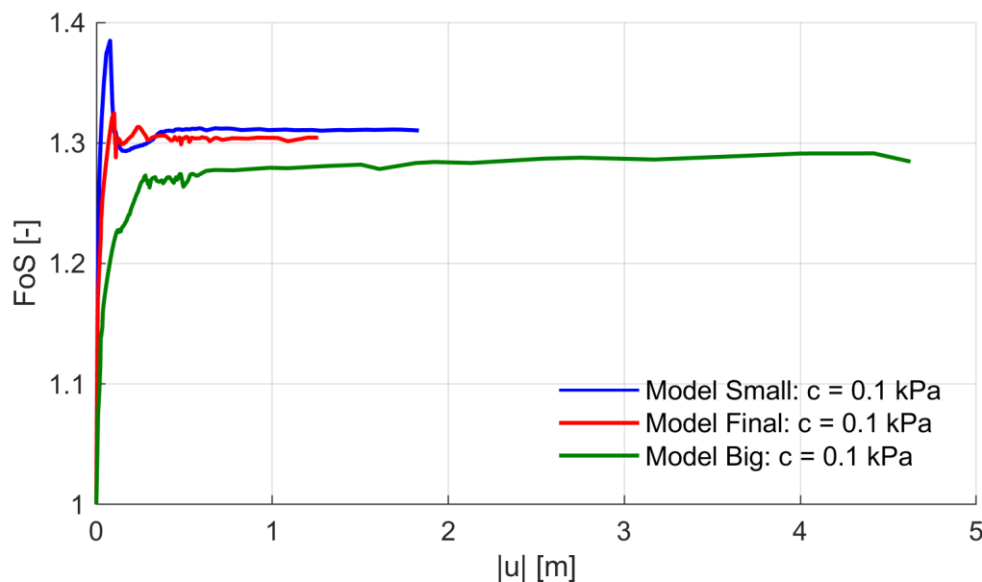


Fig. 55: *FoS* after φ - c reduction Plastic nil step for $c = 0.1$ kPa

Fig. 56 also shows that *FMs* for all geometries are to be found in the lower part of the slope. While the models ‘Small’ and ‘Final’ basically show identical failure behaviour, the slip circle in model ‘Big’ differs noticeably.

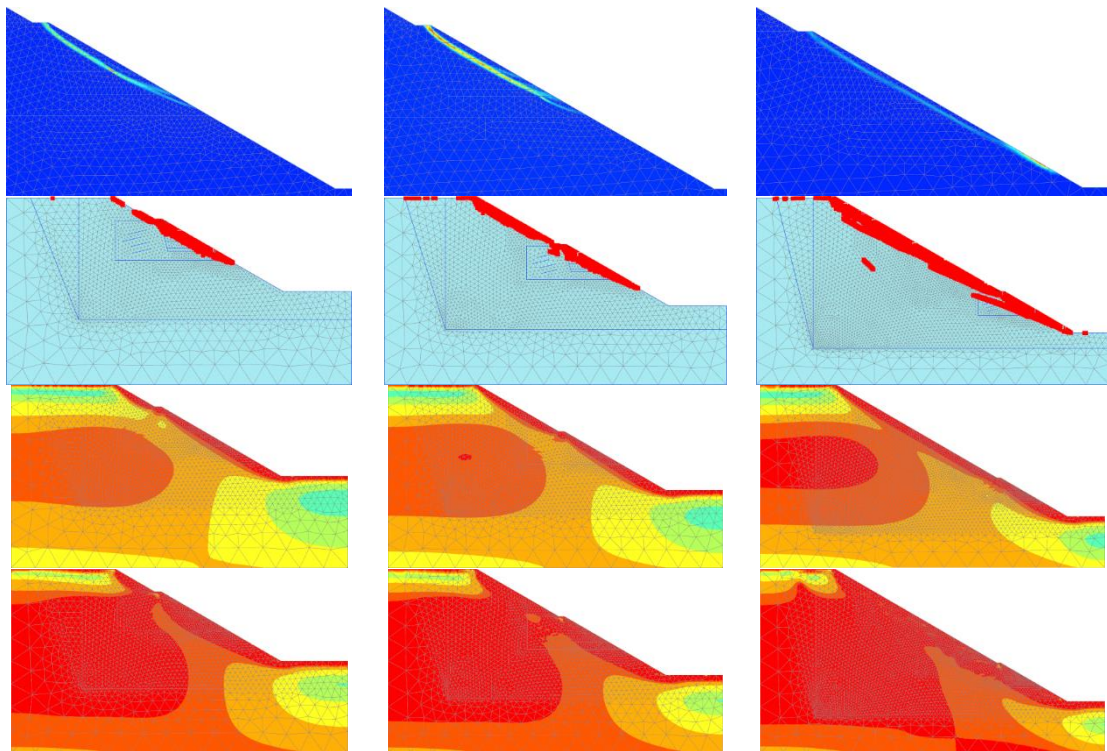


Fig. 56: Incremental deviatoric strains and plastic points after as well as τ_{rel} before/after ϕ - c reduction Plastic nil step for $c = 0.1$ kPa; left: ‘Small’; centre: ‘Final’; right: ‘Big’

Compared to a cohesion of 0.1 kPa, Fig. 57 exhibits significantly higher values in the *FoS* for the *FEA* carried out with $c = 1$ kPa. The biggest increment between 0.1 kPa and 1 kPa is to be found for the dimension ‘Final.’ While a cohesion of 0.1 kPa for this geometry leads to an *FoS* of 1.30, a cohesion of 1 kPa plots an *FoS* at a magnitude of 1.38 and therefore a deviation of 0.08.

Moreover, the *FMs* for a cohesion of 1 kPa, seen in Fig. 58, show a completely different behaviour compared to Fig. 56. For the dimensions ‘Final’ and ‘Big’, the *FM* shifts into the area of the upper slope. Failure for the dimension ‘Small’ still occurs in the lower slope, but now with an increased mass of the failing soil body.

The comparison of the model dimensions and the cohesion variations respectively provide an illustrative example of the importance of selecting suitable model dimensions.

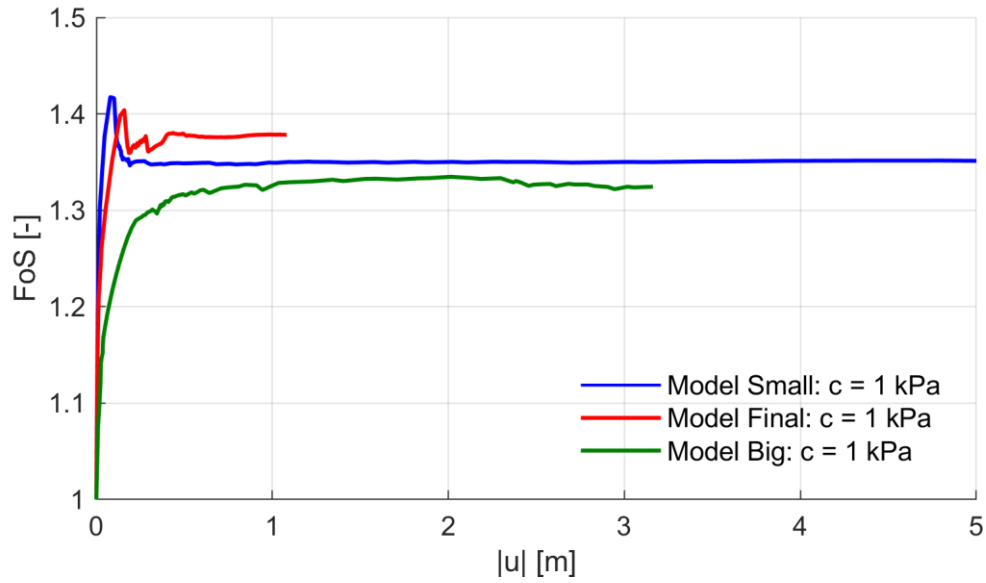


Fig. 57: FoS after ϕ - c reduction Plastic nil step for $c = 1$ kPa

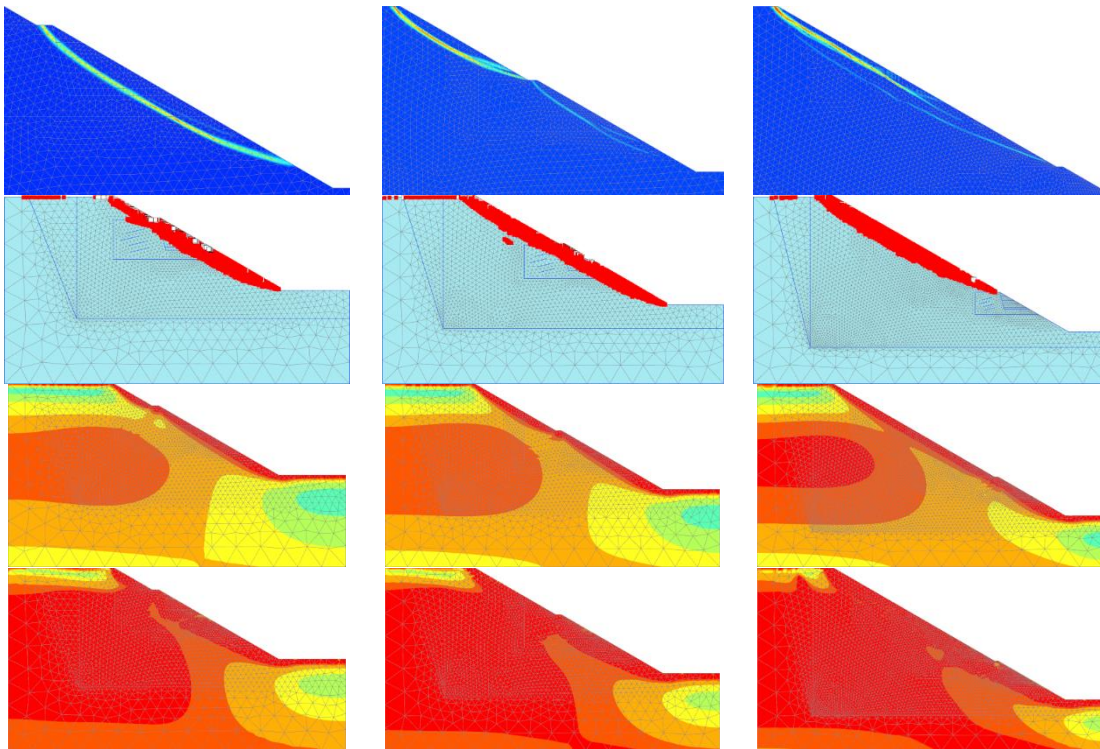


Fig. 58: Incremental deviatoric strains and plastic points after as well as τ_{rel} before/after ϕ - c reduction Plastic nil step for $c = 1$ kPa; left: 'Small'; centre: 'Final'; right: 'Big'

Fig. 59 portrays the FoS for the FEA computed with a cohesion of 3 kPa. The smallest model shows an FoS of 1.43, while the largest model exhibits an FoS of 1.35. In between, the dimension ‘Final’ plots an FoS in the order of 1.42.

As shown in Fig. 60, the FM s for $c = 3$ kPa vary between the three geometries. Compared to models ‘Small’ and ‘Big’, where failure occurs in the lower and upper slope, respectively, the FM of model ‘Final’ extends over the total height.

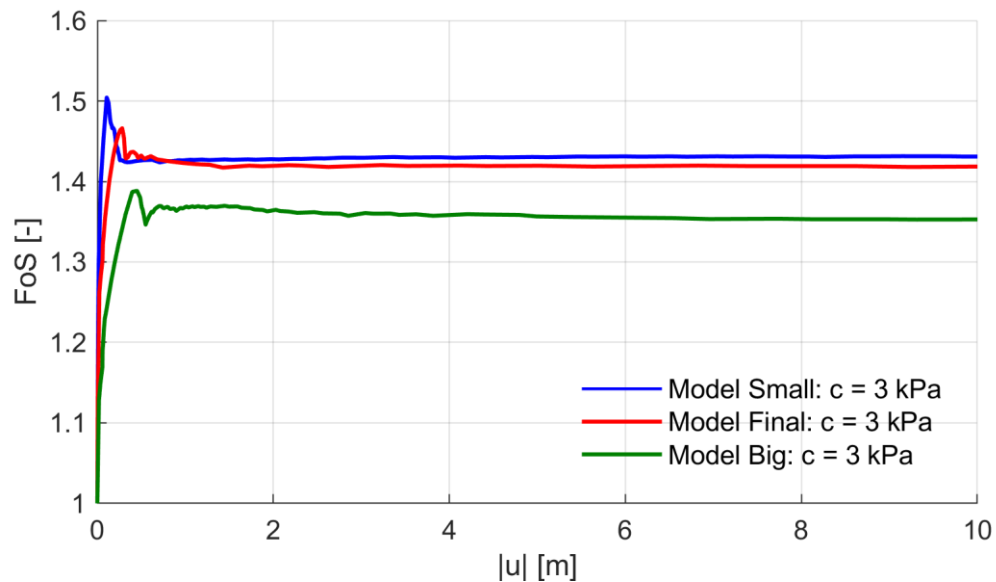


Fig. 59: FoS after ϕ - c reduction Plastic nil step for $c = 3$ kPa

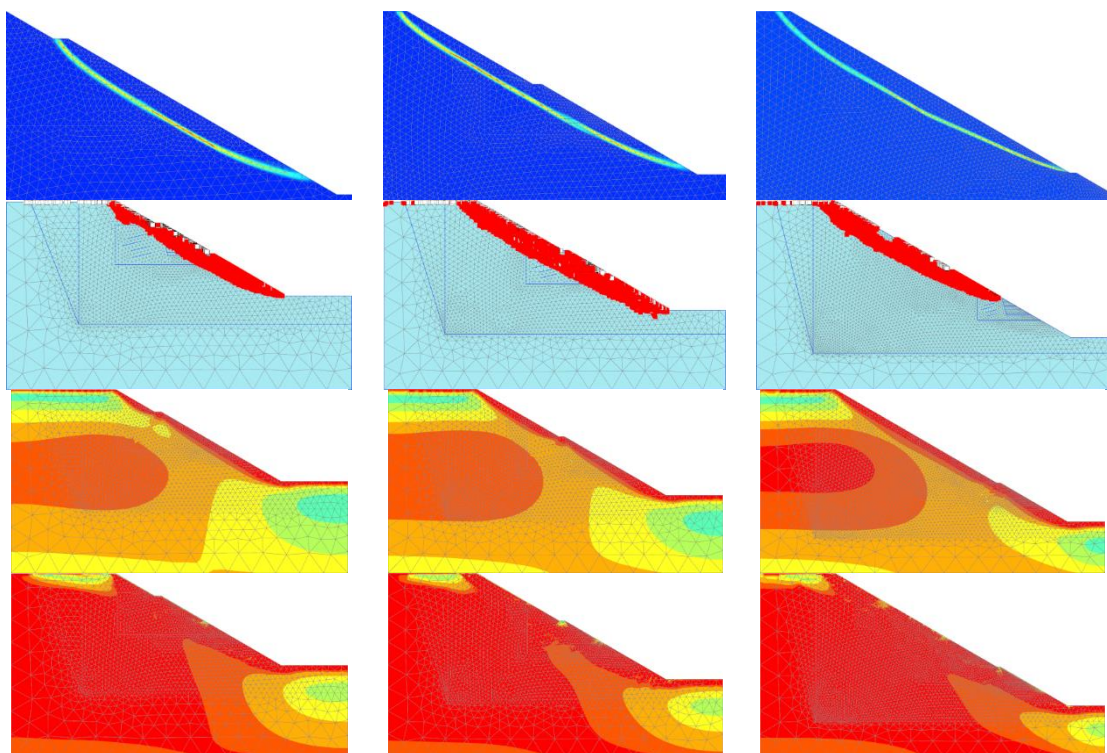


Fig. 60: Incremental deviatoric strains and plastic points after as well as τ_{rel} before/after ϕ - c reduction Plastic nil step for $c = 3$ kPa; left: ‘Small’; centre: ‘Final’; right: ‘Big’

For the sake of completeness, Fig. 61 portrays the FoS for $c = 5$ kPa, where model ‘Small’ plots an FoS of 1.50; model ‘Final’, an FoS of 1.46; and model ‘Big’, an FoS of 1.40.

The FMs for a cohesion of 5 kPa, shown in Fig. 62, are similar to the FMs for a cohesion of 3 kPa, with the only noticeable difference from model ‘Small’ being where the slip circle also connects into the upper slope now.

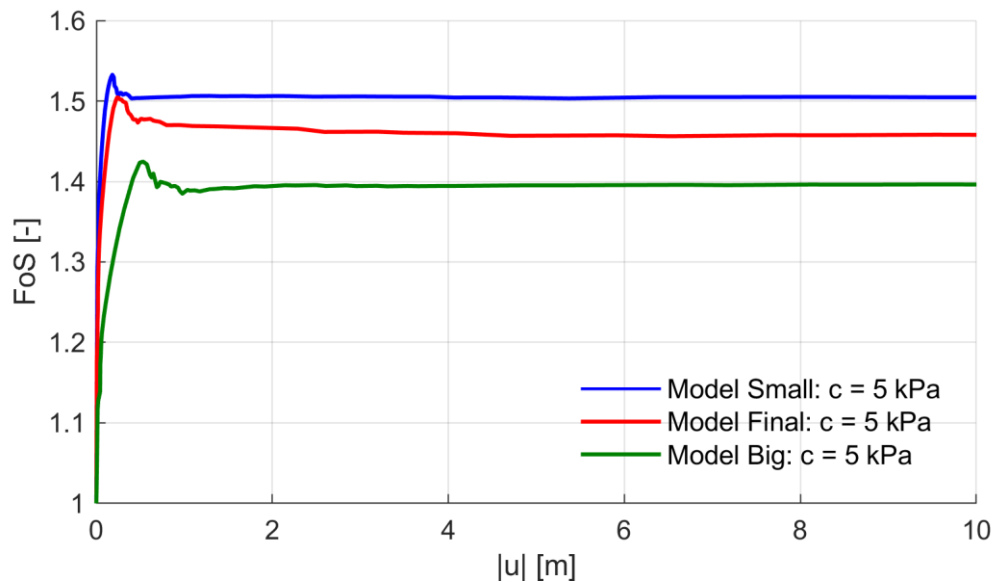


Fig. 61: FoS after ϕ - c reduction Plastic nil step for $c = 5$ kPa

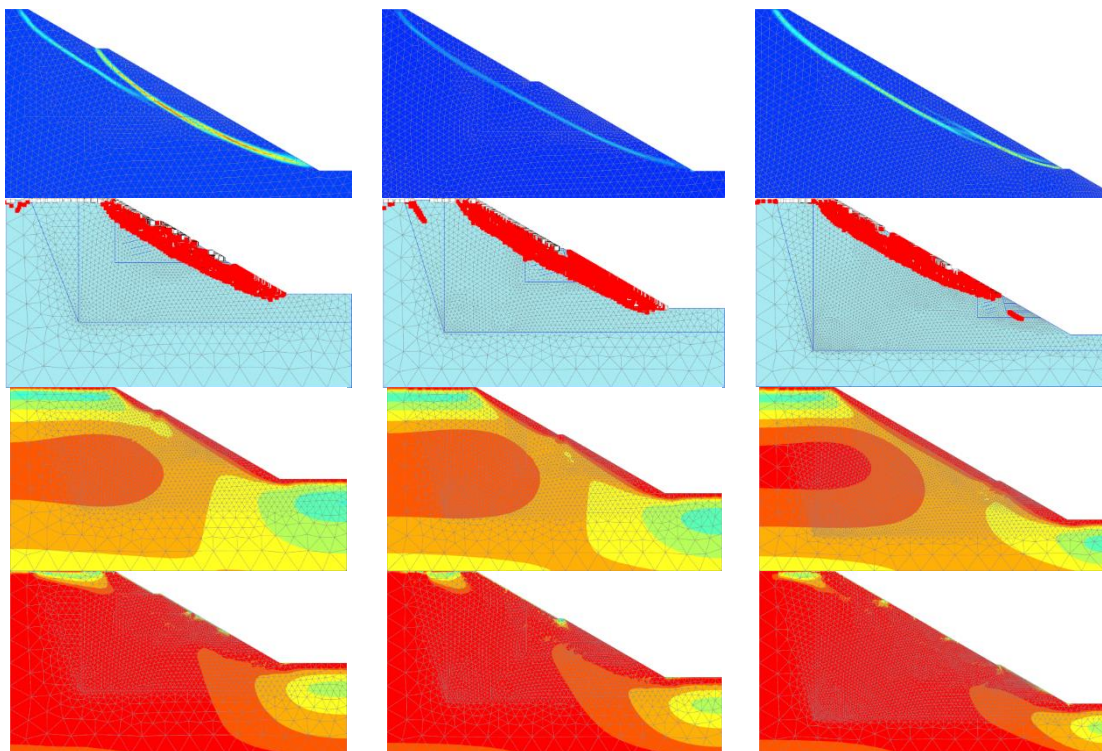


Fig. 62: Incremental deviatoric strains and plastic points after as well as τ_{rel} before/after ϕ - c reduction Plastic nil step for $c = 5$ kPa; left: ‘Small’; centre: ‘Final’; right: ‘Big’

Tab. 15 summarises the FoS for the three model dimensions and all modifications in cohesion. While all values of the cohesion show the lowest FoS for the largest model, the model ‘Small’ has the highest FoS . The sole exception to this concerns $c = 1$ kPa, where the highest FoS appears for model dimension ‘Final.’

Tab. 15: FoS after ϕ - c reduction Plastic nil step for different model dimensions with varying cohesion

| Cohesion [kPa] | FoS ‘Small’ [-] | FoS ‘Final’ [-] | FoS ‘Big’ [-] |
|----------------|-------------------|-------------------|-----------------|
| 0.1 | 1.31 | 1.30 | 1.28 |
| 1 | 1.35 | 1.38 | 1.32 |
| 3 | 1.43 | 1.42 | 1.35 |
| 5 | 1.50 | 1.46 | 1.40 |

At this point it should be mentioned that some major numerical problems were encountered during the computation of the initial conditions. In an early step, a Poisson’s ratio ν' of 0.20 was chosen for the material representing the soil (i.e. deviant to 0.30 as stated in Tab. 9). This led the model, probably as a result of the so called ϕ - ν inequality, to fail either during the Initial phase or Plastic nil step. For more details and numerical studies on the ϕ - ν inequality, reference is made to Oberhollenzer (2017).

A comparison between the Initial phase and Plastic nil step for model dimensions ‘Final’, with regard to the FoS and FM , respectively, is presented in Fig. 63 to Fig. 66. In principle, both phases show comparable FM s, which would consequently result in both phases having a similar FoS .

The FoS for these two phases, calculated with $c = 0.1$ kPa, is portrayed in Fig. 63. A larger FoS , having a value of 1.33, can be observed for the Initial phase. For all modifications in cohesion, $c = 0.1$ kPa shows the largest divergence, with a deviation of 0.03 in the FoS between Initial phase and Plastic nil step.

Fig. 64 shows the incremental deviatoric strains and plastic points for both phases, calculated with a cohesion of 0.1 kPa. The behaviour in the lower part of the slope, where failure occurs, is almost identical. In contrast to the Plastic nil step, the Initial phase shows observable deviatoric strains also in the area of the upper slope.

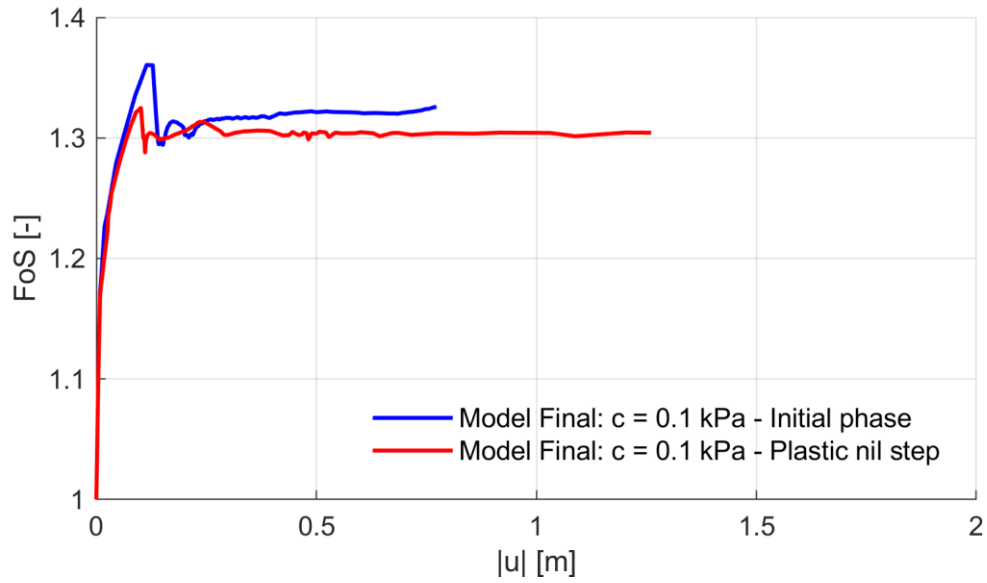


Fig. 63: FoS after ϕ - c reduction Initial phase and Plastic nil step for $c = 0.1$ kPa

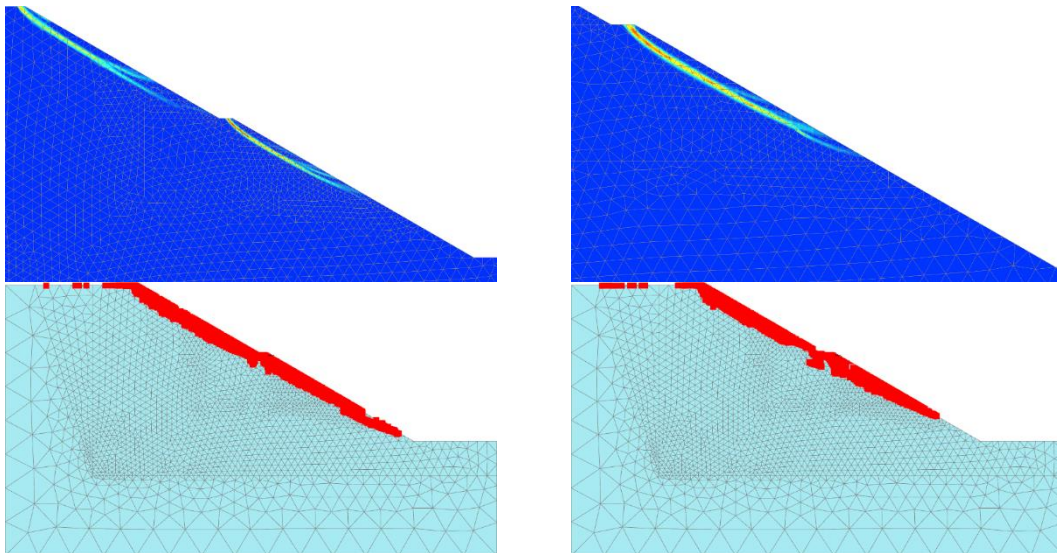


Fig. 64: Incremental deviatoric strains and plastic points after ϕ - c reduction for $c = 0.1$ kPa; left: Initial phase; right: Plastic nil step

A perfect match in the FoS , portrayed in Fig. 65, is achieved for the model computed with a cohesion of 5 kPa.

Consequently, the FM s in Fig. 66 basically show no difference.

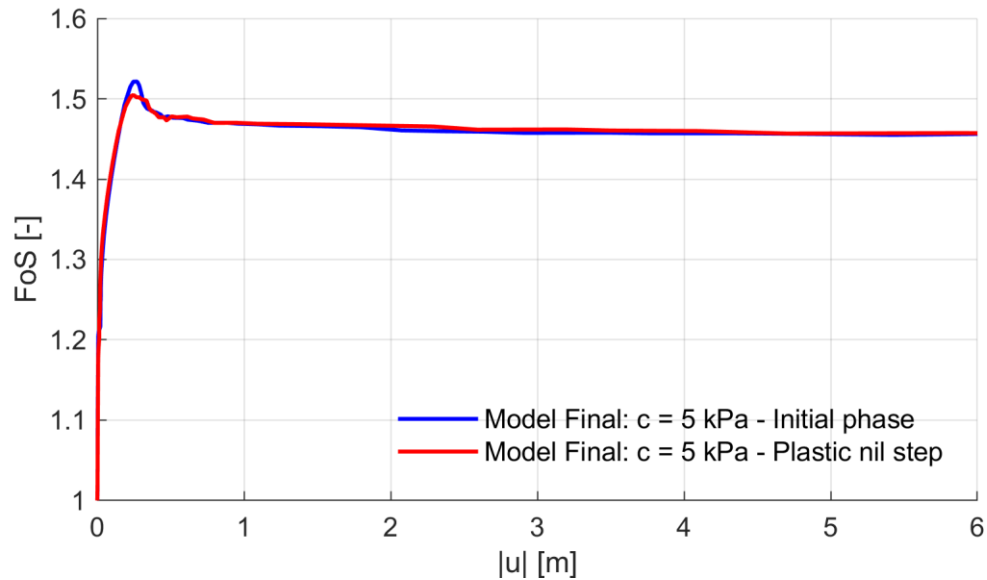


Fig. 65: FoS after φ - c reduction Initial phase and Plastic nil step for $c = 5$ kPa

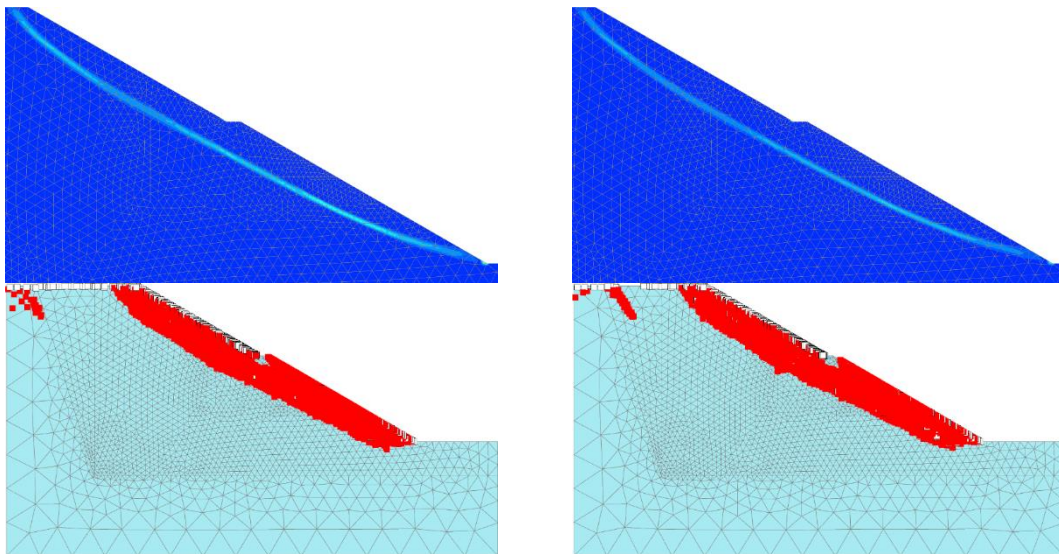


Fig. 66: Incremental deviatoric strains and plastic points after φ - c reduction for $c = 5$ kPa; left: Initial phase; right: Plastic nil step

Tab. 16 compares the FoS between the Initial phase and Plastic nil step for all modifications of the cohesion.

Tab. 16: FoS after φ - c reduction in the Initial phase and Plastic nil step for model dimensions 'Final', with varying cohesion

| Cohesion [kPa] | FoS Initial phase [-] | FoS Plastic nil step [-] |
|----------------|-------------------------|----------------------------|
| 0.1 | 1.33 | 1.30 |
| 1 | 1.37 | 1.38 |
| 3 | 1.43 | 1.42 |
| 5 | 1.46 | 1.46 |

The results presented in Fig. 67 to Fig. 73 show evaluations made for the finished RW (i.e. prior to the failure of ground anchors). For this purpose, the calculation phase Construction fill was analysed. All results represent $FEAs$ conducted using the MC model with the fixed anchor length discretised as a geogrid. The interface strength of the presented $FEAs$, expressed in PLAXIS 2D (Brinkgreve *et al.*, 2018b) by means of the R_{inter} value, was set to 0.90. Results of calculation phases that were evaluated during the construction of the wall (i.e. calculation phases which include pre-stressing of the anchors were analysed) and evaluations with other cohesion values are given in the appendix, section 8.1.

The FoS can be seen in Fig. 67. While $c = 0.1$ kPa shows the minimum FoS of 1.33, the maximum FoS , of course, appears for $c = 5$ kPa in the order of 1.54. In between, for a cohesion of 1 kPa and 3 kPa, safety margins of 1.37 and 1.45, respectively, are present.

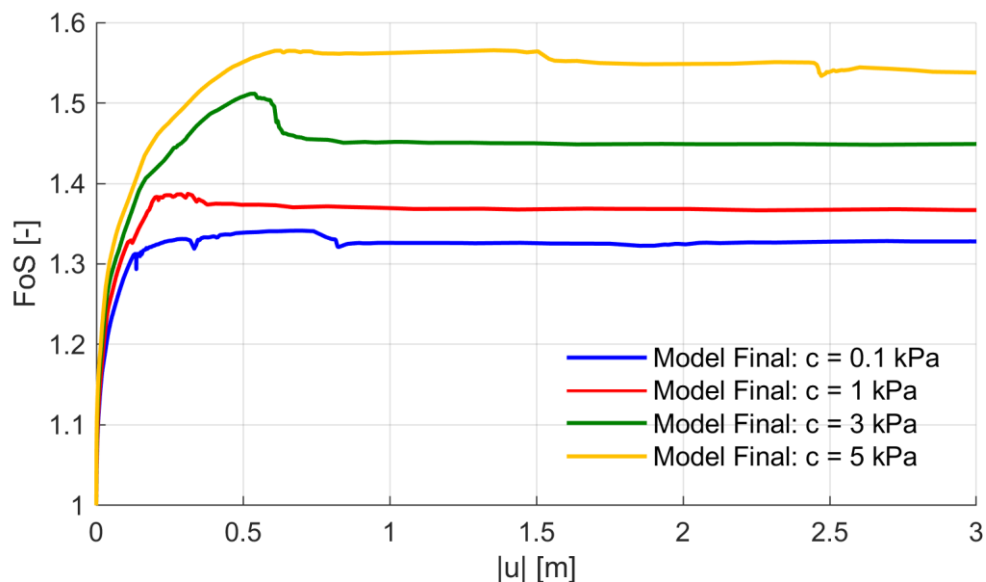


Fig. 67: FoS after φ - c reduction Construction fill

Fig. 68 represents the FM_s after the φ - c reduction Construction fill for a cohesion of 0.1 kPa and 5 kPa. All variations of the cohesion, including 1 kPa and 3 kPa, show failure in the slope above the RW . The only remarkable difference is the mass of the failing soil, which increases with rising cohesion.

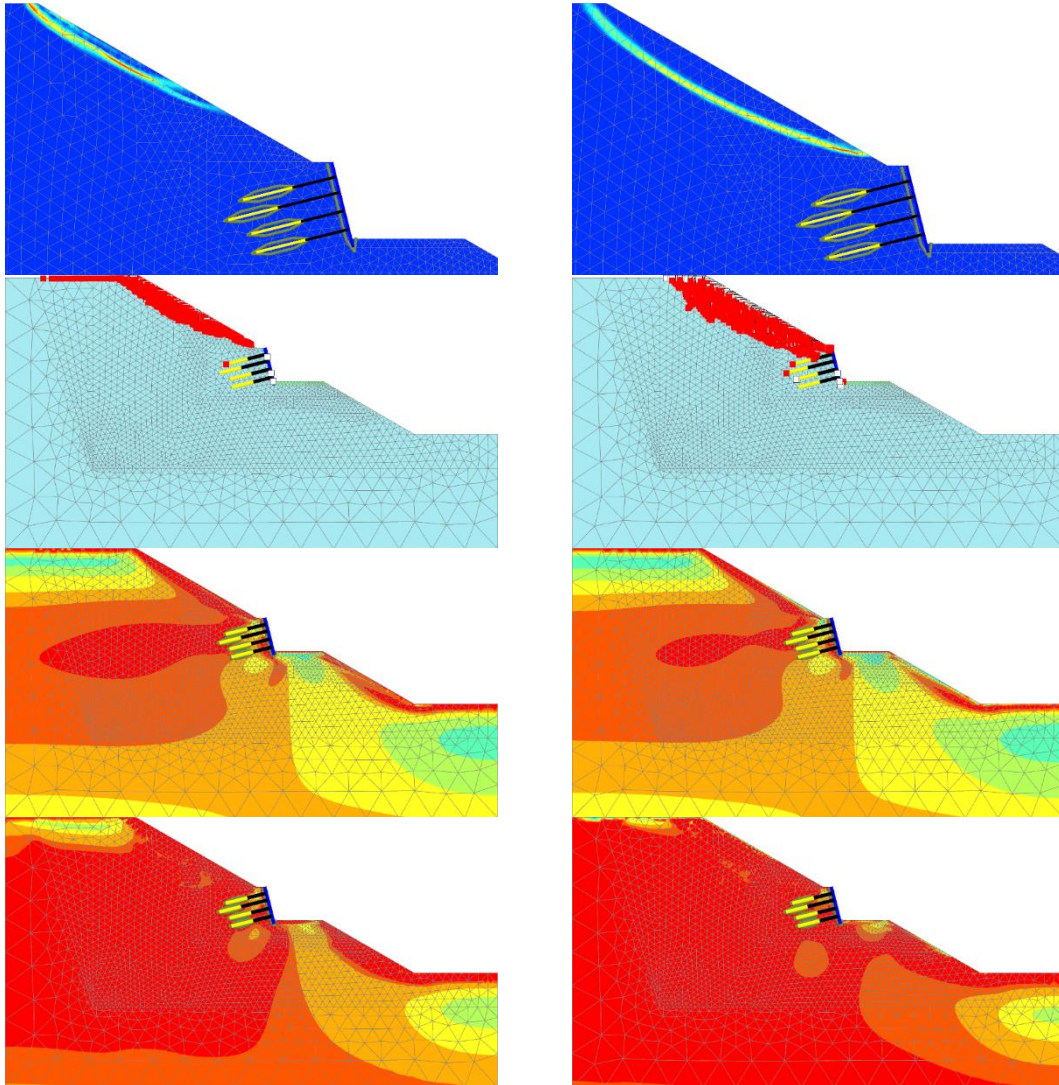


Fig. 68: Incremental deviatoric strains and plastic points after as well as τ_{rel} before/after φ - c reduction Construction fill; left: $c = 0.1$ kPa; right: $c = 5$ kPa

Fig. 69, where the true length of the RW is plotted with its actual inclination (i.e. 14° inclined towards the vertical), shows the BM_s M_{min} and M_{max} after the calculation phase Construction fill. These BM_s represent the minimum and maximum values, respectively – in other words, the envelope up to the phase Construction fill (Brinkgreve *et al.*, 2018b). Therefore, it is not mandatory that minimum or maximum BM_s occur during Construction fill (i.e. M_{min} and M_{max} can also result from a previous calculation phase). Fig. 69 reveals no significant differences in the BM_s for all modifications in cohesion. The minimum value of -596 kNm/m is to be found for $c = 0.1$ kPa, located on the level of anchor 3. In contrast, the FEA with $c = 5$ kPa shows M_{max} with a value of 65 kNm/m.

In Fig. 70, minimum and maximum values can again be seen, but now representing *SF* distributions. As with previous *BM*s, the *SF* distributions are almost identical for all values of the cohesion. While $c = 5$ kPa reveals the minimum value of -220 kN/m at anchor 1, the maximum *SF* occurs at anchor 4, with 257 kN/m for a cohesion of 1 kPa.

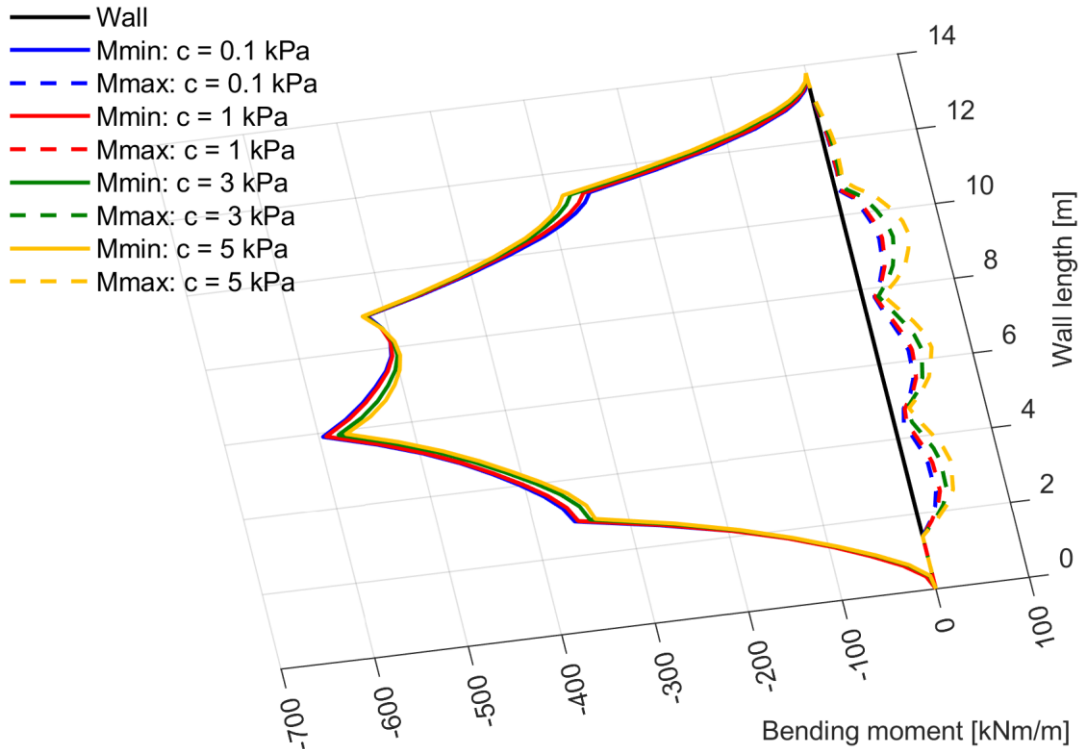


Fig. 69: *BM*s M_{min}/M_{max} after Construction fill

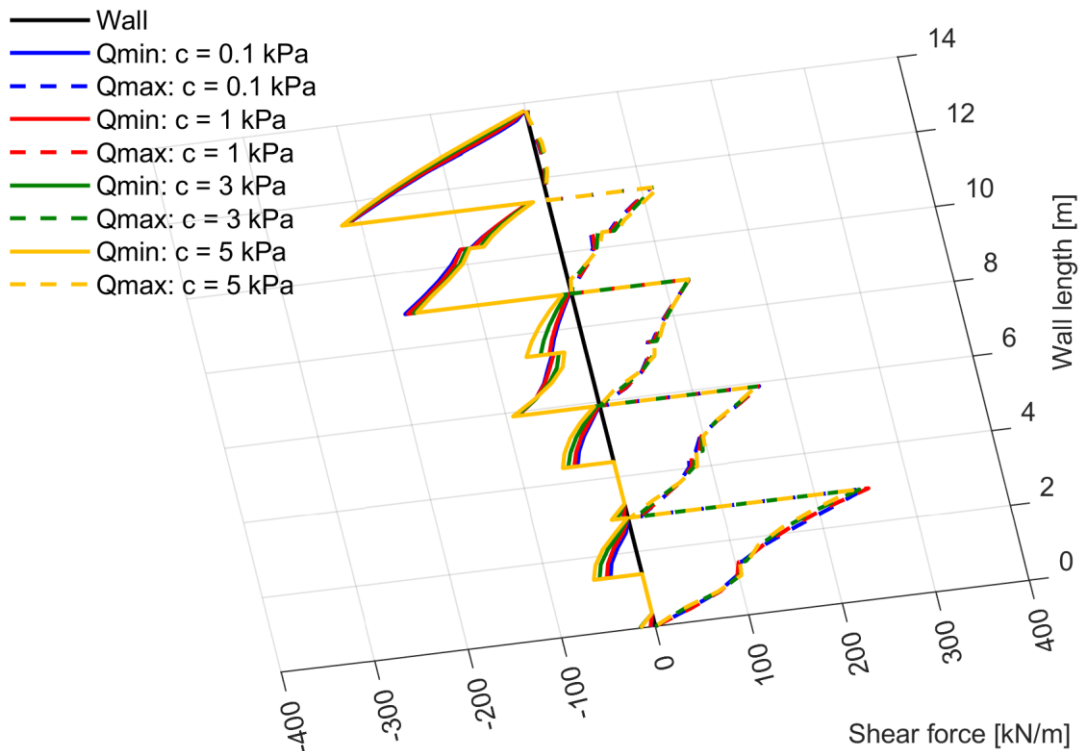


Fig. 70: *SF*s Q_{min}/Q_{max} after Construction fill

Fig. 71, where the true length of the wall (i.e. not the projected length) is plotted vertically on the y-ordinate, portrays the horizontal displacements u_x . The maximum horizontal displacement, with a magnitude of 9.20 cm, is to be found between anchor 2 and anchor 3 for a cohesion of 0.1 kPa. Deviations, though small, can be primarily found at the top of the wall and close to the wall base.

Total displacements $|u|$ are shown in Fig. 72. In contrast to the horizontal displacements, the maximum total displacement, with a value of 12 cm, is located at the top of the wall. Again, differences between all cohesion values are small.

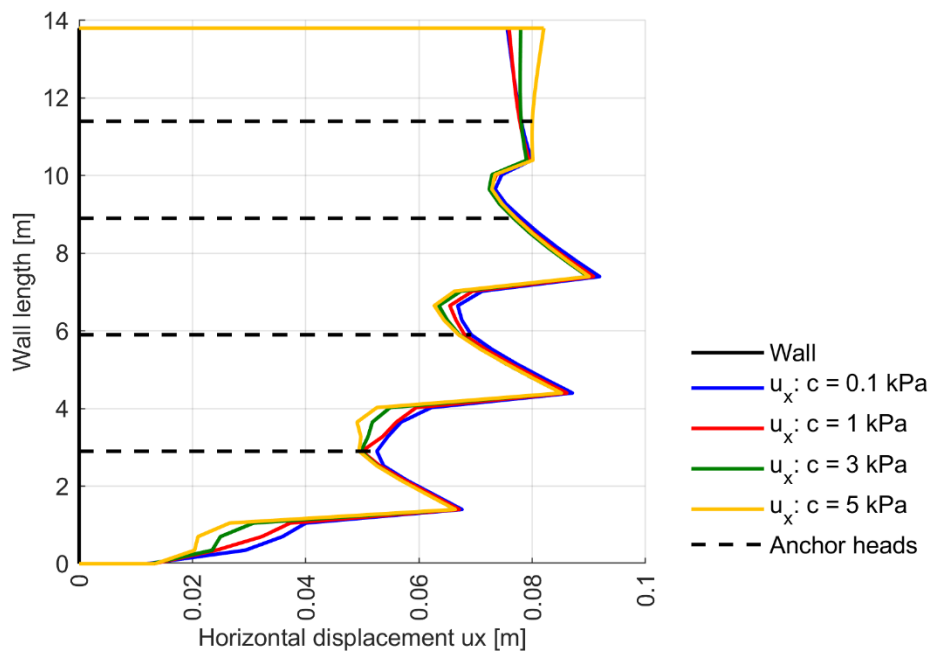


Fig. 71: Horizontal displacements u_x after Construction fill

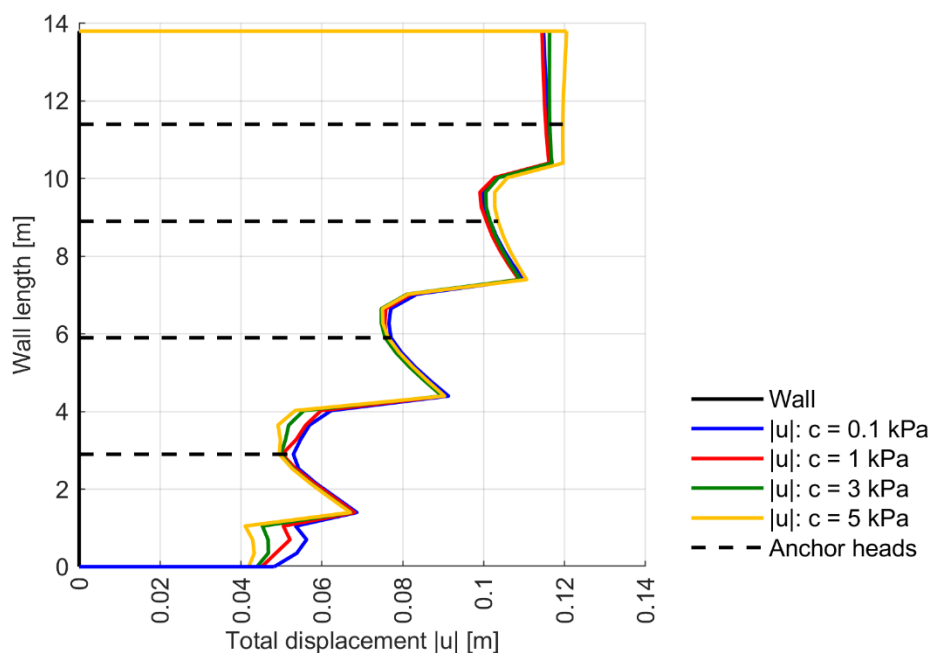


Fig. 72: Total displacements $|u|$ after Construction fill

Visualised for $c = 0.1$ kPa, the evolution of anchor forces over the calculation phases can be observed in Fig. 73. As already discussed in section 4.2, each anchor is pre-stressed with 800 kN after its installation. Since the installation and the pre-stressing of an anchor row were modelled in separate calculation phases, the anchors already show a certain anchor force before their associated pre-stressing phase. From a practical point of view, however, this anchor force can only be generated because of an interlock (i.e. by the anchor head after pre-stressing the anchor) between the tendon and the substructure. Moreover, linear elastic material behaviour was assumed for the anchor tendons, consequently overstressing was excluded. While anchor 1 and anchor 2 show the biggest increment in the anchor force between installation and pre-stressing of the tendon, the maximum increment for anchor 3 and anchor 4 is found between pre-stressing and excavation of the next level. Moreover, Fig. 73 reveals the trend that anchor forces (after a substantial increase in the beginning) tend to become more or less constant. Ranked from highest to lowest anchor force for the calculation phase Construction fill (i.e. anchor 3, anchor 4, anchor 2 and anchor 1) the other *FEAs* (using different effective cohesion values) show the same behaviour with just small deviations in the anchor force.

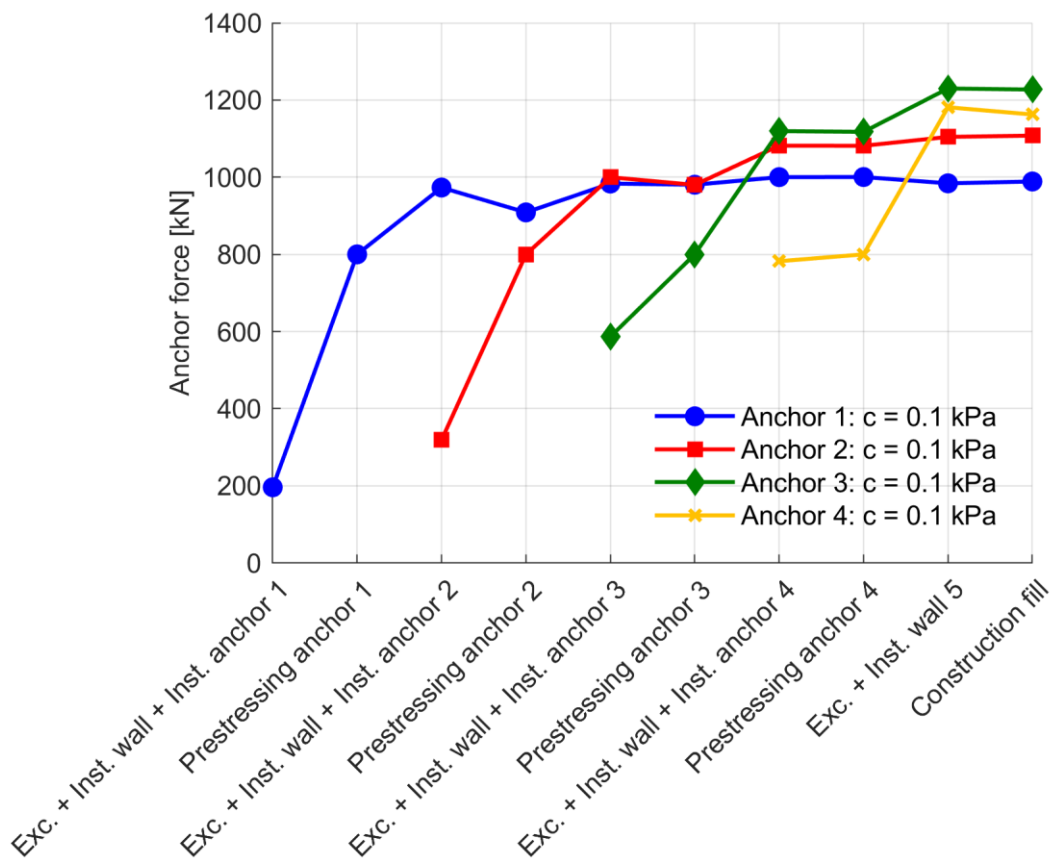


Fig. 73: Evolution of anchor forces over calculation phases for $c = 0.1$ kPa

Tab. 17 gives a tabulated summary of the previously presented results after the calculation phase Construction fill.

Tab. 17: Results of calculation phase Construction fill

| | Cohesion [kPa] | | | | [%] |
|----------------------|----------------|-------|-------|-------|-------|
| | 0.1 | 1 | 3 | 5 | 5/0.1 |
| FoS [-] | 1.33 | 1.37 | 1.45 | 1.54 | 115.8 |
| M_{min} [kNm/m] | -596 | -592 | -579 | -571 | 95.8 |
| M_{max} [kNm/m] | 34 | 38 | 48 | 65 | 191.2 |
| Q_{min} [kN/m] | -217 | -218 | -219 | -220 | 101.4 |
| Q_{max} [kN/m] | 253 | 257 | 247 | 240 | 94.9 |
| $u_{x,max}$ [cm] | 9.20 | 9.10 | 9.00 | 9.00 | 97.8 |
| $ u _{max}$ [cm] | 11.70 | 11.60 | 11.70 | 12.00 | 102.6 |
| $F_{Anchor\ 3}$ [kN] | 1227 | 1220 | 1221 | 1222 | 99.6 |
| $F_{Anchor\ 4}$ [kN] | 1163 | 1163 | 1159 | 1165 | 100.2 |
| $F_{Anchor\ 2}$ [kN] | 1108 | 1103 | 1104 | 1108 | 100.0 |
| $F_{Anchor\ 1}$ [kN] | 989 | 993 | 1010 | 1028 | 103.9 |

Results related to the failure of ground anchors are presented in Fig. 74 to Fig. 87. As already seen in Tab. 14 and Fig. 54, four different cases of row-wise ground anchor failure were investigated.

Fig. 74 portrays the FoS , computed with a cohesion of 0.1 kPa, after the ϕ - c reduction Construction fill and the four ground anchor failure cases, respectively. As expected, the calculation phase Construction fill exhibits the maximum FoS of 1.33, while the FoS (slightly) decreases for all failure cases. Nevertheless, the FoS remains more or less constant for all anchor failure cases.

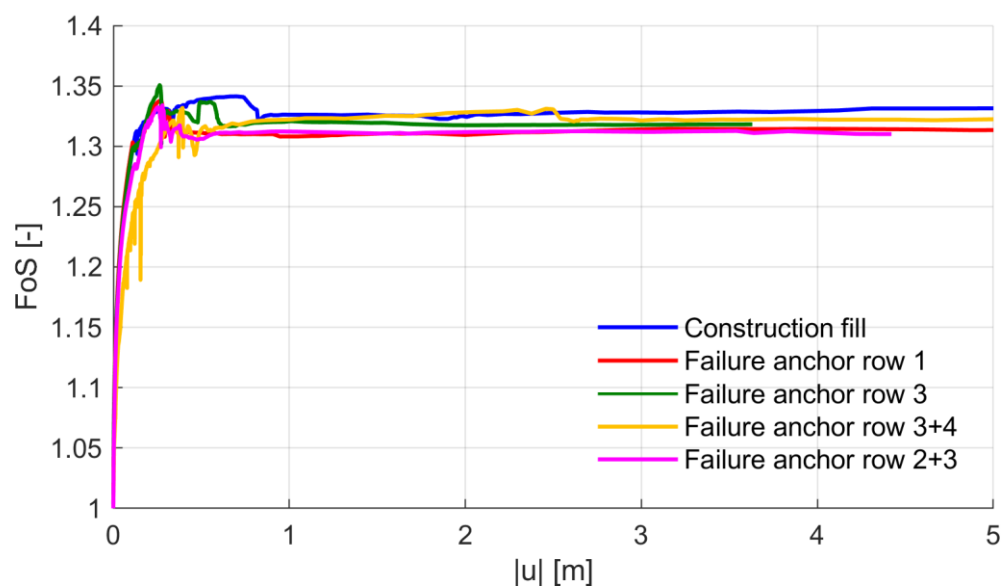


Fig. 74: FoS after ϕ - c reduction Construction fill and Failure cases for $c = 0.1$ kPa

FMs are visualised in Fig. 75, where very similar *FMs* in the slope above the *RW* (which would explain the similar safety margins from Fig. 74) can be observed.

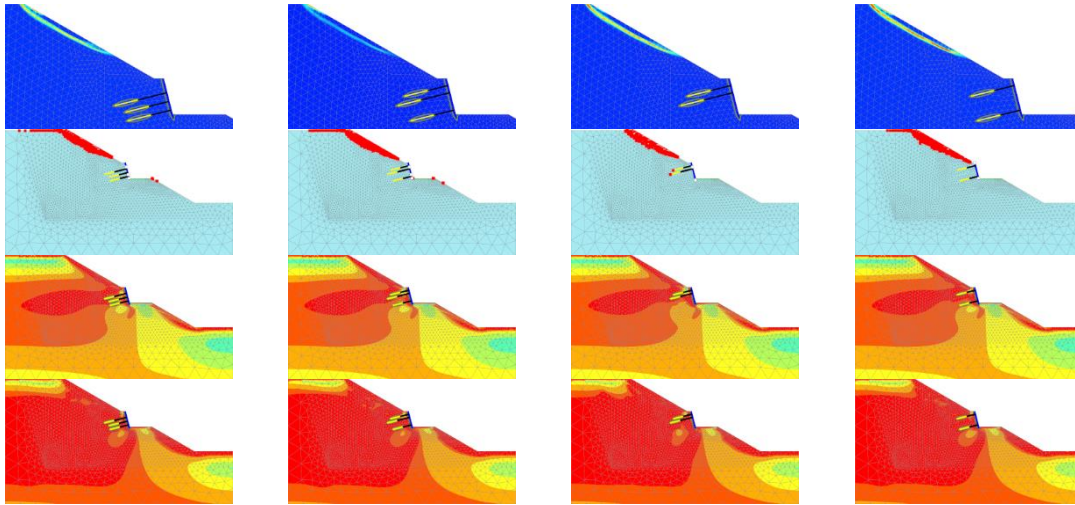


Fig. 75: Incremental deviatoric strains and plastic points after as well as τ_{rel} before/after ϕ - c reduction Failure cases for $c = 0.1$ kPa; left: Failure anchor row 1; centre left: Failure anchor row 3; centre right: Failure anchor row 3+4; right: Failure anchor row 2+3

In Fig. 76 the *FoS* for the *FEA* with a cohesion of 5 kPa is shown. Contrary to the statement made for $c = 0.1$ kPa, where Construction fill exhibits a higher *FoS* than the failure cases, the *FoS* increases for some failure phases. This increase can most likely be explained by the occurrence of stress redistributions. While both cases of single row anchor failure lead to a slight increase, both double row anchor failure cases show a decrease in the *FoS*. In contrast to a slight decrease for the phase Failure anchor row 2+3, the phase Failure anchor row 3+4 results in a significant decrease of the safety margin. Between the calculation phase Construction fill with an *FoS* of 1.54 and the calculation phase Failure anchor row 3+4 with an *FoS* of 1.45, a divergence of 0.09 is present.

Since the area near the wall base is increasingly exposed to de-icing agents and is therefore particularly susceptible to corrosion, the significant decrease in the *FoS* for ground anchor failure close to the wall base is critical. Special attention should be paid to these anchors during design as well as during construction.

The *FMs*, as shown in Fig. 77, confirm the results from Fig. 76. While the calculation phases Failure anchor row 1, 3 and 2+3 basically show the same *FMs*, the failure behaviour from the calculation phase Failure anchor row 3+4 is substantially different. In contrast to failure in the upper slope, the *FM* extends beneath the anchors and touches the wall base.

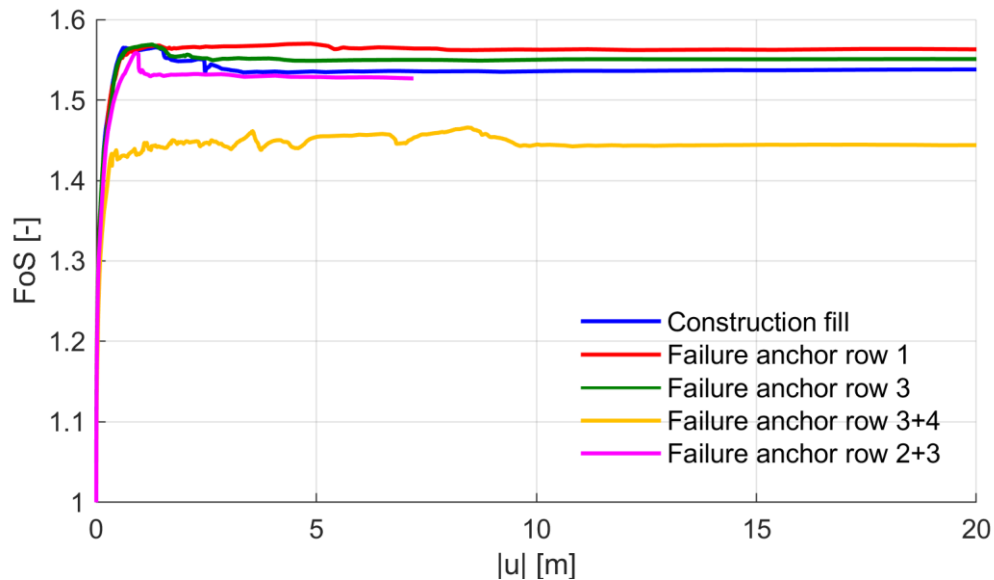


Fig. 76: FoS after ϕ - c reduction Construction fill and Failure cases for $c = 5$ kPa

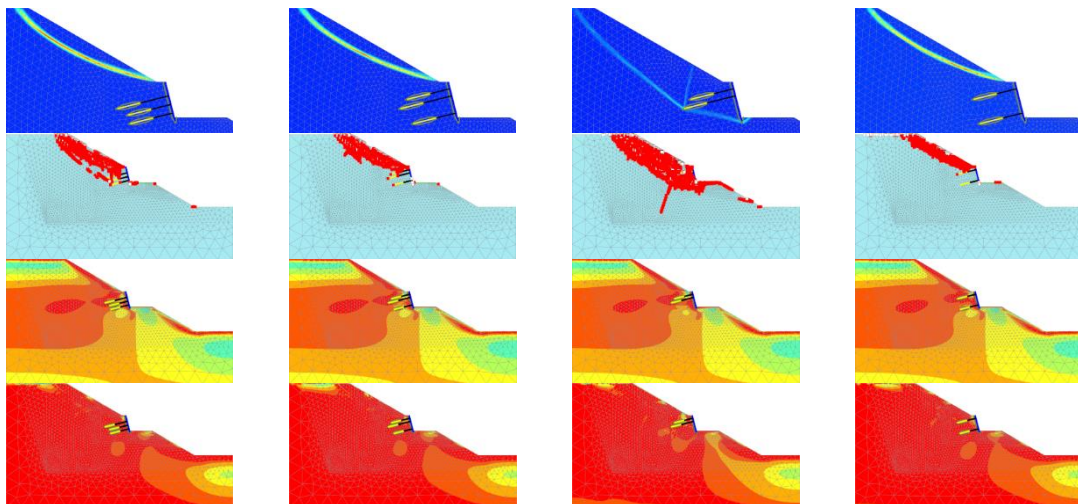


Fig. 77: Incremental deviatoric strains and plastic points after as well as τ_{rel} before/after ϕ - c reduction Failure cases for $c = 5$ kPa; left: Failure anchor row 1; centre left: Failure anchor row 3; centre right: Failure anchor row 3+4; right: Failure anchor row 2+3

How the different ground anchor failure cases affect the BM distribution is shown for a cohesion of 0.1 kPa in Fig. 78. In contrast to Fig. 69, where M_{min} and M_{max} are plotted, Fig. 78 portrays actual BM s from the actual calculation phases. The wall length, plotted vertically now, represents the true length of the wall. It can be observed that only the calculation phase Failure anchor row 1 leads to an increase in the minimum value from the calculation phase Construction fill. The figure also shows that the phase Failure anchor row 3+4 causes a significant change from negative to positive BM s close to the wall base, which would require additional arrangement of reinforcement in this area.

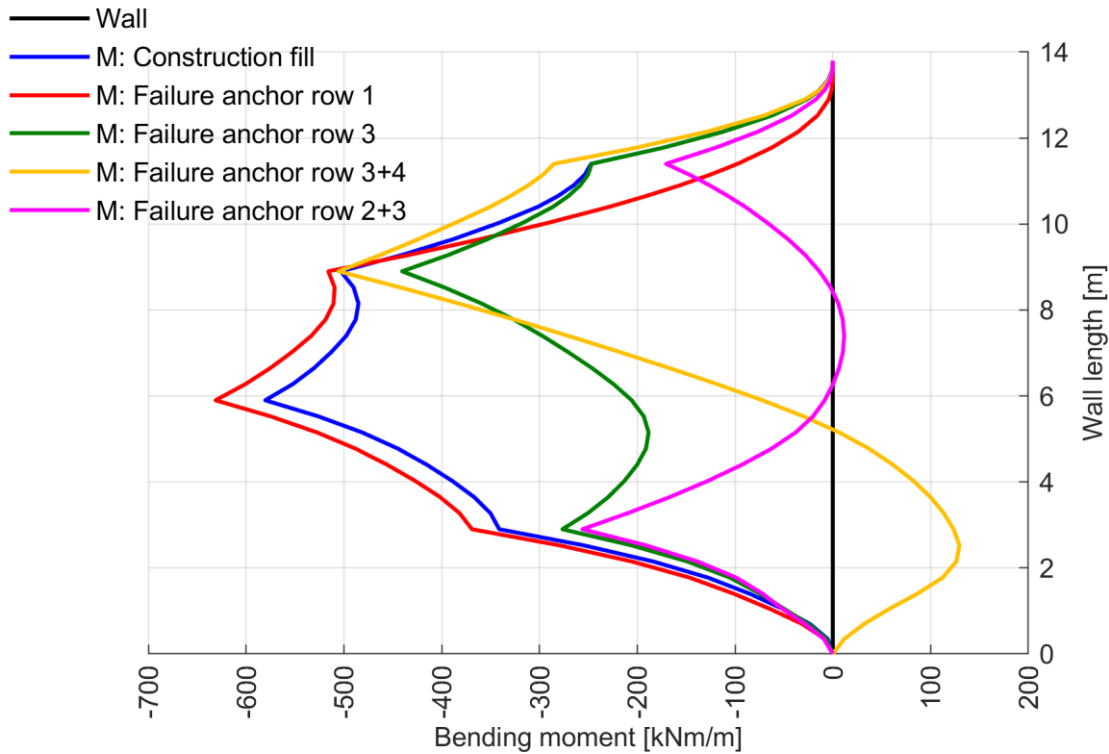


Fig. 78: $BM_s M_{actual}$ after Construction fill and Failure cases for $c = 0.1$ kPa

Fig. 79 portrays the ratio of the minimum BM from the different failure cases to the minimum BM occurring after the calculation phase Construction fill. For example, Fig. 78 shows a minimum value in the magnitude of -631 kNm/m for Failure anchor row 1, while Construction fill exhibits a minimum value of -580 kNm/m. This ratio, 1.09 for Failure anchor row 1 with $c = 0.1$ kPa, between minimal values, is plotted in Fig. 79 disregarding the location of the minimum value between both phases.

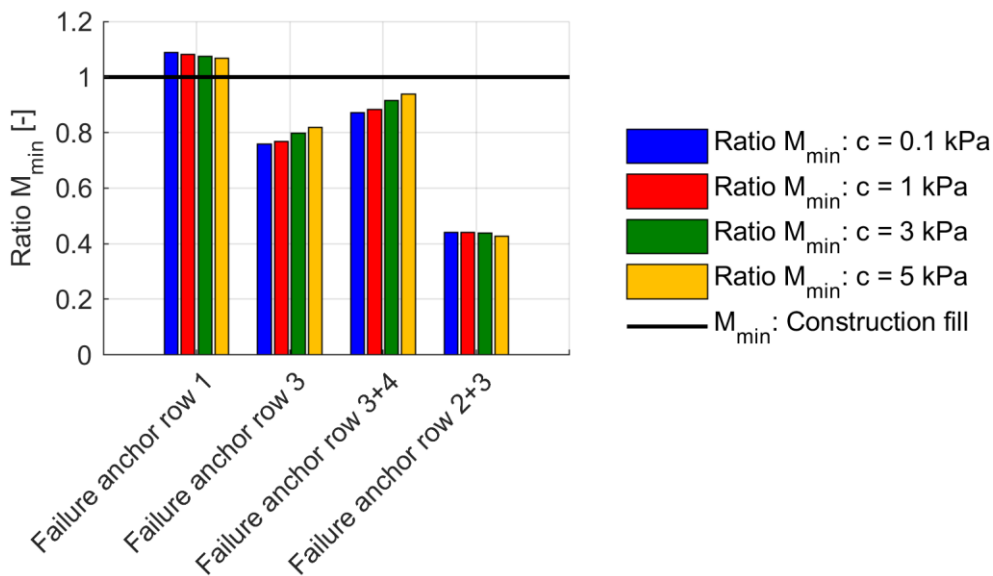


Fig. 79: BM_s : Ratio M_{min}

The change in the SF distribution for $c = 0.1$ kPa can be observed in Fig. 80. Again, the phase Construction fill and the four failure cases are plotted.

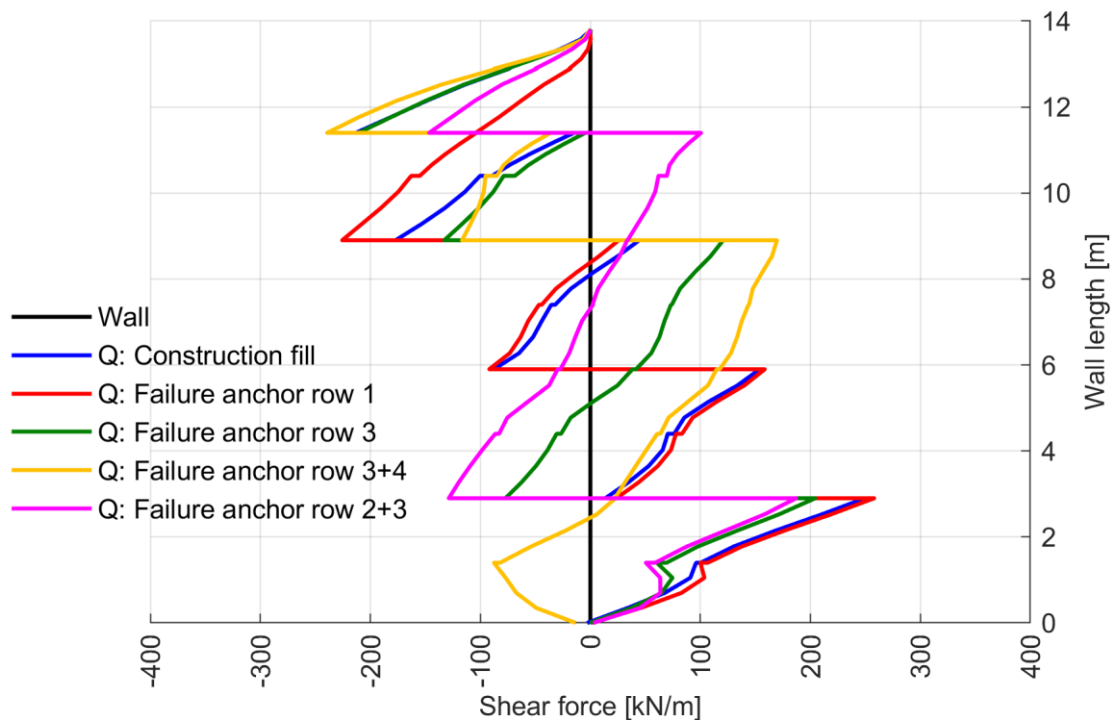


Fig. 80: SF s Q_{actual} after Construction fill and Failure cases for $c = 0.1$ kPa

Fig. 81 reveals that Failure anchor row 3+4 especially reduces the minimum SF after the calculation phase Construction fill. The FEA conducted with a cohesion of 0.1 kPa, where Failure anchor row 3+4 and Construction fill show a minimum SF of -239 kN/m and -213 kN/m, respectively, results in the maximum ratio of 1.12. While the single row failure cases show a ratio of around 1.00, the ratio for Failure anchor row 2+3 appears to be significantly below 1.00.

The same procedure was done for the maximum SF values, as shown in Fig. 82. The maximum SF from Construction fill is just increased, though slightly, by Failure anchor row 1 for all variations of the cohesion.

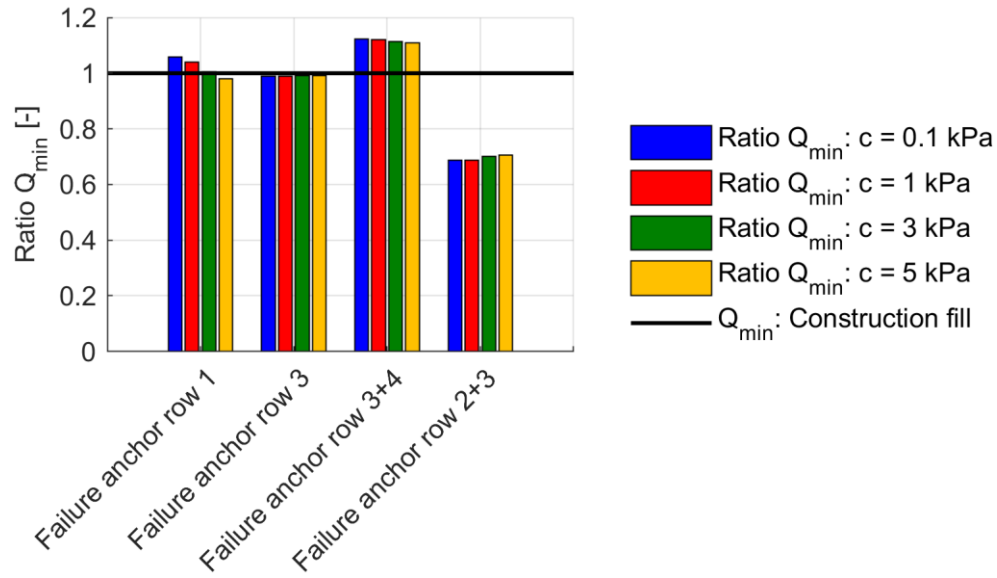
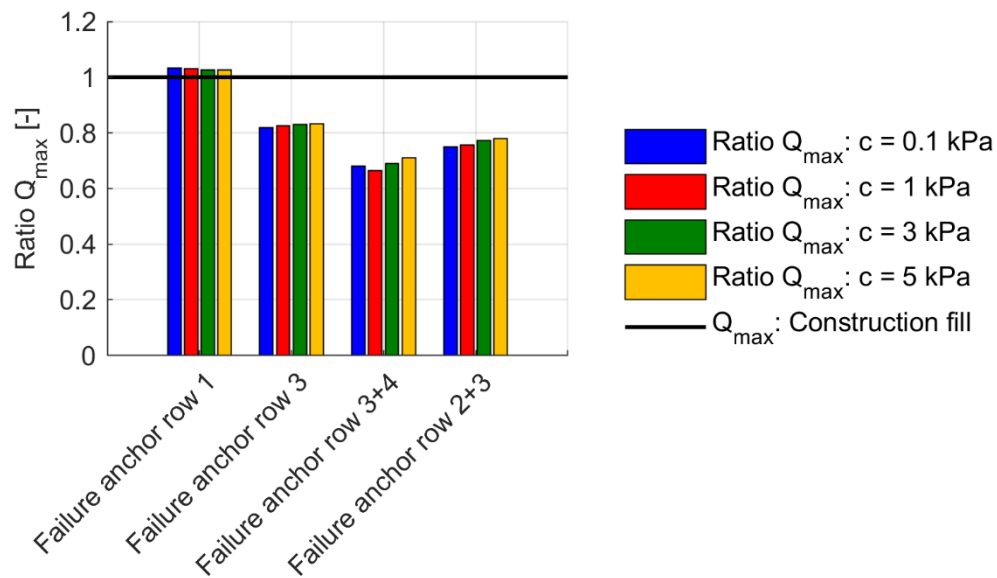
Fig. 81: SFs : Ratio Q_{min} Fig. 82: SFs : Ratio Q_{max}

Fig. 83 portrays the horizontal displacements u_x caused by the failure of ground anchors, compared to the horizontal displacements u_x after the calculation phase Construction fill. As expected, double row anchor failure cases show a larger increment than single row anchor failure. Nevertheless, Failure anchor row 1 leads to the maximum horizontal displacement at the top of the wall.

As shown in Fig. 84, all failure cases lead to an increase of the maximum horizontal displacement u_x from the calculation phase Construction fill. This increase seems to be plausible because the structure is missing support when anchors fail. As mentioned before, Failure anchor row 3+4 and Failure anchor row 2+3 show a larger increment than single row anchor failure. The maximum ratio of 1.30 appears for Failure anchor row 3+4, calculated with a cohesion of 0.1 kPa.

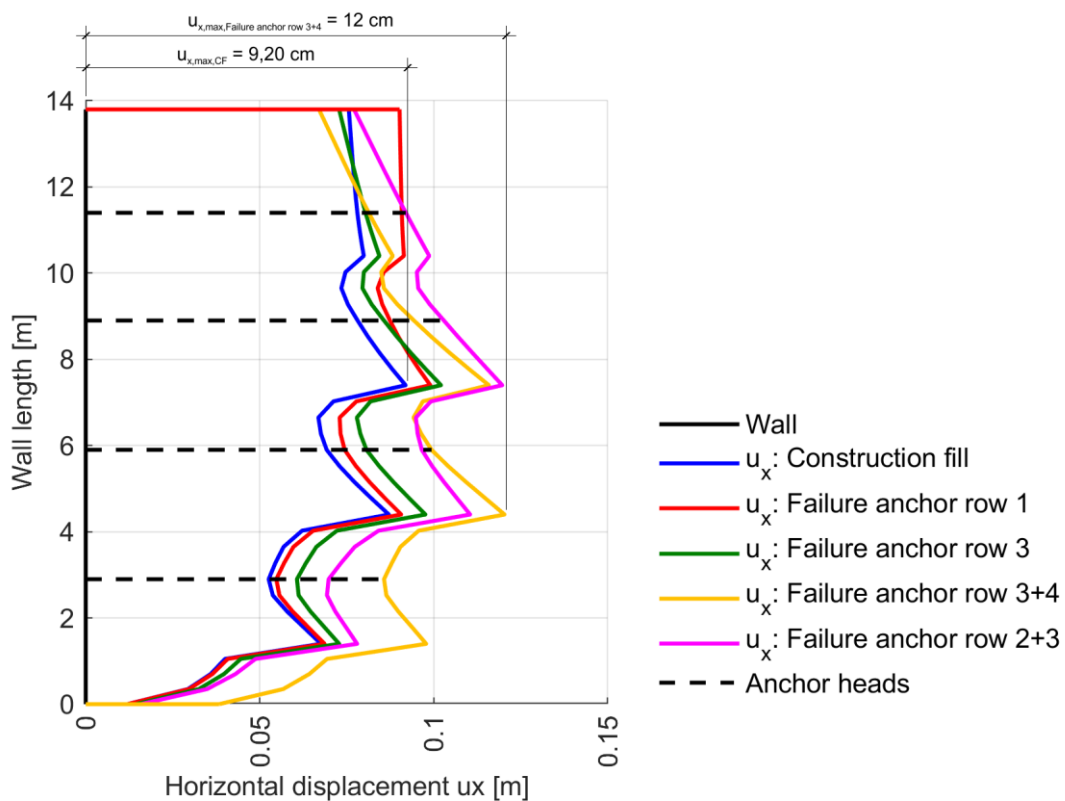


Fig. 83: Horizontal displacements u_x after Construction fill and Failure cases for $c = 0.1\ kPa$

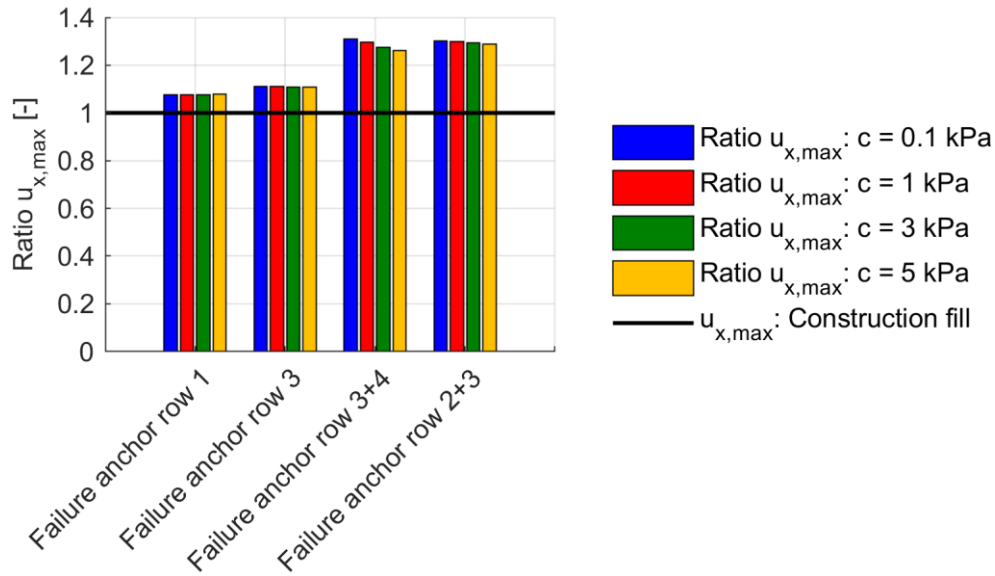


Fig. 84: Horizontal displacements: Ratio $u_{x,max}$

Total displacements $|u|$ are shown in Fig. 85, where Failure anchor row 2+3 shows the maximum displacement of 13.50 cm between anchor 2 and anchor 3.

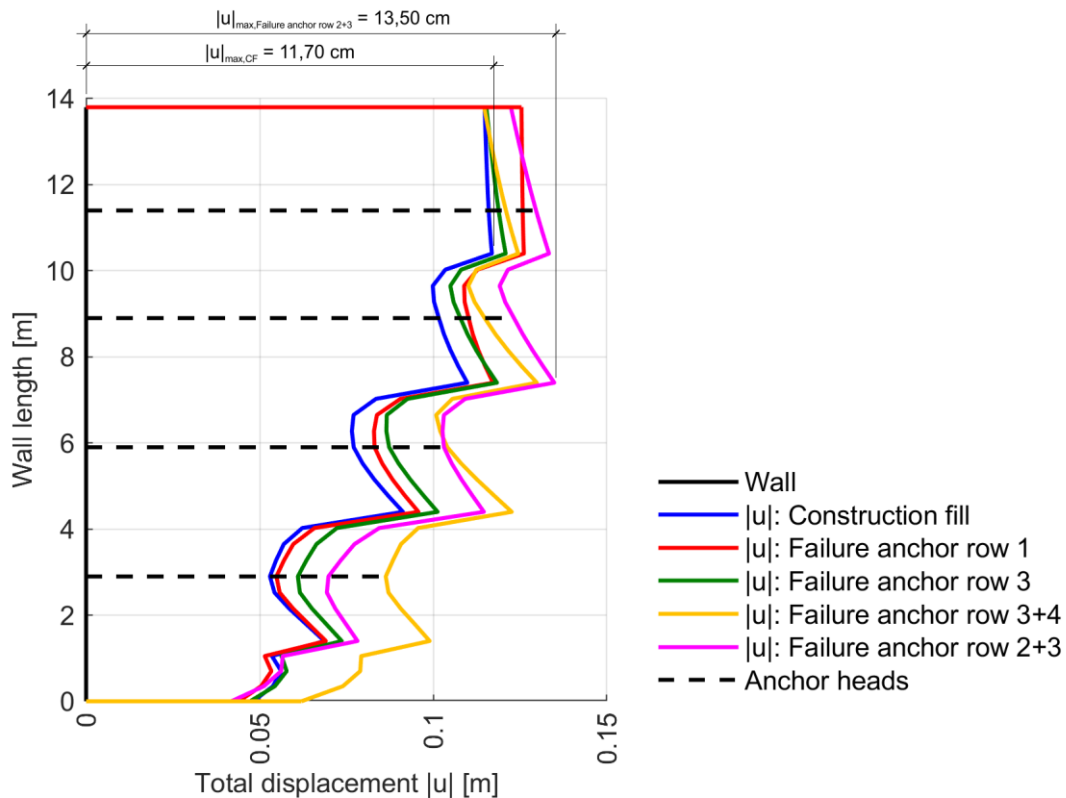


Fig. 85: Total displacements $|u|$ after Construction fill and anchor Failure cases for $c = 0.1$ kPa

As before, all *FEAs* show ratios of the total displacements $|u|$ above 1.00, as shown in Fig. 86. The maximum ratio, in the magnitude of 1.15 for $c = 0.1$ kPa, occurs for the phase Failure anchor row 2+3.

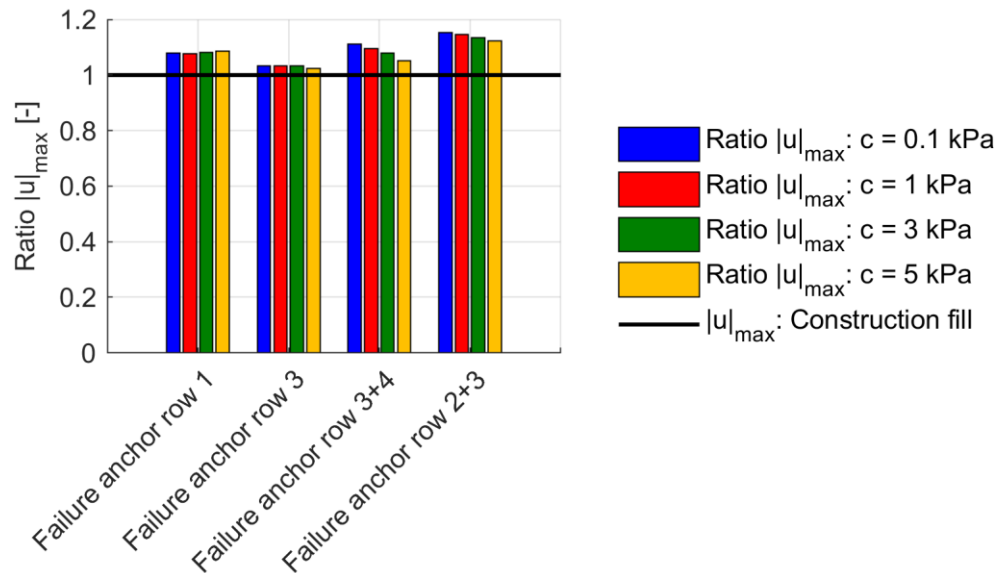


Fig. 86: Total displacements: Ratio $|u|_{\max}$

The redistribution of anchor forces, shown for a cohesion of 0.1 kPa can be seen in Fig. 87, which reveals that especially anchors situated close to a failed element show an increase in its anchor force. If the failed elements are situated in the centre (i.e. force redistribution upwards and downwards is possible), the force increment in the lower anchor appears to be higher than the force increment in the upper anchor. Therefore, more load is redistributed to the anchors below the failed elements than to the anchors above the failed elements. The maximum anchor force resulting from the four failure cases occurs at anchor 4 when anchor 2 and anchor 3 fail simultaneously. It must be said that the anchor tendons were discretised as elastic node-to-node anchors; therefore, they show unlimited capacity. Under practical conditions, anchors could be overstressed because of the occurring force redistribution, which would consequently cause them to fail as well.

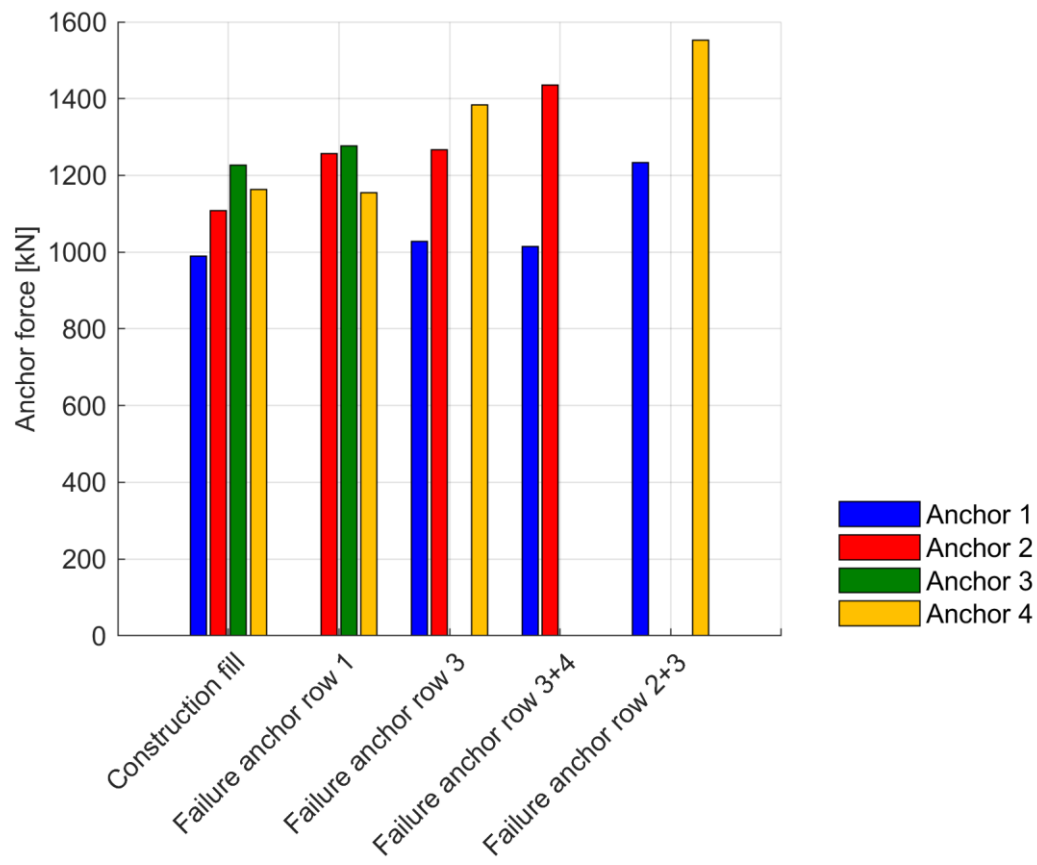


Fig. 87: Anchor forces after Construction fill and Failure cases for $c = 0.1$ kPa
A summary of previously presented results is given in Tab. 18:

Tab. 18: Results of the calculation phases Construction fill and Failure cases

| | Cohesion [kPa] | | | |
|--|----------------|-------|-------|-------|
| | 0.1 | 1 | 3 | 5 |
| FoS_{CF} [-] | 1.33 | 1.37 | 1.45 | 1.54 |
| $FoS_{Failure}$ anchor row 1 [-] | 1.31 | 1.38 | 1.46 | 1.56 |
| $FoS_{Failure}$ anchor row 3 [-] | 1.32 | 1.39 | 1.46 | 1.55 |
| $FoS_{Failure}$ anchor row 3+4 [-] | 1.32 | 1.37 | 1.43 | 1.45 |
| $FoS_{Failure}$ anchor row 2+3 [-] | 1.31 | 1.38 | 1.48 | 1.53 |
| $M_{act,min,CF}$ [kNm/m] | -580 | -578 | -565 | -559 |
| $M_{act,min,Failure}$ anchor row 1 [kNm/m] | -631 | -624 | -608 | -597 |
| $M_{act,min,Failure}$ anchor row 3 [kNm/m] | -440 | -444 | -452 | -457 |
| $M_{act,min,Failure}$ anchor row 3+4 [kNm/m] | -505 | -511 | -517 | -524 |
| $M_{act,min,Failure}$ anchor row 2+3 [kNm/m] | -256 | -254 | -248 | -238 |
| $Q_{act,min,CF}$ [kN/m] | -213 | -214 | -216 | -218 |
| $Q_{act,min,Failure}$ anchor row 1 [kN/m] | -226 | -223 | -217 | -214 |
| $Q_{act,min,Failure}$ anchor row 3 [kN/m] | -211 | -212 | -214 | -216 |
| $Q_{act,min,Failure}$ anchor row 3+4 [kN/m] | -239 | -240 | -240 | -242 |
| $Q_{act,min,Failure}$ anchor row 2+3 [kN/m] | -146 | -147 | -151 | -154 |
| $Q_{act,max,CF}$ [kN/m] | 250 | 253 | 244 | 237 |
| $Q_{act,max,Failure}$ anchor row 1 [kN/m] | 258 | 261 | 250 | 243 |
| $Q_{act,max,Failure}$ anchor row 3 [kN/m] | 204 | 209 | 202 | 197 |
| $Q_{act,max,Failure}$ anchor row 3+4 [kN/m] | 170 | 168 | 168 | 168 |
| $Q_{act,max,Failure}$ anchor row 2+3 [kN/m] | 187 | 192 | 188 | 185 |
| $u_{x,max,CF}$ [cm] | 9.20 | 9.10 | 9.00 | 9.00 |
| $u_{x,max,Failure}$ anchor row 1 [cm] | 9.90 | 9.80 | 9.70 | 9.70 |
| $u_{x,max,Failure}$ anchor row 3 [cm] | 10.20 | 10.10 | 10.00 | 10.00 |
| $u_{x,max,Failure}$ anchor row 3+4 [cm] | 12.00 | 11.80 | 11.50 | 11.40 |
| $u_{x,max,Failure}$ anchor row 2+3 [cm] | 12.00 | 11.80 | 11.60 | 11.60 |
| $ u _{max,CF}$ [cm] | 11.70 | 11.60 | 11.70 | 12.00 |
| $ u _{max,Failure}$ anchor row 1 [cm] | 12.60 | 12.50 | 12.60 | 13.10 |
| $ u _{max,Failure}$ anchor row 3 [cm] | 12.10 | 12.00 | 12.10 | 12.30 |
| $ u _{max,Failure}$ anchor row 3+4 [cm] | 13.00 | 12.70 | 12.60 | 12.70 |
| $ u _{max,Failure}$ anchor row 2+3 [cm] | 13.50 | 13.30 | 13.30 | 13.50 |
| $F_{max,Anchor 3,CF}$ [kN] | 1227 | 1220 | 1221 | 1222 |
| $F_{max,Anchor 3,Failure}$ anchor row 1 [kN] | 1277 | 1269 | 1269 | 1269 |
| $F_{max,Anchor 4,Failure}$ anchor row 3 [kN] | 1384 | 1381 | 1369 | 1369 |
| $F_{max,Anchor 2,Failure}$ anchor row 3+4 [kN] | 1435 | 1420 | 1403 | 1398 |
| $F_{max,Anchor 4,Failure}$ anchor row 2+3 [kN] | 1552 | 1543 | 1523 | 1514 |

Fig. 88 to Fig. 110 depict some selected evaluations related to *FEAs*, where the fixed anchor length was discretised with *EBs*. As stated in section 4.2, *FEAs* were performed with constant and linear distribution of the skin resistance. As for previous results, the evaluations shown represent *FEAs* conducted with the *MC* model, a R_{inter} value of 0.90 and pre-stressed anchors. More evaluations are given within the appendix, in section 8.2 and 8.3.

Fig. 88 shows the FoS for the FEA performed with a cohesion of 0.1 kPa and with constant distribution of the skin resistance. While no meaningful divergence between Construction fill and Failure anchor row 1, 3+4 and 2+3 can be observed, Failure anchor row 3 plots a marginal increased FoS of 1.33.

The FMS s, related to the FoS plotted in Fig. 88, are visualised in Fig. 89. Similar behaviour (as for the FEA conducted with geogrids (see Fig. 75)) can be observed in the area of the upper slope.

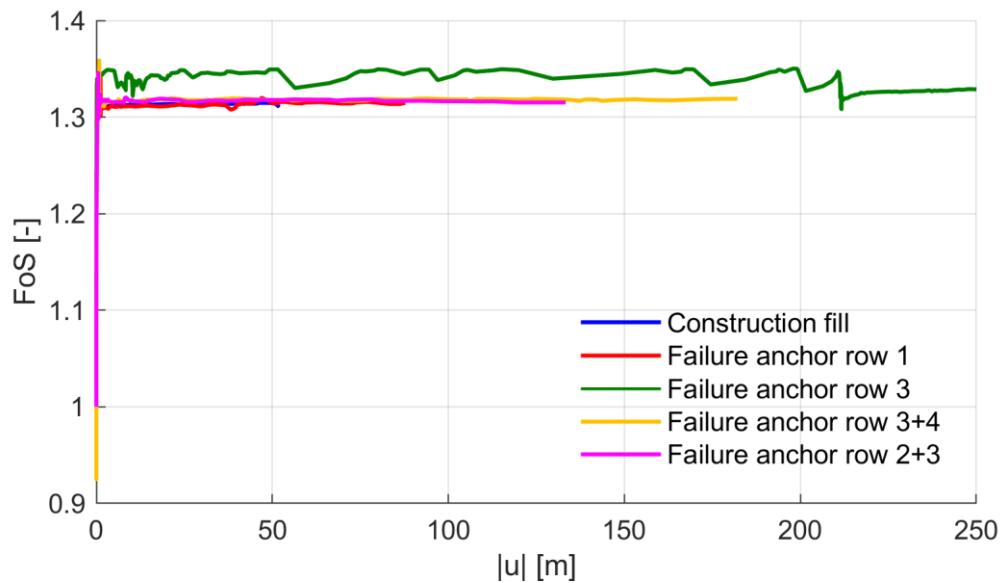


Fig. 88: FoS after ϕ - c reduction Construction fill and Failure cases for $c = 0.1$ kPa; EB s with constant skin resistance

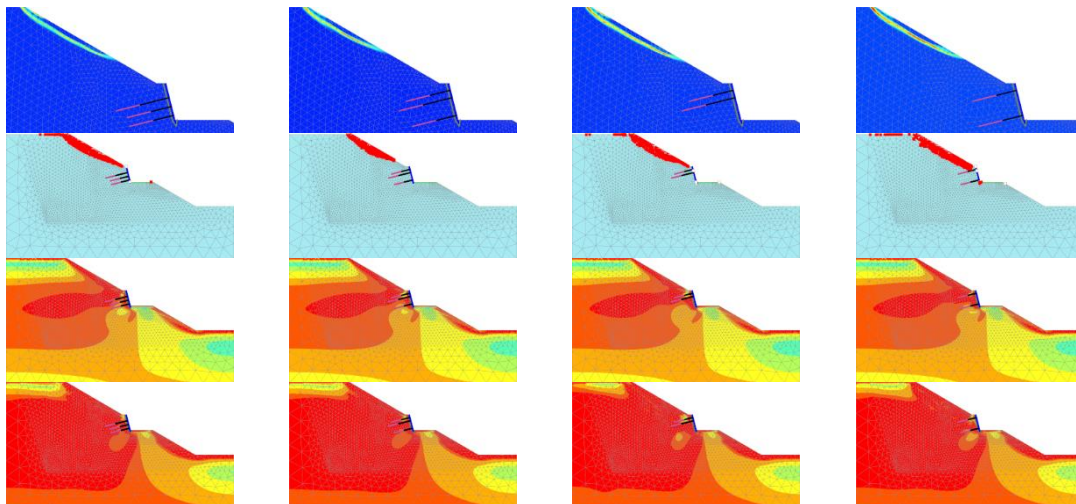


Fig. 89: Incremental deviatoric strains and plastic points after as well as τ_{rel} before/after ϕ - c reduction Failure cases for $c = 0.1$ kPa; EB s with constant skin resistance; left: Failure anchor row 1; centre left: Failure anchor row 3; centre right: Failure anchor row 3+4; right: Failure anchor row 2+3

Fig. 90 shows the FoS for the FEA conducted with linear skin resistance distribution. As seen, the FoS is almost identical to Fig. 88.

In principle, the failure behaviour does not substantially differ from the FMs seen in Fig. 89. Therefore, the FMs for the FEA computed with linear skin resistance are not shown.

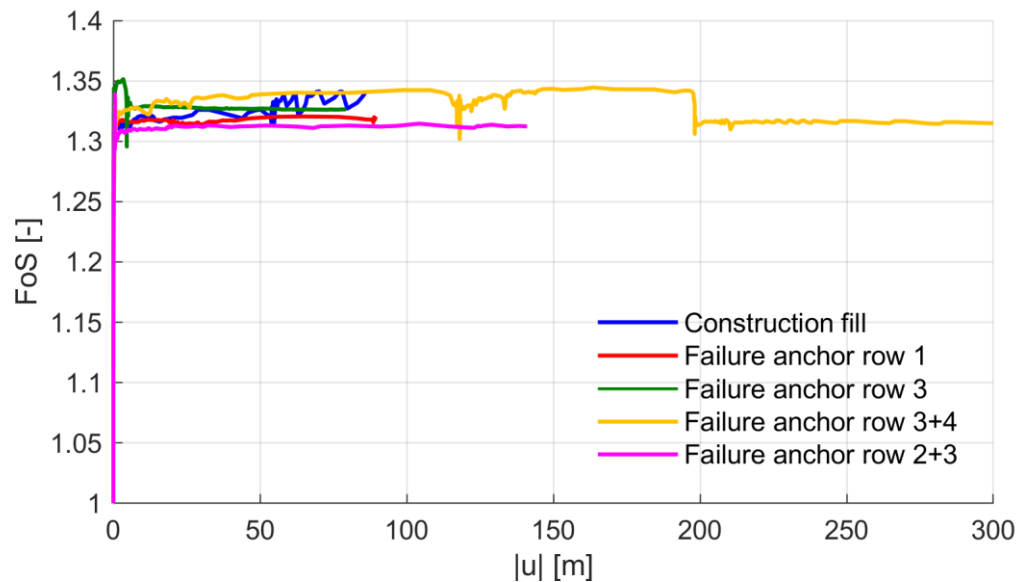


Fig. 90: FoS after φ - c reduction Construction fill and Failure cases for $c = 0.1$ kPa; EBs with linear skin resistance

For all ground anchor failure cases, Fig. 91 shows a lower FoS than the FoS resulting from the phase Construction fill. Like Fig. 76, Failure anchor row 3+4 exhibits a significant decrease in the FoS .

Fig. 92 shows the FMs for the FEA with constant skin resistance and a cohesion of 5 kPa. Compared to FMs resulting from the FEA with geogrids (see Fig. 77), similar behaviour can be observed. The only notable difference concerns Failure anchor row 1, where observable incremental deviatoric strains occur over the total height of the slope.

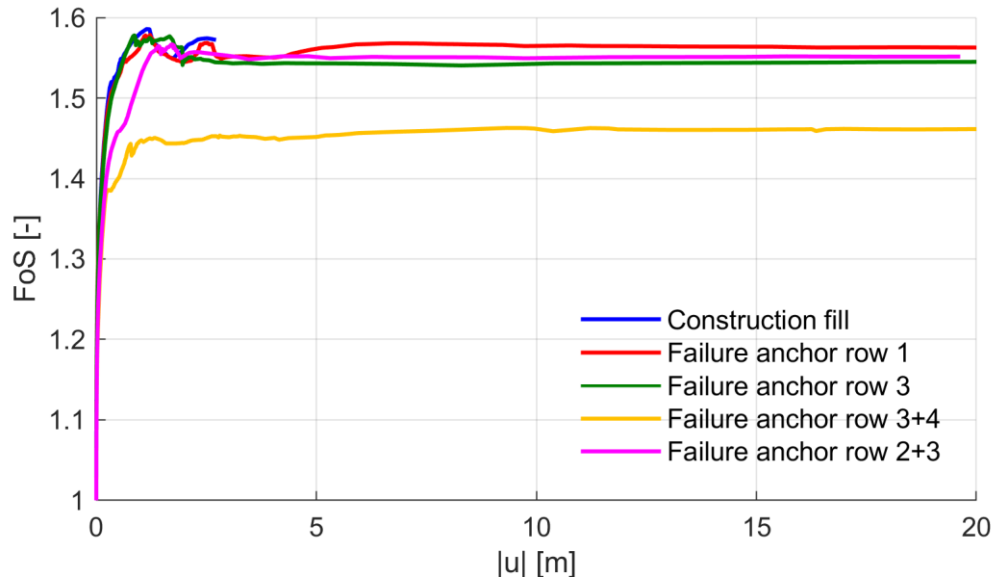


Fig. 91: FoS after ϕ - c reduction Construction fill and Failure cases for $c = 5$ kPa; EBs with constant skin resistance

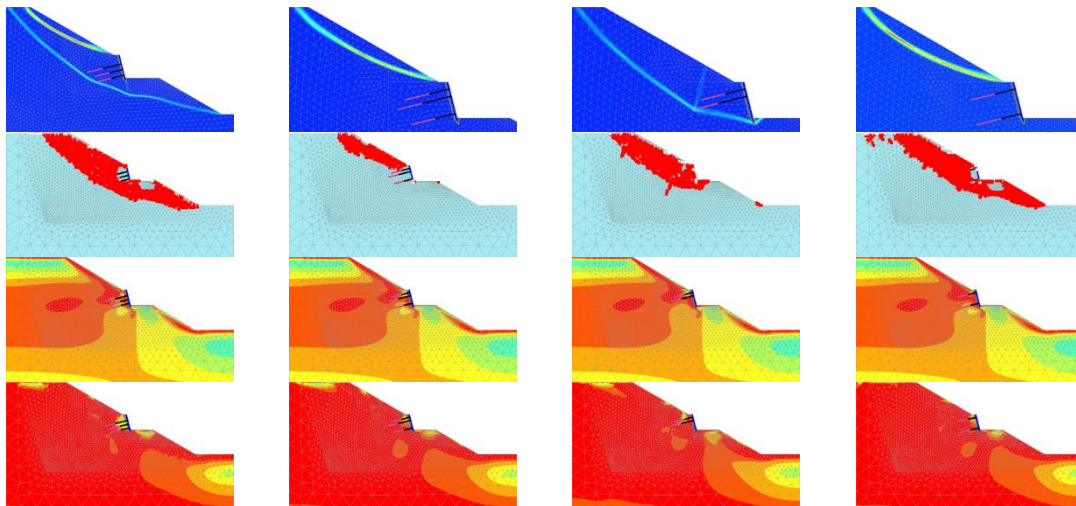


Fig. 92: Incremental deviatoric strains and plastic points after as well as τ_{rel} before/after ϕ - c reduction Failure cases for $c = 5$ kPa; EBs with constant skin resistance; left: Failure anchor row 1; centre left: Failure anchor row 3; centre right: Failure anchor row 3+4; right: Failure anchor row 2+3

In Fig. 93, the FoS for the FEA performed with $c = 5$ kPa and linear distribution of the skin resistance can be seen. Again, Construction fill results in the highest FoS , while all failure cases lead to a decrease.

FMs are visualised in Fig. 94, where deviations, compared to Fig. 92, can be mainly observed for Failure anchor row 1 and Failure anchor row 2+3.

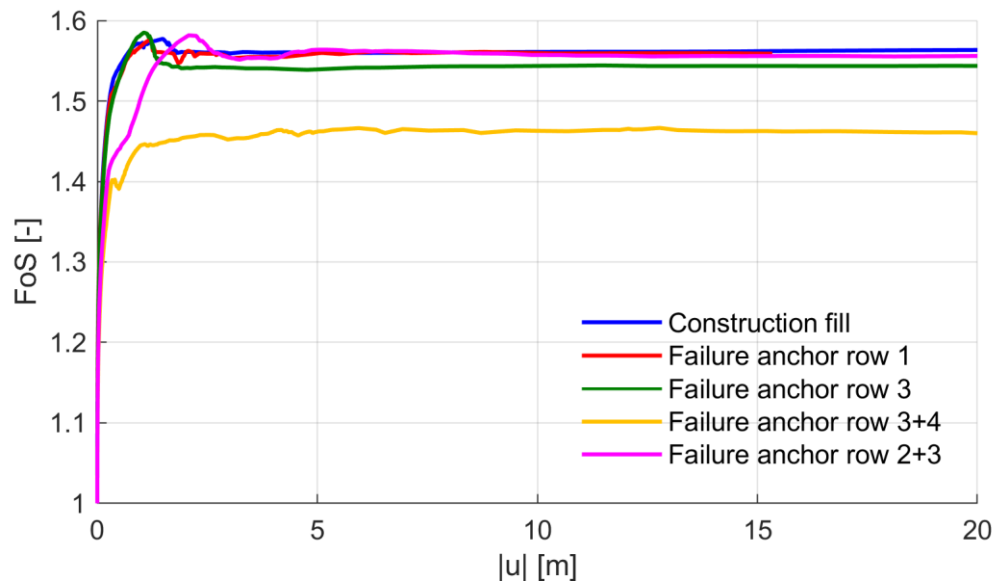


Fig. 93: FoS after ϕ - c reduction Construction fill and Failure cases for $c = 5$ kPa; EBs with linear skin resistance

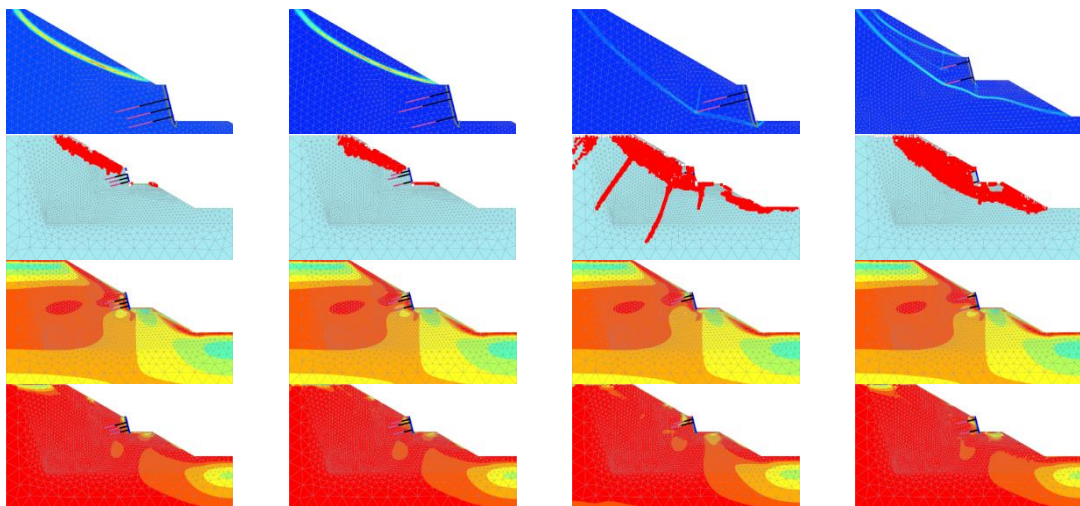


Fig. 94: Incremental deviatoric strains and plastic points after as well as τ_{rel} before/after ϕ - c reduction Failure cases for $c = 5$ kPa; EBs with linear skin resistance; left: Failure anchor row 1; centre left: Failure anchor row 3; centre right: Failure anchor row 3+4; right: Failure anchor row 2+3

BM s are visualised in Fig. 95 and Fig. 96. A comparison between constant and linear skin resistance reveals deviations which seem to be low or nearly non-existent. Nevertheless, for all variations in cohesion, $FEAs$ with constant skin resistance resulted in the minimum BM values. When compared with Fig. 78, where the fixed anchor length was discretised with geogrids, both double row anchor failure cases especially seem to differ significantly. The biggest divergence, at a magnitude of 100 kNm/m, is to be found for Failure anchor row 3+4, where Fig. 78 shows a minimum value of -505 kNm/m. However, when calculated with EBs and a linear distribution of the skin resistance, a minimum value of -405 kNm/m is generated. What does not change is the fact that only Failure anchor row 1 reduces the minimum BM from the phase Construction fill.

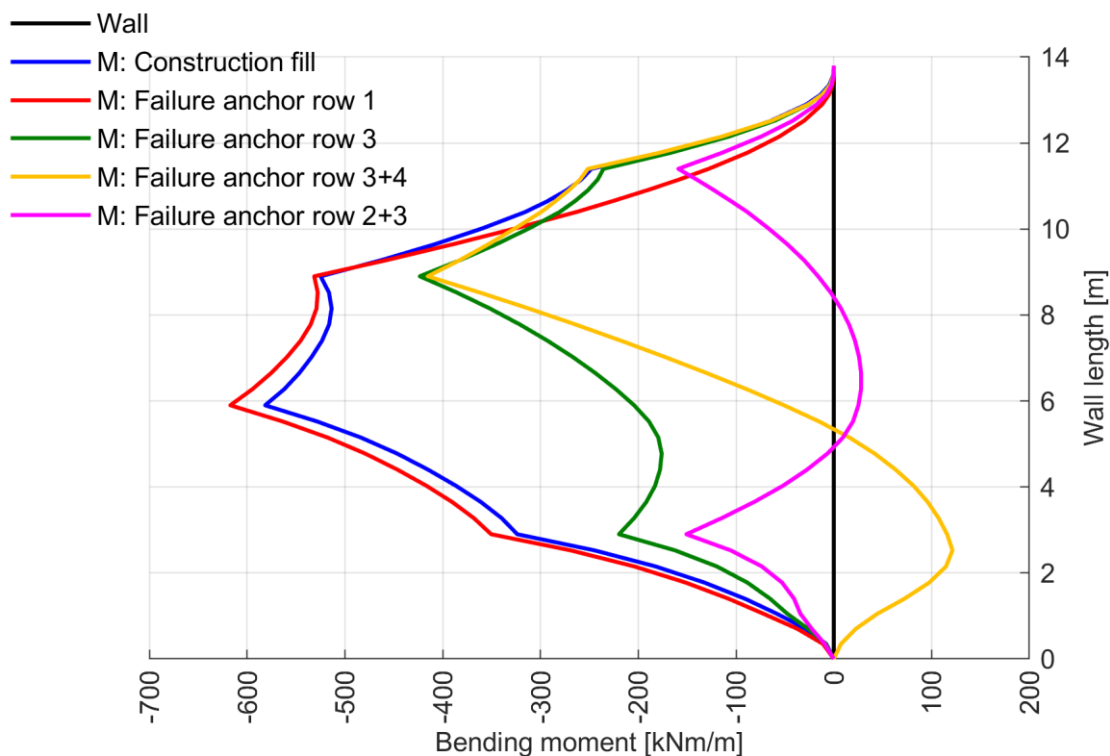


Fig. 95: BM s M_{actual} after Construction fill and Failure cases for $c = 0.1$ kPa; EBs with constant skin resistance

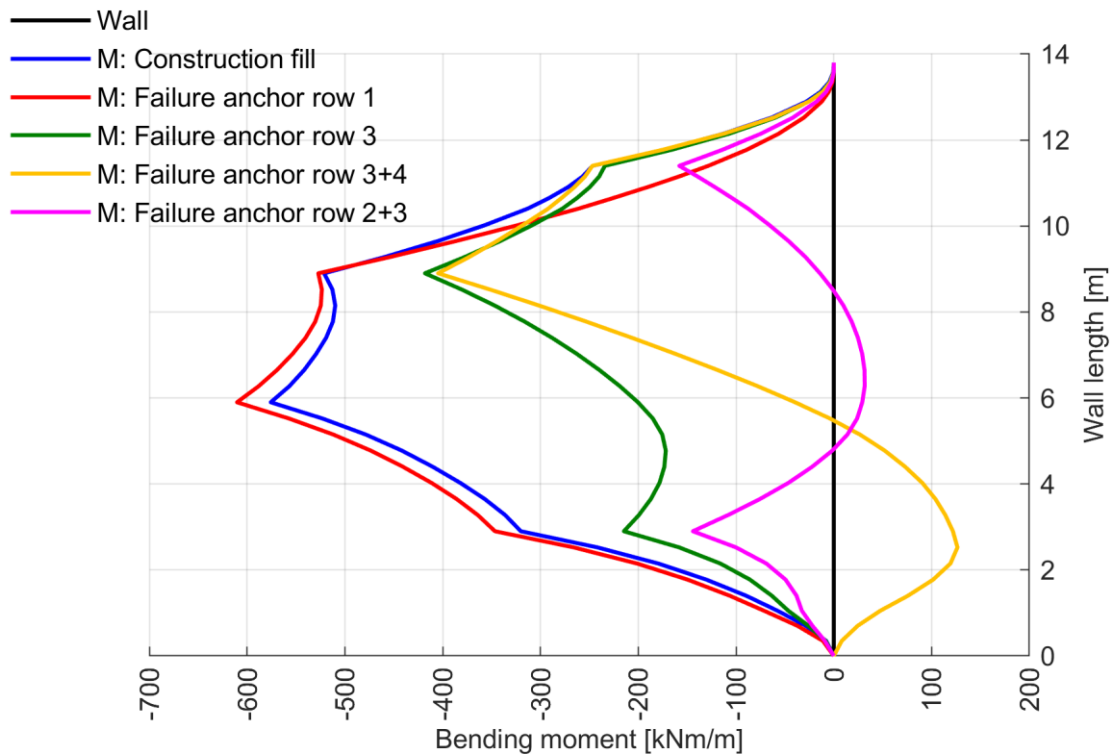


Fig. 96: $BM_s M_{actual}$ after Construction fill and Failure cases for $c = 0.1$ kPa; EBs with linear skin resistance

Fig. 97 portrays the ratio of the minimum BM_s . Because no significant deviations between both skin resistance options occur, only the constant distribution is shown. Again, only Failure anchor row 1 shows a ratio above 1.00. As stated above, especially minimum BM_s resulting from double row anchor failure cases differ from minimum values calculated with geogrids. Therefore, their ratios diverge when compared with Fig. 98 (identical with Fig. 79).

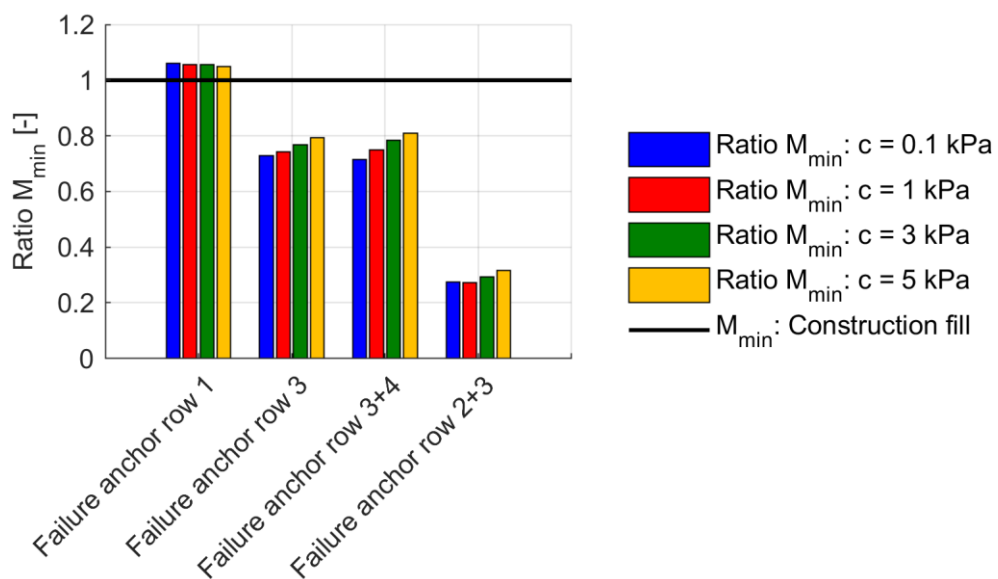


Fig. 97: BM_s : Ratio M_{min} ; EBs with constant skin resistance

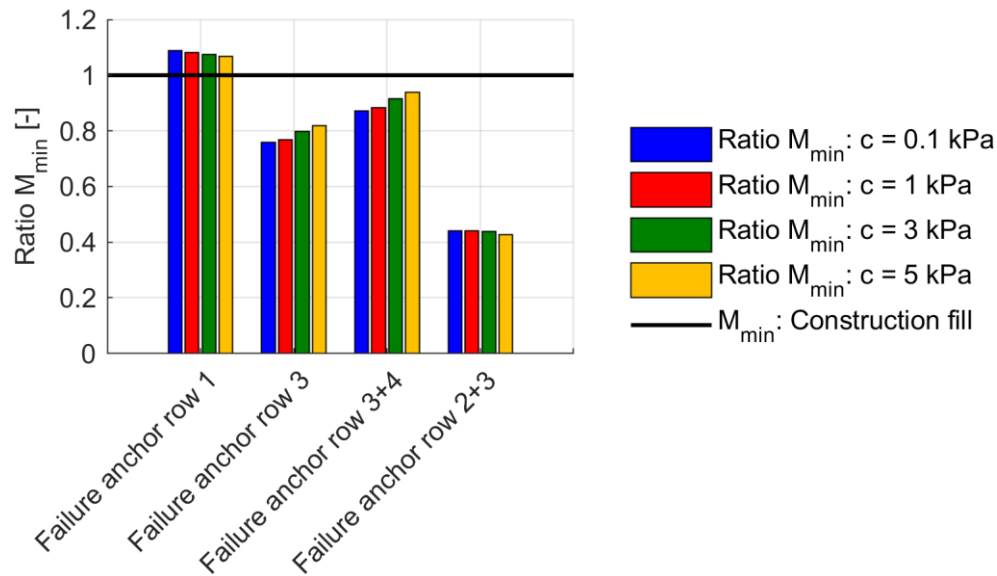


Fig. 98: BM_s : Ratio M_{min}

As with the presented BM_s , Fig. 99 and Fig. 100, which portray the SF distributions, reveal deviations between both skin resistance options that are not worth mentioning. However, when compared to SF_s resulting from the FEA conducted with geogrids (see Fig. 80), the largest divergence between minimum SF_s , again, occurs for Failure anchor row 3+4, and the largest divergence between maximum values presents for Failure anchor row 2+3. Expressed in numbers, deviations of 35 kN/m for Failure anchor row 3+4 and 56 kN/m for Failure anchor row 2+3 seem to appear between the FEA done with geogrids and the FEA computed with EB_s and linear skin resistance.

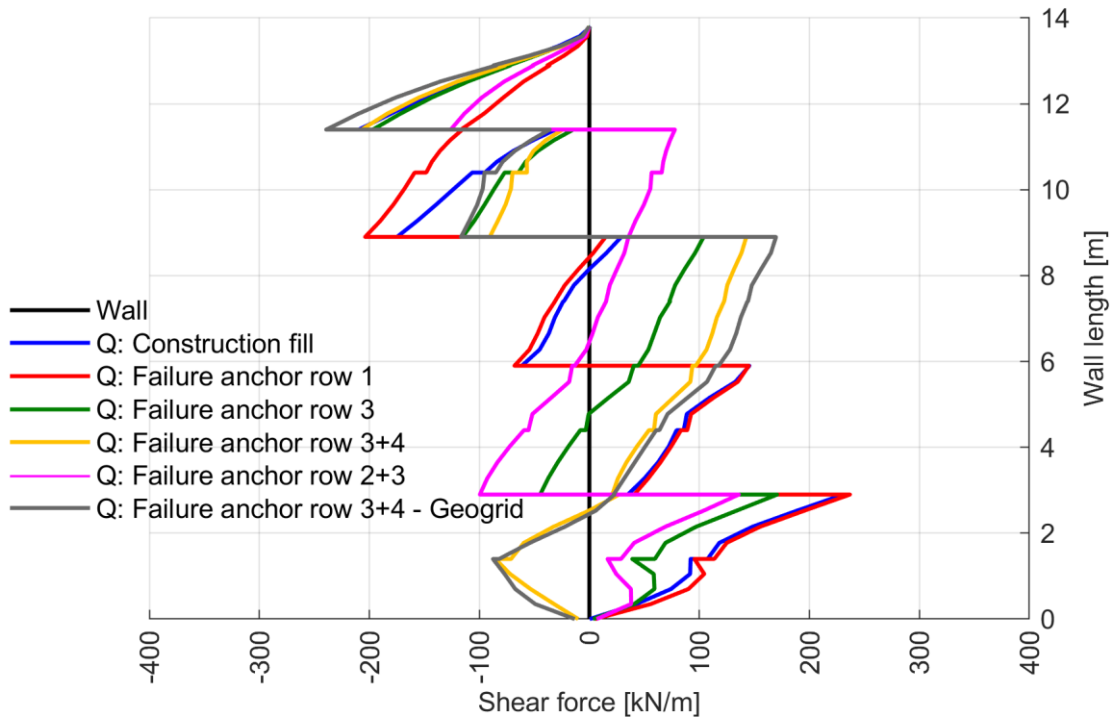


Fig. 99: $SFs Q_{actual}$ after Construction fill and Failure cases for $c = 0.1$ kPa; EBs with constant skin resistance

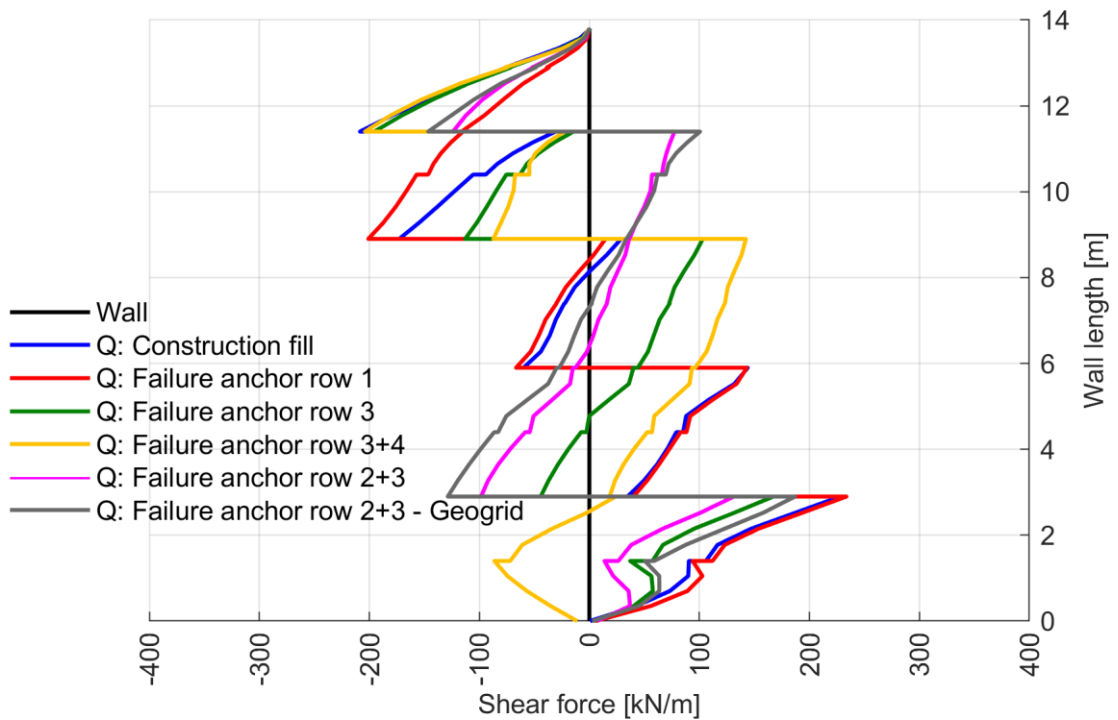


Fig. 100: $SFs Q_{actual}$ after Construction fill and Failure cases for $c = 0.1$ kPa; EBs with linear skin resistance

Congruent to similar SF distributions, neither ratios of minimum values as shown in Fig. 101, nor ratios of maximum values as shown in Fig. 102, diverge significantly from ratios obtained from $FEAs$ done with linear distribution of the skin resistance. Both figures reveal similar behaviour, as shown for geogrids in Fig. 81 and Fig. 82. While minimum values are mainly affected (though the ratios seem to be lower than in Fig. 81) by Failure anchor row 3+4, the maximum SFs from the phase Construction fill, again, slightly increase because of the failure of anchor row 1.

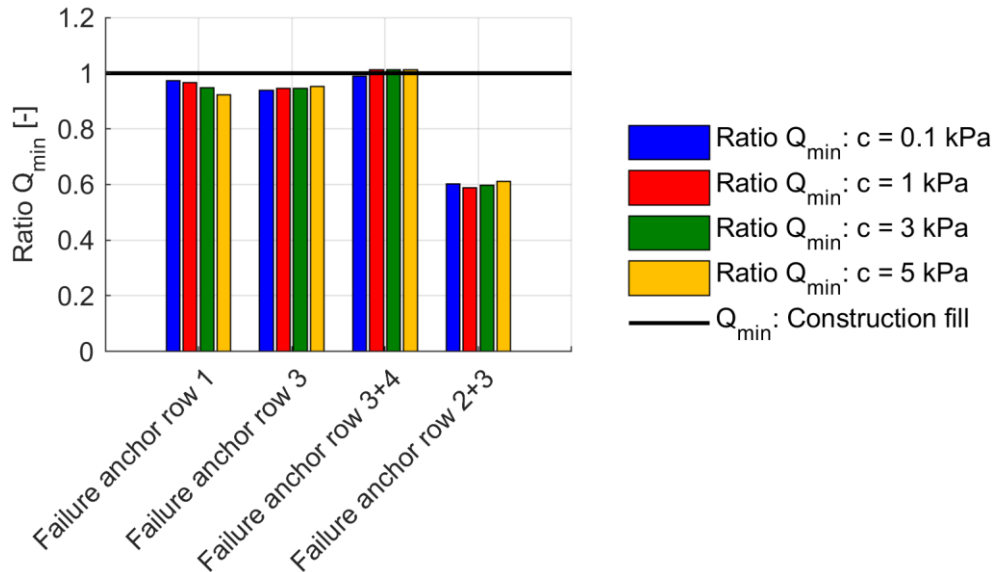


Fig. 101: SFs : Ratio Q_{min} ; EBs with constant skin resistance

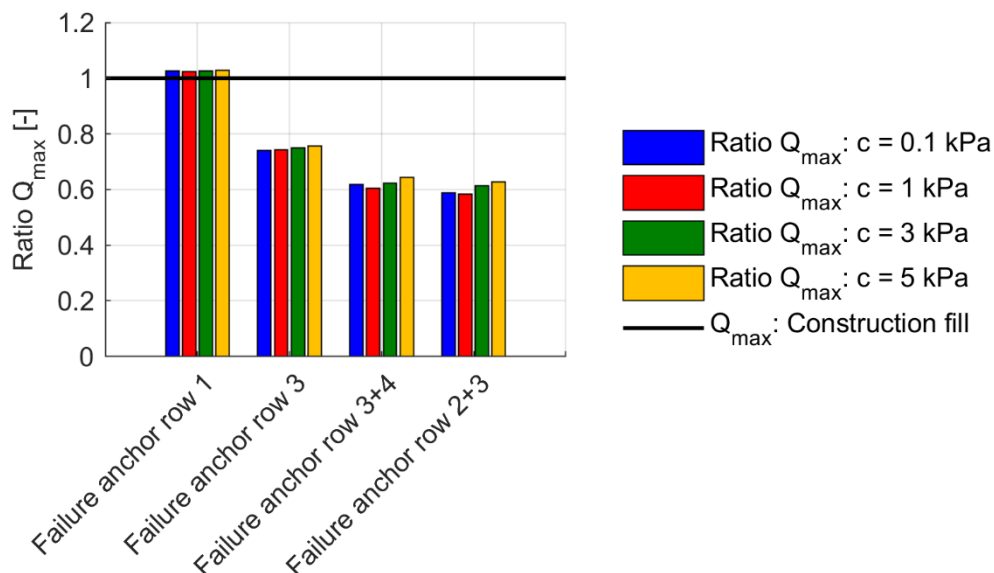


Fig. 102: SFs : Ratio Q_{max} ; EBs with constant skin resistance

Horizontal displacements u_x are depicted in Fig. 103 and Fig. 104. No significant deviations appear between the constant and linear distribution of the skin resistance. A comparison with Fig. 83, where the fixed anchor length was discretised with geogrid elements, reveals higher horizontal displacements for both *EB* options. Deviations are apparent in the maximum values (related to Fig. 83), which appear to be slightly higher for linear than constant skin resistance distribution, in the order of 2.20 cm for the calculation phase Construction fill and 2.70 cm for Failure anchor row 3+4, respectively.

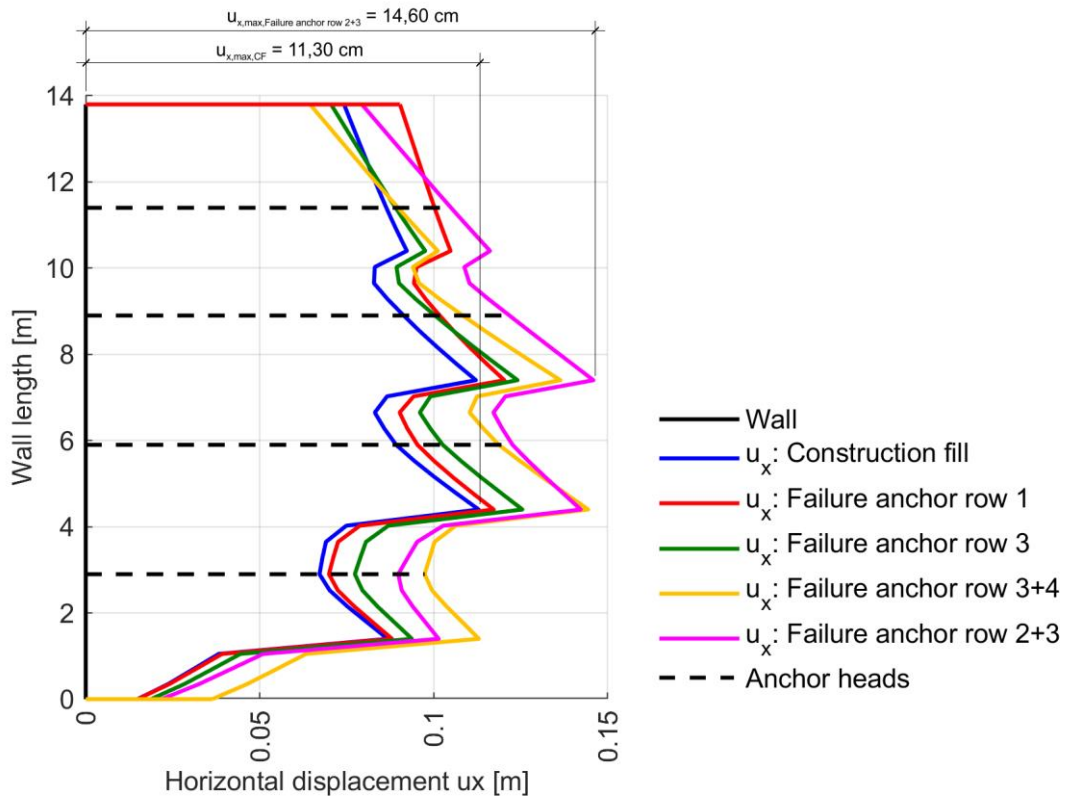


Fig. 103: Horizontal displacements u_x after Construction fill and Failure cases for $c = 0.1\ kPa$; *EBs* with constant skin resistance

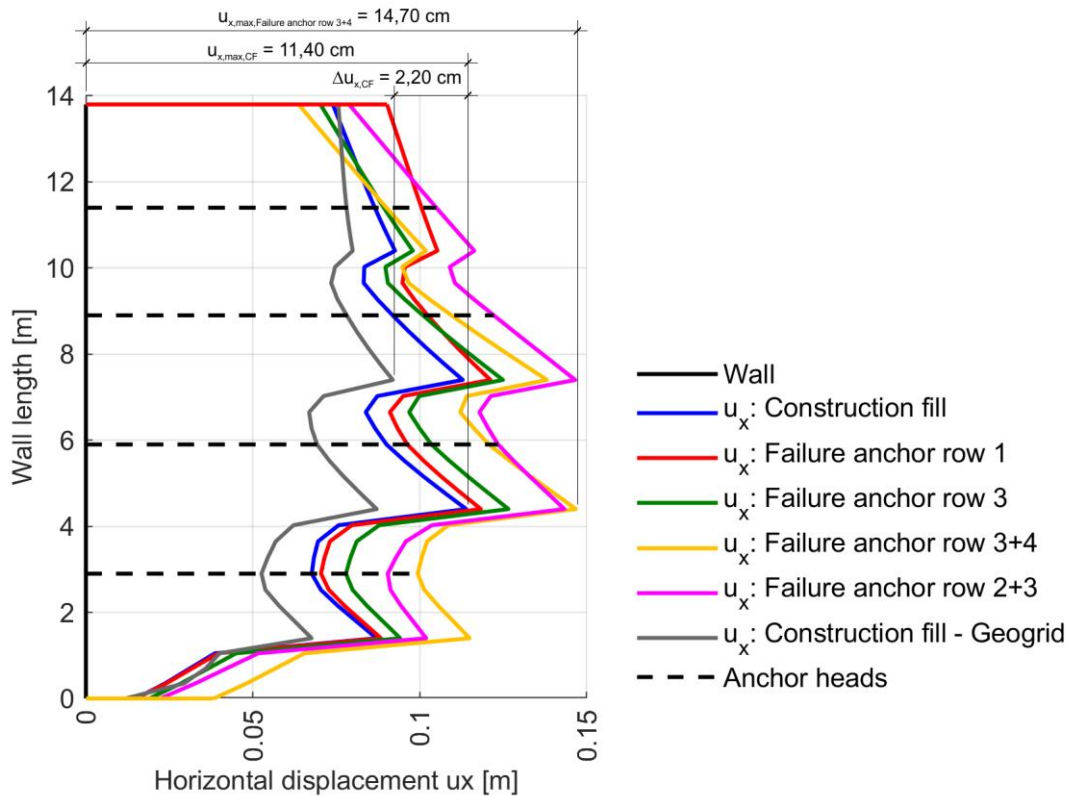


Fig. 104: Horizontal displacements u_x after Construction fill and Failure cases for $c = 0.1\ kPa$; *EBs* with linear skin resistance

Consequently, the ratios of the maximum horizontal displacements u_x , which can be seen in Fig. 105, do not differ significantly between both options. Like Fig. 84, Fig. 105 shows ratios above 1.00 for all failure cases and modifications of the cohesion. As the increment of the horizontal displacements is higher for double row anchor failure, their ratios appear to be larger compared to the ratios resulting from both single row anchor failure cases.

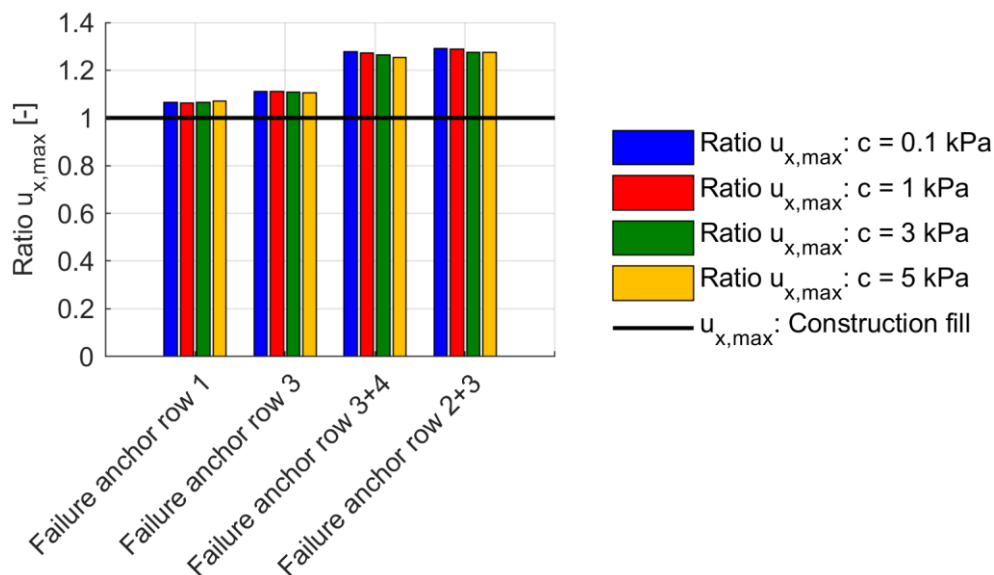


Fig. 105: Horizontal displacements: Ratio $u_{x,max}$; *EBs* with constant skin resistance

Fig. 106 and Fig. 107 show total displacements $|u|$. As with horizontal displacements, the total displacements $|u|$ seem to be slightly larger for linear skin resistance. Between maximum displacements calculated with linear skin resistance and Fig. 85, divergences of 1.60 cm after the calculation phase Construction fill and 2.70 cm after the failure of anchor row 2+3 are present.

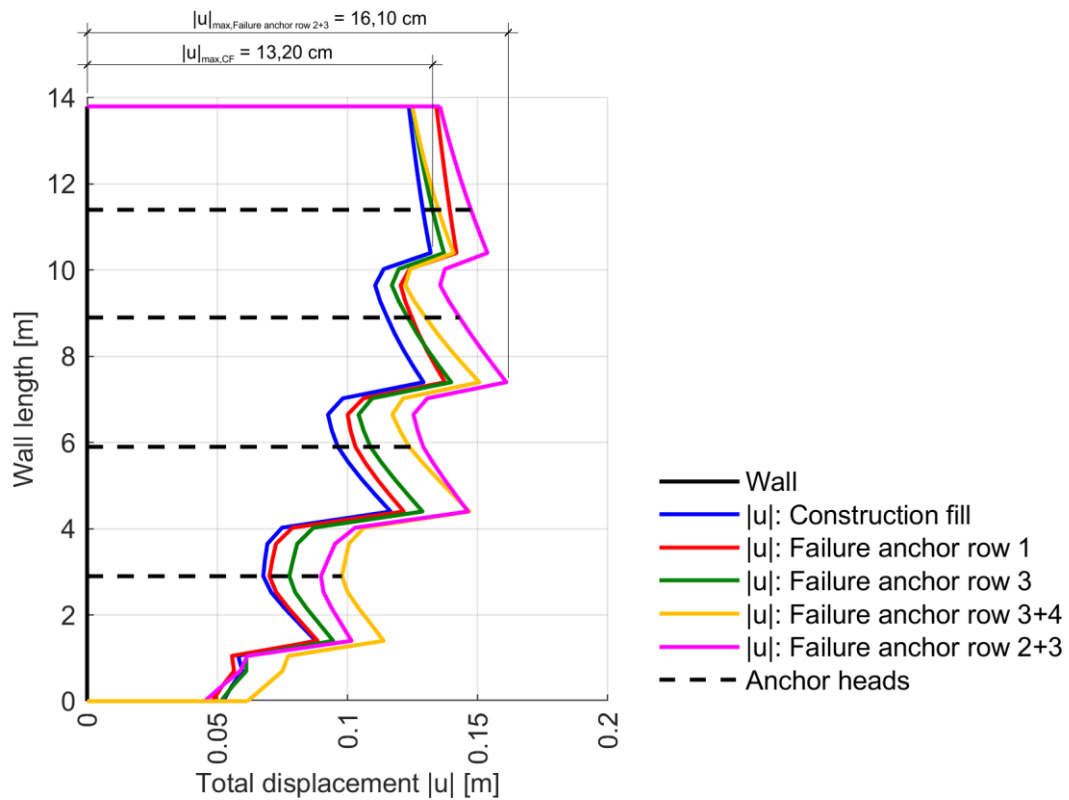


Fig. 106: Total displacements $|u|$ after Construction fill and Failure cases for $c = 0.1 \text{ kPa}$; *EBs* with constant skin resistance

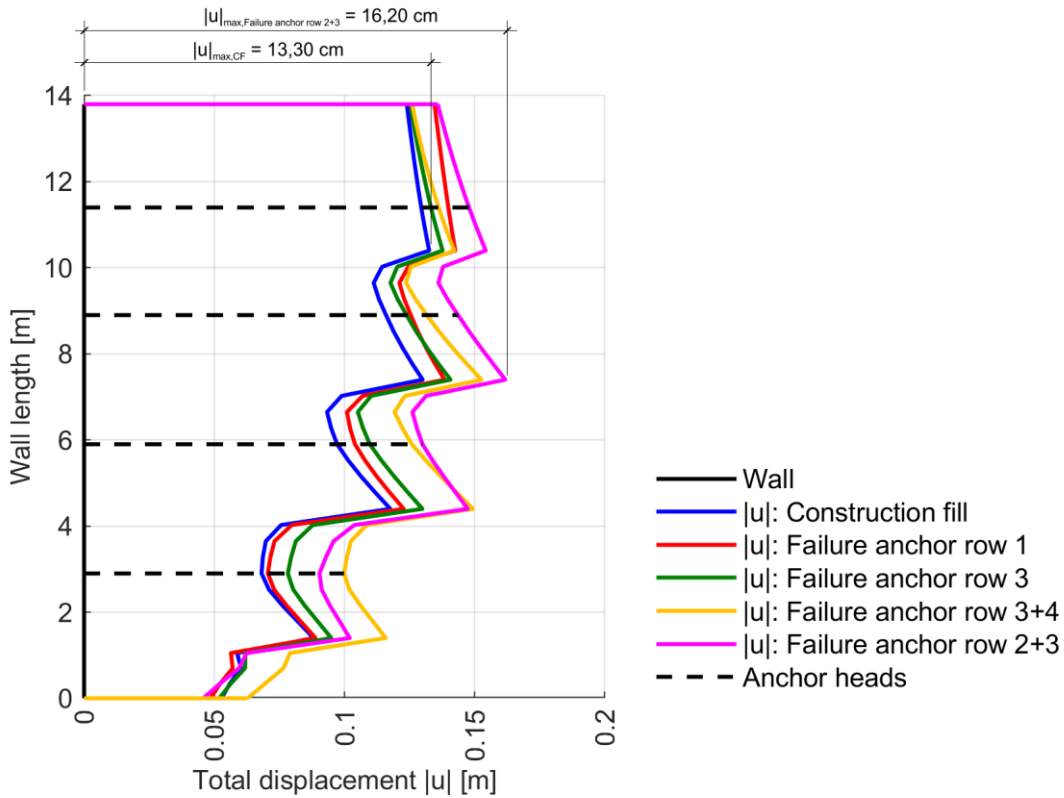


Fig. 107: Total displacements $|u|$ after Construction fill and Failure cases for $c = 0.1$ kPa; *EBs* with linear skin resistance

Fig. 108 portrays the ratios of the maximum total displacements $|u|$. Again, all values appear to be above 1.00 as displacements increase. The ratios resulting from *FEAs* computed with geogrids are depicted in Fig. 86.

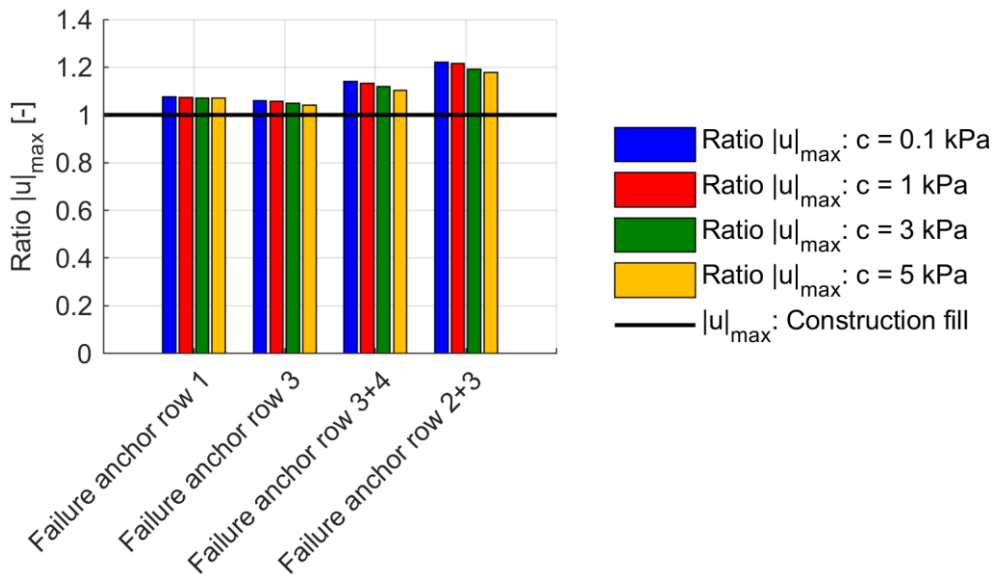


Fig. 108: Total displacements: Ratio $|u|_{max}$; *EBs* with constant skin resistance

Fig. 109 and Fig. 110 show the redistribution of anchor forces for both skin resistance options, again, for a cohesion of 0.1 kPa. It seems that there is a trend – namely, that anchor forces are slightly larger for constant distribution of the skin resistance. Nonetheless, the difference is not significant, with the maximum deviation of 24 kN occurring for Failure anchor row 2+3 at anchor 4. In contrast, significant deviations can be observed when Fig. 109 is compared with the redistribution of anchor forces calculated with geogrids in Fig. 87. The most obvious difference is the change of the maximum anchor force from Failure anchor row 2+3 in Fig. 87 to Failure anchor row 3+4 in Fig. 109. While anchor 4 shows the maximum force of 1552 kN in Fig. 87, anchor 2 reveals the maximum anchor force in the magnitude of 1167 kN in Fig. 109. The maximum divergence of 435 kN can be found for anchor 4 after the failure of anchor row 2+3, where 1552 kN is opposite to 1117 kN occurring for linear skin resistance. What does not change between the geogrids and *EBs* is the tendency for the force increment in the anchors below the failed elements to be higher than the force increment in the anchors above the failed elements.

Tab. 19 and Tab. 20 summarise the presented results.

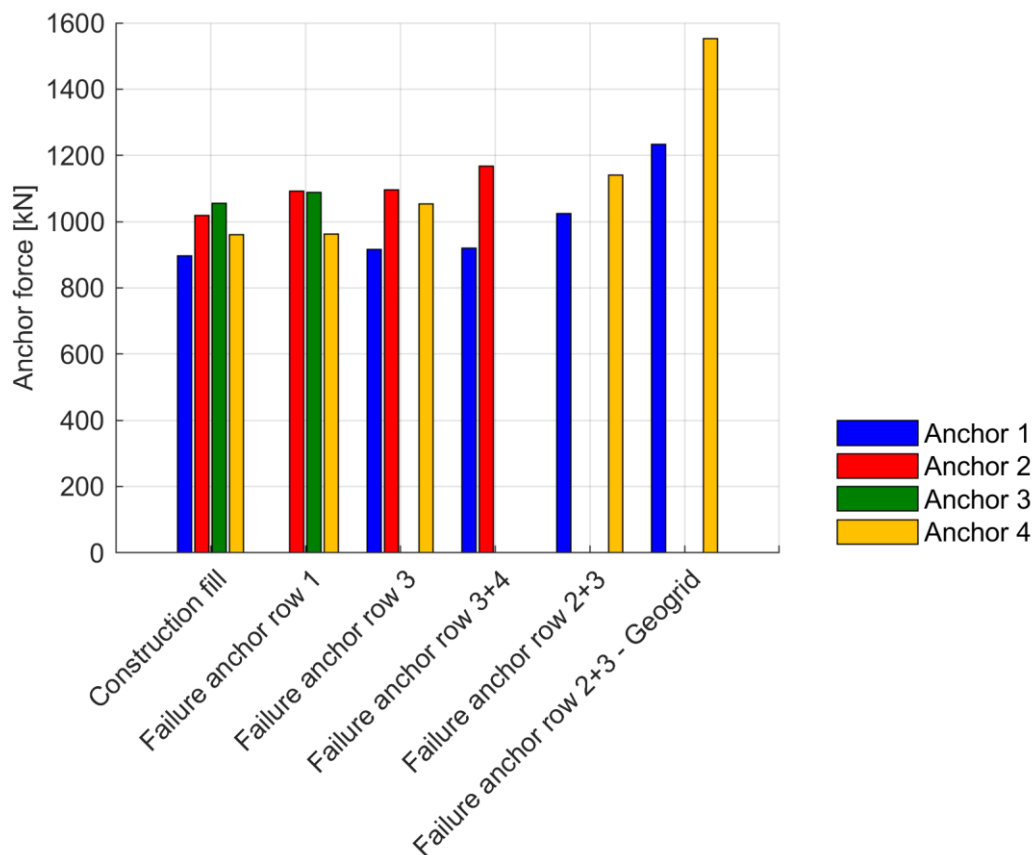


Fig. 109: Anchor forces after Construction fill and Failure cases for $c = 0.1$ kPa; *EBs* with constant skin resistance

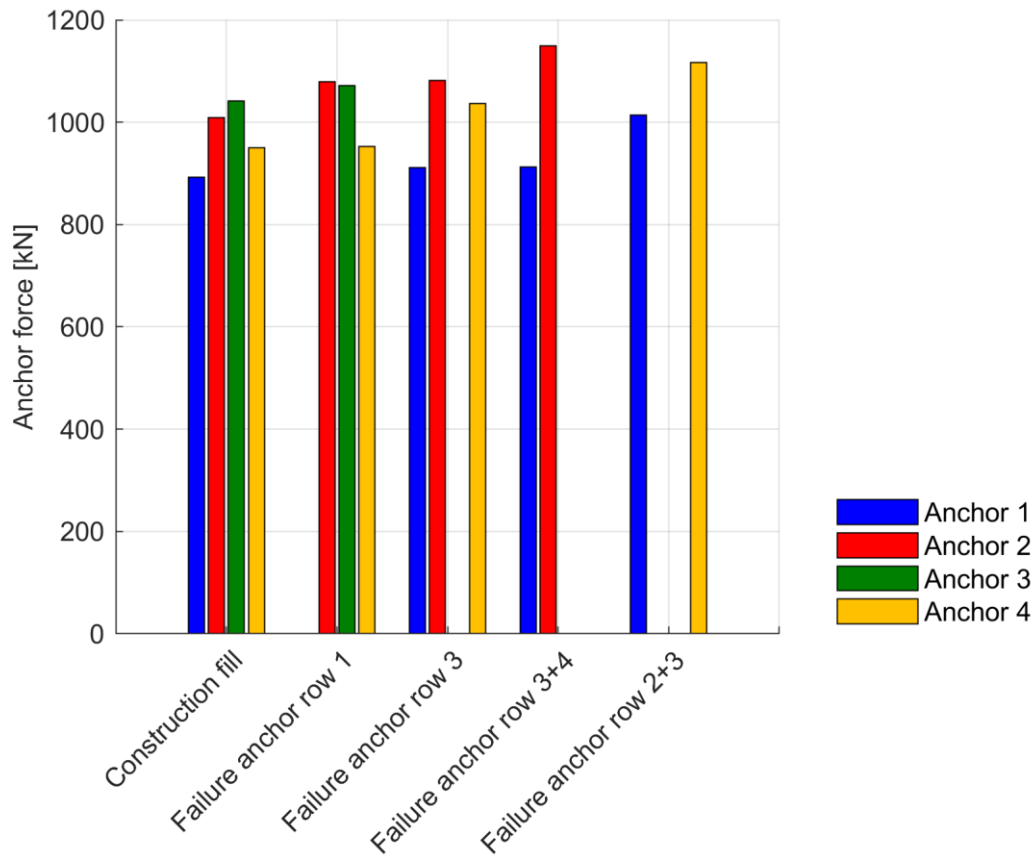


Fig. 110: Anchor forces after Construction fill and Failure cases for $c = 0.1$ kPa; *EBs* with linear skin resistance

Tab. 19: Results of the calculation phases Construction fill and Failure cases; EBs with constant skin resistance

| | Cohesion [kPa] | | | |
|--|----------------|-------|-------|-------|
| | 0.1 | 1 | 3 | 5 |
| FoS_{CF} [-] | 1.31 | 1.37 | 1.47 | 1.57 |
| $FoS_{Failure}$ anchor row 1 [-] | 1.31 | 1.38 | 1.45 | 1.57 |
| $FoS_{Failure}$ anchor row 3 [-] | 1.33 | 1.39 | 1.47 | 1.55 |
| $FoS_{Failure}$ anchor row 3+4 [-] | 1.32 | 1.38 | 1.43 | 1.46 |
| $FoS_{Failure}$ anchor row 2+3 [-] | 1.32 | 1.38 | 1.47 | 1.55 |
| $M_{act,min,CF}$ [kNm/m] | -582 | -582 | -568 | -561 |
| $M_{act,min,Failure}$ anchor row 1 [kNm/m] | -617 | -615 | -600 | -589 |
| $M_{act,min,Failure}$ anchor row 3 [kNm/m] | -423 | -432 | -436 | -445 |
| $M_{act,min,Failure}$ anchor row 3+4 [kNm/m] | -415 | -436 | -445 | -455 |
| $M_{act,min,Failure}$ anchor row 2+3 [kNm/m] | -159 | -159 | -167 | -177 |
| $Q_{act,min,CF}$ [kN/m] | -210 | -210 | -211 | -213 |
| $Q_{act,min,Failure}$ anchor row 1 [kN/m] | -204 | -203 | -200 | -196 |
| $Q_{act,min,Failure}$ anchor row 3 [kN/m] | -197 | -198 | -199 | -203 |
| $Q_{act,min,Failure}$ anchor row 3+4 [kN/m] | -207 | -213 | -213 | -216 |
| $Q_{act,min,Failure}$ anchor row 2+3 [kN/m] | -126 | -123 | -126 | -130 |
| $Q_{act,max,CF}$ [kN/m] | 231 | 234 | 226 | 218 |
| $Q_{act,max,Failure}$ anchor row 1 [kN/m] | 237 | 239 | 231 | 224 |
| $Q_{act,max,Failure}$ anchor row 3 [kN/m] | 171 | 174 | 169 | 165 |
| $Q_{act,max,Failure}$ anchor row 3+4 [kN/m] | 143 | 141 | 140 | 140 |
| $Q_{act,max,Failure}$ anchor row 2+3 [kN/m] | 136 | 137 | 138 | 137 |
| $u_{x,max,CF}$ [cm] | 11.30 | 11.10 | 10.90 | 10.70 |
| $u_{x,max,Failure}$ anchor row 1 [cm] | 12.00 | 11.80 | 11.60 | 11.40 |
| $u_{x,max,Failure}$ anchor row 3 [cm] | 12.50 | 12.30 | 12.00 | 11.80 |
| $u_{x,max,Failure}$ anchor row 3+4 [cm] | 14.40 | 14.10 | 13.70 | 13.40 |
| $u_{x,max,Failure}$ anchor row 2+3 [cm] | 14.60 | 14.20 | 13.80 | 13.60 |
| $ u _{max,CF}$ [cm] | 13.20 | 13.00 | 12.90 | 13.00 |
| $ u _{max,Failure}$ anchor row 1 [cm] | 14.20 | 13.90 | 13.80 | 13.90 |
| $ u _{max,Failure}$ anchor row 3 [cm] | 14.00 | 13.70 | 13.60 | 13.50 |
| $ u _{max,Failure}$ anchor row 3+4 [cm] | 15.10 | 14.70 | 14.50 | 14.30 |
| $ u _{max,Failure}$ anchor row 2+3 [cm] | 16.10 | 15.70 | 15.40 | 15.30 |
| $F_{max,Anchor 3,CF}$ [kN] | 1056 | 1051 | 1048 | 1044 |
| $F_{max,Anchor 2,Failure}$ anchor row 1 [kN] | 1093 | 1086 | 1081 | 1078 |
| $F_{max,Anchor 2,Failure}$ anchor row 3 [kN] | 1096 | 1091 | 1087 | 1084 |
| $F_{max,Anchor 2,Failure}$ anchor row 3+4 [kN] | 1167 | 1160 | 1149 | 1142 |
| $F_{max,Anchor 4,Failure}$ anchor row 2+3 [kN] | 1141 | 1135 | 1110 | 1104 |

Tab. 20: Results of the calculation phases Construction fill and Failure cases; *EBs* with linear skin resistance

| | Cohesion [kPa] | | | |
|--|----------------|-------|-------|-------|
| | 0.1 | 1 | 3 | 5 |
| FoS_{CF} [-] | 1.34 | 1.37 | 1.48 | 1.57 |
| $FoS_{Failure}$ anchor row 1 [-] | 1.32 | 1.36 | 1.46 | 1.56 |
| $FoS_{Failure}$ anchor row 3 [-] | 1.33 | 1.36 | 1.46 | 1.54 |
| $FoS_{Failure}$ anchor row 3+4 [-] | 1.31 | 1.38 | 1.45 | 1.47 |
| $FoS_{Failure}$ anchor row 2+3 [-] | 1.31 | 1.38 | 1.47 | 1.56 |
| $M_{act,min,CF}$ [kNm/m] | -576 | -575 | -565 | -555 |
| $M_{act,min,Failure}$ anchor row 1 [kNm/m] | -610 | -607 | -595 | -582 |
| $M_{act,min,Failure}$ anchor row 3 [kNm/m] | -418 | -424 | -434 | -440 |
| $M_{act,min,Failure}$ anchor row 3+4 [kNm/m] | -405 | -424 | -437 | -446 |
| $M_{act,min,Failure}$ anchor row 2+3 [kNm/m] | -158 | -157 | -165 | -175 |
| $Q_{act,min,CF}$ [kN/m] | -209 | -209 | -210 | -211 |
| $Q_{act,min,Failure}$ anchor row 1 [kN/m] | -201 | -200 | -197 | -193 |
| $Q_{act,min,Failure}$ anchor row 3 [kN/m] | -196 | -196 | -199 | -201 |
| $Q_{act,min,Failure}$ anchor row 3+4 [kN/m] | -204 | -209 | -211 | -213 |
| $Q_{act,min,Failure}$ anchor row 2+3 [kN/m] | -124 | -122 | -125 | -128 |
| $Q_{act,max,CF}$ [kN/m] | 228 | 231 | 224 | 216 |
| $Q_{act,max,Failure}$ anchor row 1 [kN/m] | 234 | 237 | 229 | 222 |
| $Q_{act,max,Failure}$ anchor row 3 [kN/m] | 167 | 171 | 167 | 163 |
| $Q_{act,max,Failure}$ anchor row 3+4 [kN/m] | 142 | 140 | 139 | 139 |
| $Q_{act,max,Failure}$ anchor row 2+3 [kN/m] | 131 | 133 | 136 | 134 |
| $u_{x,max,CF}$ [cm] | 11.40 | 11.10 | 10.90 | 10.70 |
| $u_{x,max,Failure}$ anchor row 1 [cm] | 12.10 | 11.90 | 11.60 | 11.50 |
| $u_{x,max,Failure}$ anchor row 3 [cm] | 12.70 | 12.40 | 12.10 | 11.80 |
| $u_{x,max,Failure}$ anchor row 3+4 [cm] | 14.70 | 14.20 | 13.80 | 13.40 |
| $u_{x,max,Failure}$ anchor row 2+3 [cm] | 14.70 | 14.30 | 13.90 | 13.70 |
| $ u _{max,CF}$ [cm] | 13.30 | 13.00 | 13.00 | 13.00 |
| $ u _{max,Failure}$ anchor row 1 [cm] | 14.30 | 14.00 | 13.90 | 13.90 |
| $ u _{max,Failure}$ anchor row 3 [cm] | 14.10 | 13.80 | 13.60 | 13.50 |
| $ u _{max,Failure}$ anchor row 3+4 [cm] | 15.30 | 14.80 | 14.50 | 14.40 |
| $ u _{max,Failure}$ anchor row 2+3 [cm] | 16.20 | 15.80 | 15.50 | 15.30 |
| $F_{max,Anchor 3,CF}$ [kN] | 1042 | 1039 | 1035 | 1030 |
| $F_{max,Anchor 2,Failure}$ anchor row 1 [kN] | 1079 | 1072 | 1068 | 1064 |
| $F_{max,Anchor 2,Failure}$ anchor row 3 [kN] | 1081 | 1075 | 1072 | 1068 |
| $F_{max,Anchor 2,Failure}$ anchor row 3+4 [kN] | 1149 | 1141 | 1130 | 1123 |
| $F_{max,Anchor 4,Failure}$ anchor row 2+3 [kN] | 1117 | 1112 | 1091 | 1083 |

Fig. 111 to Fig. 118 show results of *FEAs* conducted using the *HSS* model, the fixed anchor length discretised by means of *EBs*, a R_{inter} value of 0.90 and prestressed anchor tendons. The presented results are obtained with constant distribution of the skin resistance, whereby FoS and FM s are presented for linear skin resistance as well. Because major numerical problems were faced during the

FEAs with a cohesion of 5 kPa, only results for $c = 0.1$ kPa are discussed in the following. In the appendix, section 8.5, results regarding linear skin resistance are given.

Fig. 111 shows the *FoS* for constant skin resistance. While the calculation phase Construction fill exhibits a safety margin of 1.31, Failure anchor row 3 plots a marginal decreased *FoS* of 1.30. In contrast, Failure anchor row 1 and both double row anchor failure cases show an increase in the *FoS*. Again, the differences are very small.

In Fig. 112, the phases Construction fill and Failure anchor row 3 show basically identical safety margins of 1.33. While the *FoS* decreases for Failure anchor row 1 and 3+4, Failure anchor row 2+3 exhibits a slight increase in the *FoS*.

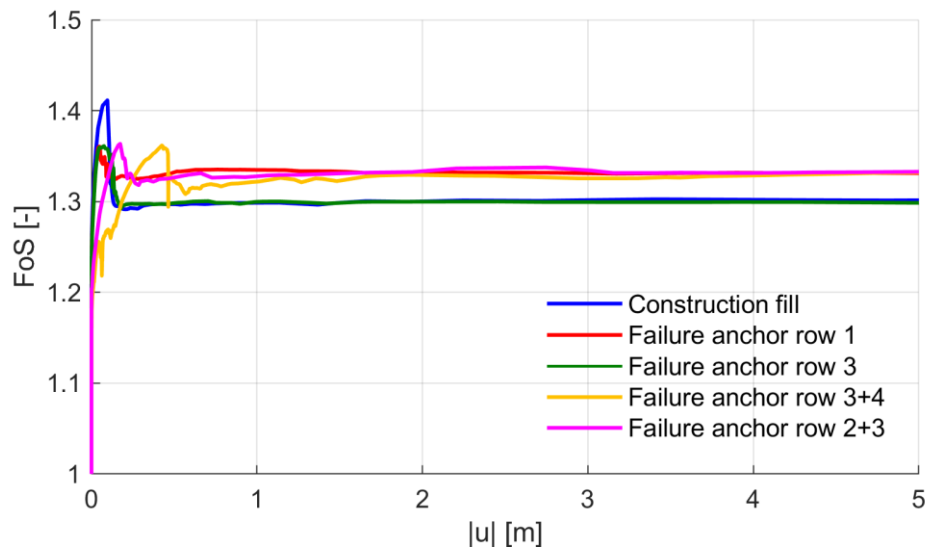


Fig. 111: *FoS* after ϕ - c reduction Construction fill and Failure cases for $c = 0.1$ kPa; *HSS* model; *EBs* with constant skin resistance

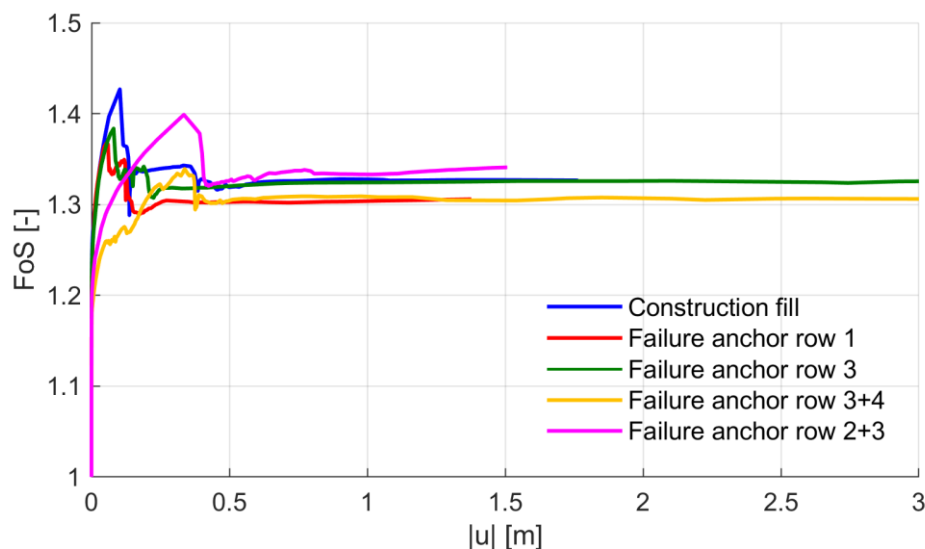


Fig. 112: *FoS* after ϕ - c reduction Construction fill and Failure cases for $c = 0.1$ kPa; *HSS* model; *EBs* with linear skin resistance

Fig. 113 shows the *FMs* related to the *FoS* plotted in Fig. 112 (*FEA* performed with linear distribution of the skin resistance). Like for the *MC* model (see Fig. 89), failure occurs in the upper slope for all failure cases.

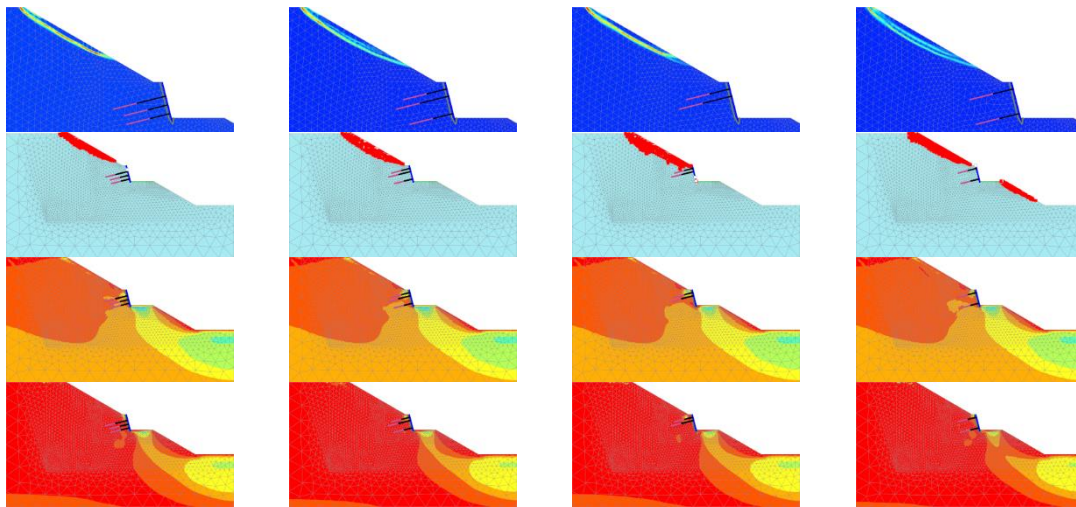


Fig. 113: Incremental deviatoric strains and plastic points after as well as τ_{rel} before/after ϕ - c reduction anchor failure for $c = 0.1$ kPa; *HSS* model; *EBs* with linear skin resistance; left: Failure anchor row 1; centre left: Failure anchor row 3; centre right: Failure anchor row 3+4; right: Failure anchor row 2+3

Compared to Fig. 95, Fig. 114 shows significantly smaller values of the minimum *BMs*. Between the *MC* and the *HSS* model, the maximum deviation of 373 kNm/m after Construction fill occurs for the *FEA* with constant skin resistance. Maximum *BMs*, however, show higher values or, in other words, they are increased compared to the *MC* model. Moreover, it was found that deviations between constant and linear skin resistance, which were nearly non-existent for the *MC* model, are more pronounced for the *HSS* model. The maximum deviation (71 kNm/m) between minimum values of both options can be found for the phase Construction fill. Up to this point, the minimum *BMs* after the phase Construction fill had only been increased by Failure anchor row 1. However, Fig. 114 now also shows a ratio above 1.00 for Failure anchor row 3+4.

Fig. 115 shows the *SF* distributions. Compared to Fig. 99, the minimum values appear to be smaller than in the *MC* model, with the maximum deviation of 99 kN/m for the phase Construction fill and for constant distribution of the skin resistance. The sole exception concerns Failure anchor row 2+3 for constant and linear skin resistance, where minimum values appear to be higher for the *HSS* model. Contrary to *BMs*, the maximum *SF* values are smaller, with a maximum divergence in the magnitude of 100 kN/m compared to the *MC* model. Again, there is one exception – namely, Failure anchor row 3+4, for which the maximum values seem to be higher for the *HSS* model and for both skin resistance options. A comparison of constant and linear skin resistance for the *HSS* model reveals maximum deviations of 14 kN/m between minimum values for the calculation phase Construction fill as well as 10 kN/m between maximum values for Failure

anchor row 2+3. This difference is not significant from a geotechnical point of view, but nevertheless shows higher divergences than for the *MC* model.

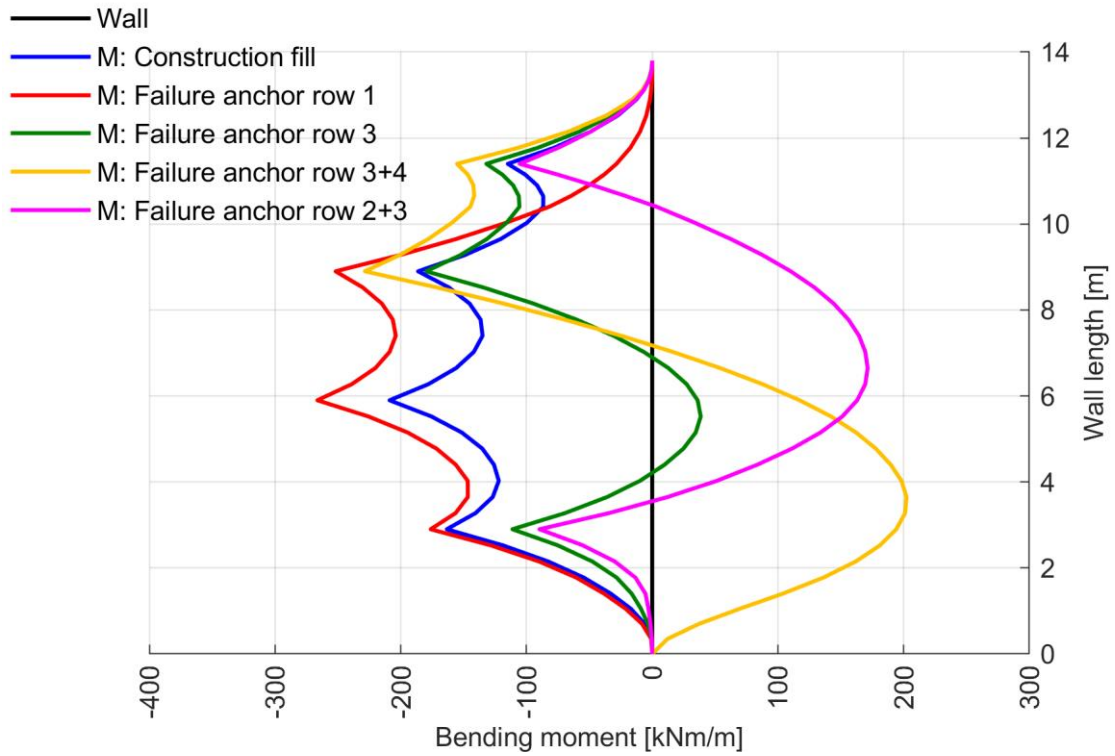


Fig. 114: $BM_s M_{actual}$ after Construction fill and Failure cases for $c = 0.1$ kPa; *HSS* model; *EBs* with constant skin resistance

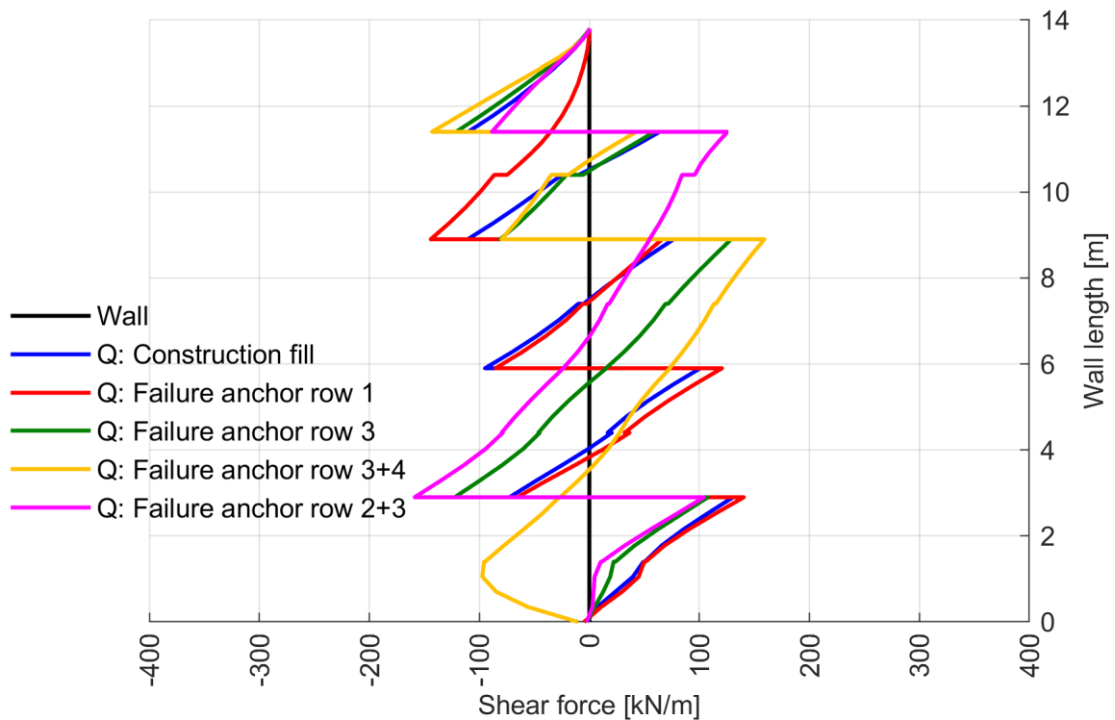


Fig. 115: $SFs Q_{actual}$ after Construction fill and Failure cases for $c = 0.1$ kPa; *HSS* model; *EBs* with constant skin resistance

In Fig. 116 the horizontal displacements u_x are depicted. When compared with Fig. 103, completely different deflection curves can be observed. While the *FEA*, conducted using the *MC* model shows the maximum horizontal displacements close to the centre of the *RW*, maximum displacements for the *HSS* model can be primarily found at the top of the wall. Moreover, the divergence in the magnitude of the maximum displacements is significant. Compared to the *MC* model, the *HSS* model shows maximum values which are reduced by a factor of almost 2.00. What does not change is the fact that displacements for linear distribution seem to be higher than displacements for constant skin resistance. Though small, deviations between both options are more pronounced for the *HSS* model than for the *MC* model. In contrast to the *MC* model, the *HSS* model is capable of accounting for a very high stiffness at a very small strain level (much stiffer behaviour at very small strains), which would explain the differences between both models. Moreover, the *HSS* model offers the advantage of its stress-dependent stiffness. While the stiffness rises with increasing stress level for the *HSS* model, the *MC* model describe stiffness with a constant elastic modulus.

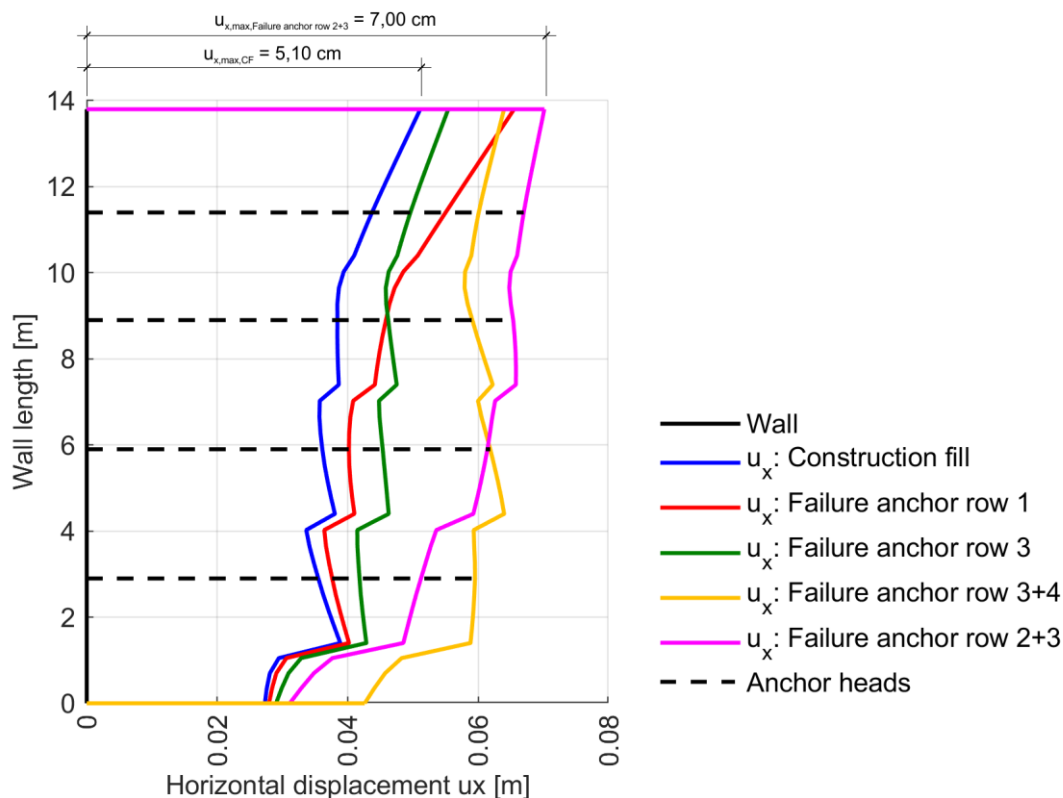


Fig. 116: Horizontal displacements u_x after Construction fill and Failure cases for $c = 0.1\ kPa$; *HSS* model; *EBs* with constant skin resistance

Similar behaviour as for horizontal displacements can be observed for the total displacements $|u|$, as shown in Fig. 117. The calculation phase Construction fill (as well as all four cases of ground anchor failure) exhibit the maximum displacement at the top of the wall; however, this result does not apply for the *MC* model shown in Fig. 106. Again, the difference between constant and linear skin resistance appears to be small but nonetheless higher than for the *MC* model.

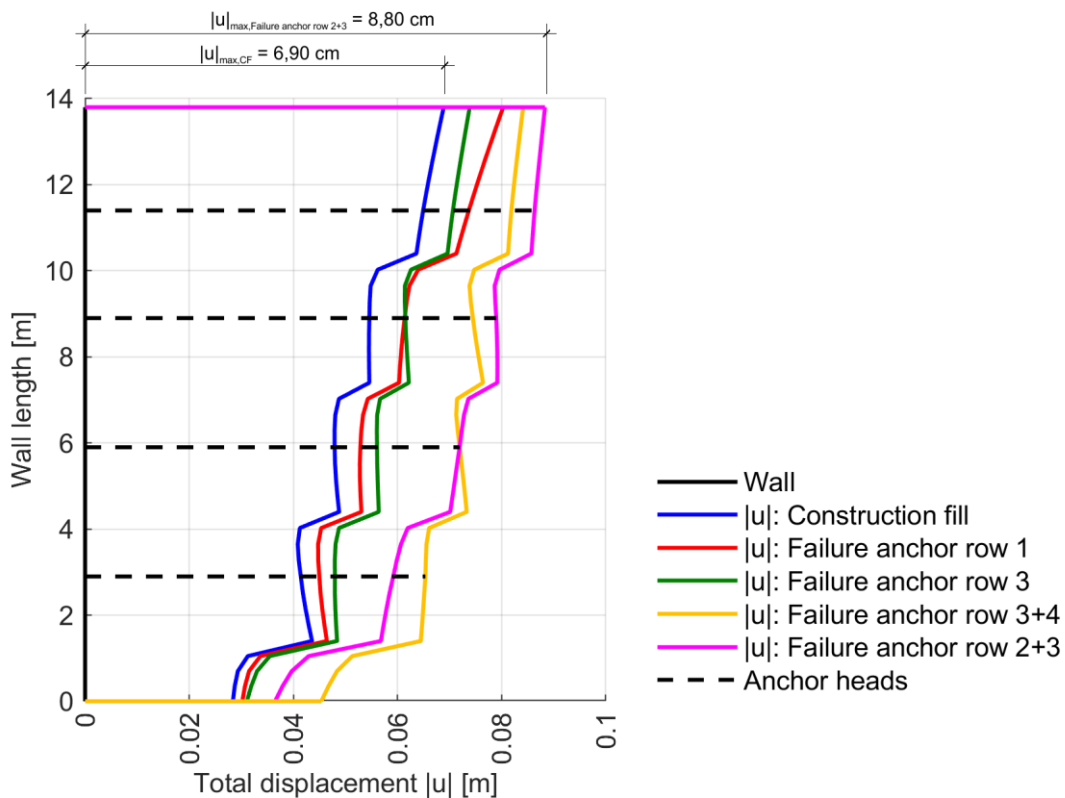


Fig. 117: Total displacements $|u|$ after Construction fill and Failure cases for $c = 0.1$ kPa; *HSS* model; *EBs* with constant skin resistance

The redistribution of anchor forces can be seen in Fig. 118. Compared to Fig. 109, where anchor 3 shows the highest anchor force after the calculation phase Construction fill, anchor 4 shows the highest anchor force for constant distribution of the skin resistance. Moreover, the maximum anchor force reached changes from anchor 2 after Failure anchor row 3+4 (in Fig. 109) to anchor 4 after Failure anchor row 2+3 (in Fig. 118). There is no uniform trend, as observed for the *MC* model, that a linear distribution of the skin resistance results in smaller maximum values compared to constant skin resistance.

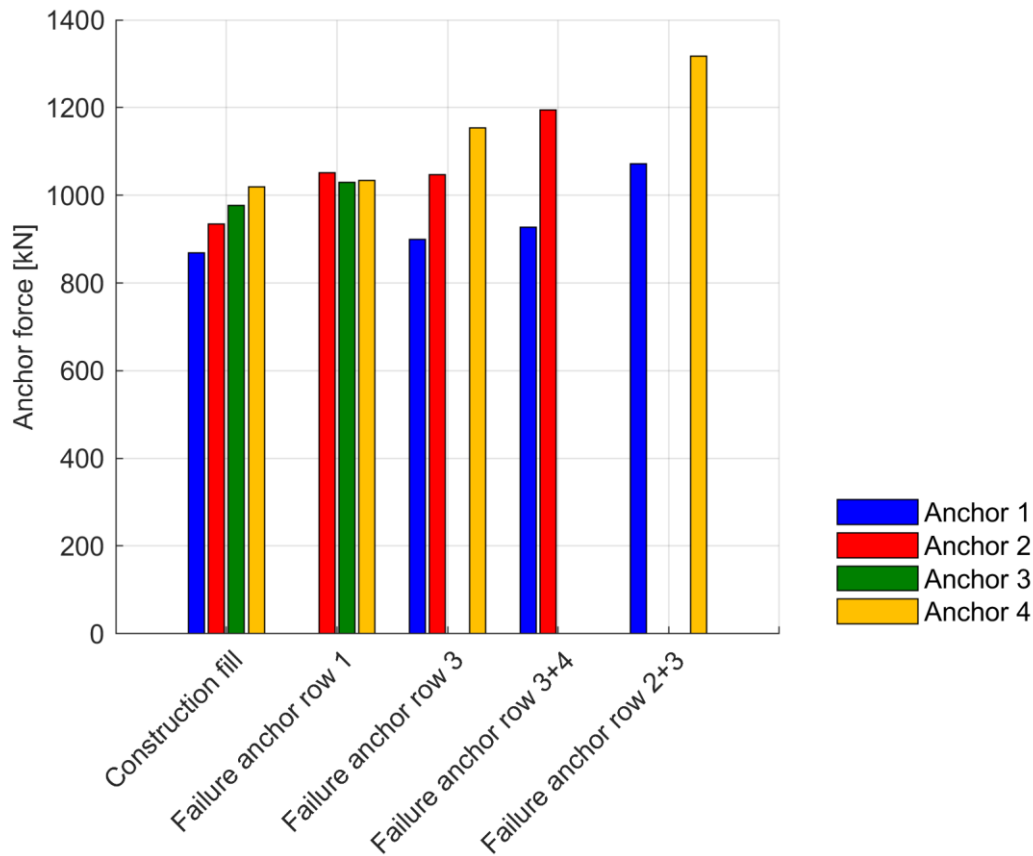


Fig. 118: Anchor forces after Construction fill and Failure cases for $c = 0.1$ kPa; *HSS* model; *EBs* with constant skin resistance

Tab. 21 portrays the presented results in table form. Regarding results representing the *FEA* conducted with the *HSS* model and the fixed anchor length discretised by means of geogrid elements, some selected evaluations are given in the appendix, section 8.4.

Tab. 21: Results of the calculation phases Construction fill and Failure cases; HSS model with $c = 0.1$ kPa

| | Cohesion [kPa] | | |
|--|----------------|----------------|--------------|
| | 0.1Geogrid | 0.1EB;Constant | 0.1EB;Linear |
| FoS_{CF} [-] | 1.31 | 1.31 | 1.33 |
| $FoS_{Failure}$ anchor row 1 [-] | 1.31 | 1.33 | 1.31 |
| $FoS_{Failure}$ anchor row 3 [-] | 1.31 | 1.30 | 1.33 |
| $FoS_{Failure}$ anchor row 3+4 [-] | 1.32 | 1.33 | 1.31 |
| $FoS_{Failure}$ anchor row 2+3 [-] | 1.32 | 1.34 | 1.34 |
| $M_{act,min,CF}$ [kNm/m] | -243 | -209 | -280 |
| $M_{act,min,Failure}$ anchor row 1 [kNm/m] | -296 | -266 | -331 |
| $M_{act,min,Failure}$ anchor row 3 [kNm/m] | -193 | -180 | -219 |
| $M_{act,min,Failure}$ anchor row 3+4 [kNm/m] | -231 | -229 | -258 |
| $M_{act,min,Failure}$ anchor row 2+3 [kNm/m] | -119 | -105 | -131 |
| $Q_{act,min,CF}$ [kN/m] | -117 | -111 | -125 |
| $Q_{act,min,Failure}$ anchor row 1 [kN/m] | -150 | -144 | -158 |
| $Q_{act,min,Failure}$ anchor row 3 [kN/m] | -122 | -122 | -130 |
| $Q_{act,min,Failure}$ anchor row 3+4 [kN/m] | -141 | -143 | -151 |
| $Q_{act,min,Failure}$ anchor row 2+3 [kN/m] | -151 | -159 | -148 |
| $Q_{act,max,CF}$ [kN/m] | 144 | 131 | 139 |
| $Q_{act,max,Failure}$ anchor row 1 [kN/m] | 152 | 140 | 147 |
| $Q_{act,max,Failure}$ anchor row 3 [kN/m] | 123 | 129 | 123 |
| $Q_{act,max,Failure}$ anchor row 3+4 [kN/m] | 153 | 159 | 155 |
| $Q_{act,max,Failure}$ anchor row 2+3 [kN/m] | 119 | 126 | 116 |
| $u_{x,max,CF}$ [cm] | 5.70 | 5.10 | 5.50 |
| $u_{x,max,Failure}$ anchor row 1 [cm] | 7.10 | 6.60 | 6.90 |
| $u_{x,max,Failure}$ anchor row 3 [cm] | 6.00 | 5.50 | 5.90 |
| $u_{x,max,Failure}$ anchor row 3+4 [cm] | 6.60 | 6.40 | 7.00 |
| $u_{x,max,Failure}$ anchor row 2+3 [cm] | 7.40 | 7.00 | 7.40 |
| $ u _{max,CF}$ [cm] | 7.40 | 6.90 | 7.40 |
| $ u _{max,Failure}$ anchor row 1 [cm] | 8.60 | 8.00 | 8.50 |
| $ u _{max,Failure}$ anchor row 3 [cm] | 7.90 | 7.40 | 7.90 |
| $ u _{max,Failure}$ anchor row 3+4 [cm] | 8.50 | 8.40 | 8.80 |
| $ u _{max,Failure}$ anchor row 2+3 [cm] | 9.20 | 8.80 | 9.30 |
| $F_{max,Anchor}$ 3/4,CF [kN] | 1036 | 1020 | 1034 |
| $F_{max,Anchor}$ 2/3/4,Failure anchor row 1 [kN] | 1047 | 1051 | 1086 |
| $F_{max,Anchor}$ 4,Failure anchor row 3 [kN] | 1187 | 1153 | 1125 |
| $F_{max,Anchor}$ 2,Failure anchor row 3+4 [kN] | 1148 | 1195 | 1217 |
| $F_{max,Anchor}$ 4,Failure anchor row 2+3 [kN] | 1357 | 1317 | 1289 |

5 Finite element analyses using PLAXIS 3D

Because ground anchor failure results in complex 3D force redistributions, this chapter deals with *FEAs* conducted using PLAXIS 3D (Brinkgreve *et al.*, 2018a). By modelling the same geometry with accordingly chosen parameters, it should be studied if the 2D *FEAs* presented above provide realistic results. For this purpose, newly introduced results are compared to those obtained from the previous chapter.

5.1 PLAXIS 3D model

FEAs in 3D were only performed for geometry ‘Final’ shown on the left-hand side in Fig. 119. While dimensions in the x-z direction are identical to the 2D model (see Fig. 49), an out-of-plane width of 20 m was considered. Therefore, with a spacing of 5 m between anchors in the y-ordinate, a grid with 16 ground anchors, seen on the right-hand side in Fig. 119, was modelled.

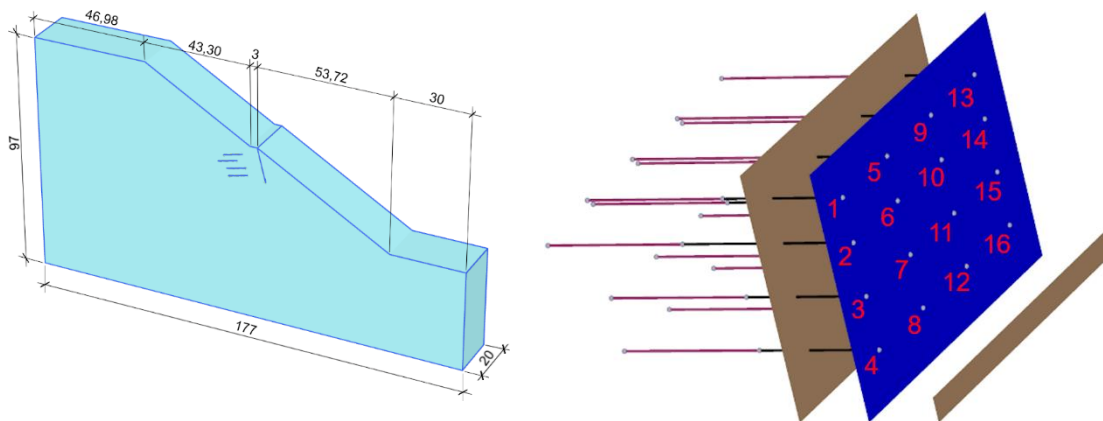


Fig. 119: Model dimensions ‘Final’ with discretised anchor grid in 3D

Input parameters of the soil and fill material are identical to those used for 2D *FEAs* and are listed in Tab. 9 for the *MC* model.

The wall was modelled with elastic plate elements and a rigid connection between panels. Its parameters can be observed in Tab. 22.

Tab. 22: Parameters of wall modelled with plate elements in 3D

| | Wall |
|-------------------------------|----------|
| Material type | Elastic |
| d [m] | 0.50 |
| γ [kN/m ³] | 25 |
| Isotropic | Yes |
| E_1 [kN/m ²] | 30000000 |
| ν_{12} [-] | 0.20 |
| G_{12} [kN/m ²] | 12500000 |
| Prevent punching | No |

As with 2D *FEAs*, node-to-node anchors were used to account for the free anchor length. Input parameters are listed in Tab. 12, whereby L_{spacing} is not required as an input for 3D *FEAs*.

Besides geogrid and *EB* elements (see Tab. 13), the fixed anchor length for the 3D model was additionally modelled by means of volume elements (*VEs*). Since the finite element model with *VEs* has to be discretised with much more finite elements, an out-of-plane width of only 5 m (i.e. anchor 1, 2, 3 and 4 from Fig. 119) was considered. Parameters of the grout body modelled with *VEs* are given in Tab. 23.

Tab. 23: Parameters of grout body modelled with *VEs* in 3D

| | Grout (<i>VEs</i>) |
|--|---------------------------|
| Material model | Linear elastic |
| Drainage type | Non-porous |
| γ_{unsat} [kN/m ³] | 24 |
| E [kN/m ²] | 16500000 |
| ν [-] | 0.20 |
| R_{inter} [-] | 1 |
| K₀ determination | Automatic |

The mesh discretisation for all geometries (i.e. the fixed anchor length modelled with geogrid, *EB* and *VEs*) is shown in Fig. 120. As PLAXIS 3D (Brinkgreve *et al.*, 2018a) does not offer an alternative, the mesh is discretised by means of 10-noded tetrahedral elements. Mesh refinements, with equivalent refinement clusters for 2D *FEAs*, are situated around anchors and close to the slope.

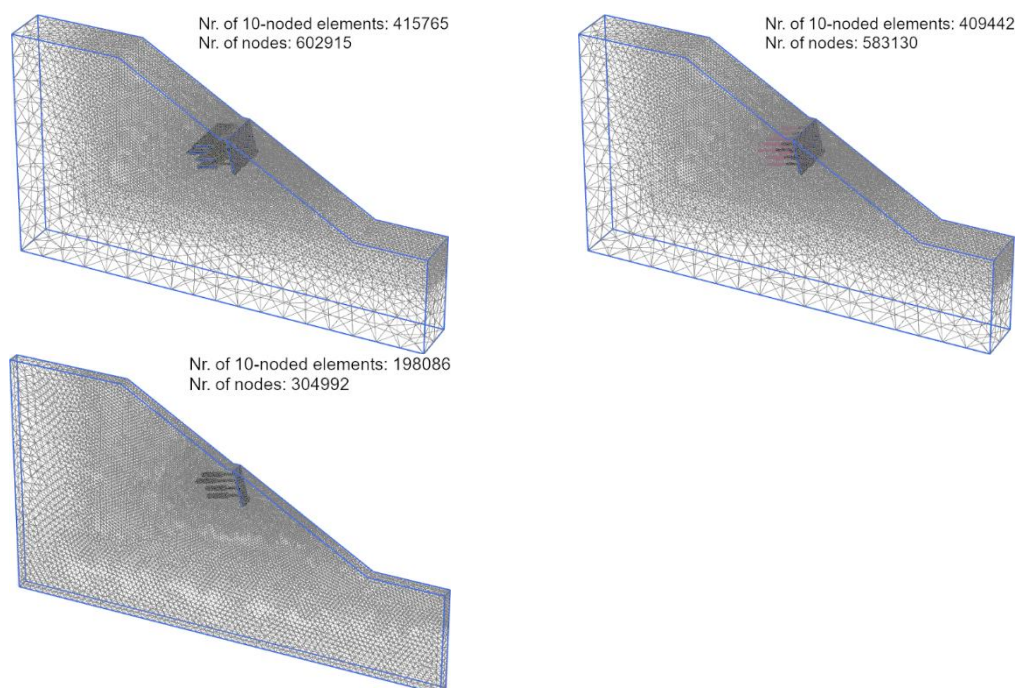


Fig. 120: Mesh discretisation for model 'Final' in 3D; top left: Geogrid; top right: *EB*; bottom left: *VE*

In contrast to 2D *FEAs*, where the failure of a complete row of anchors was simulated, 3D *FEAs* implicate the failure of one or two single anchors. While the Initial phase, Plastic nil step and phases during the construction of the wall were identical to those for 2D *FEAs* (see Tab. 14), five individual failure cases were investigated in 3D. Corresponding to Fig. 119, which shows the consecutive numbering of the anchors, these 3D *FEAs* contained the failure cases shown in Tab. 24. Again, free and fixed anchor length were deactivated during the failure phase when the fixed anchor length was modelled with *EBs* or *VEs*. To represent individual ground anchor failure for *FEAs* conducted with the fixed anchor length discretised by means of geogrid elements, only the free anchor length was deactivated during the associated failure phase.

Tab. 24: Failure cases for 3D *FEAs*

| ID | Stage | Start from phase | Counterpart in 2D |
|----|---------------------|-------------------|------------------------|
| 1 | Failure anchor 5 | Construction fill | Failure anchor row 1 |
| 2 | Failure anchor 7 | Construction fill | Failure anchor row 3 |
| 3 | Failure anchor 7+8 | Construction fill | Failure anchor row 3+4 |
| 4 | Failure anchor 6+7 | Construction fill | Failure anchor row 2+3 |
| 5 | Failure anchor 8+12 | Construction fill | - |

5.2 Results

Fig. 121 to Fig. 126 portray the *FoS* and *FMs* respectively, representing initial conditions with varying cohesion (evaluations done after the calculation phase Plastic nil step). These results show comparisons between 2D and 3D *FEAs* conducted with the *MC* model.

For all variations of the cohesion, the *FoS* resulting from 3D *FEAs* is increased compared to the *FoS* resulting from 2D *FEAs* for geometry ‘Final’, as shown in Fig. 121, Fig. 123 and Fig. 125. While $c = 1$ kPa, shown in Fig. 123, shows the lowest divergence in the magnitude of 0.03, the maximum deviation of 0.06 is found for Fig. 125, where the *FoS* for a cohesion of 5 kPa is portrayed. The higher *FoS* for 3D *FEAs* can most likely be explained by the different mesh discretisation and the different shape functions used in 2D and 3D.

As visualised in Fig. 122, Fig. 124 and Fig. 126, the failure behaviour from 2D *FEAs* is in agreement with the 3D analyses. Though the *FoS* between geometry ‘Final’ shows the maximum divergence for a cohesion of 5 kPa, almost identical *FMs* (extending over the total height of the lower and upper slope) can be observed in Fig. 126.

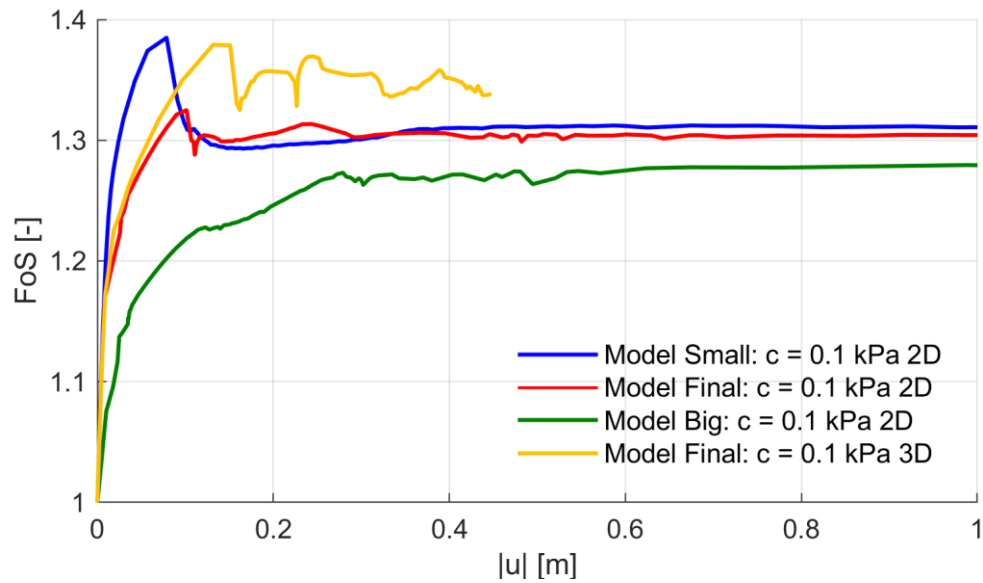


Fig. 121: FoS after ϕ - c reduction Plastic nil step for $c = 0.1$ kPa; 2D vs. 3D

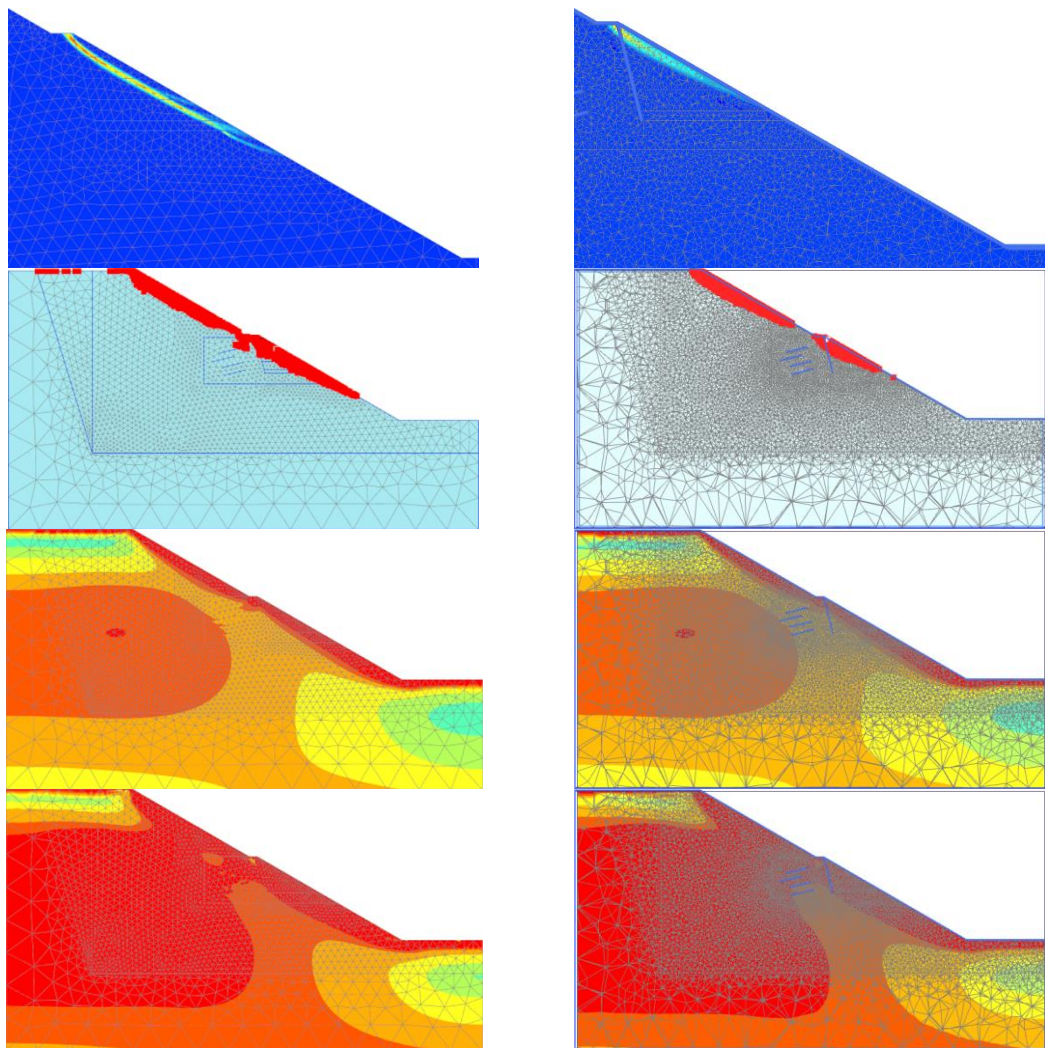


Fig. 122: Incremental deviatoric strains and plastic points after as well as τ_{rel} before/after ϕ - c reduction Plastic nil step for model dimensions 'Final' with $c = 0.1$ kPa; left: 2D; right: 3D at $y = 10$ m

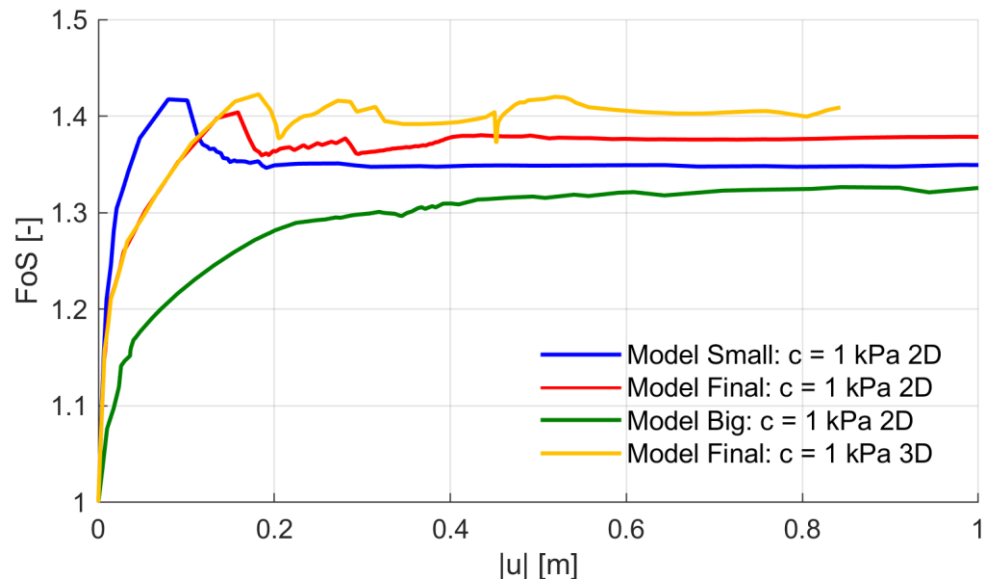


Fig. 123: FoS after ϕ - c reduction Plastic nil step for $c = 1$ kPa; 2D vs. 3D

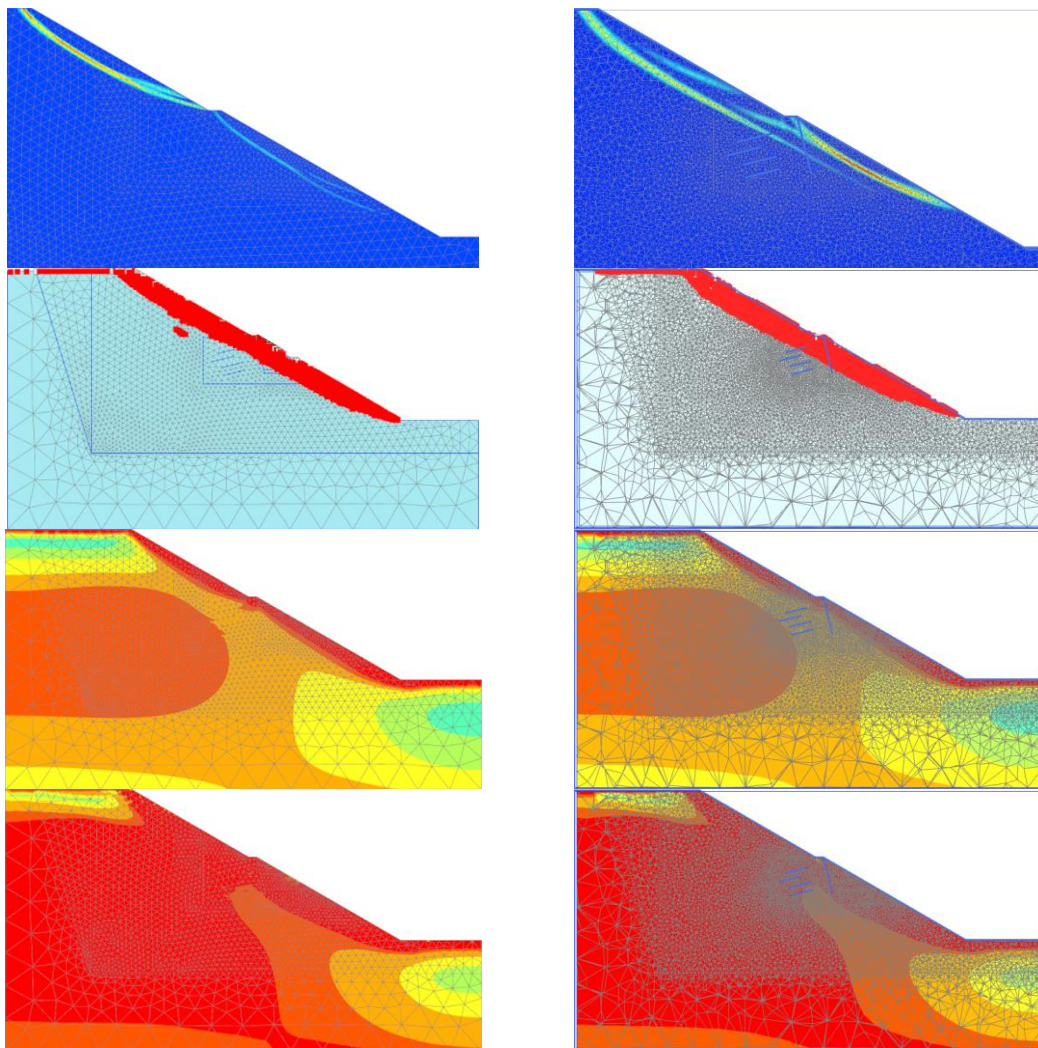


Fig. 124: Incremental deviatoric strains and plastic points after as well as τ_{rel} before/after ϕ - c reduction Plastic nil step for model dimensions 'Final' with $c = 1$ kPa; left: 2D; right: 3D at $y = 10$ m

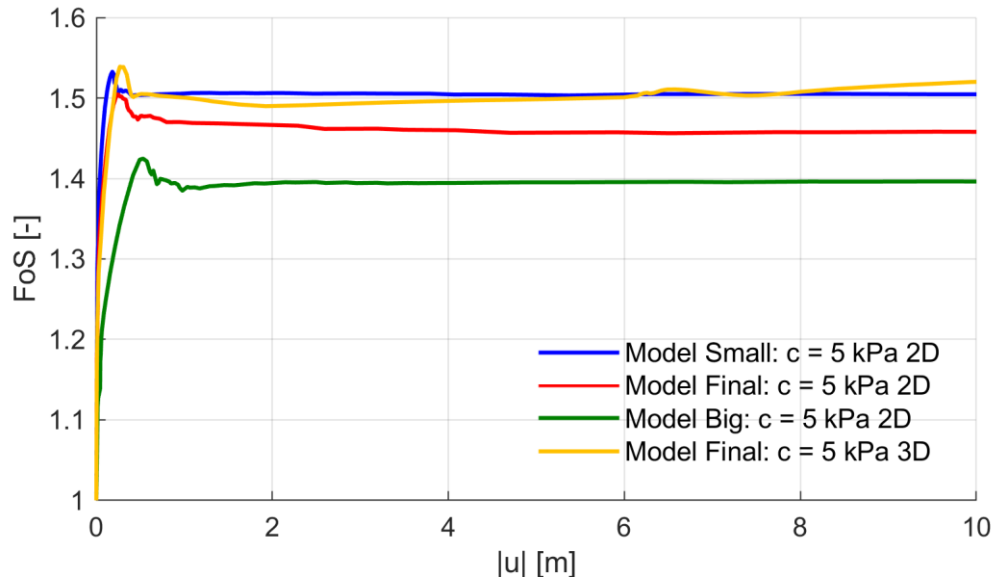


Fig. 125: FoS after ϕ -c reduction Plastic nil step for $c = 5$ kPa; 2D vs. 3D

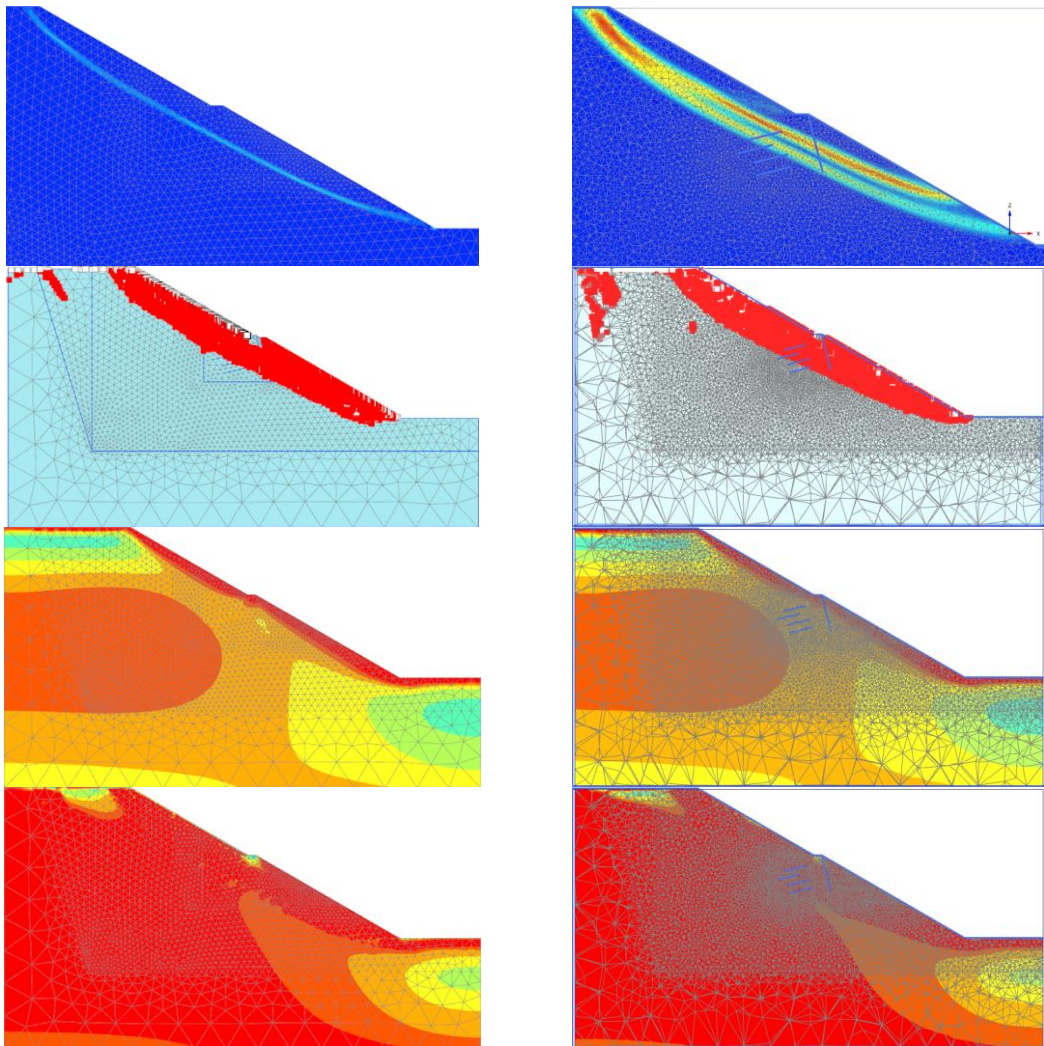


Fig. 126: Incremental deviatoric strains and plastic points after as well as τ_{rel} before/after ϕ -c reduction Plastic nil step for model dimensions 'Final' with $c = 5$ kPa; left: 2D; right: 3D at $y = 10$ m

Fig. 127 to Fig. 137 show results of the *FEA* conducted with the *MC* model, whereby the fixed anchor length, surrounded by interfaces with a R_{inter} value of 1.00 was discretised by means of geogrid elements. All introduced results, except for *FoS* and *FMs* (where $c = 5$ kPa is also shown), represent the *FEA* computed with a cohesion of 0.1 kPa.

Fig. 127 shows the *FoS* for all variations in cohesion prior to the failure of ground anchors (i.e. the calculation phase Construction fill). As previously discussed, an increase in the safety margins for 3D *FEAs* over 2D *FEAs* can be observed. Regarding the 3D *FEA* with the lowest cohesion value (i.e. 0.1 kPa), a decrease in the *FoS* was observed at the end of the associated failure phase. This numerical issue would require further investigations concerning *FoS* and *FM*.

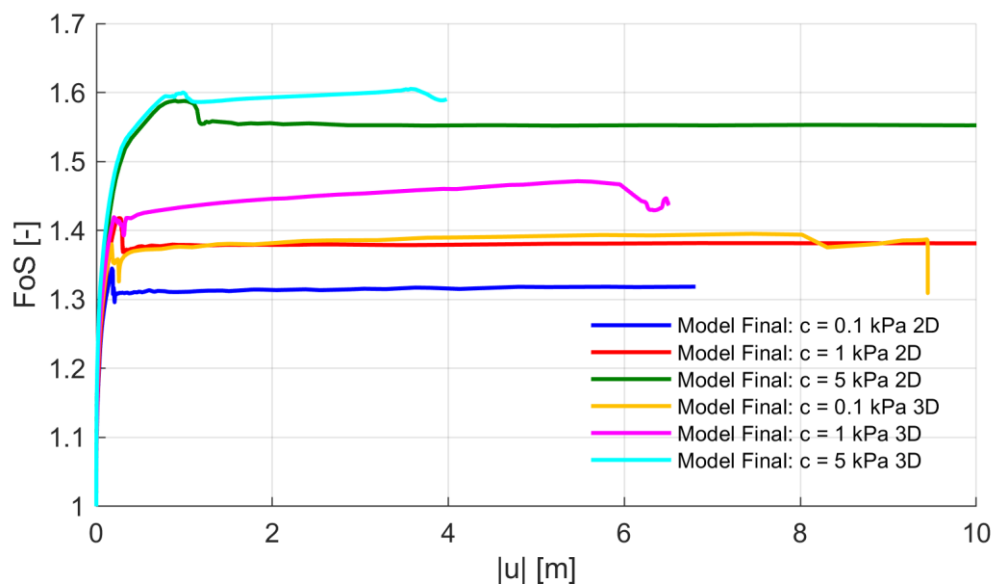


Fig. 127: *FoS* after ϕ - c reduction Construction fill; 2D vs. 3D

Visualised for a cohesion of 5 kPa, *FMs* are represented by Fig. 128. While 2D *FEAs* show failure in the slope above the *RW* for all cohesion modifications, the 3D *FEA* conducted with $c = 5$ kPa exhibits a completely different failure behaviour. Besides observable incremental deviatoric strains above the *RW*, the *FM* computed with 3D *FEA* extends over the total model height.

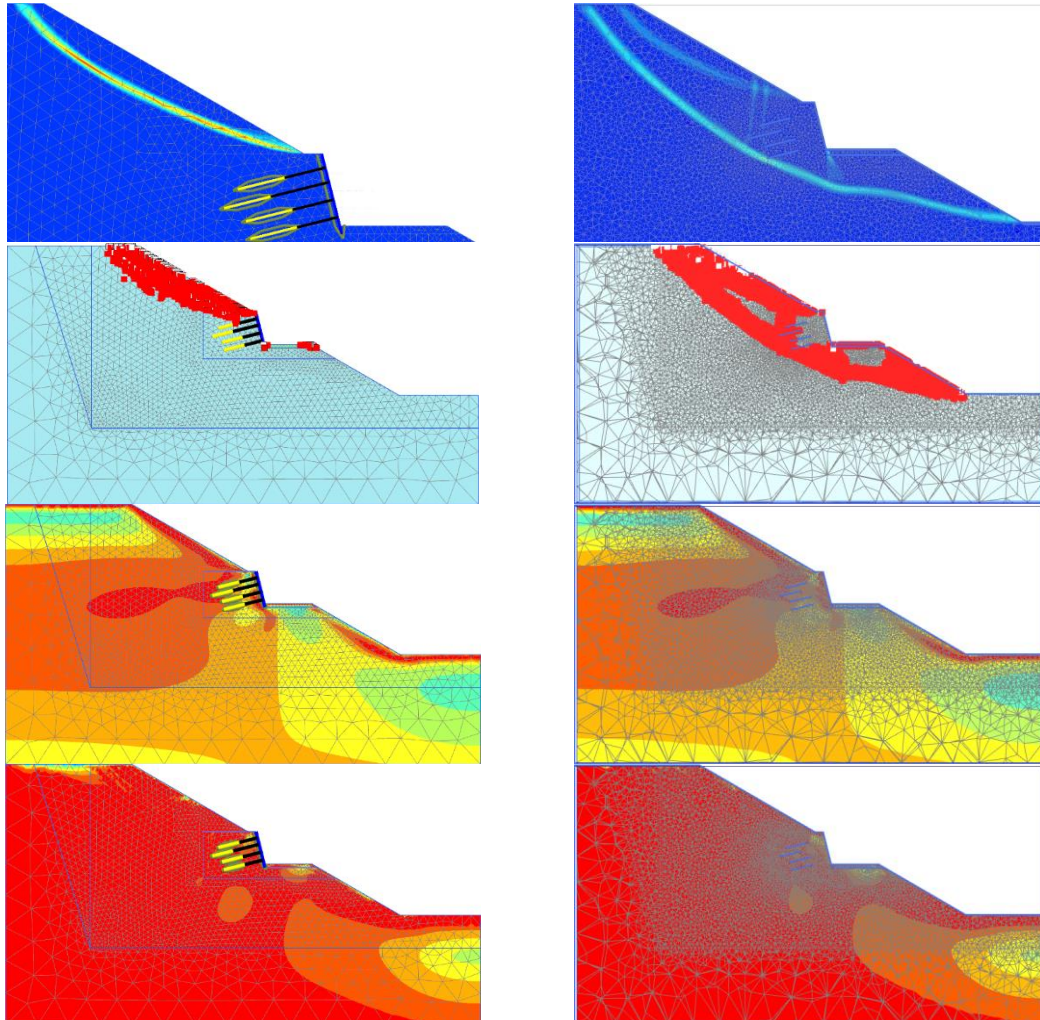


Fig. 128: Incremental deviatoric strains and plastic points after as well as τ_{rel} before/after ϕ - c reduction Construction fill for model dimensions 'Final' with $c = 5$ kPa; left: 2D; right: 3D at $y = 10$ m

In Fig. 129 and Fig. 130, the FoS for the five failure cases for a cohesion of 0.1 kPa and 5 kPa, respectively, can be found. Again, probably because of numerical reasons mentioned before, the FEA conducted with a cohesion of 0.1 kPa shows a sudden decrease at the end of an associated safety phase. For the 2D FEA with $c = 5$ kPa, a significant decrease in the FoS after Failure anchor row 3+4 could be determined. Fig. 130, however, reveals almost identical safety margins in 3D for the calculation phase Construction fill and the five failure cases, respectively. As for 3D $FEAs$, just one or two anchors fail; therefore, support is still guaranteed by the remaining anchors in the out-of-plane direction. Consequently, similar safety margins are plausible from a numerical point of view, but unrealistic from a practical point of view.

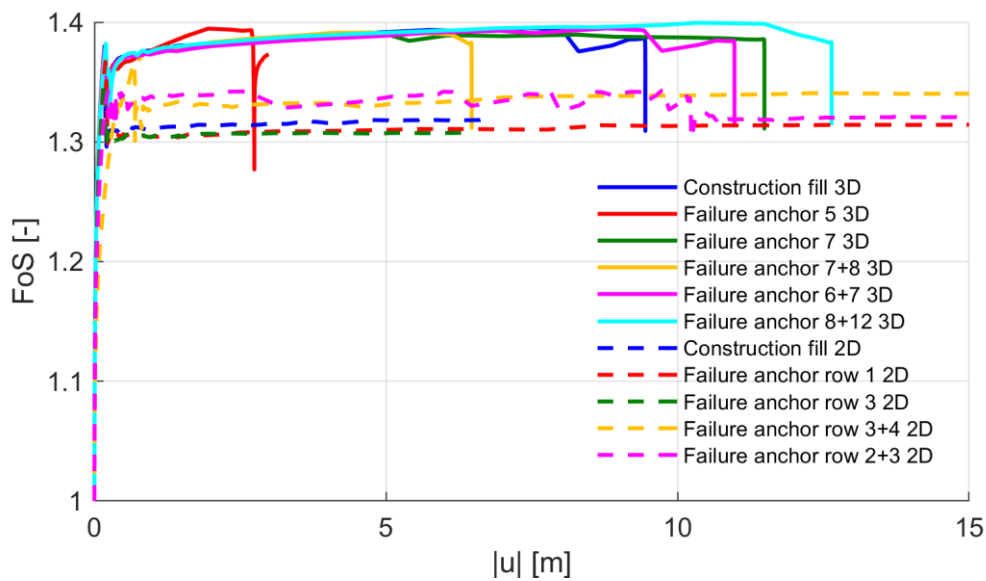


Fig. 129: FoS after ϕ - c reduction Construction fill and Failure cases for $c = 0.1$ kPa; 2D vs. 3D

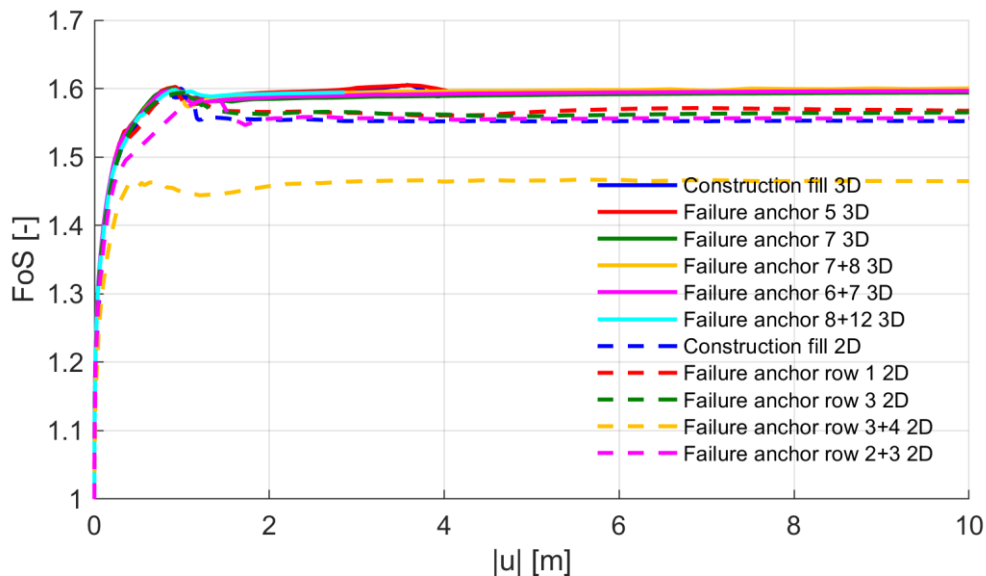


Fig. 130: FoS after ϕ - c reduction Construction fill and Failure cases for $c = 5$ kPa; 2D vs. 3D

*FM*s of the five failure cases calculated with a cohesion of 5 kPa can be observed in Fig. 131. While Failure anchor 5 shows continuous incremental deviatoric strains extending over the total model height, all other failure cases exhibit pronounced slip circles in the slope above the *RW*. The *FEA* conducted in 2D is shown in Fig. 77.

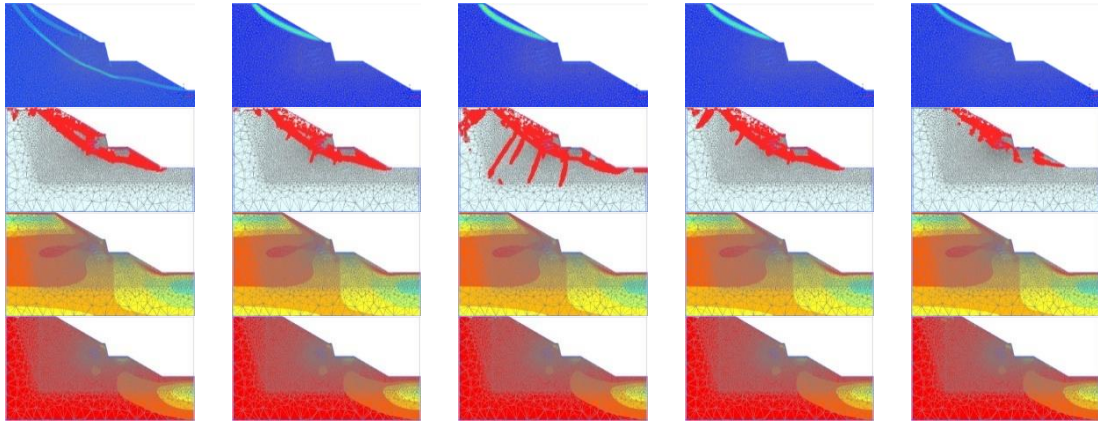


Fig. 131: Incremental deviatoric strains and plastic points after as well as τ_{rel} before/after ϕ - c reduction Failure cases for $c = 5$ kPa at $y = 10$ m; left: Failure anchor 5; centre left: Failure anchor 7; centre: Failure anchor 7+8; centre right: Failure anchor 6+7; right: Failure anchor 8+12

Fig. 132 shows the *BM* distributions for the calculation phase Construction fill, as well as both single anchor failure cases. Prior to the failure of ground anchors, a divergence between the 2D and 3D *FEA* at a magnitude of 129 kNm/m is present. As with the 2D *FEA*, failure near the top of the *RW* results in an increase of the minimum *BM* value. It must be noted that distributions representing the 3D *FEA* correspond to a cross section at $y = 7.50$ m, which correlates to the cross section through anchors 5, 6, 7 and 8, where, of course, local peaks are located.

Fig. 133 compares the *BM* distribution resulting from the 2D *FEA* with the 3D *BM* distributions at $y = 7.50$ m and $y = 10$ m. The latter represents a cross section in the centre of the 3D model and thus between two anchor columns. It can be observed that the 2D distribution corresponds almost to the average of both 3D distributions. This average would represent a good approximate/average solution; nevertheless, the retaining structure would have to be dimensioned according to minimum *BM* values, which would consequently be underestimated by the 2D *FEA*.

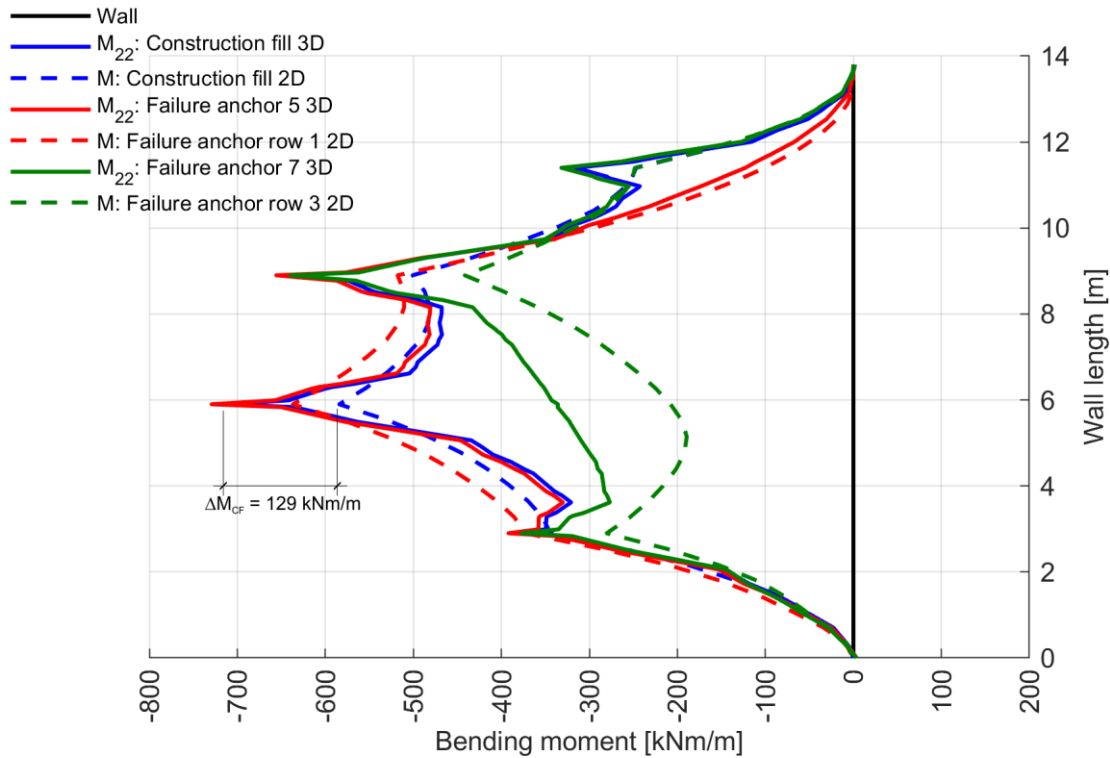


Fig. 132: $BM_s M_{22,actual}$ after Construction fill and single anchor failure cases for $c = 0.1 \text{ kPa}$; 2D vs. 3D at $y = 7.50 \text{ m}$

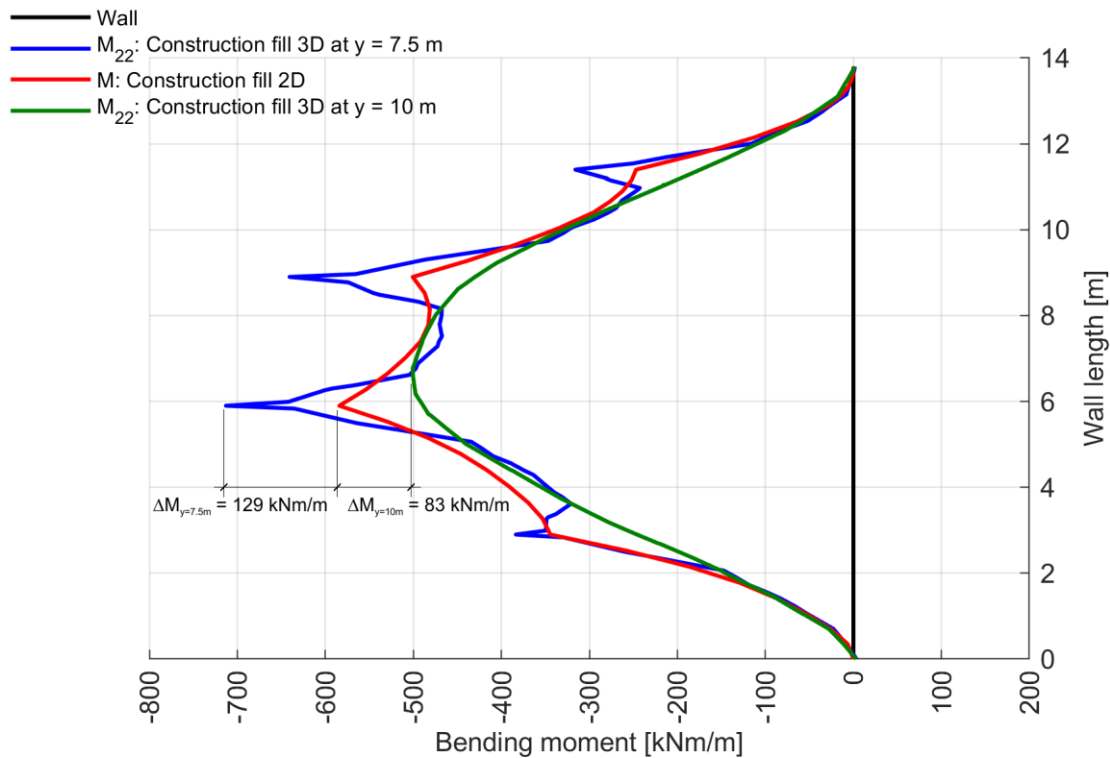


Fig. 133: $BM_s M_{22,actual}$ after Construction fill for $c = 0.1 \text{ kPa}$; 2D vs. 3D at $y = 7.50/10 \text{ m}$
Highly underestimated minimum and maximum values for the 2D FEA are also to be found for SFs, as shown in Fig. 134.

As shown in Fig. 135, where again the 3D SF distribution at $y = 10 \text{ m}$ is added, deviations occur after the calculation phase Construction fill – namely, a

magnitude of 321 kN/m between minimum values and of 291 kN/m between maximum values.

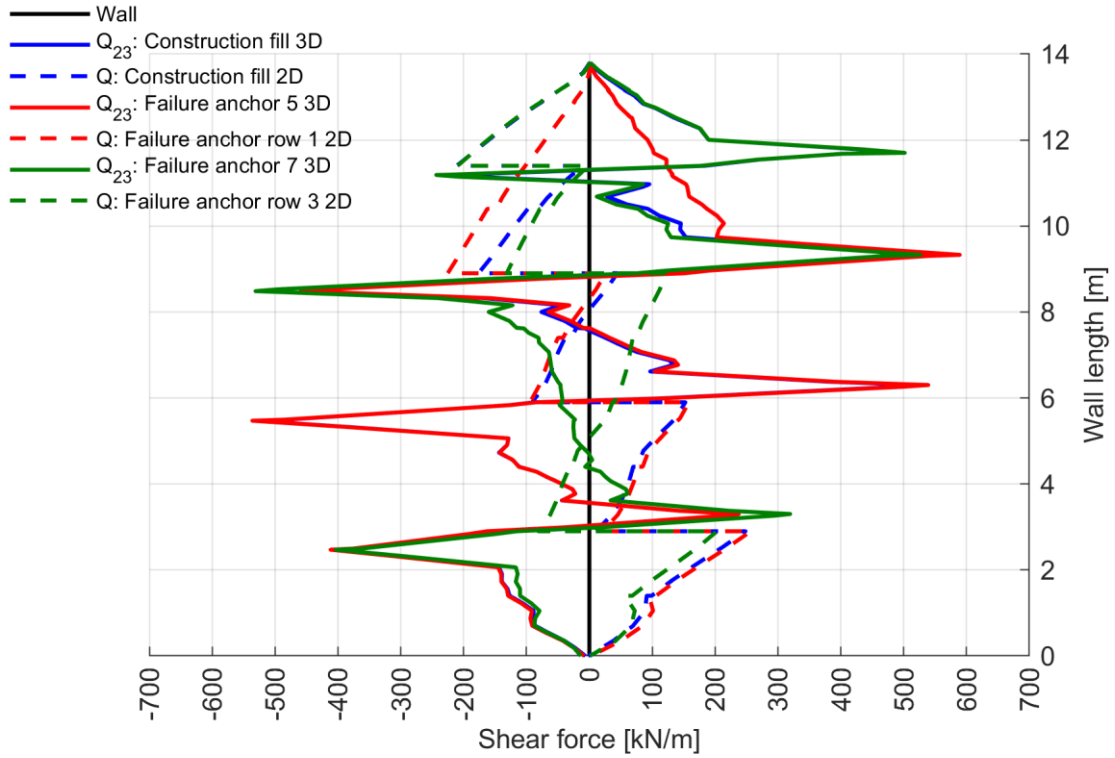


Fig. 134: $SFs Q_{23,actual}$ after Construction fill and single anchor failure cases for $c = 0.1$ kPa; 2D vs. 3D at $y = 7.50$ m

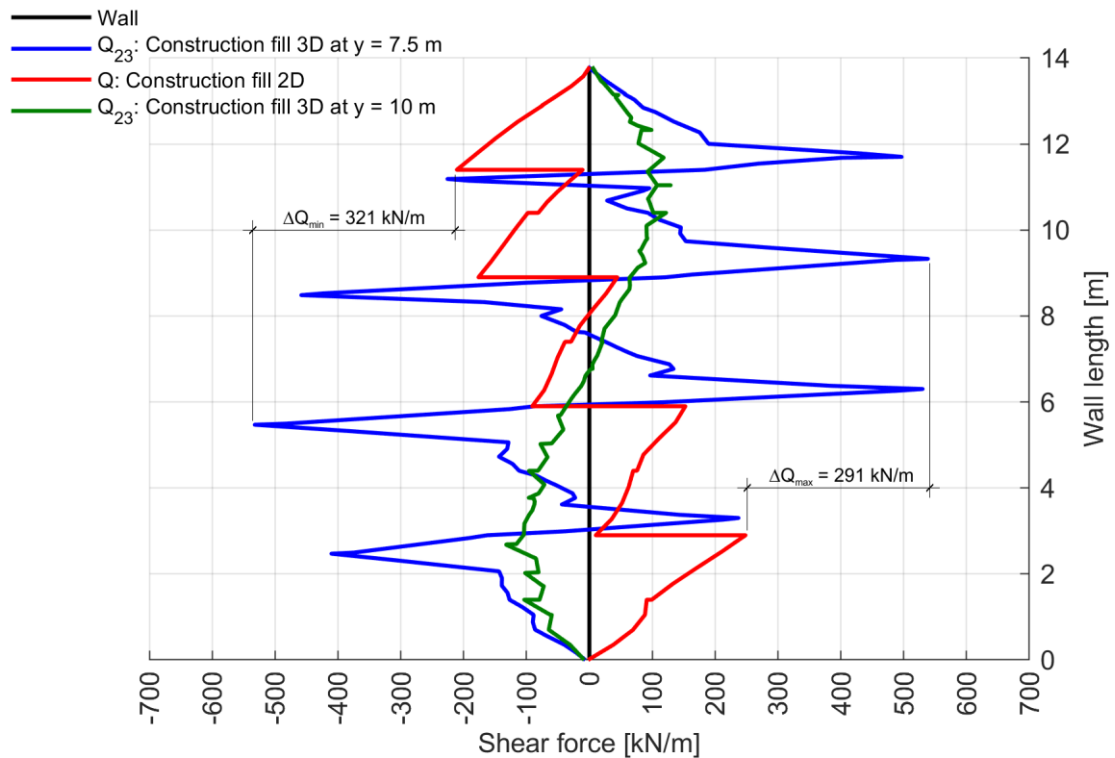


Fig. 135: $SFs Q_{23,actual}$ after Construction fill for $c = 0.1$ kPa; 2D vs. 3D at $y = 7.50/10$ m

Fig. 136 shows the horizontal displacements u_x , the 3D deflection curves are again taken at $y = 7.50$ m. As shown, Construction fill, which should basically deliver very similar results, gives significant deviations of up to 5.70 cm. Moreover, displacements for all failure cases seem to be significantly larger for the 3D *FEA*. Since $y = 7.50$ m correlates to the cross section where the failed anchors are situated, it was initially assumed that the higher deformations are just locally situated. Deflection curves (obtained with 3D *FEA*) at $y = 10$ m or $y = 12.50$ m, however, did not show significant deviations to deflection curves at $y = 7.50$ m. This behaviour is not clear at the moment and requires further clarification (research).

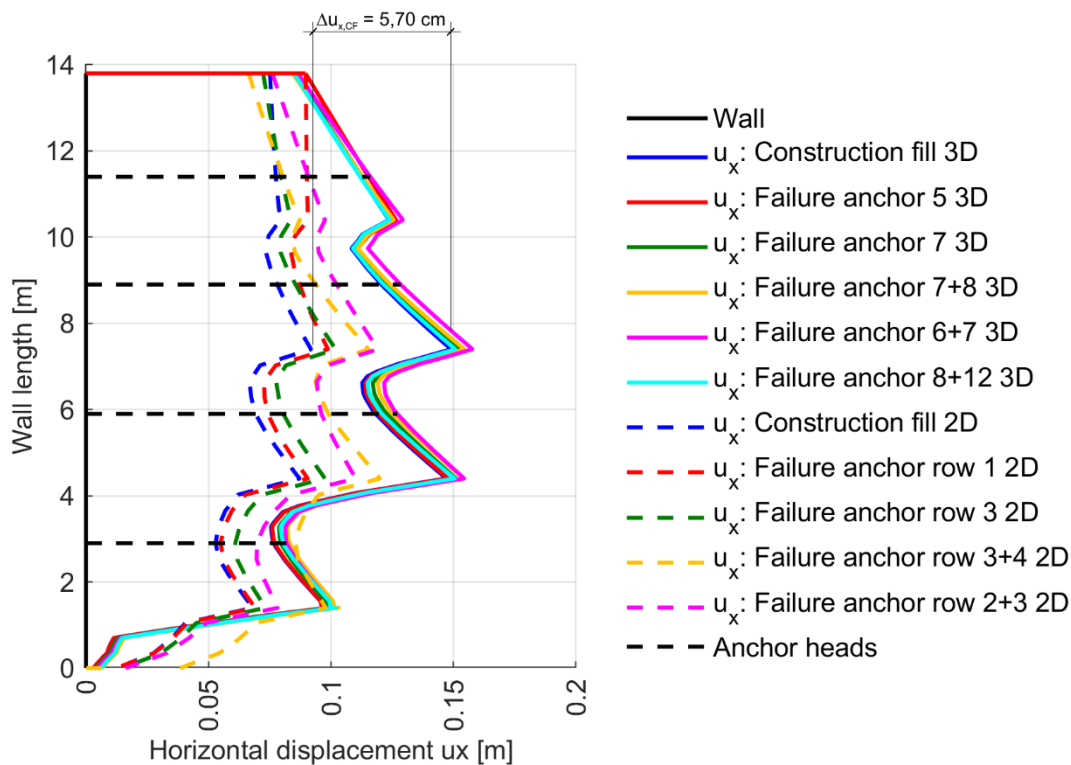


Fig. 136: Horizontal displacements u_x after Construction fill and Failure cases for $c = 0.1$ kPa; 2D vs. 3D at $y = 7.50$ m

The same conclusions as for horizontal displacements can be drawn for the total displacements $|u|$ shown in Fig. 137. Again, while no significant deviations between the five failure cases for the 3D *FEA* are obvious, excessive divergences compared to the 2D *FEA* were found.

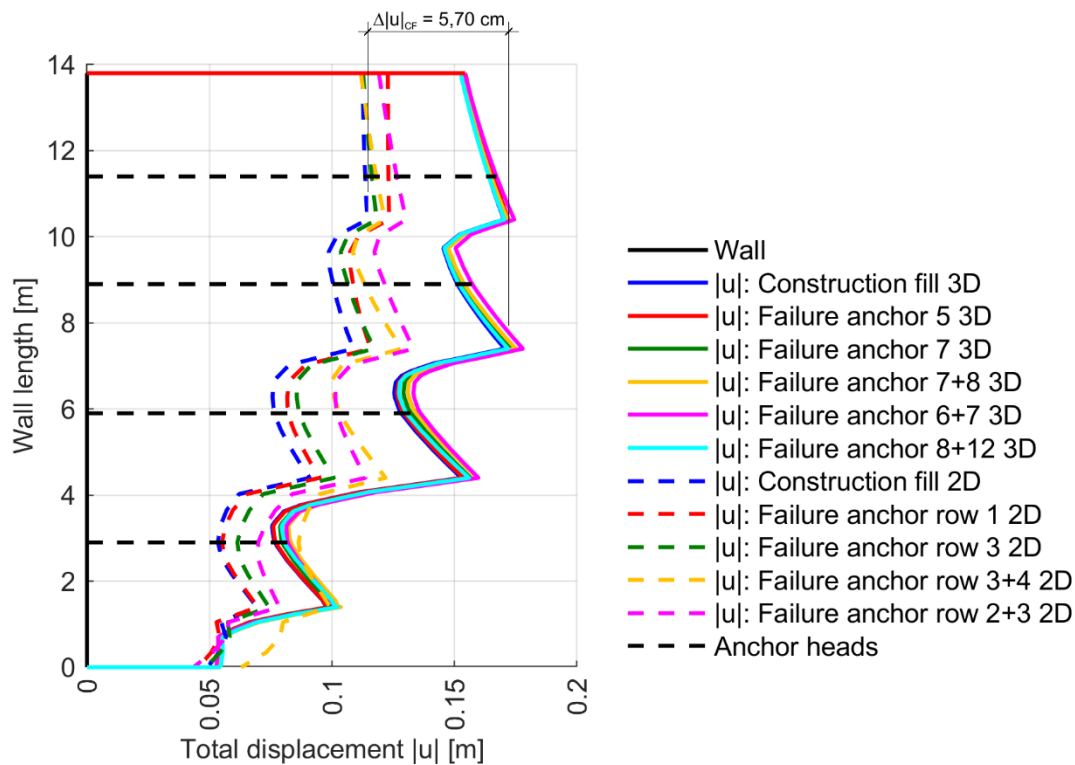


Fig. 137: Total displacements $|u|$ after Construction fill and Failure cases for $c = 0.1$ kPa; 2D vs. 3D at $y = 7.50$ m

The following results (Fig. 138 to Fig. 143) represent the *FEA* conducted with the *MC* model and a cohesion of 0.1 kPa, whereby the fixed anchor length was modelled with *EB* elements and a linear distribution of the skin resistance. A R_{inter} value (plate) of 0.90 as well as pre-stressing of anchor tendons was considered. Results showing the *FEA* describing constant skin resistance are given in the appendix, section 8.7.

Again, *BMs* in Fig. 138, which now show the phase Construction fill and the two double anchor failure cases, show excessive deviations between the 2D and 3D *FEA*. After the calculation phase Construction fill, a divergence between minimum values in the order of 321 kNm/m occurs. Furthermore, a remarkable difference in the *BM* distributions close to the centre of the *RW* can be observed. While here Failure anchor row 2+3, representing the 2D *FEA*, causes a change from negative to positive values, the *BM* distribution for Failure anchor 6+7, representing the 3D *FEA*, develops in the opposite direction.

For the *FEA* conducted with geogrid elements, the 2D *BM* distribution seemed to be the average of the 3D *BM* distributions at $y = 7.5$ m and $y = 10$ m. However, this finding does not apply for the *FEA* performed with *EB* elements. As shown in Fig. 139, the *BM* distribution resulting from the 2D *FEA* appears to be enveloped by both 3D *BM* distributions (i.e. *BMs* appear to be smaller, in terms of amount, compared to both 3D distributions).

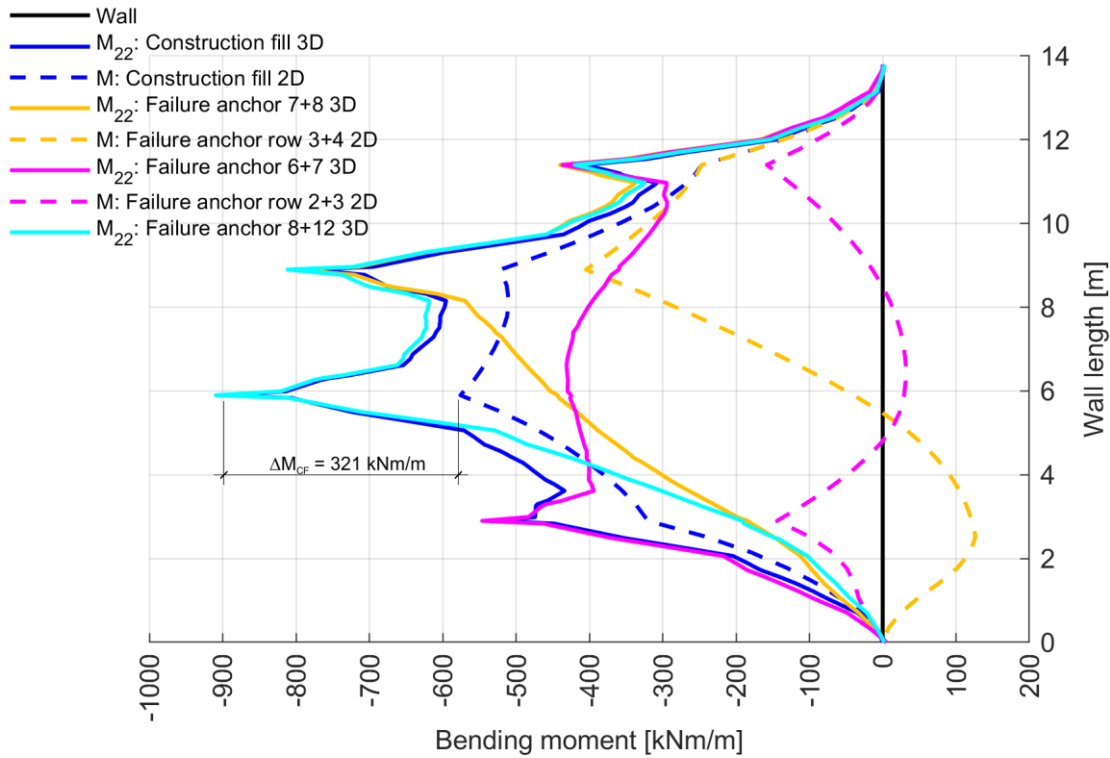


Fig. 138: $BM_s M_{22,actual}$ after Construction fill and double anchor failure cases for $c = 0.1 \text{ kPa}$; EBs with linear skin resistance; 2D vs. 3D at $y = 7.50 \text{ m}$

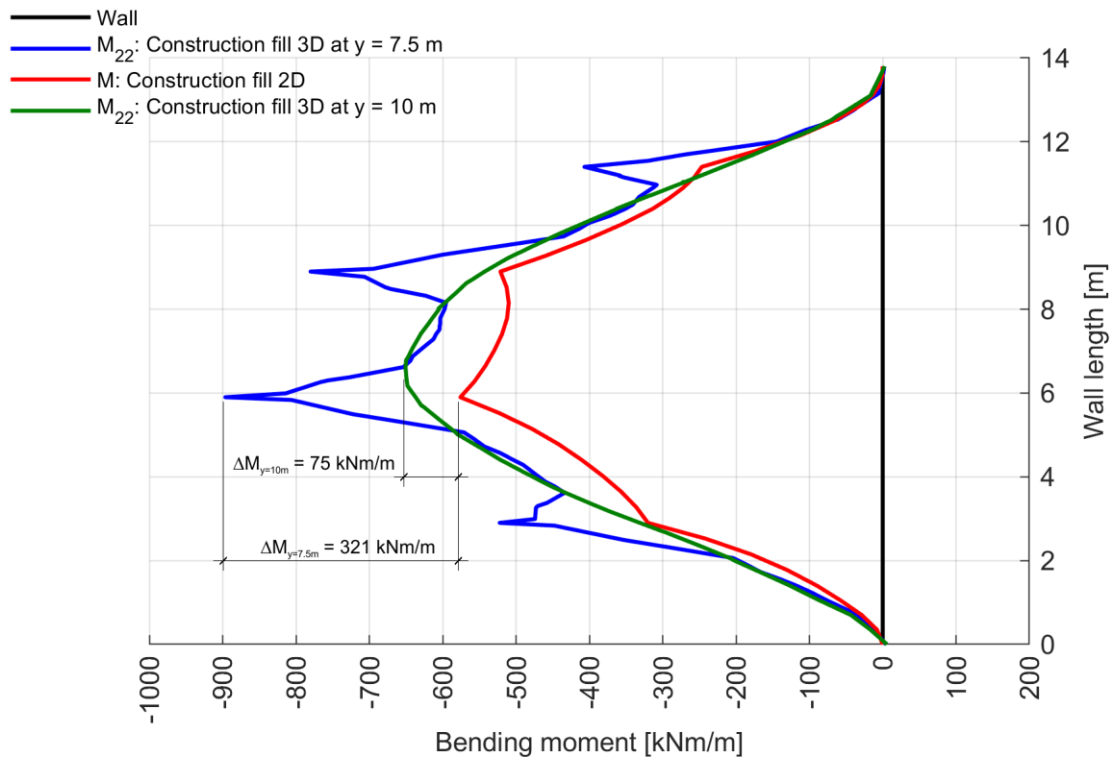


Fig. 139: $BM_s M_{22,actual}$ after Construction fill for $c = 0.1 \text{ kPa}$; EBs with linear skin resistance; 2D vs. 3D at $y = 7.50/10 \text{ m}$

Fig. 140 shows the SF distributions after the calculation phase Construction fill and the three double anchor failure cases. As with the single anchor failure cases shown in Fig. 134, SFs are significantly underestimated by the 2D FEA.

Even higher deviations than for the *FEA* conducted with geogrids can be observed in Fig. 141 – namely, 411 kN/m between minimum values and 422 kN/m between maximum values.

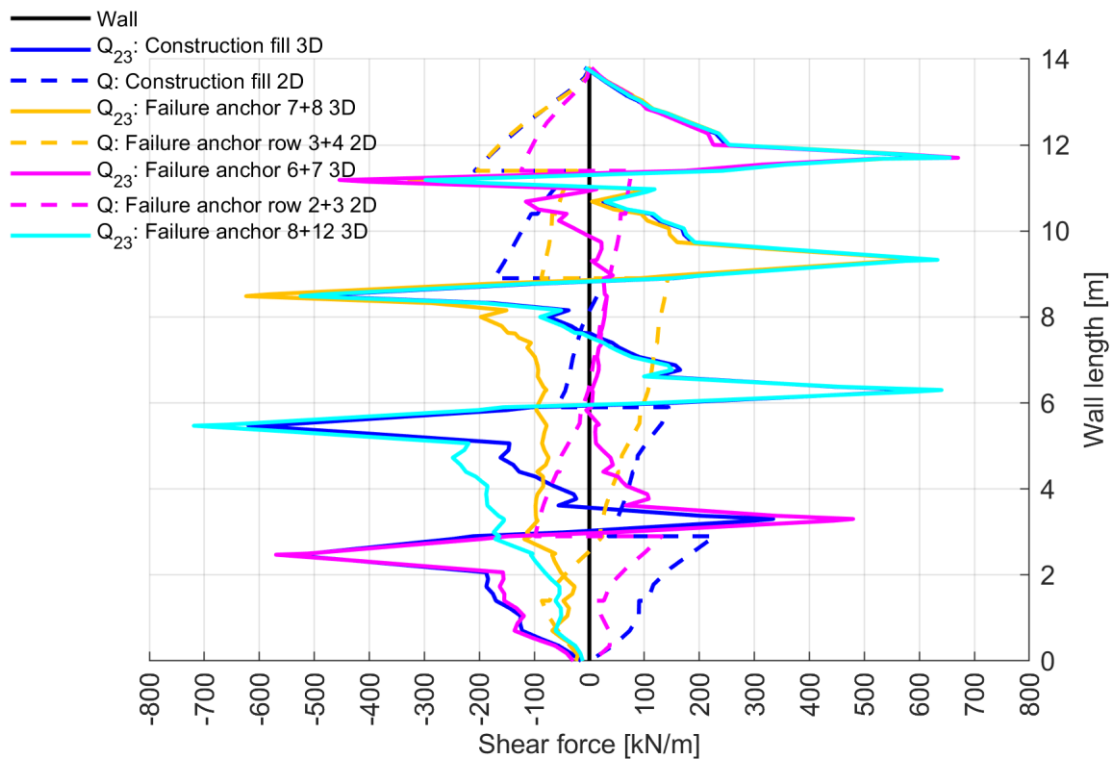


Fig. 140: *SFs* $Q_{23,actual}$ after Construction fill and double anchor failure cases for $c = 0.1$ kPa; *EBs* with linear skin resistance; 2D vs. 3D at $y = 7.50$ m

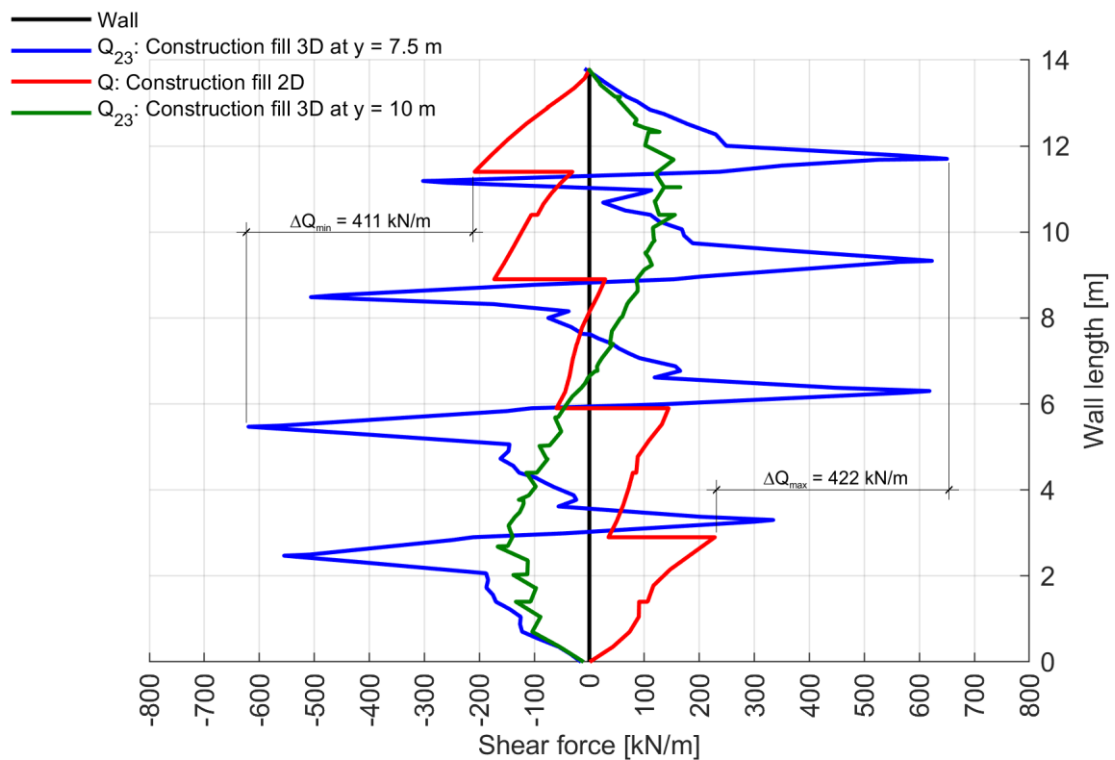


Fig. 141: *SFs* $Q_{23,actual}$ after Construction fill for $c = 0.1$ kPa; *EBs* with linear skin resistance; 2D vs. 3D at $y = 7.50/10$ m

In Fig. 142, again, horizontal displacements u_x , for the 3D *FEA* taken at $y = 7.50$ m, are portrayed. Compared to Fig. 136, where displacements for all failure cases were significantly larger for the 3D *FEA*, horizontal displacements do seem to coincide more accurately with the 2D *FEA* for the *EB* option. Between the five failure cases investigated in 3D, again no significant deviations can be found. Moreover, horizontal displacements depicted at $y = 10$ m do not diverge significantly from those shown in Fig. 142.

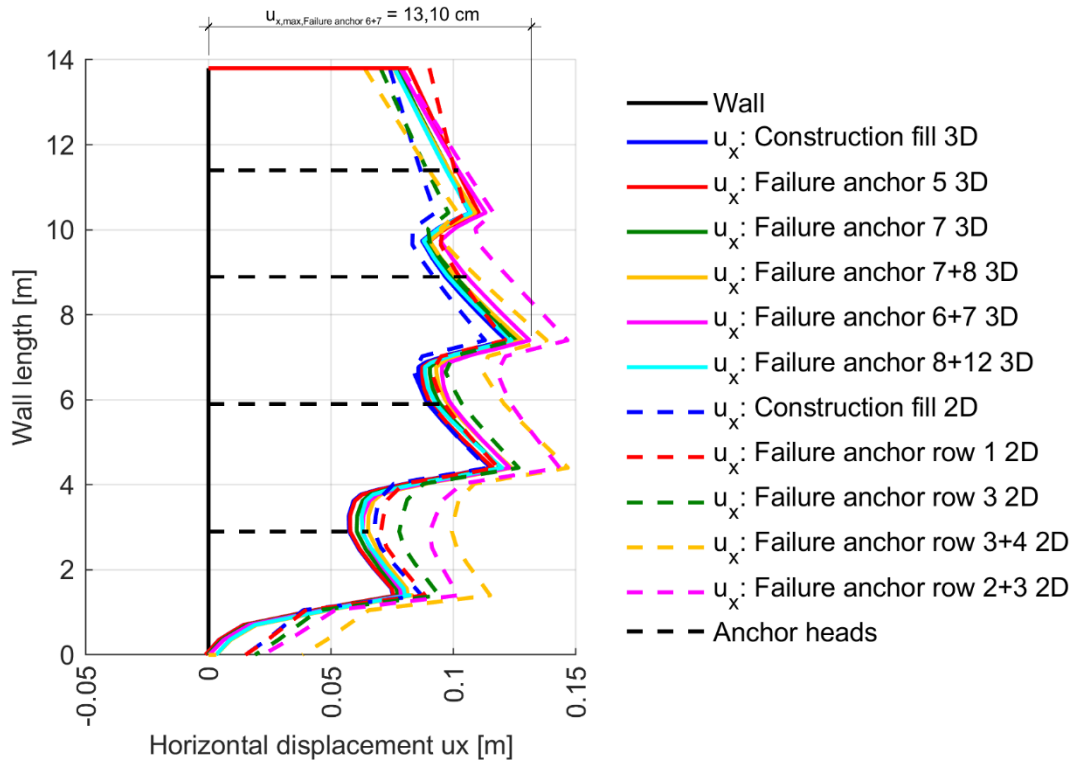


Fig. 142: Horizontal displacements u_x after Construction fill and Failure cases for $c = 0.1$ kPa; *EBs* with linear skin resistance; 2D vs. 3D at $y = 7.50$ m

Total displacements $|u|$ are shown in Fig. 143. While displacements representing the 3D *FEA* seem to be larger at the top of the wall, 2D deflection curves show higher values close to the wall base.

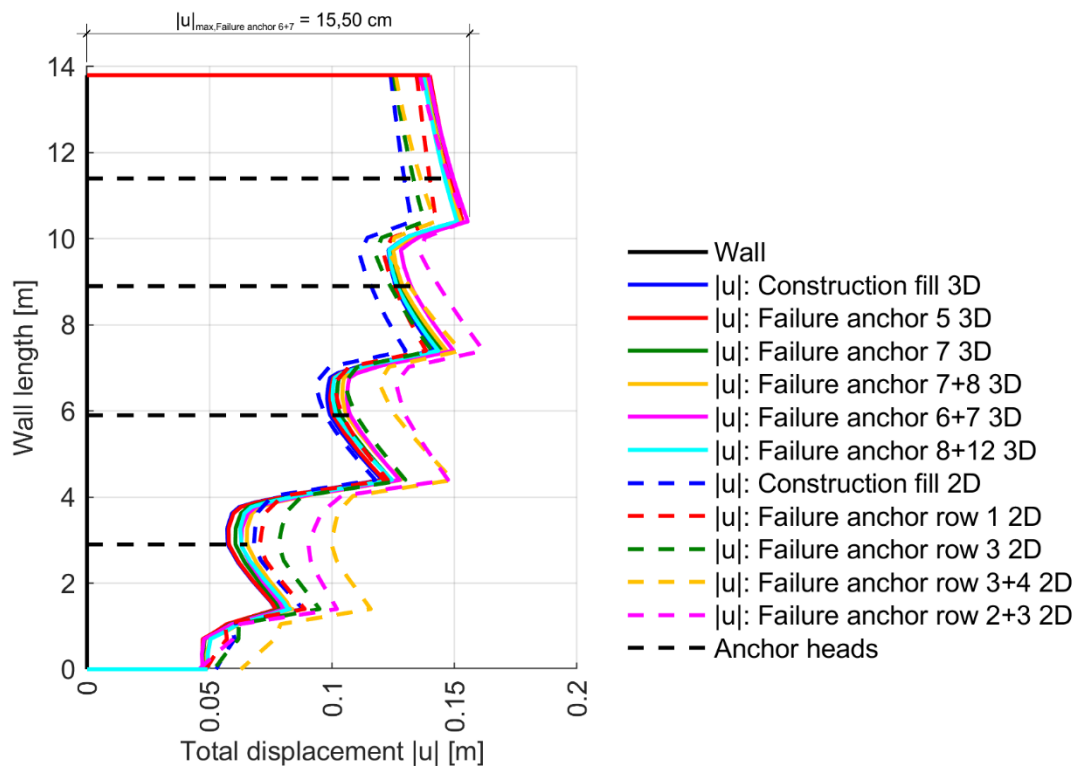


Fig. 143: Total displacements $|u|$ after Construction fill and Failure cases for $c = 0.1$ kPa; EBs with linear skin resistance; 2D vs. 3D at $y = 7.50$ m

Results taken from the *FEA* describing the fixed anchor length by means of *VEs* are given in Fig. 144 to Fig. 151, where, again the *MC* model with a cohesion of 0.1 kPa was utilised. It should be mentioned that an out-of-plane width of only 5 m was used here. Consequently, the failure cases for this model represent row-wise failure. Nevertheless, this model can probably be seen as the most accurate discretisation performed. Its results, whereby a R_{inter} value of 1.00 was applied, are alternately compared to those resulting from the 2D and 3D *FEAs* conducted with *EBs* and constant distribution of skin resistance.

Fig. 144 and Fig. 145 show the *BM* distributions of both double row anchor failure cases compared to the 2D and 3D distributions obtained from the *FEAs* with *EBs* and constant skin resistance. Fig. 144 reveals significant deviations between the 2D and 3D *FEAs* (e.g. 254 kNm/m for Construction fill), although both *FEAs* represent row-wise anchor failure. As it can be seen in Fig. 145, all distributions resulting from the *FEA* conducted with *VEs* are enveloped by the 3D distributions resulting from the *FEA* performed with *EBs*. In other words, the *FEA* computed with *VEs* leads to smaller *BMs*. While Construction fill shows relatively good agreement, Failure anchor row 3+4 and 2+3 diverge at the level of the associated failed elements.

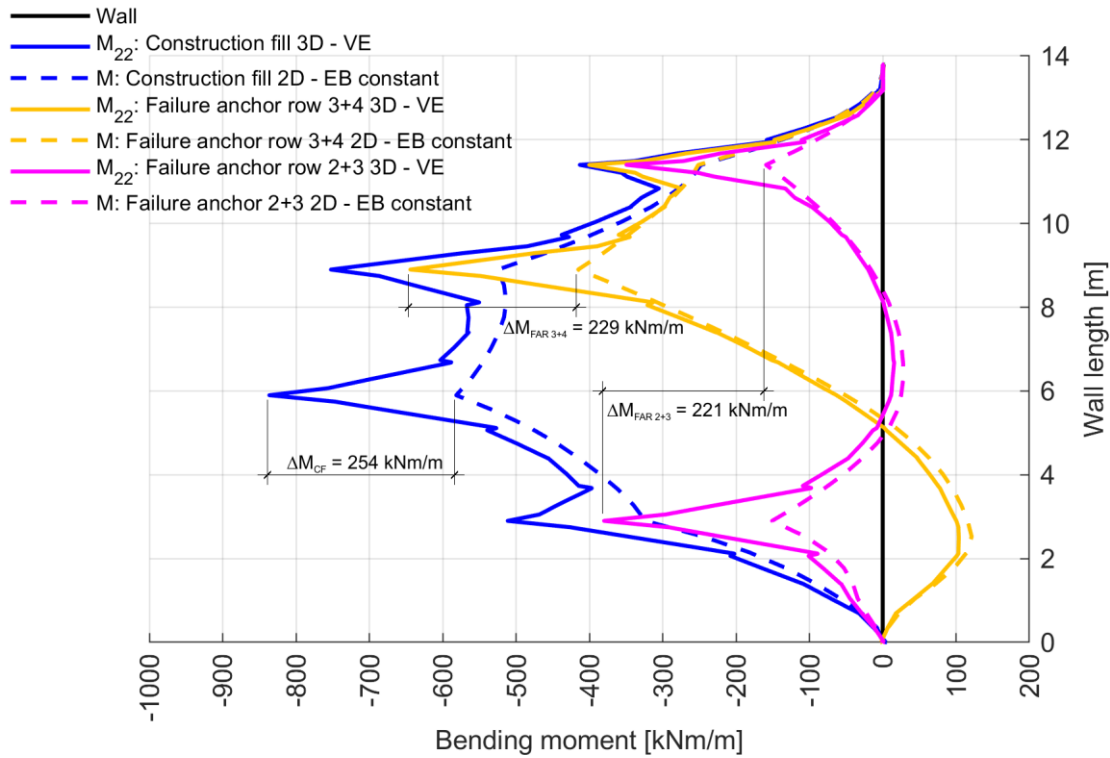


Fig. 144: $BM_s M_{22,actual}$ after Construction fill and single anchor failure cases for $c = 0.1$ kPa; VEs 3D at $y = 2.50$ m vs. EBs with constant skin resistance 2D

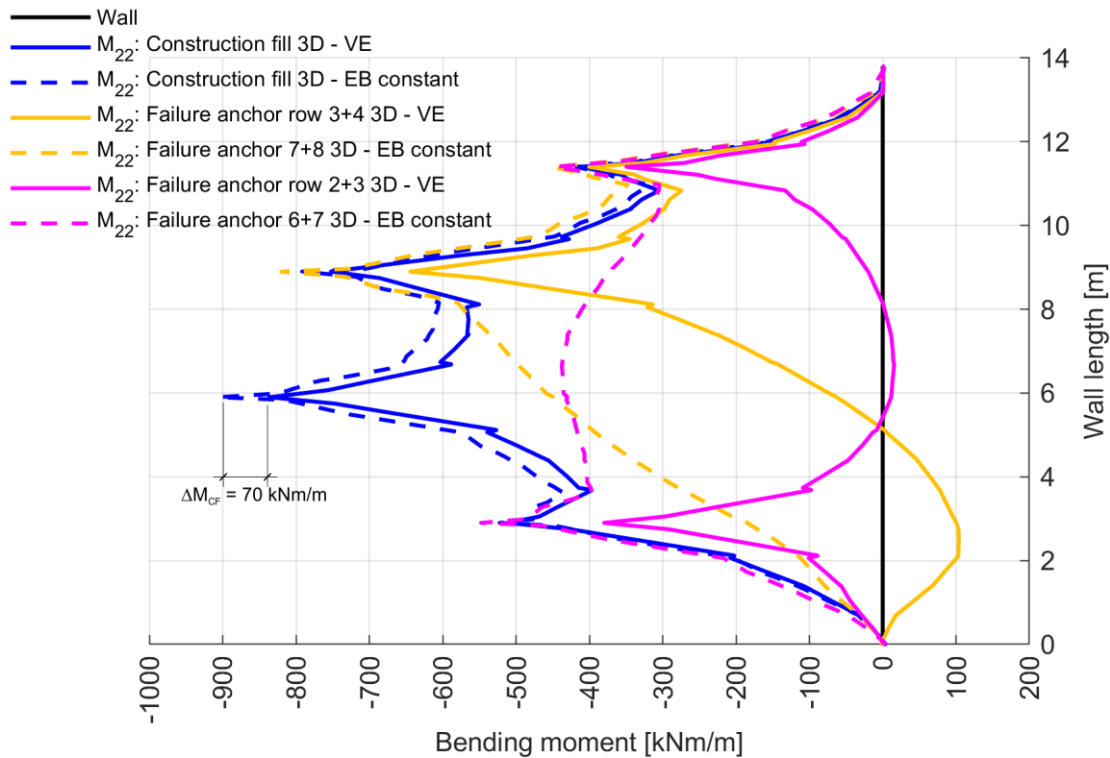


Fig. 145: $BM_s M_{22,actual}$ after Construction fill and double anchor failure cases for $c = 0.1$ kPa; VEs 3D at $y = 2.50$ m vs. EBs with constant skin resistance 3D at $y = 7.50$ m

In Fig. 146, the BM distributions after the phase Construction fill at $y = 2.50$ m and $y = 5$ m are opposed to those at $y = 7.50$ m and $y = 10$ m. As discussed, the distributions representing the VE model are enveloped with deviations of 70 kNm/m between the cross section through anchors and 57 kNm/m among the cross section between two anchor columns.

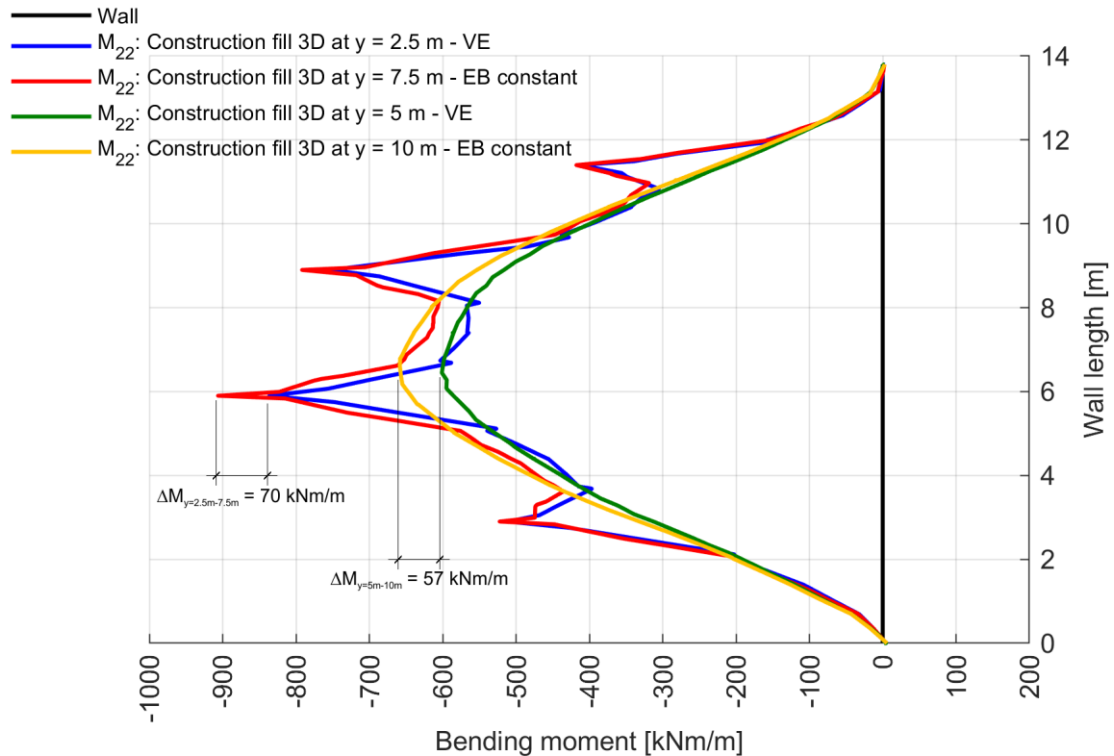


Fig. 146: BM s $M_{22,actual}$ after Construction fill for $c = 0.1$ kPa; VE s 3D at $y = 2.50/5$ m vs. EB s with constant skin resistance 3D at $y = 7.50/10$ m

3D SF distributions are shown in Fig. 147 and Fig. 148. Even though the FEA conducted with VE s represents row-wise anchor failure (whereas the FEA conducted with EB s represents individual anchor failure), SFs seem to be in good agreement with the EB analysis. At the moment this seems not to be logical. In contrast to BM s, SFs appear to yield larger minimum and maximum values for the VE model. Deviations can mainly be found for double row anchor failure cases in Fig. 148 at the location of the failed elements.

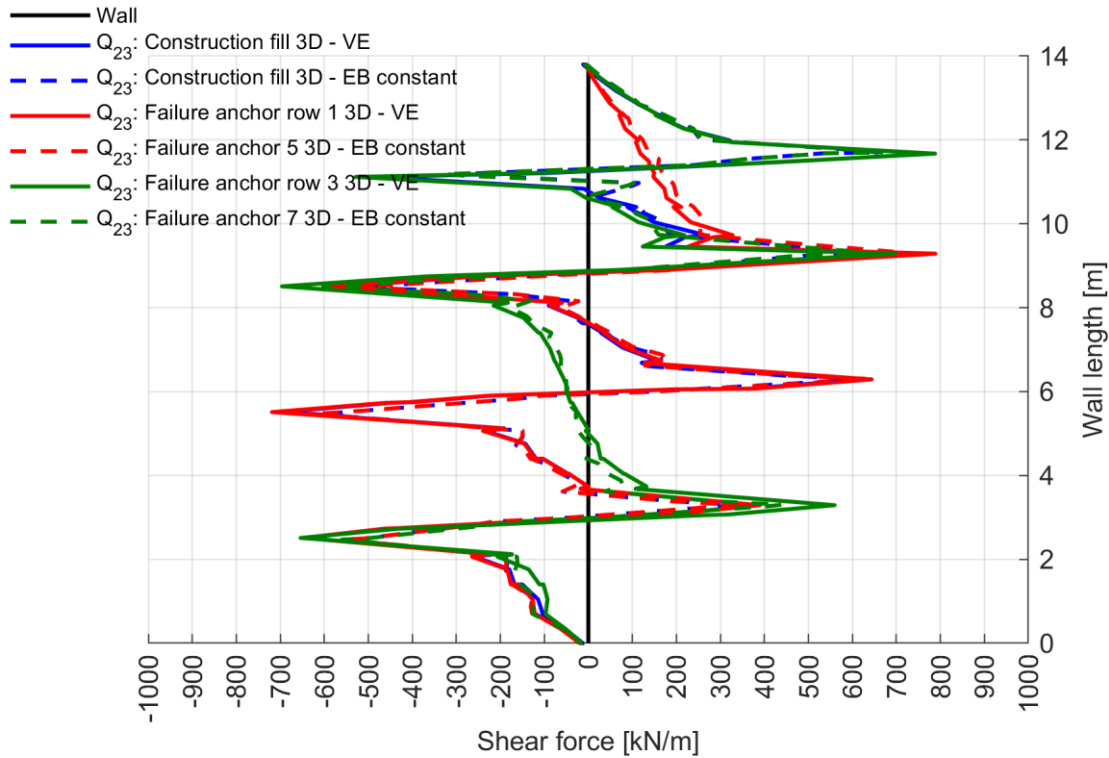


Fig. 147: $SFs Q_{23,actual}$ after Construction fill and single anchor failure cases for $c = 0.1 \text{ kPa}$; VEs 3D at $y = 2.50 \text{ m}$ vs. EBs with constant skin resistance 3D at $y = 7.50 \text{ m}$

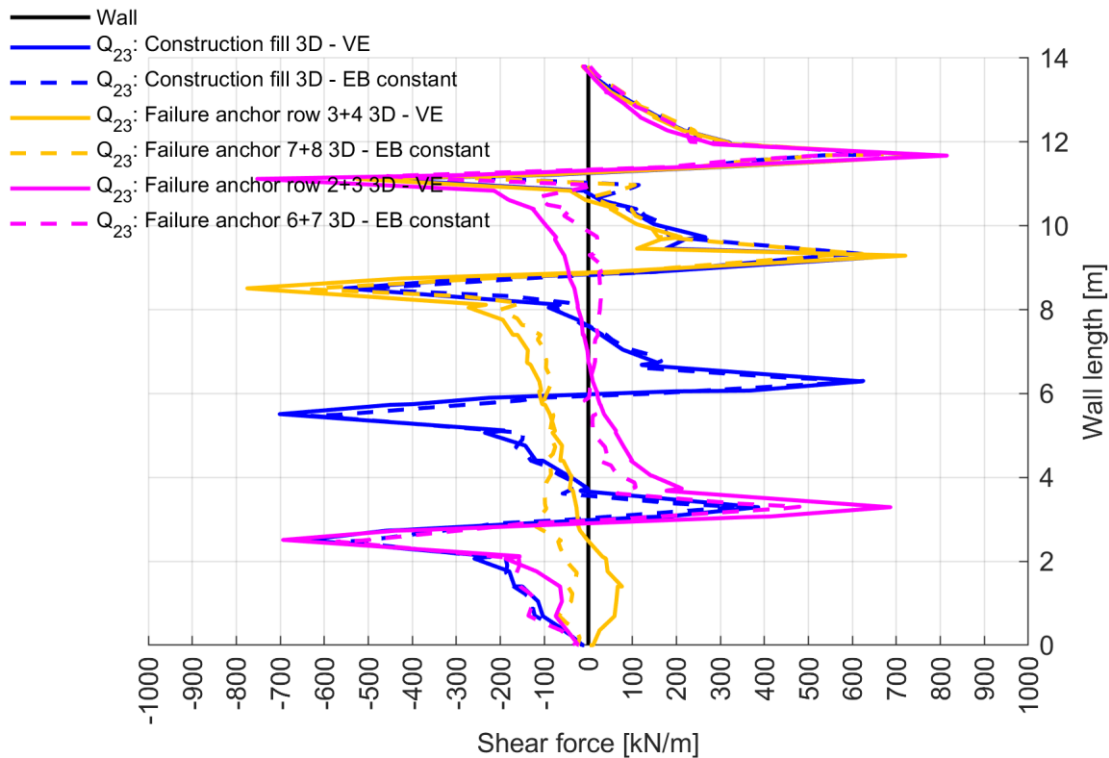


Fig. 148: $SFs Q_{23,actual}$ after Construction fill and double anchor failure cases for $c = 0.1 \text{ kPa}$; VEs 3D at $y = 2.50 \text{ m}$ vs. EBs with constant skin resistance 3D at $y = 7.50 \text{ m}$

Fig. 149 presents divergences in SFs after the phase Construction fill at a magnitude of 72 kNm/m between minimum values and 122 kNm/m between maximum values for the cross section through anchors.

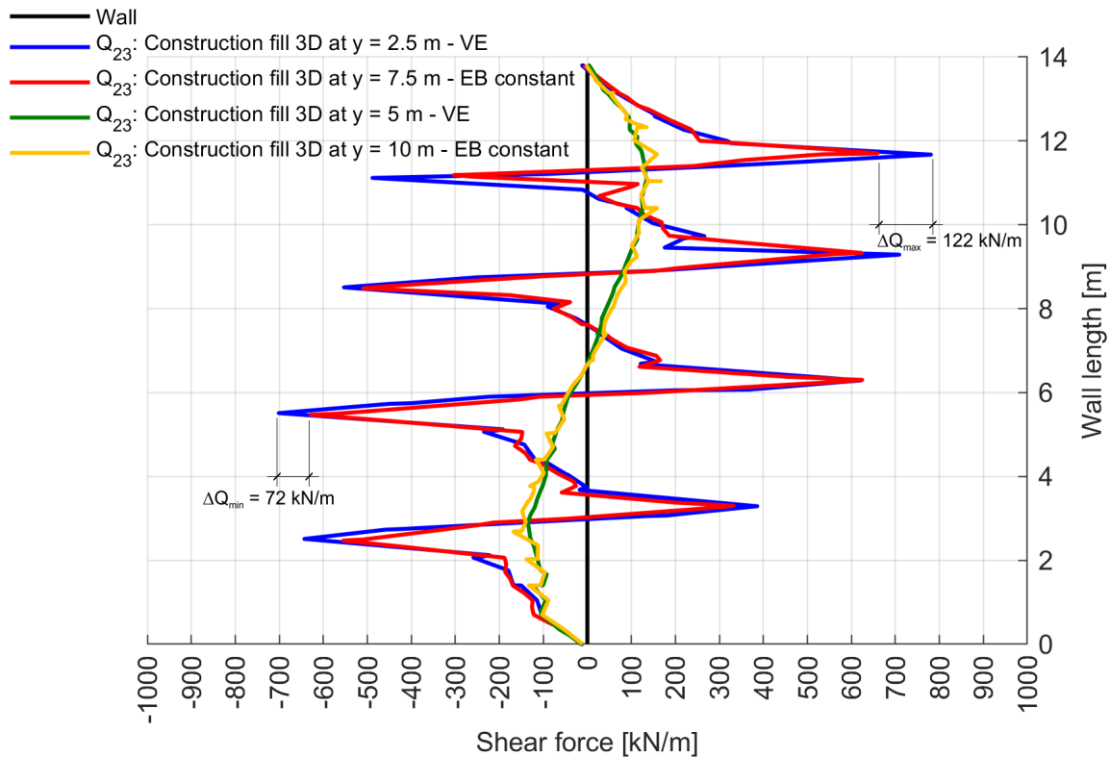


Fig. 149: SFs $Q_{23,actual}$ after Construction fill for $c = 0.1$ kPa; VEs 3D at $y = 2.5/5$ m vs. EBs with constant skin resistance 3D at $y = 7.5/10$ m

Fig. 150 compares the horizontal displacements u_x resulting from the FEA where the fixed anchor length was discretised with VEs to 2D deflection curves. The figure reveals larger horizontal displacements for the VE model. The maximum deviation, with a magnitude of 1.90 cm, occurs for Failure anchor row 2+3.

Almost same results are observable for the total displacements $|u|$, where Fig. 151 exhibits a maximum divergence of 2.00 cm after Failure anchor row 2+3.

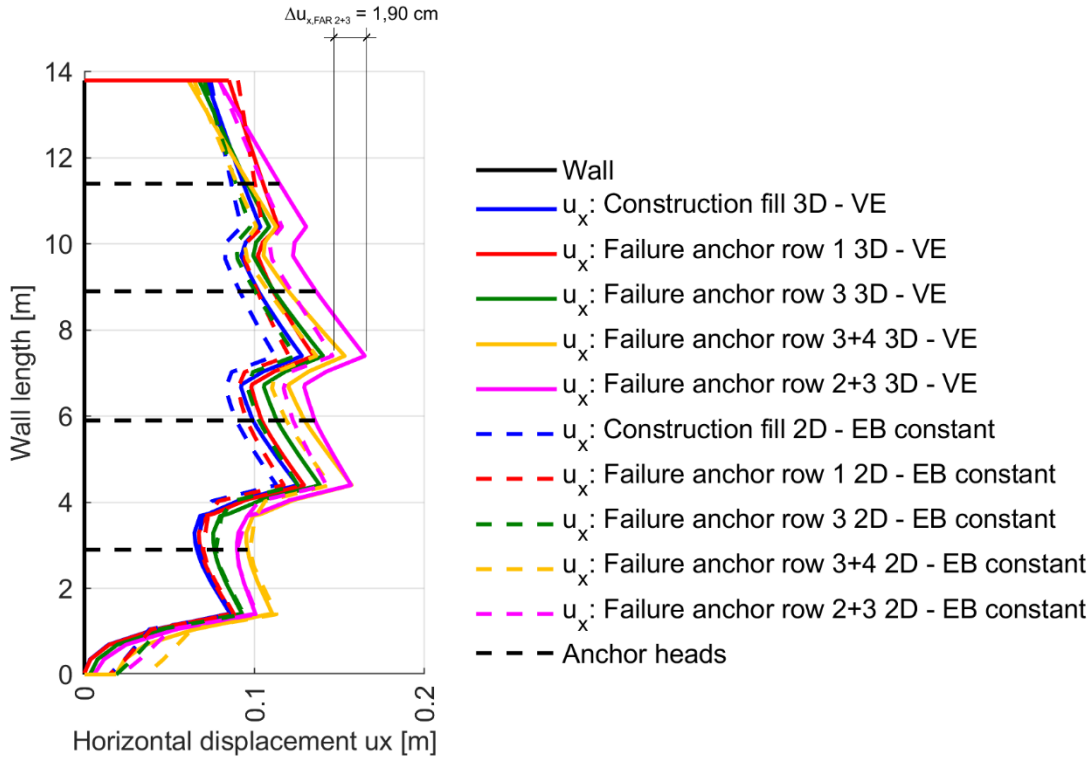


Fig. 150: Horizontal displacements u_x after Construction fill and Failure cases for $c = 0.1$ kPa; VEs 3D at $y = 2.50$ m vs. EBs with constant skin resistance 2D

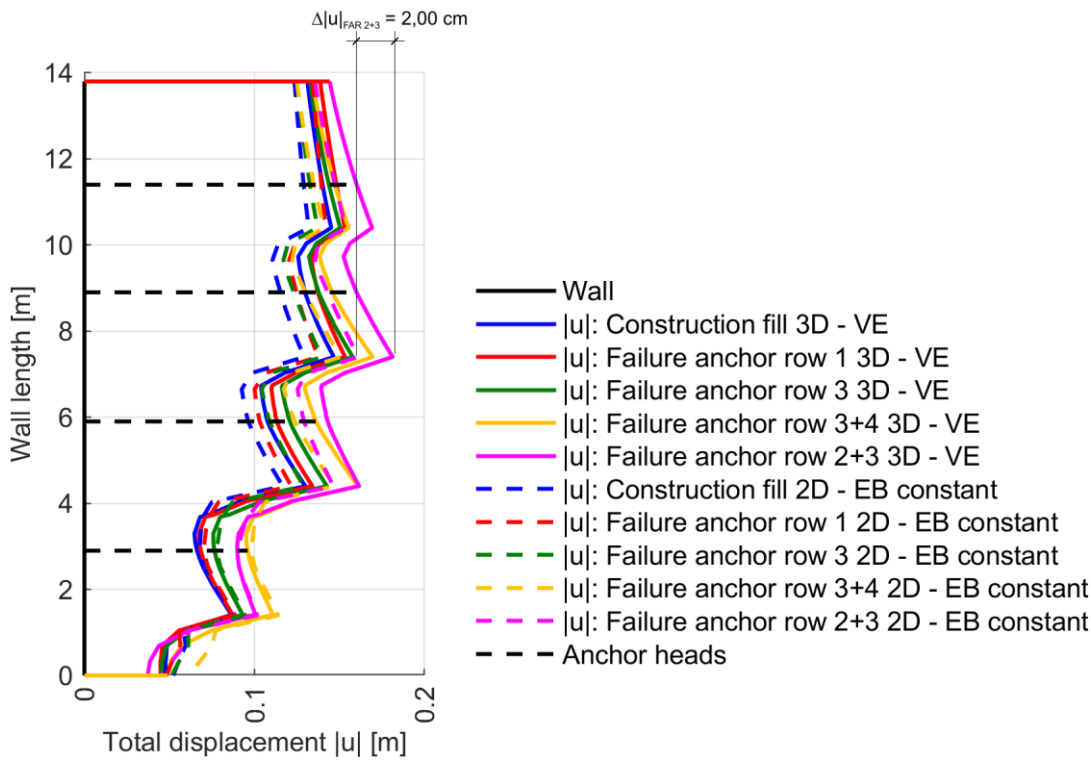


Fig. 151: Total displacements $|u|$ after Construction fill and Failure cases for $c = 0.1$ kPa; VEs 3D at $y = 2.50$ m vs. EBs with constant skin resistance 2D

6 Conclusion

Since the failure of ground anchors is generally associated with complex 3D effects, both 2D and 3D numerical studies were conducted in order to identify whether these effects can be realistically simulated by 2D plane strain analyses. Within the scope of this thesis, internal forces, as well as displacements were evaluated. In some cases, it was found that 2D finite element analyses significantly underestimate these results. Based on these findings, it is concluded that future numerical studies regarding the failure of anchors should follow a 3D approach rather than focusing solely on a 2D representation of the boundary value problem.

The results showed that a significant reduction in the safety factor could be determined for row-wise ground anchor failure near the wall base. Since this area is increasingly exposed to the impact of de-icing agents, special emphasis during design and execution should be placed on these anchors. Individual ground anchor failure, in contrast, did not indicate significant differences between safety factors before and after the failure of the considered anchors.

Internal forces within the concrete components (i.e. within the retaining wall) were found to be negatively affected primarily by failure close to the wall base and failure at the top of the retaining structure. While bending moments revealed adverse responses especially for failure near the top of the retaining structure, shear forces are unfavourably afflicted by failure close to the wall base and failure near the top. Unsatisfactory agreement of internal forces was obtained from the comparison of 2D and 3D analyses, where, as stated, 2D evaluations underestimate the 3D results (i.e. bending moments, shear forces and displacements).

Concerning horizontal as well as total displacements, the deflections for double row anchor failure appeared to be larger than the displacement increment for single row anchor failure. Also, with respect to displacements (depending on the modelling approach of the fixed anchor length), the comparison between the 2D and 3D analyses showed significant differences.

The investigations related to the force redistributions as a consequence of anchor failure provide evidence that especially anchors close to the failed tension members experience an increase in the anchor force. For failed elements situated in the centre, the force increment in the anchor below was (slightly) larger than the force increment in the anchor above the failed element. It has to be mentioned that the anchor tendons were modelled as elastic node-to-node anchors; therefore, failure of those elements as a result of force redistributions was excluded in the finite element analyses. Moreover, investigations regarding the redistribution of anchor forces should be pursued based on 3D finite element analyses since 2D plane strain analyses are not capable of simulating horizontal rearrangements.

No significant differences between the constant and linear distribution of the skin resistance when using embedded beams could be identified. Nevertheless, deviations between both skin resistance options were more pronounced when using the Hardening soil small model than for the Mohr-Coulomb model.

Besides ground anchor failure, the work comprises studies of different model dimensions and studies related to the effect of a varying cohesion. These studies show that appropriate modelling of the geometry and carefully chosen parameters are basic requirements for successful numerical analyses.

7 Bibliography

3G Gruppe Geotechnik Graz ZT GmbH (2017), *Geotechnisches Gutachten zur Baugrunderkundung*, Graz.

Adam, D., Breit, K., Stadler, J., Kohlböck, D. and Kainrath, A. (2017), 'Analyse des Tragverhaltens vorgespannter Anker unter Verwendung eines gekoppelten Federmodells', *Bauingenieur*, No. 92, pp. 165–173.

Adam, D. and Waibel, P.C. (2012), 'Böschungen und konstruktive Hangsicherungen, Baugruben', in Boley, C. (Ed.), *Handbuch Geotechnik: Grundlagen - Anwendungen - Praxiserfahrungen, Praxis*, Vieweg + Teubner, Wiesbaden, pp. 623–779.

ANP - Systems GmbH (2018), *Zulassung: ANP Litzenanker*, Wien, available at: https://www.anp-systems.at/fileadmin/user_upload/BMVIT-327120_0008_18_-_Litzenanker.pdf (accessed 25 March 2020).

Austrian Standards Institute (2009), *Eurocode 7: Entwurf, Berechnung und Bemessung in der Geotechnik: Teil 1: Allgemeine Regeln* No. ÖNORM EN 1997-1, Wien.

Austrian Standards Institute (2010), *Ausführungen von Arbeiten im Spezialtiefbau - Bodenvernagelungen* No. ÖNORM EN 14490, Wien.

Austrian Standards Institute (2013), *Eurocode 7: Entwurf, Berechnung und Bemessung in der Geotechnik: Teil 1: Allgemeine Regeln - Nationale Festlegungen zu ÖNORM EN 1997-1 und nationale Ergänzungen* No. ÖNORM B 1997-1-1, Wien.

Austrian Standards Institute (2014), *Eurocode 7: Entwurf, Berechnung und Bemessung in der Geotechnik: Teil 1: Allgemeine Regeln* No. ÖNORM EN 1997-1, Wien.

Austrian Standards Institute (2015a), *Ausführungen von Arbeiten im Spezialtiefbau - Verdrängungspfähle* No. ÖNORM EN 12699, Wien.

Austrian Standards Institute (2015b), *Ausführungen von Arbeiten im Spezialtiefbau - Verpressanker* No. ÖNORM EN 1537, Wien.

Austrian Standards Institute (2015c), *Korrosion von Metallen und Legierungen - Grundbegriffe* No. ÖNORM EN ISO 8044, Wien.

Austrian Standards Institute (2016), *Ausführungen von Arbeiten im Spezialtiefbau - Mikropfähle* No. ÖNORM EN 14199, Wien.

- Austrian Standards Institute (2019), *Geotechnische Erkundung und Untersuchung - Prüfung von geotechnischen Bauwerken und Bauwerksteilen: Teil 5: Prüfung von Verpressankern* No. ÖNORM EN ISO 22477-5, Wien.
- BAUER Spezialtiefbau GmbH (2013), 'Der BAUER Anker', available at: https://www.bauer.de/export/shared/documents/pdf/bst/print/905_025_1_Anker.pdf (accessed 8 October 2019).
- Benz, T. (2007), 'Small-Strain Stiffness of Soils and its Numerical Consequences', Dissertation, Institut für Geotechnik, Universität Stuttgart, Stuttgart, 2007.
- Brady, K.C., McMahan, W. and Turner, M.J. (1997), 'Limit State Design in Ground Anchorage Practice', in Littlejohn, G.S. (Ed.), *Ground anchorages and anchored structures: Proceedings of the international conference organized by the Institution of Civil Engineers and held in London, UK, on 20-21 March 1997*, Thomas Telford, London, pp. 76–88.
- Brinkgreve, R.B.J., Kumarswamy, S. and Swolfs (2018a), *PLAXIS 3D 2018: Reference Manual*, Delft, Netherlands.
- Brinkgreve, R.B.J., Kumarswamy, S., Swolfs, W.M. and Foria, F. (2018b), *PLAXIS 2D 2018: Reference Manual*, Delft, Netherlands.
- British Standards Institution (1994), *Code of practice for earth retaining structures* No. BS 8002:1994, London.
- Burtscher, S.L., Rebhan, M.J., Marte, R. and Scharinger, F. (2017), 'Neue Methoden zur Korrosionsdetektion an Litzen- und Stabankersystemen', in Dietzel, M., Kieffer, S., Marte, R., Schubert, W. and Schweiger, H.F. (Eds.), *Beiträge zum 32. Christian Veder Kolloquium: Zuelemente in der Geotechnik - Anker | Nägel | Zugpfähle*, Graz, Technische Universität Graz, Graz, pp. 71–86.
- Dausch, G. and Zimbelmann, J. (2012), 'Geotechnische Bauverfahren', in Boley, C. (Ed.), *Handbuch Geotechnik: Grundlagen - Anwendungen - Praxiserfahrungen, Praxis*, Vieweg + Teubner, Wiesbaden, pp. 397–468.
- Deutsche Gesellschaft für Geotechnik e.V. (2012), *Empfehlungen des Arbeitskreises „Baugruben“ EAB*, 5., ergänzte und erweiterte Auflage, 2. korrigierter Nachdruck, Ernst & Sohn, Berlin.
- DSI Underground Austria GmbH (2019), *Zulassung: Nachspannbarer Dywidag-Litzenanker mit 2-15 Litzen*, Wien, available at: <https://www.dsiunderground.at/fileadmin/downloads/dsi-underground.at/dsi-bmvit-de-02.pdf> (accessed 25 March 2020).

- DSI Underground GmbH (2019a), available at:
<https://www.dsiunderground.at/produkte/geotechnische-systeme/ankersysteme/dywidag-litzenanker> (accessed 6 October 2019).
- DSI Underground GmbH (2019b), available at:
<https://www.dsiunderground.at/produkte/geotechnische-systeme/ankersysteme/dywidag-stabanker> (accessed 6 October 2019).
- DSI Underground GmbH (2019c), ‘Geotechnische Systeme’, available at:
<https://www.dsiunderground.at/fileadmin/downloads/dsi-underground.at/dsi-alwag-systems-geotechnical-product-range-de.pdf> (accessed 7 October 2019).
- Ducksch, A. and Ammann, M. (2018), ‘Wie aus einer Kiesgrube eine Baugrube wird - Coop Schafisheim, Kanton Aargau (CH)’, in Dietzel, M., Kieffer, S., Marte, R., Schubert, W. and Schweiger, H.F. (Eds.), *Beiträge zum 33. Christian Veder Kolloquium: Tiefe Baugruben und Schächte im Boden, Graz*, Technische Universität Graz, Graz, pp. 245–260.
- Ebeling, R.M., White, B.C., Evans, J.A., Haskins, R.W. and Miller, E.L. (2016), *Corrosion Induced Loss of Capacity of Post-Tensioned Seven Wire Strand Cable Used in Multistrand Anchor Systems Installed at Corps Projects*, Vicksburg, available at: <https://erdc-library.erdc.dren.mil/jspui/handle/11681/21664> (accessed 9 March 2020).
- Fédération Internationale de la Précontrainte (FIP) (1986), *Corrosion and corrosion protection of prestressed ground anchorages, FIP state of the art report*, Thomas Telford, London.
- Hanel, J. and Prehn, W. (2006), ‘Beurteilung der Standsicherheit und Gebrauchstauglichkeit von dauerhaft rückverankerten Bauwerken’, *Bautechnik*, No. 83, pp. 688–694.
- Haskins, R.W., White, B.C., Ebeling, R.M. and Evans, J.A. (2016), ‘Relating Corroded Seven-Strand, Posttensioned Cable Cross-Sectional Properties to Load Capacity’, *Journal of Engineering*, Vol. 2016.
- Hechendorfer, S. and Haag, N. (2018), ‘Komplexe Schitzwandelemente - Herstellung der Baugrube für den Neubau des GLC an der ETH Zürich’, in Dietzel, M., Kieffer, S., Marte, R., Schubert, W. and Schweiger, H.F. (Eds.), *Beiträge zum 33. Christian Veder Kolloquium: Tiefe Baugruben und Schächte im Boden, Graz*, Technische Universität Graz, Graz, pp. 133–147.
- Jarred, D.J. and Haberfield, C.M. (1997), ‘Tendon/Grout Interface Performance in Grouted Anchors’, in Littlejohn, G.S. (Ed.), *Ground anchorages and anchored structures: Proceedings of the international conference organized*

by the Institution of Civil Engineers and held in London, UK, on 20-21 March 1997, Thomas Telford, London, pp. 3–12.

Katzenbach, R. and Bergmann, C. (2018), ‘Schächte als Elemente einer großräumigen Hangsicherung’, in Dietzel, M., Kieffer, S., Marte, R., Schubert, W. and Schweiger, H.F. (Eds.), *Beiträge zum 33. Christian Veder Kolloquium: Tiefe Baugruben und Schächte im Boden*, Graz, Technische Universität Graz, Graz, pp. 33–47.

Kolymbas, D. (2019), *Geotechnik: Bodenmechanik, Grundbau und Tunnelbau*, 5. Aufl. 2019, Springer Vieweg, Berlin, Heidelberg.

Kranz, E. (1953), *Über die Verankerung von Spundwänden*, 2nd ed., Ernst & Sohn, Berlin.

Markl, N. and Bahr, G. (2018), ‘Eine tiefe Baugrube unter besonderen Randbedingungen in der Salzburger Innenstadt zwischen West- und Stadtbahn - Bauvorhaben Perron’, in Dietzel, M., Kieffer, S., Marte, R., Schubert, W. and Schweiger, H.F. (Eds.), *Beiträge zum 33. Christian Veder Kolloquium: Tiefe Baugruben und Schächte im Boden*, Graz, Technische Universität Graz, Graz, pp. 103–118.

Marte, R. (2018), *Anchorage: Grouted anchors, Injection piles, Soil nails*, Acc. to ÖNORM EN 1997-1-1:2013, *Advanced Soil Mechanics and Foundation Engineering*.

Möller, G. (2016), *Geotechnik: Grundbau*, Ernst & Sohn, Berlin.

Nürnberger, U. (1995), *Korrosion und Korrosionsschutz im Bauwesen: Band 1*, Bauverlag GmbH, Wiesbaden und Berlin.

Oberhollenzer, S. (2017), ‘Numerical studies on slope stability analysis’, Masterarbeit, Institut für Bodenmechanik und Grundbau, Technische Universität Graz, Graz, 2017.

Ostermayer, H. (1982), ‘Verpreßanker’, in Smolczyk, U. (Ed.), *Grundbau Taschenbuch*, Teil 2, 3rd ed., Ernst & Sohn, Berlin, pp. 287–322.

Ostermayer, H. (1993), ‘35 Jahre Verpreßanker im Boden’, in Englert, K. and Stocker, M. (Eds.), *40 Jahre Spezialtiefbau 1953 - 1993: Technische und rechtliche Entwicklungen: Festschrift für Karlheinz Bauer zum 65. Geburtstag*, Werner-Verlag, Düsseldorf, pp. 65–95.

Ostermayer, H., Barley and Tony (2003), ‘Ground anchors’, in Smolczyk, U. (Ed.), *Geotechnical Engineering Handbook: Volume 2: Procedures*, Ernst & Sohn, Berlin, pp. 169–220.

- Pong, K.F., Foo, S.L., Chinnaswamy, C.G., Ng, C.C.D. and Chow, W.L. (2012), 'Design considerations for one-strut failure according to TR26 - a practical approach for practising engineers', *The IES Journal Part A: Civil & Structural Engineering*, Vol. 5 No. 3, pp. 166–180.
- Sabatini, P.J., Pass, D.G. and Bachus, R.C. (1999), *Geotechnical Engineering Circular No. 4: Ground anchors and anchored systems*, Washington DC.
- Scheele, F. (1982), 'Tragfähigkeit von Verpreßankern in nichtbindem Boden', Lehrstuhl und Prüfamnt für Grundbau, Bodenmechanik und Felsmechanik, Universität München, München, 1982.
- Schmidt, H.-H., Buchmaier, R.F. and Vogt-Breyer, C. (2017), *Grundlagen der Geotechnik: Geotechnik nach Eurocode*, 5. Aufl. 2017, Springer Fachmedien Wiesbaden; Imprint; Springer Vieweg, Wiesbaden.
- Spring Singapore (2010), *Technical reference for deep excavation*, Vol. 93.020 No. TR 26:2010, Spring Singapore, Singapore.
- Verein Deutscher Ingenieure (2003), *Systematische Berechnung hochbeanspruchter Schraubenverbindungen: Zylindrische Einschraubenverbindungen*, Vol. 21.060.10 No. VDI 2230 Blatt 1, Beuth, Düsseldorf.
- Warren, T.W., White, B.C. and Ebeling, R.M. (2017), *Corroded Anchor Structure Stability/Reliability (CAS_Stab-R) Software for Hydraulic Structures*, Vicksburg, available at: <https://erdc-library.erdc.dren.mil/jspui/handle/11681/26273> (accessed 9 March 2020).
- Wichter, L. and Meiniger, W. (2000), *Verankerungen und Vernagelungen im Grundbau, Bauingenieur-Praxis*, Ernst & Sohn, Berlin.
- Wichter, L. and Meiniger, W. (2018), 'Verpressanker, Bodennägel und Zugpfähle', in Witt, K.J. (Ed.), *Grundbau Taschenbuch*, Teil 2: Geotechnische Verfahren, 8th ed., Ernst & Sohn, Berlin, pp. 375–468.
- Xanthakos, P.P. (1991), *Ground anchors and anchored structures*, J. Wiley, New York.
- Zhang, W., Zhang, R., Fu, Y., Goh, A.T.C. and Zhang, F. (2018), '2D and 3D numerical analysis on strut responses due to one-strut failure', *Geomechanics and Engineering*, Vol. 15 No. 4, pp. 965–972.
- Zhao, W., Han, J.-Y., Chen, Y., Jia, P.-J., Li, S.-G., Li, Y. and Zhao, Z. (2018), 'A numerical study on the influence of anchorage failure for a deep excavation retained by anchored pile walls', *Advances in Mechanical Engineering*, 10(2), pp. 1–17.

8 Appendix

8.1 $MC_{R_{inter}=0.9}$ _Geogrid_AncorPre-stressed in 2D

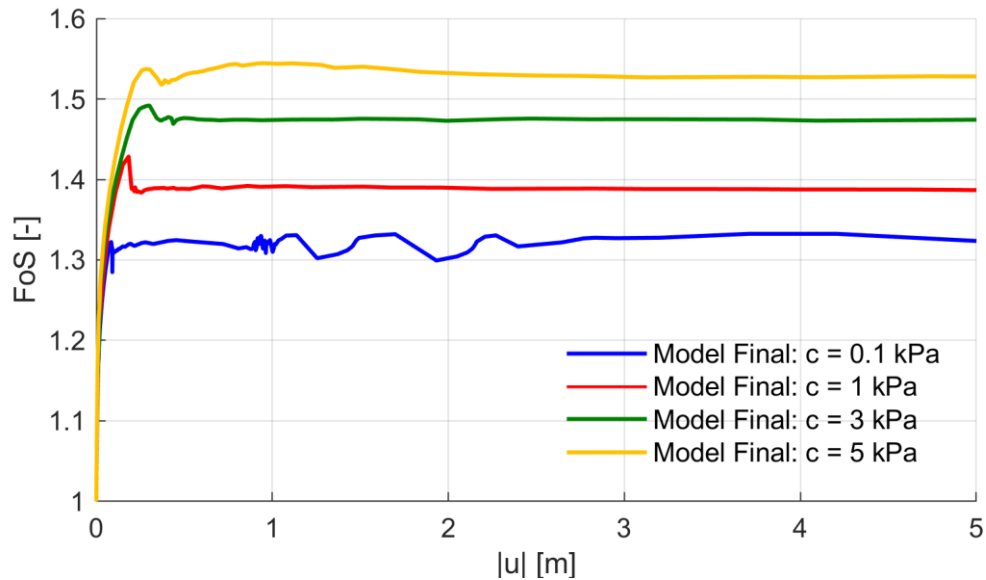


Fig. 152: FoS after ϕ - c reduction Pre-stressing anchor 1

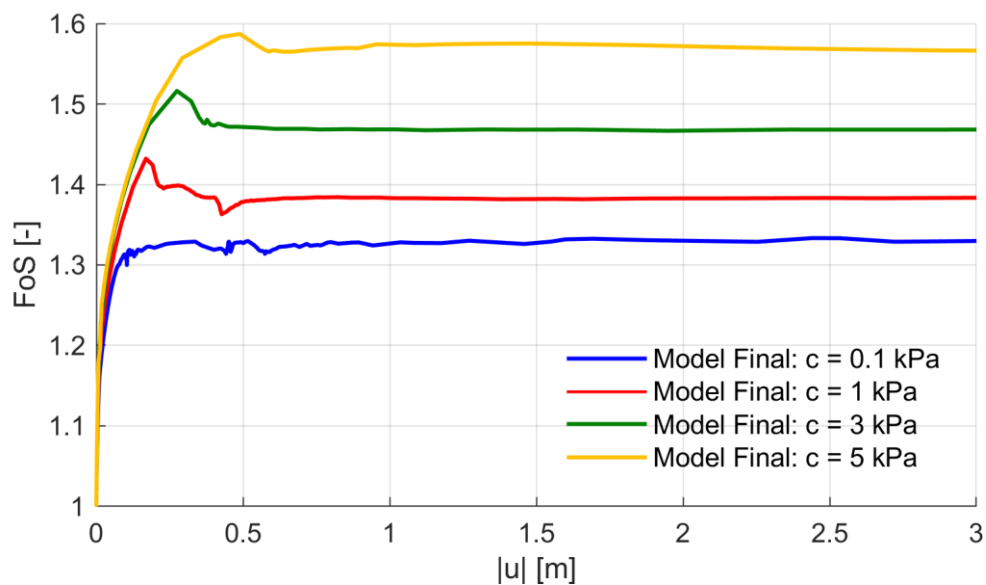
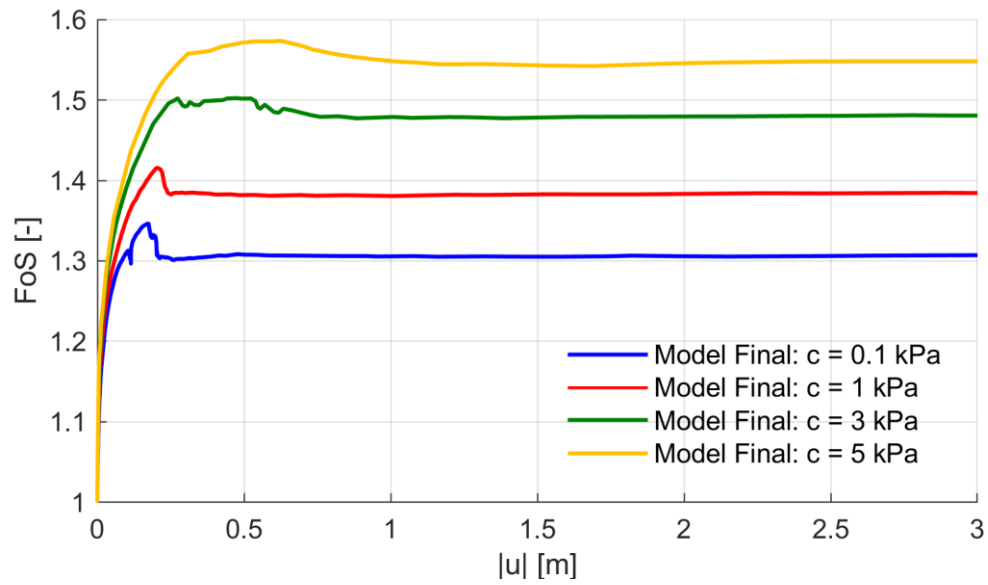
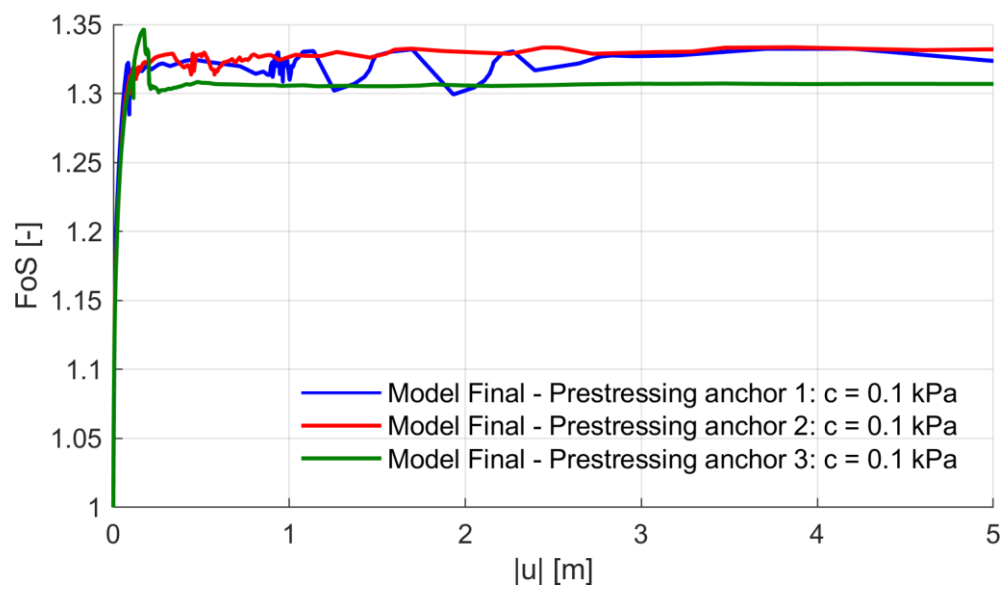


Fig. 153: FoS after ϕ - c reduction Pre-stressing anchor 2

Fig. 154: FoS after ϕ - c reduction Pre-stressing anchor 3Fig. 155: FoS after ϕ - c reduction Pre-stressing anchor 1, 2 and 3 for $c = 0.1$ kPa

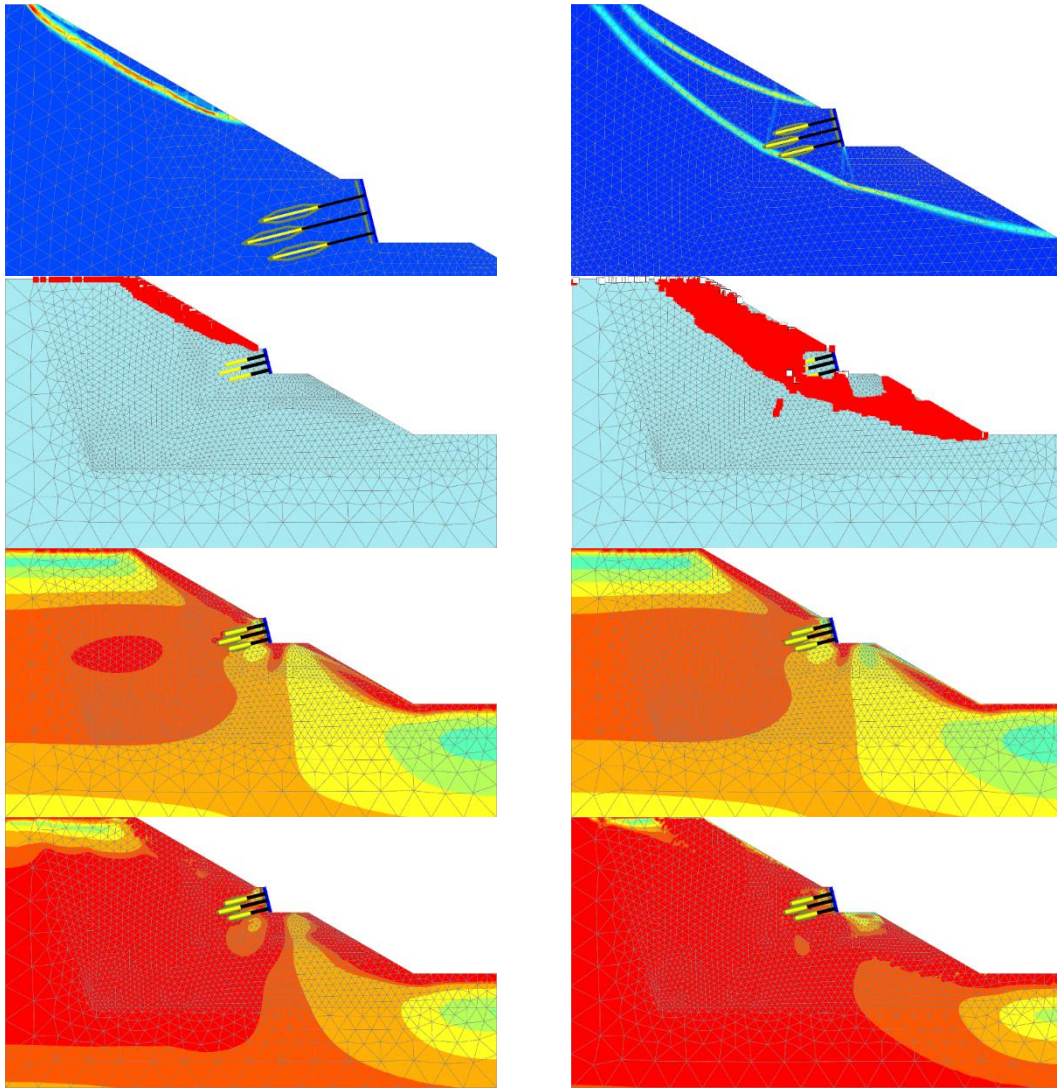


Fig. 156: Incremental deviatoric strains and plastic points after as well as τ_{rel} before/after ϕ - c reduction Pre-stressing anchor 3; left: $c = 0.1$ kPa; right: $c = 5$ kPa

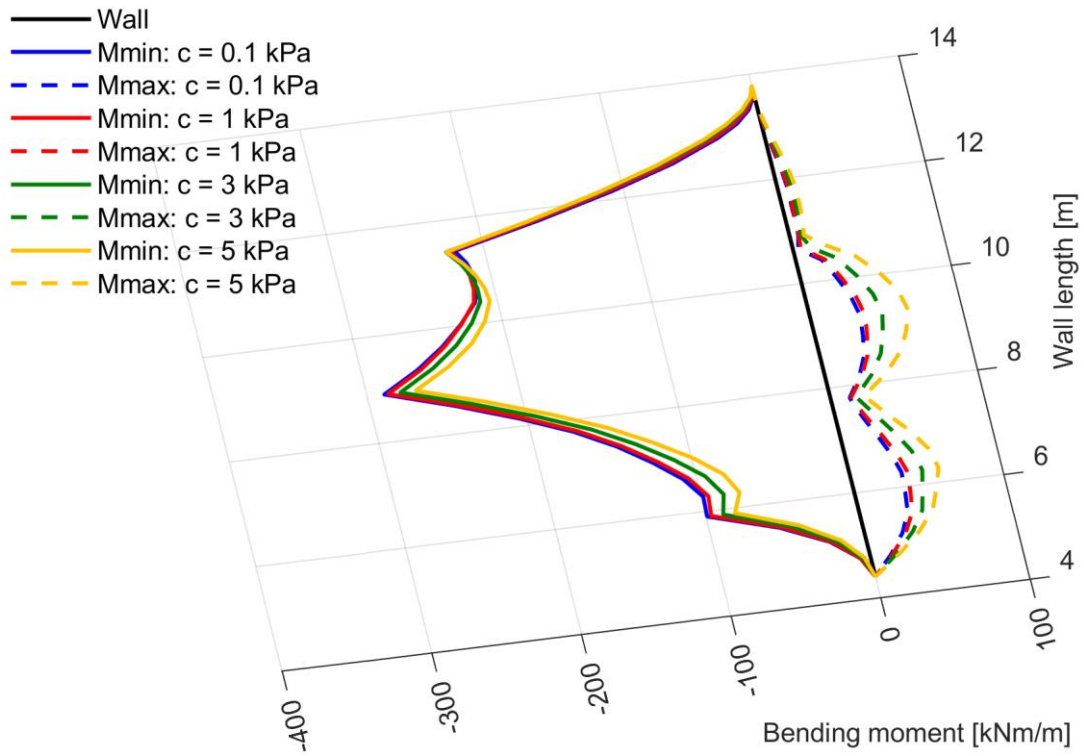


Fig. 157: $BM_s M_{min}/M_{max}$ after Pre-stressing anchor 3

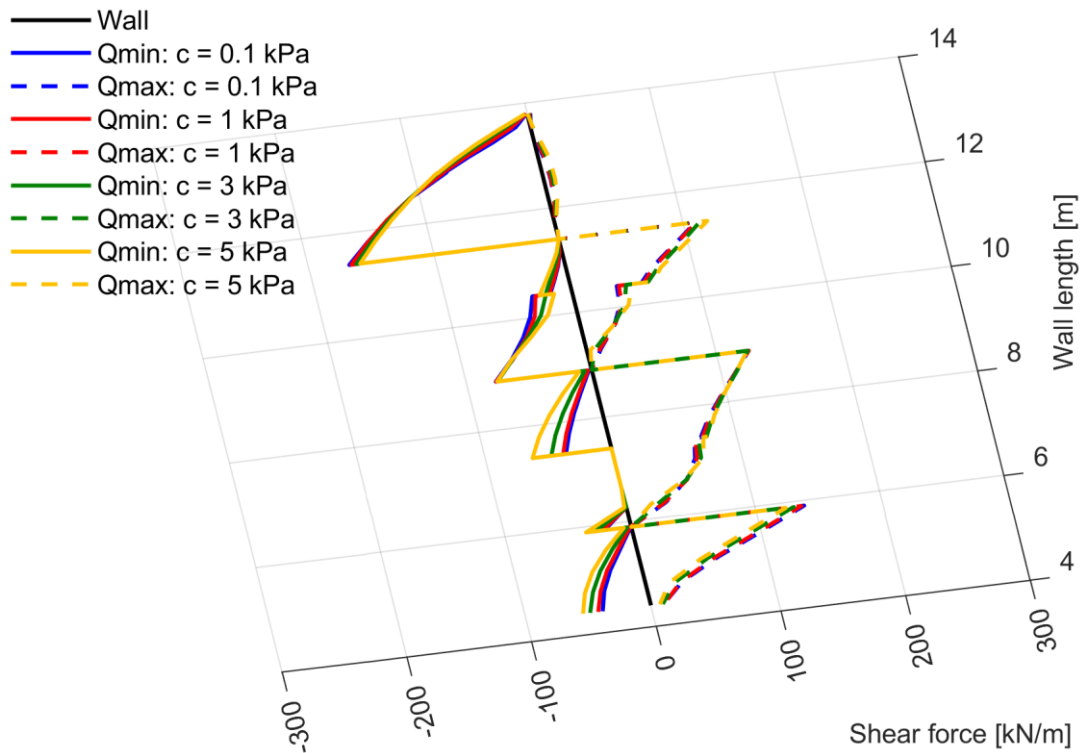


Fig. 158: $SF_s Q_{min}/Q_{max}$ after Pre-stressing anchor 3

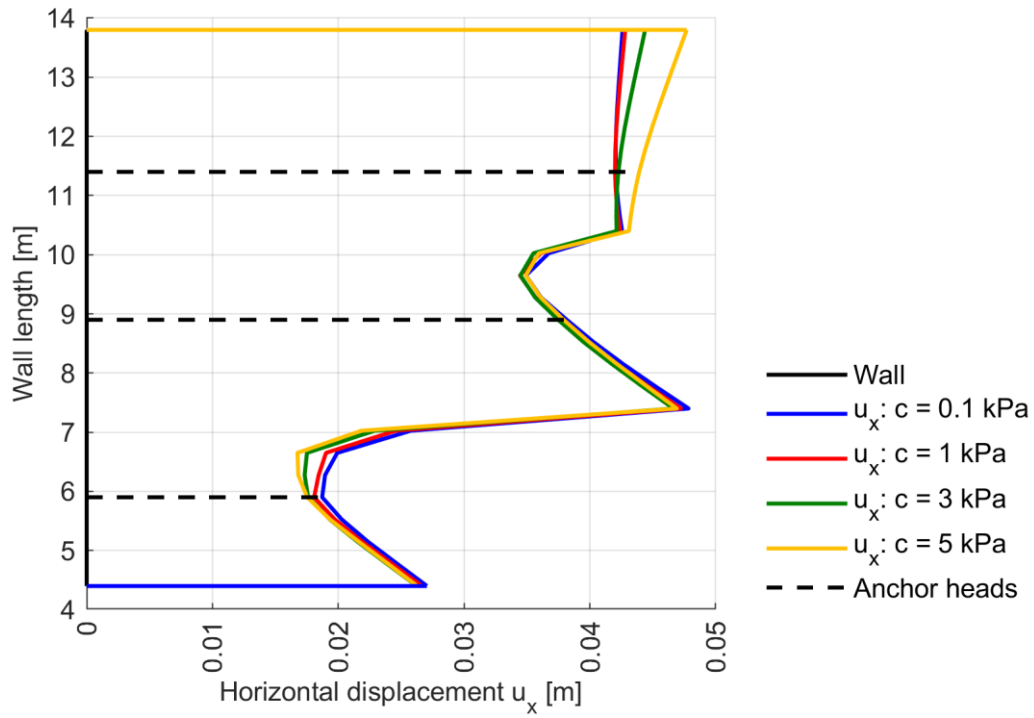


Fig. 159: Horizontal displacements u_x after Pre-stressing anchor 3

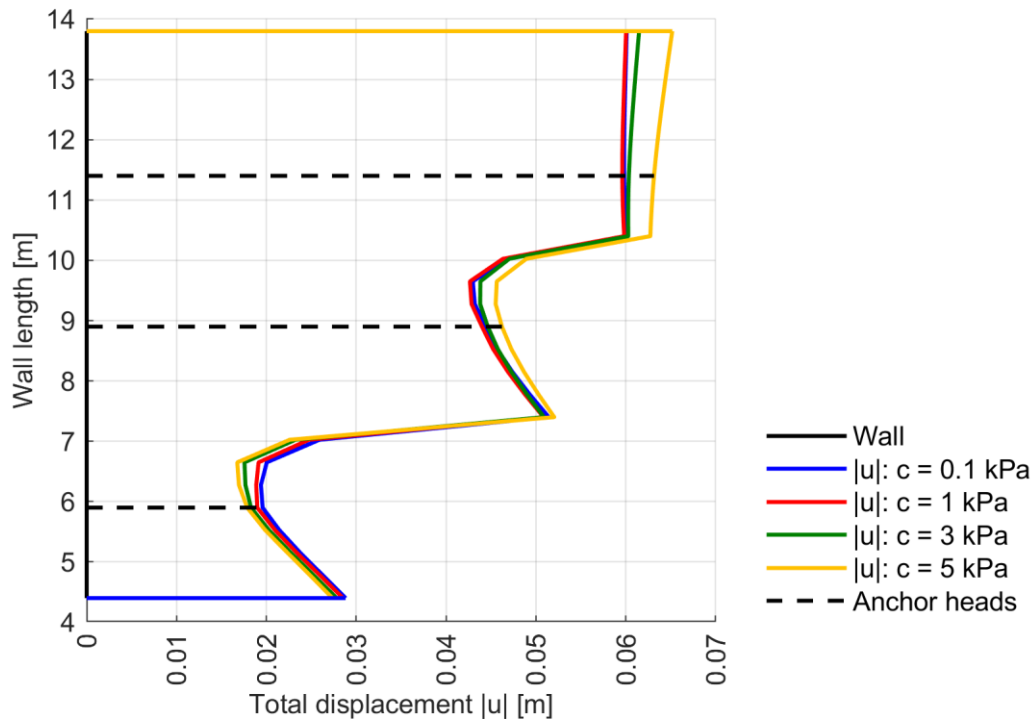


Fig. 160: Total displacements $|u|$ after Pre-stressing anchor 3

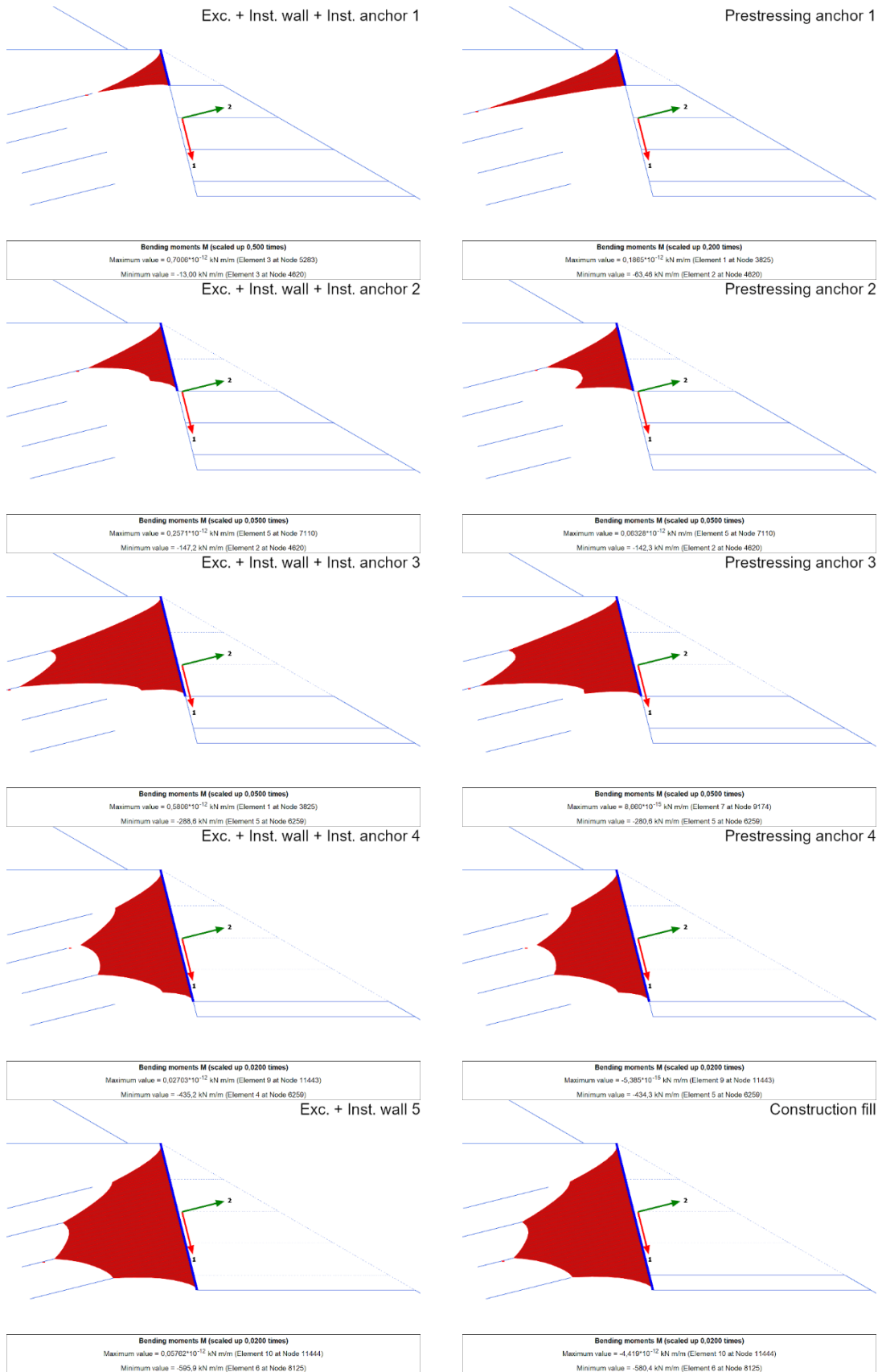


Fig. 161: Evolution of BMs over calculation phases for $c = 0.1$ kPa

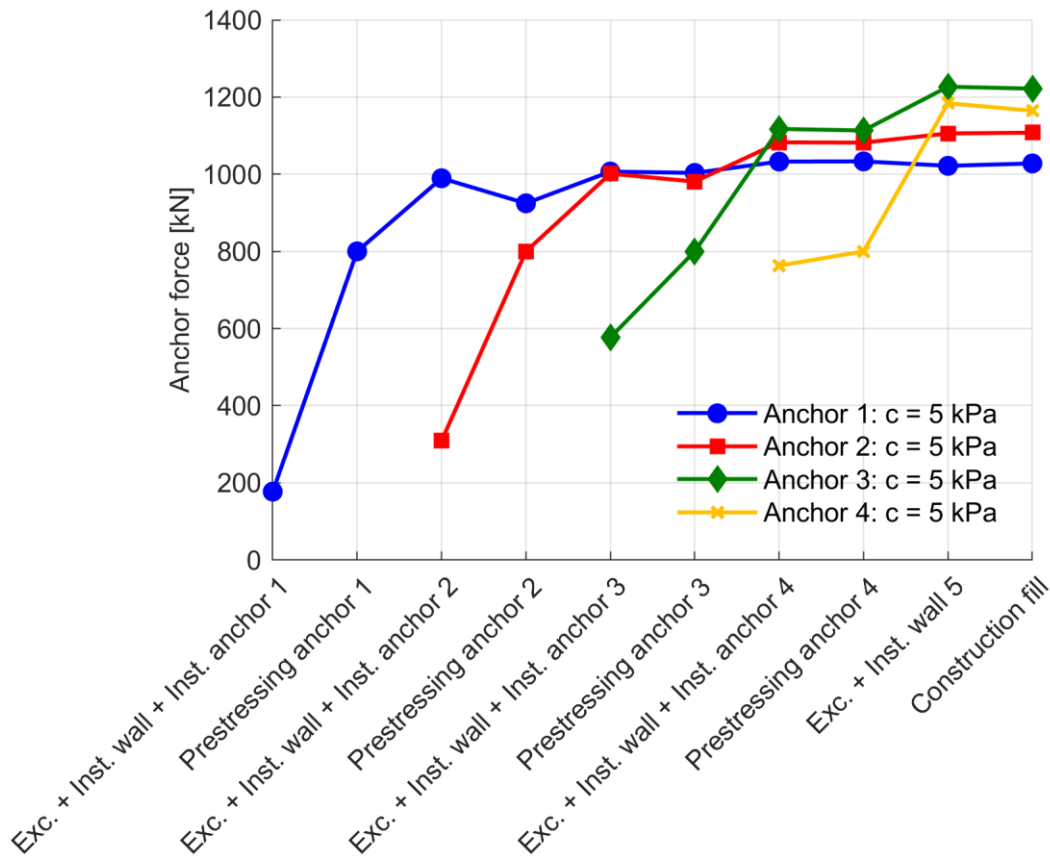


Fig. 162: Evolution of anchor forces over calculation phases for $c = 5$ kPa

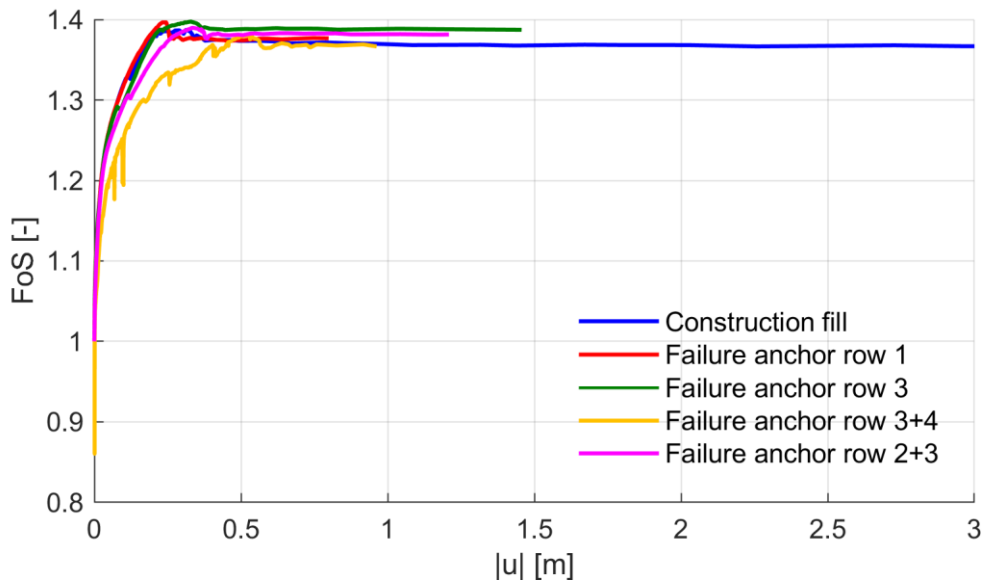


Fig. 163: FoS after ϕ - c reduction Construction fill and Failure cases for $c = 1$ kPa

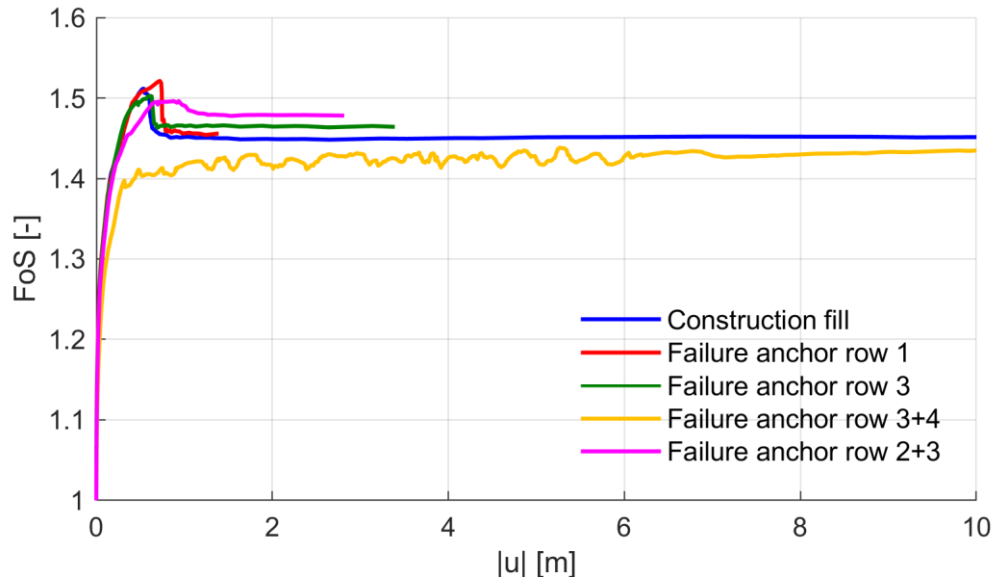


Fig. 164: FoS after ϕ - c reduction Construction fill and Failure cases for $c = 3$ kPa

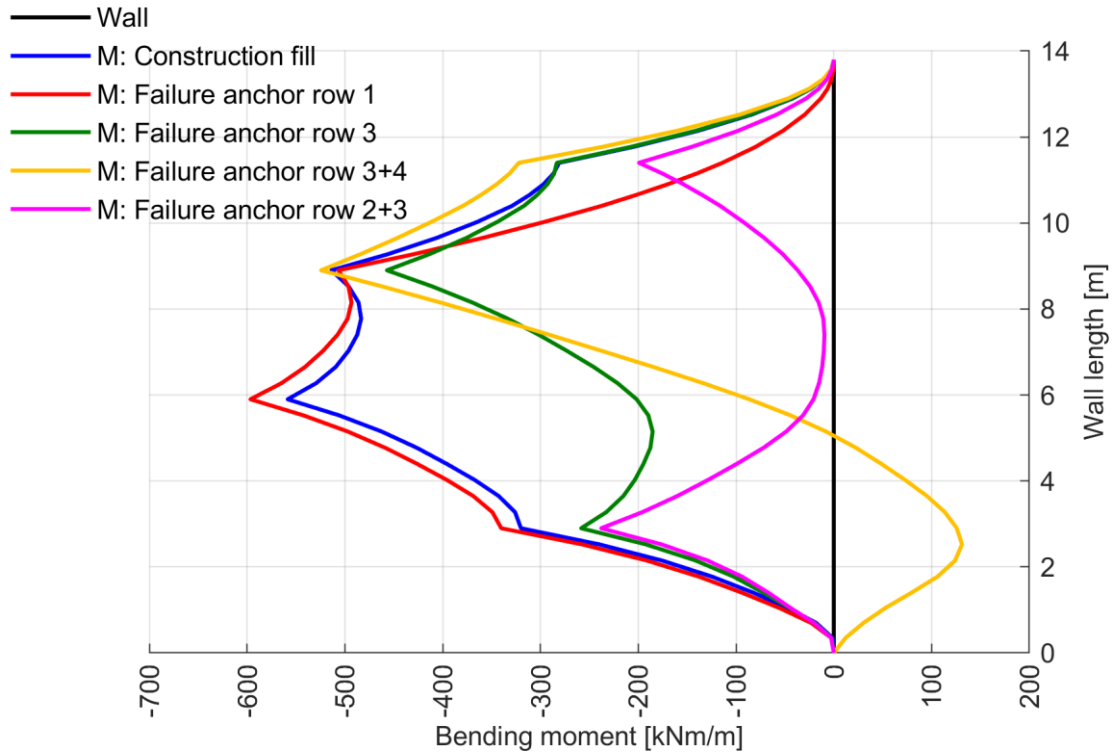


Fig. 165: $BM_s M_{actual}$ after Construction fill and Failure cases for $c = 5$ kPa

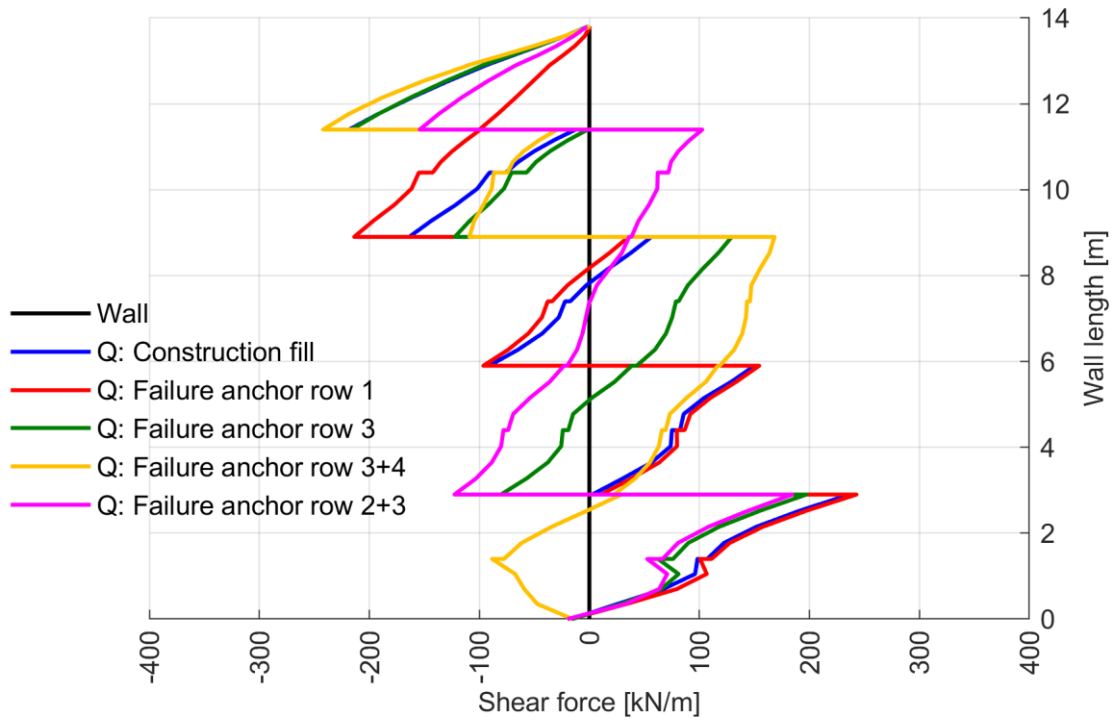


Fig. 166: $SFs Q_{actual}$ after Construction fill and Failure cases for $c = 5$ kPa

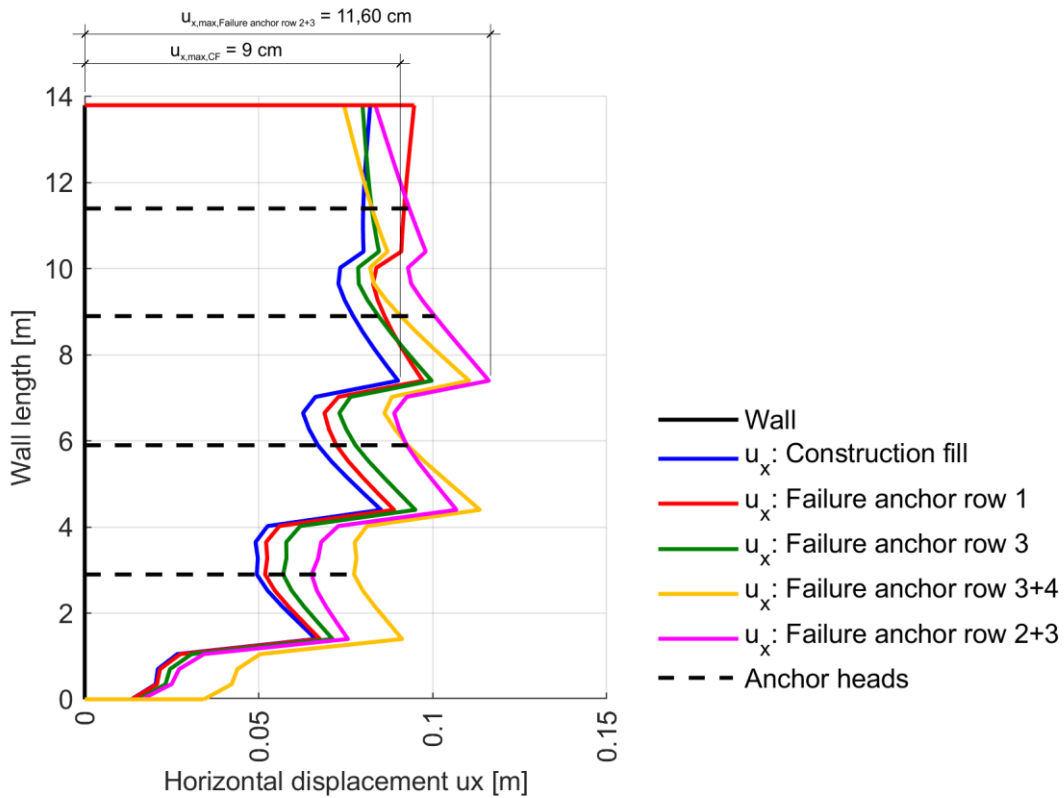


Fig. 167: Horizontal displacements u_x after Construction fill and Failure cases for $c = 5$ kPa

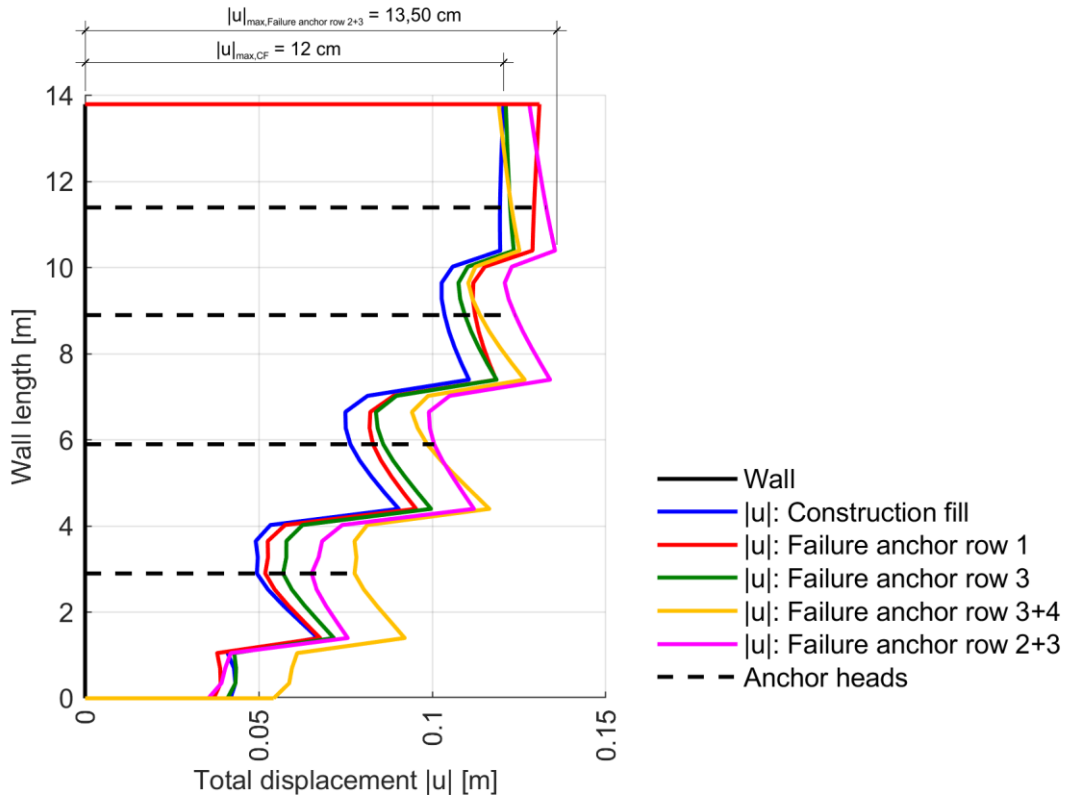


Fig. 168: Total displacements $|u|$ after Construction fill and Failure cases for $c = 5 \text{ kPa}$

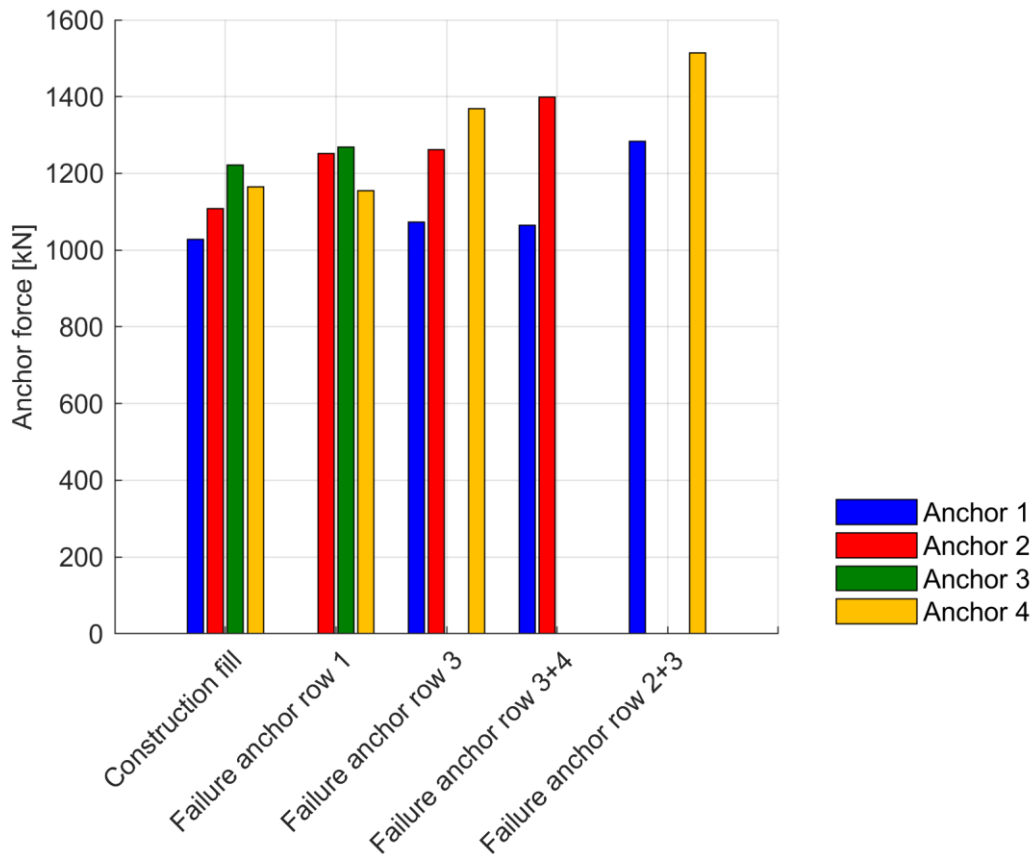


Fig. 169: Anchor forces after Construction fill and Failure cases for $c = 5 \text{ kPa}$

8.2 $MC_{R_{inter}=0.9_EB_Constant_Anchor}$ Pre-stressed in 2D

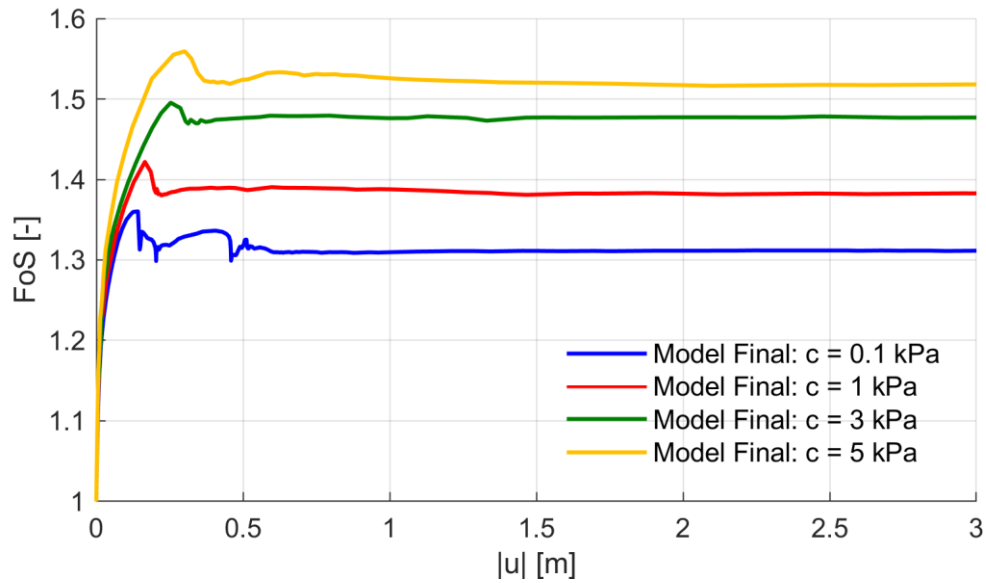


Fig. 170: FoS after ϕ - c reduction Pre-stressing anchor 1; EBs with constant skin resistance

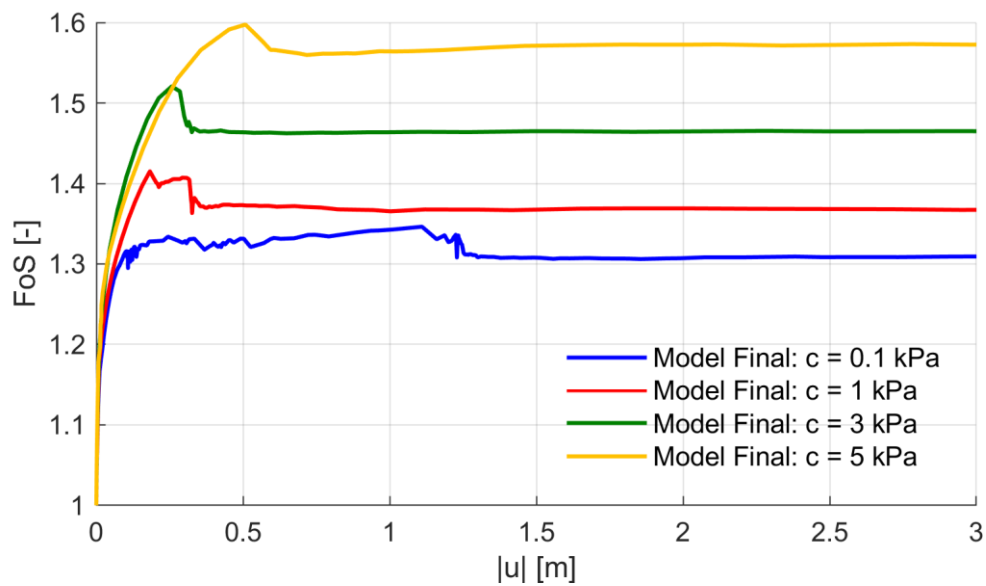


Fig. 171: FoS after ϕ - c reduction Pre-stressing anchor 2; EBs with constant skin resistance

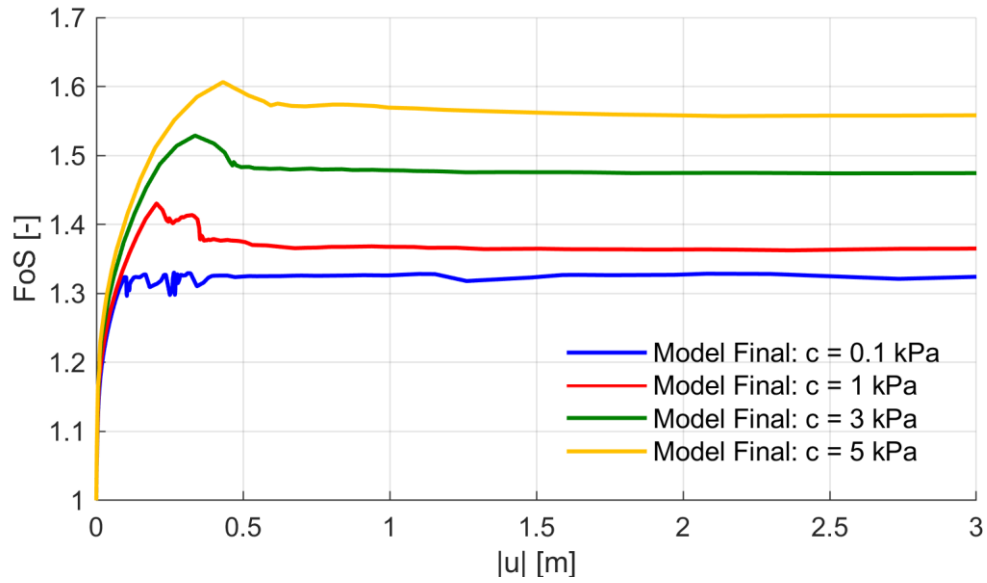


Fig. 172: FoS after ϕ - c reduction Pre-stressing anchor 3; EBs with constant skin resistance

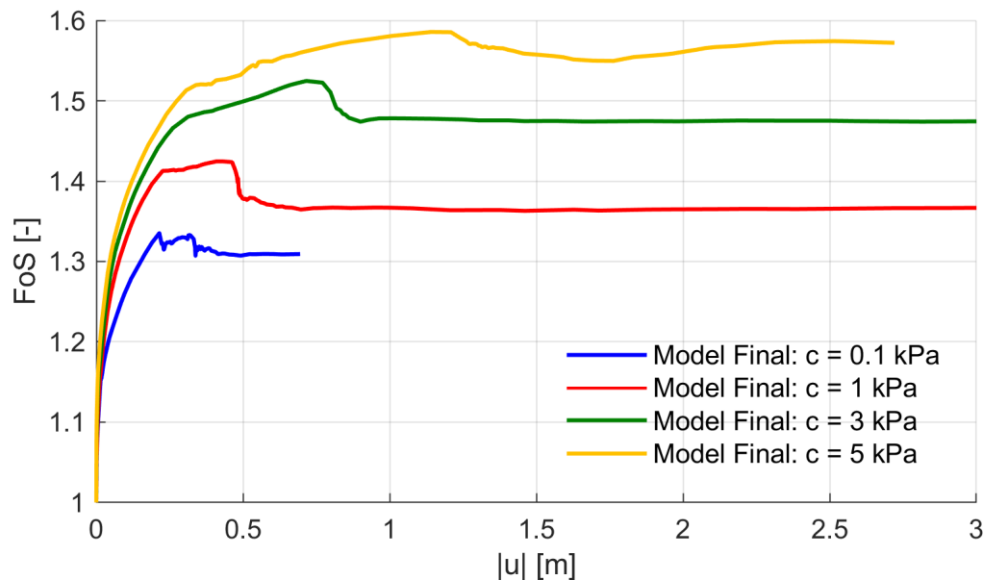


Fig. 173: FoS after ϕ - c reduction Construction fill; EBs with constant skin resistance

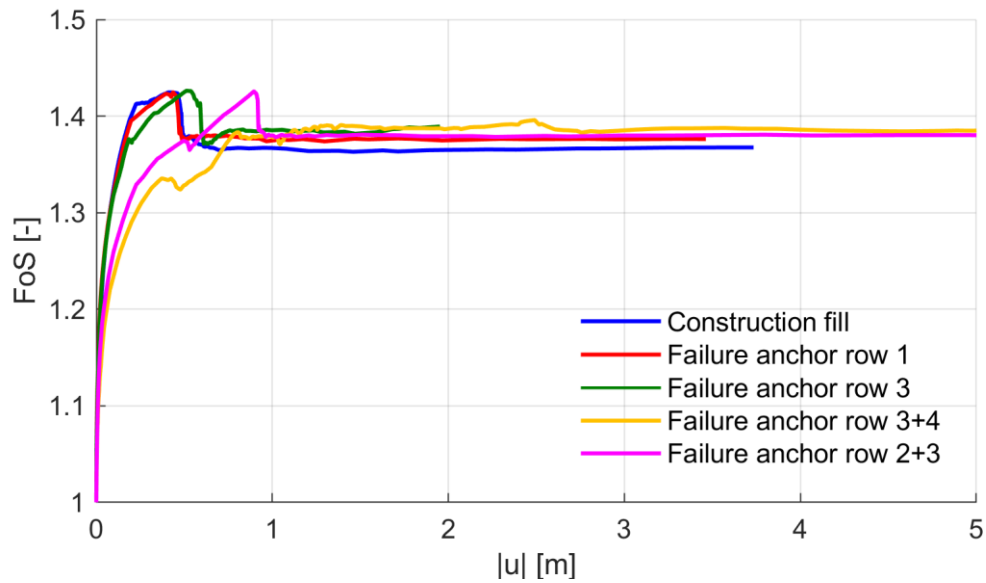


Fig. 174: FoS after ϕ - c reduction Construction fill and Failure cases for $c = 1$ kPa; EBs with constant skin resistance

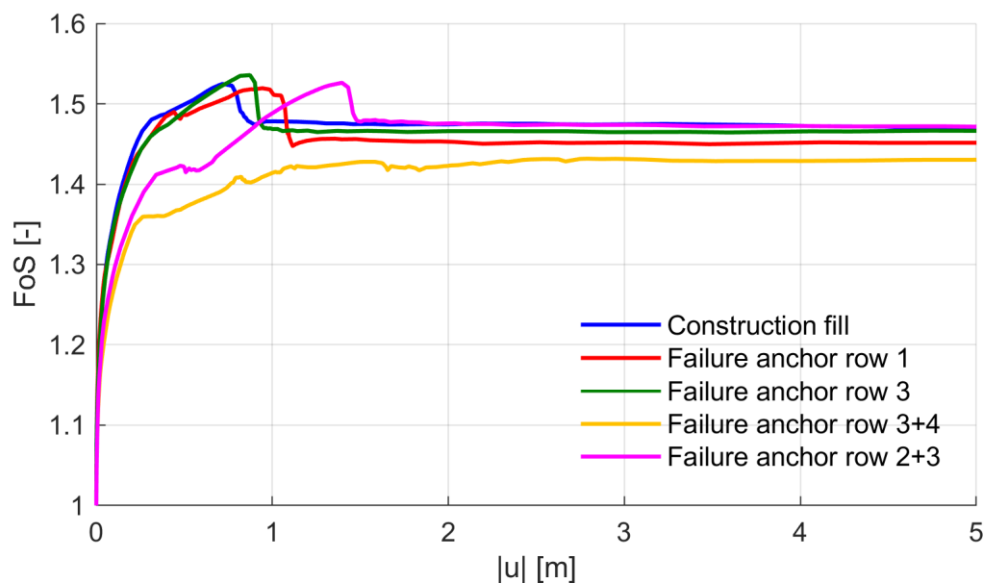


Fig. 175: FoS after ϕ - c reduction Construction fill and Failure cases for $c = 3$ kPa; EBs with constant skin resistance

8.3 $MC_{R_{inter}=0.9_EB_Linear_Anchor}$ Pre-stressed in 2D

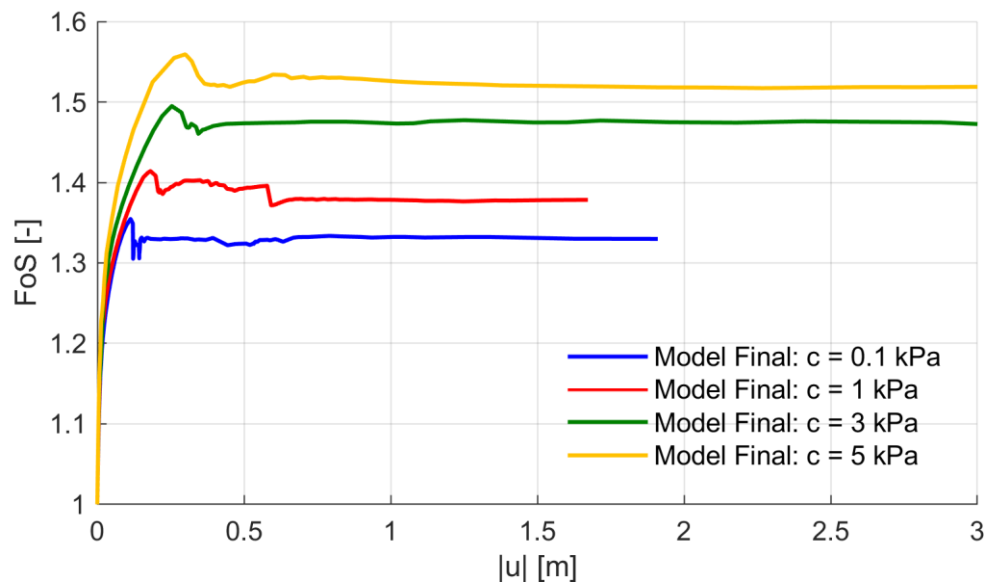


Fig. 176: FoS after ϕ - c reduction Pre-stressing anchor 1; EBs with linear skin resistance

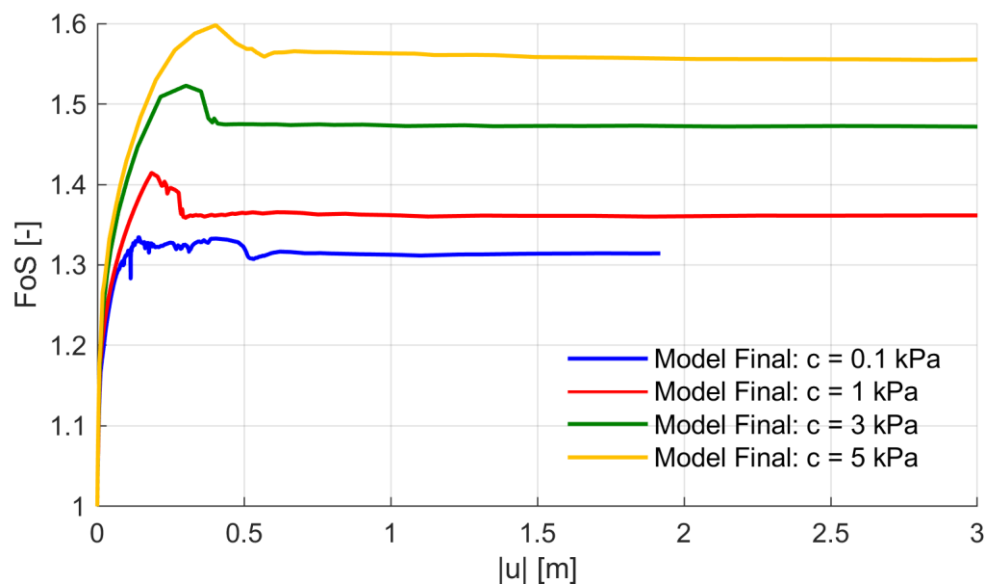


Fig. 177: FoS after ϕ - c reduction Pre-stressing anchor 2; EBs with linear skin resistance

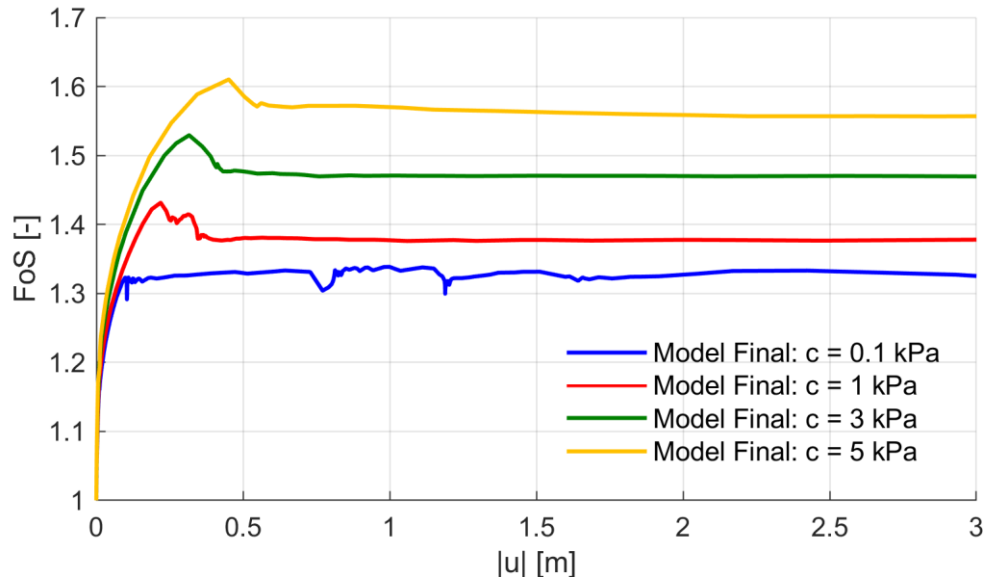


Fig. 178: FoS after ϕ - c reduction Pre-stressing anchor 3; EBs with linear skin resistance

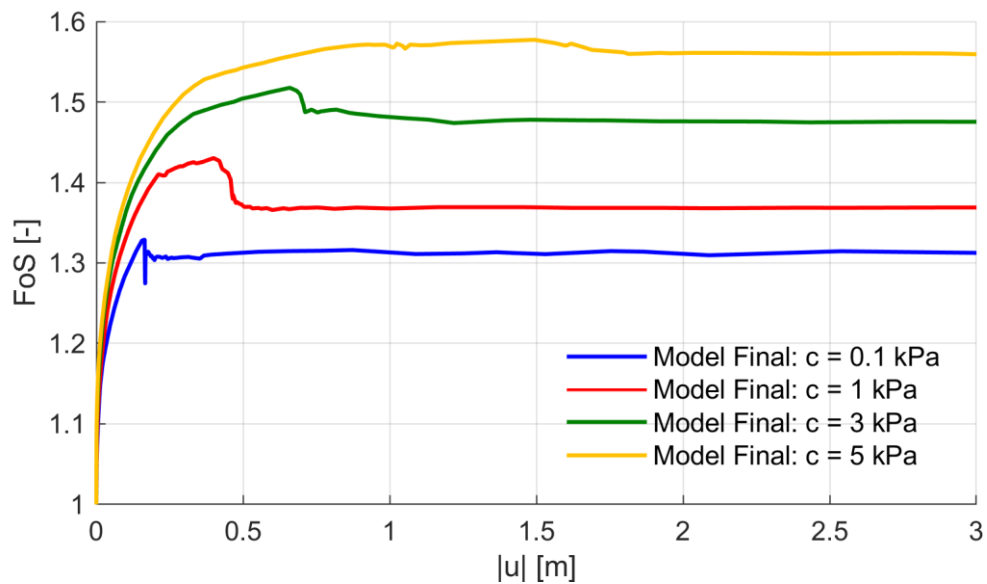


Fig. 179: FoS after ϕ - c reduction Construction fill; EBs with linear skin resistance

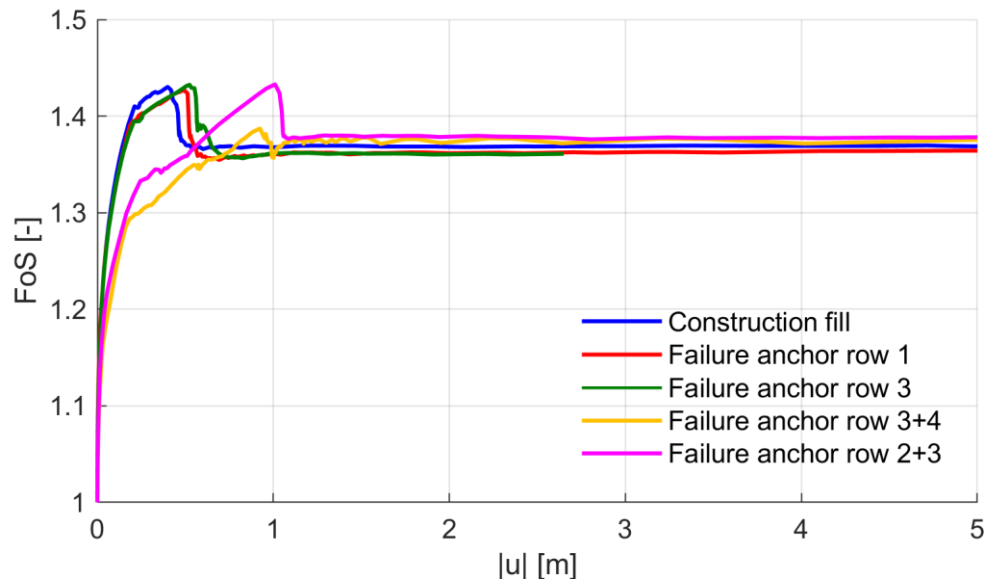


Fig. 180: FoS after φ - c reduction Construction fill and Failure cases for $c = 1$ kPa; EBs with linear skin resistance

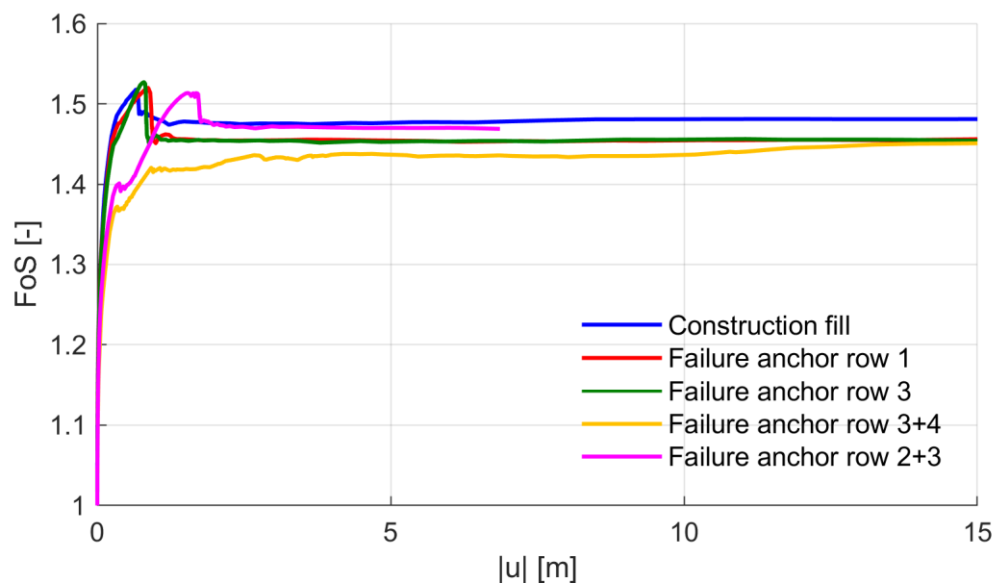


Fig. 181: FoS after φ - c reduction Construction fill and Failure cases for $c = 3$ kPa; EBs with linear skin resistance

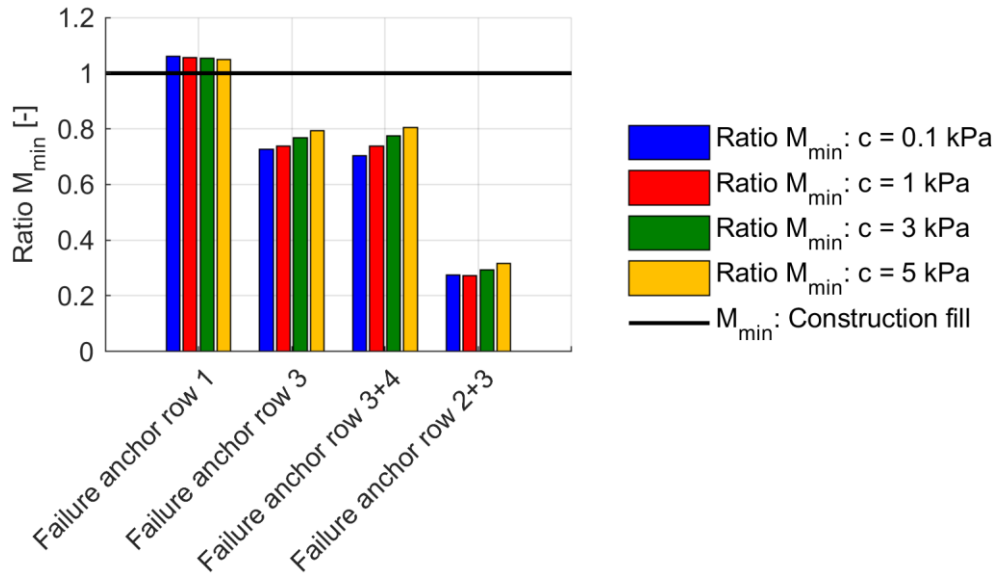


Fig. 182: *BM*s: Ratio M_{\min} ; *EB*s with linear skin resistance

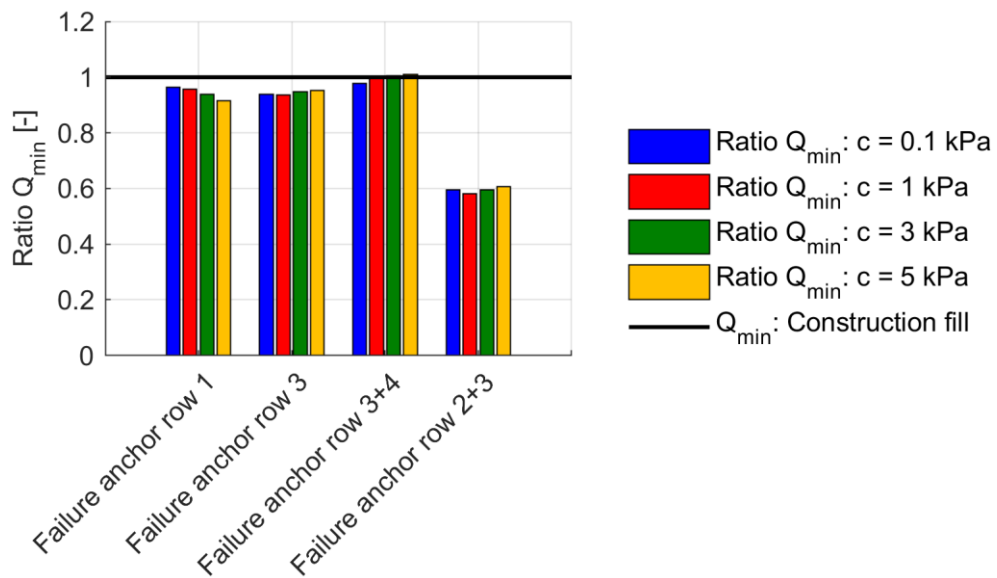


Fig. 183: *SF*s: Ratio Q_{\min} ; *EB*s with linear skin resistance

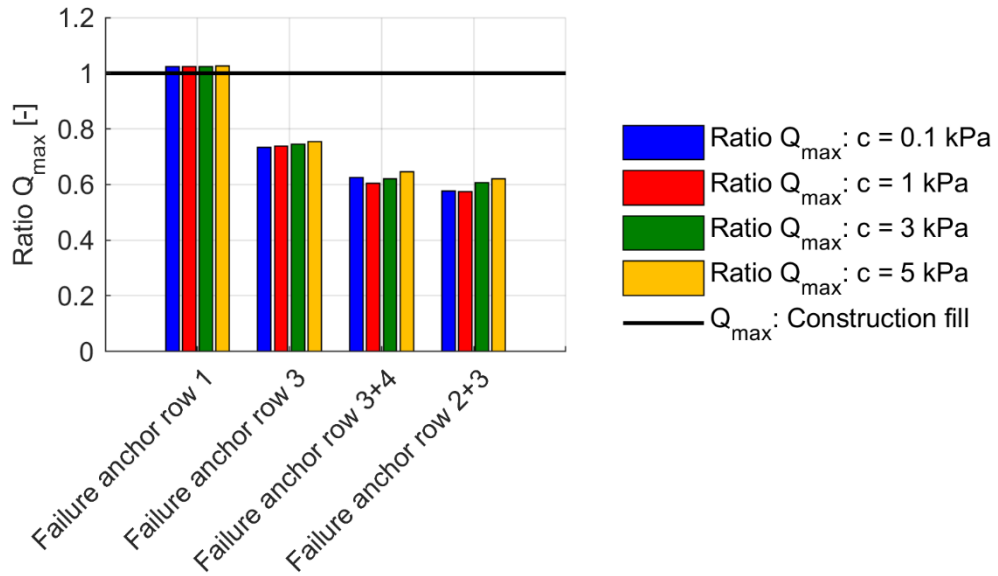


Fig. 184: SFs: Ratio Q_{\max} ; EBs with linear skin resistance

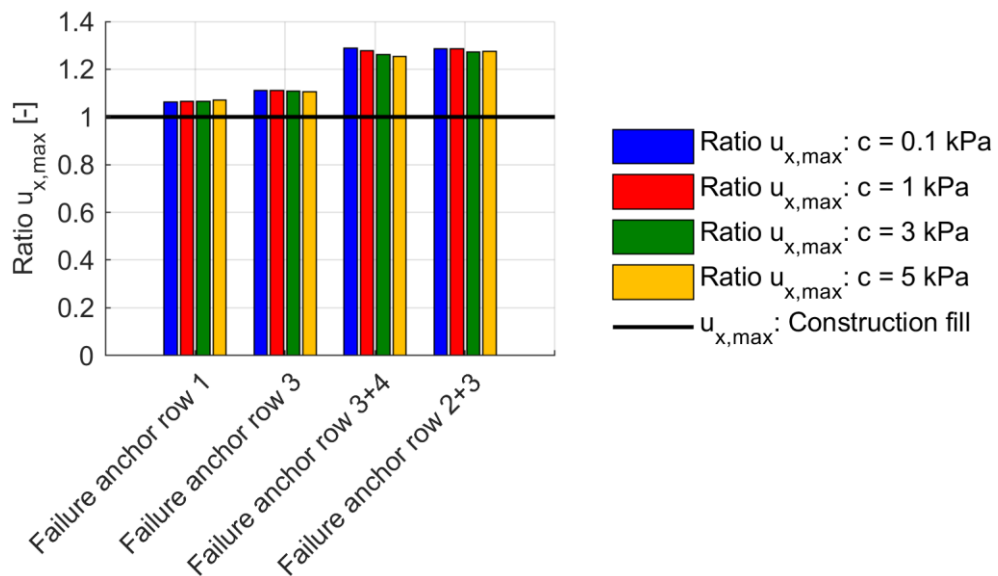


Fig. 185: Horizontal displacements: Ratio $u_{x,\max}$; EBs with linear skin resistance

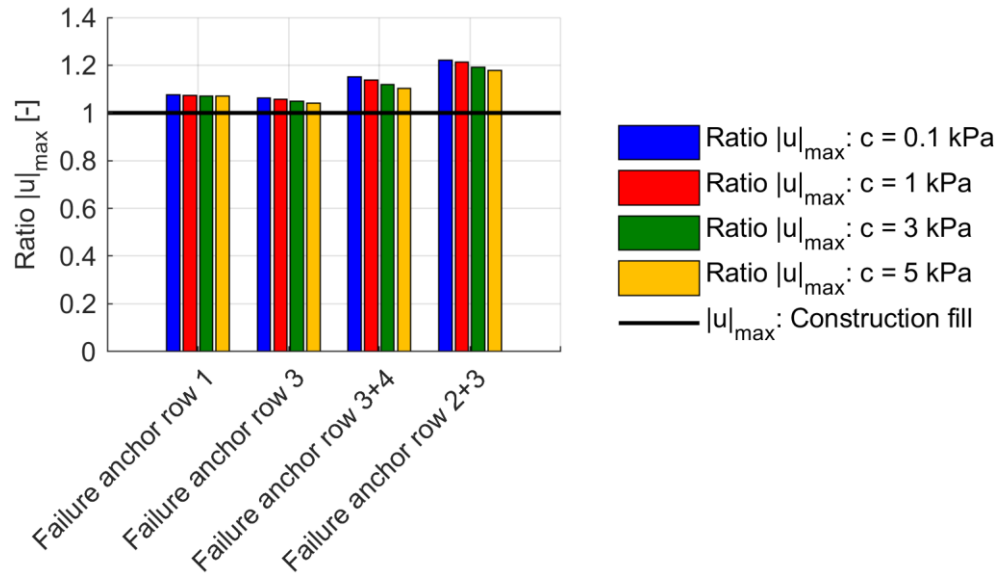


Fig. 186: Total displacements: Ratio $|u|_{\max}$; *EBs* with linear skin resistance

8.4 HSS_R_{inter}=0.9_Geogrid_AnchorPre-stressed in 2D

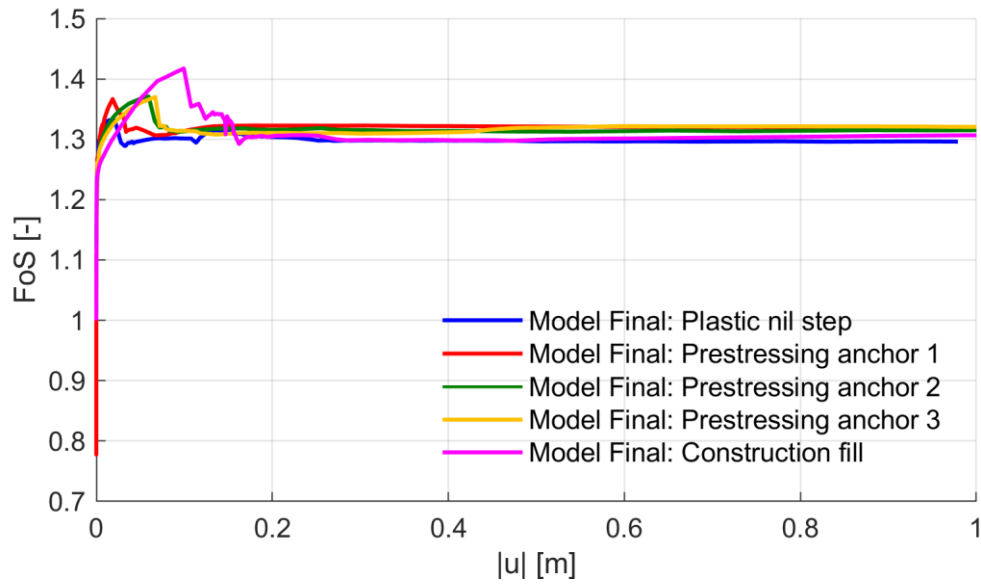


Fig. 187: FoS after φ - c reduction during construction of the RW for $c = 0.1$ kPa; HSS model

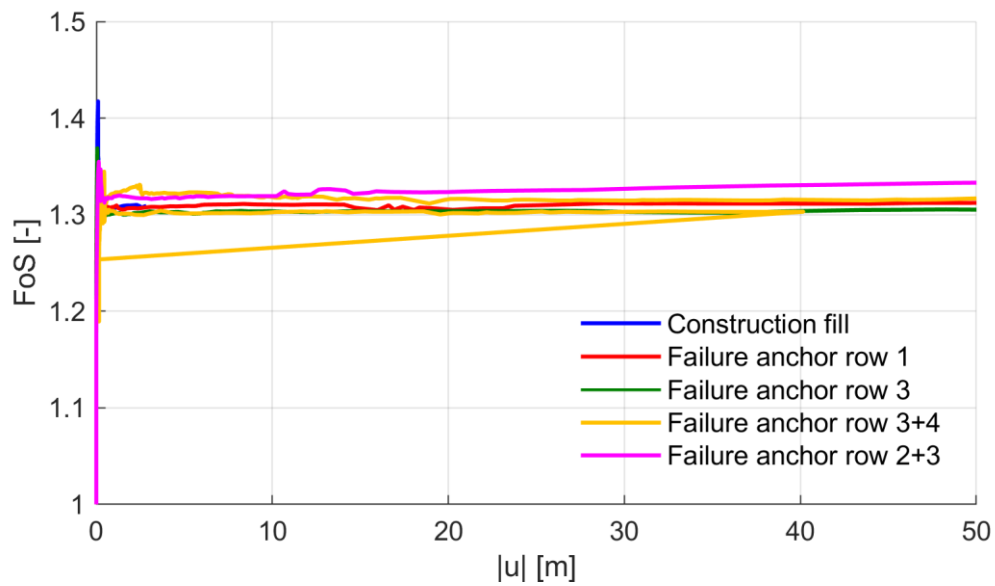


Fig. 188: FoS after φ - c reduction Construction fill and Failure cases for $c = 0.1$ kPa; HSS model

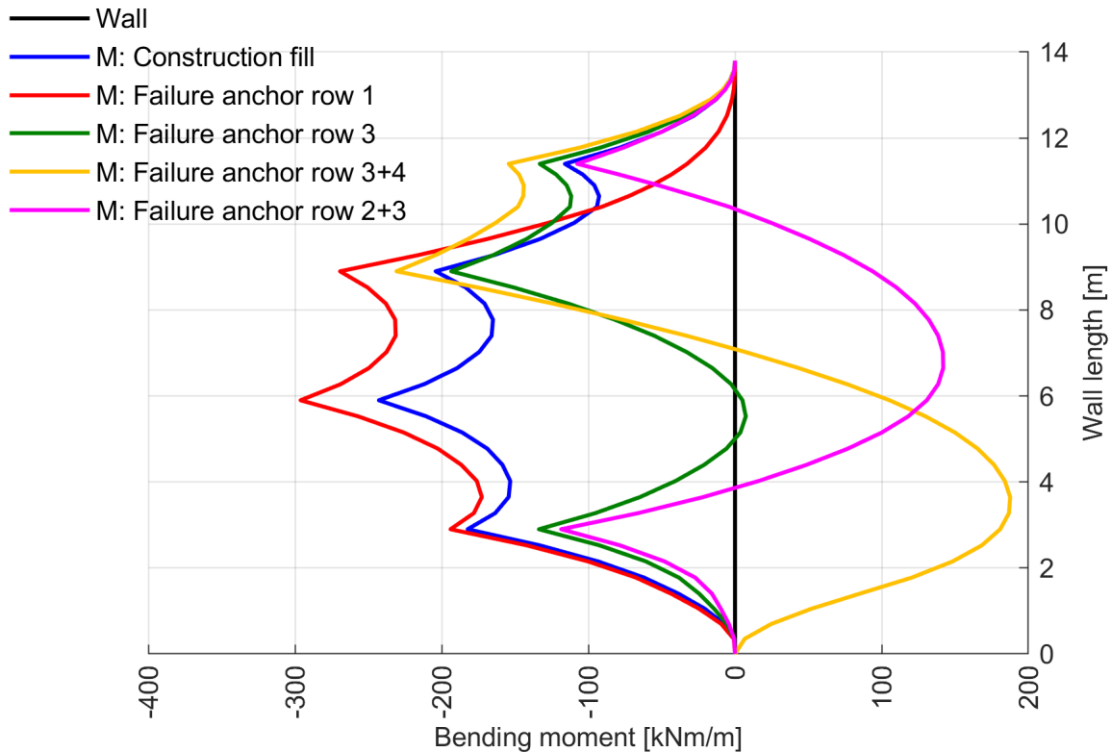


Fig. 189: $BM_s M_{actual}$ after Construction fill and Failure cases for $c = 0.1$ kPa; *HSS* model

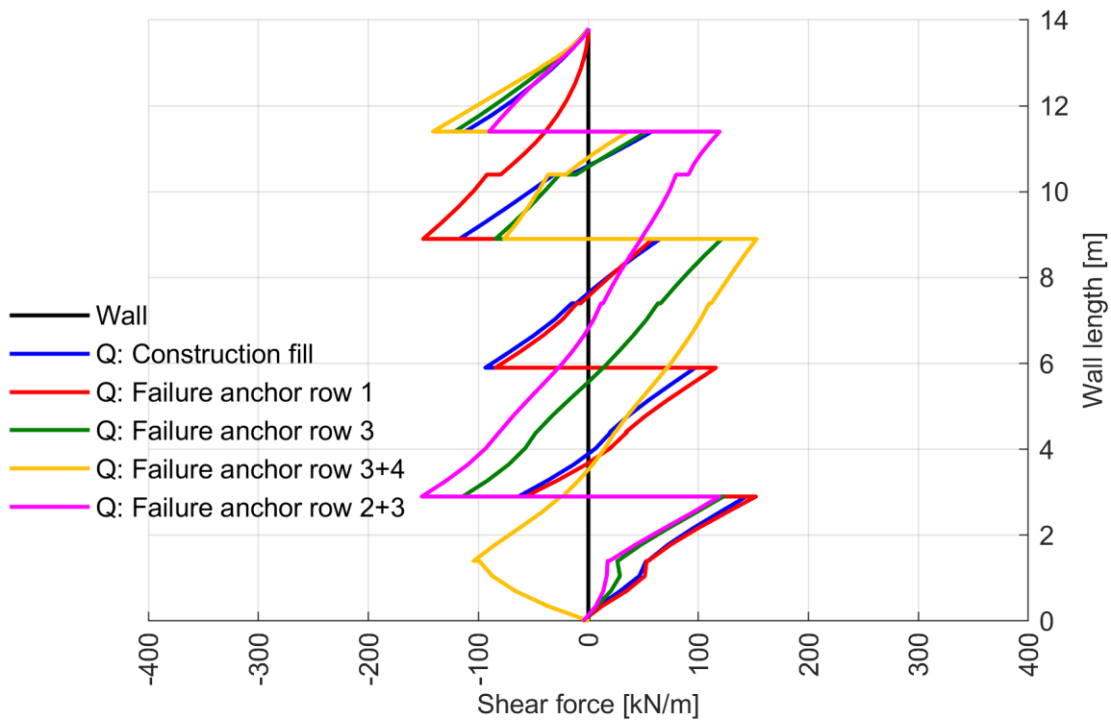


Fig. 190: $SFs Q_{actual}$ after Construction fill and Failure cases for $c = 0.1$ kPa; *HSS* model

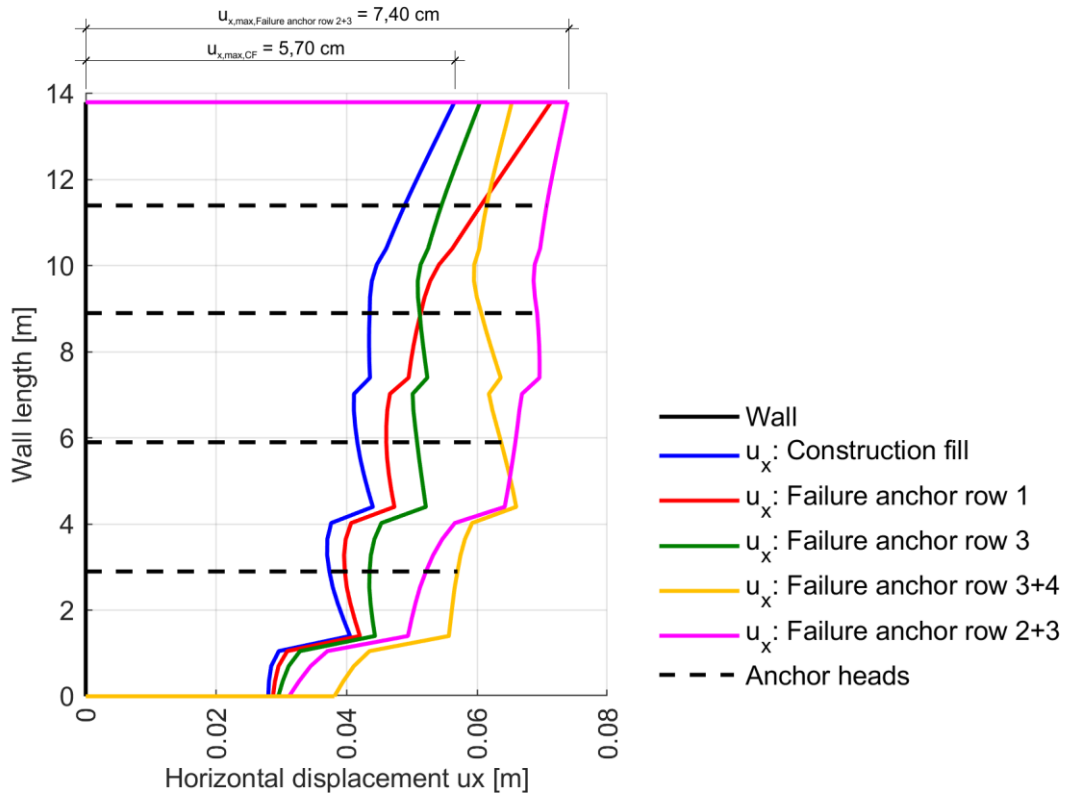


Fig. 191: Horizontal displacements u_x after Construction fill and Failure cases for $c = 0.1$ kPa; *HSS* model

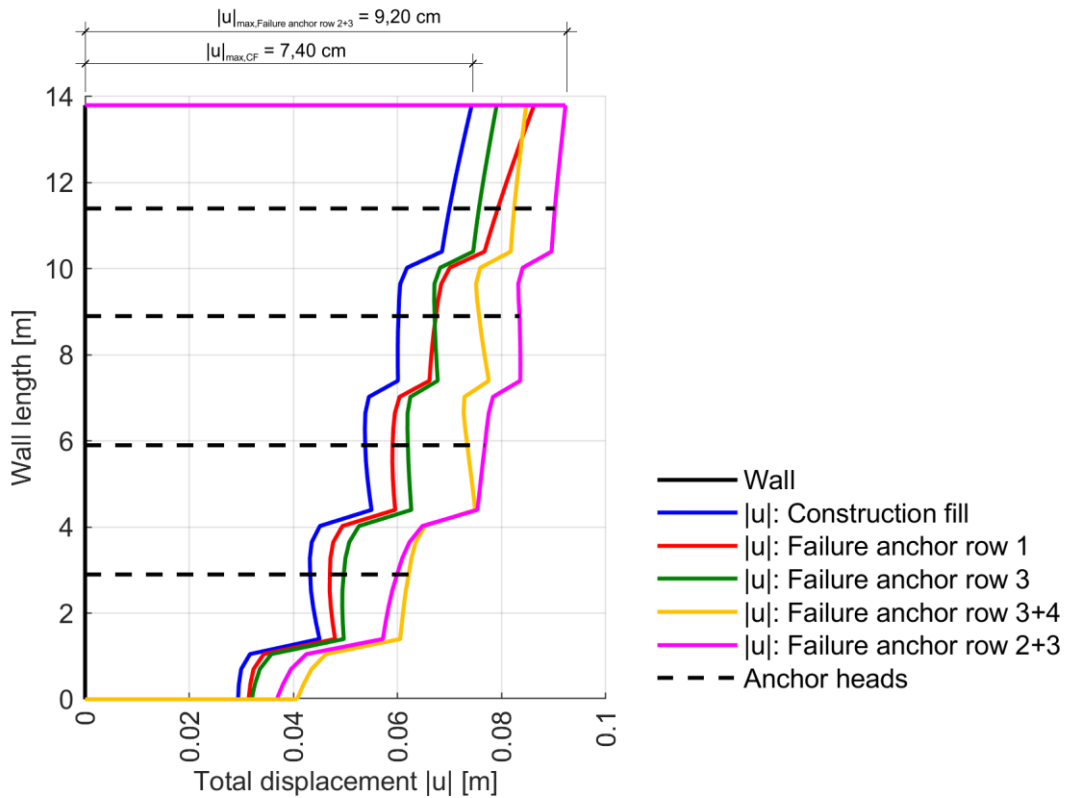


Fig. 192: Total displacements $|u|$ after Construction fill and Failure cases for $c = 0.1$ kPa; *HSS* model

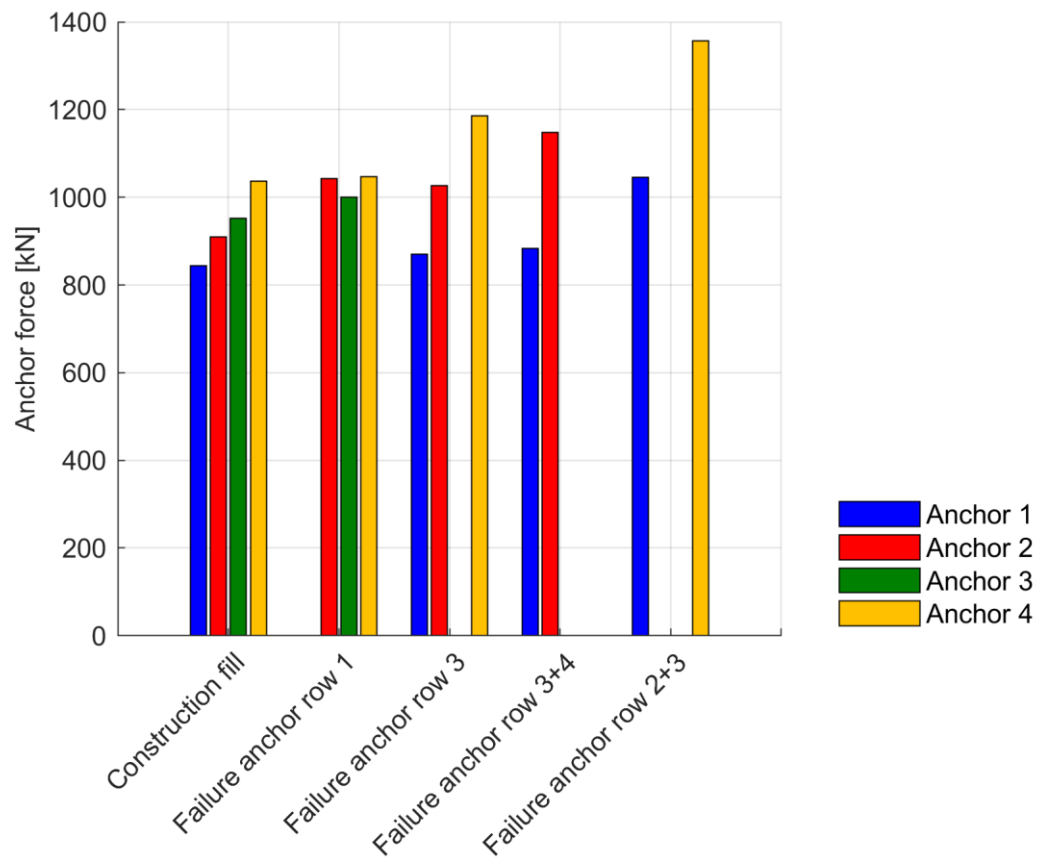


Fig. 193: Anchor forces after Construction fill and Failure cases for $c = 0.1$ kPa; *HSS* model

8.5 $HSS_{R_{inter}=0.9_EB_Linear_Anchor}$ Pre-stressed in 2D

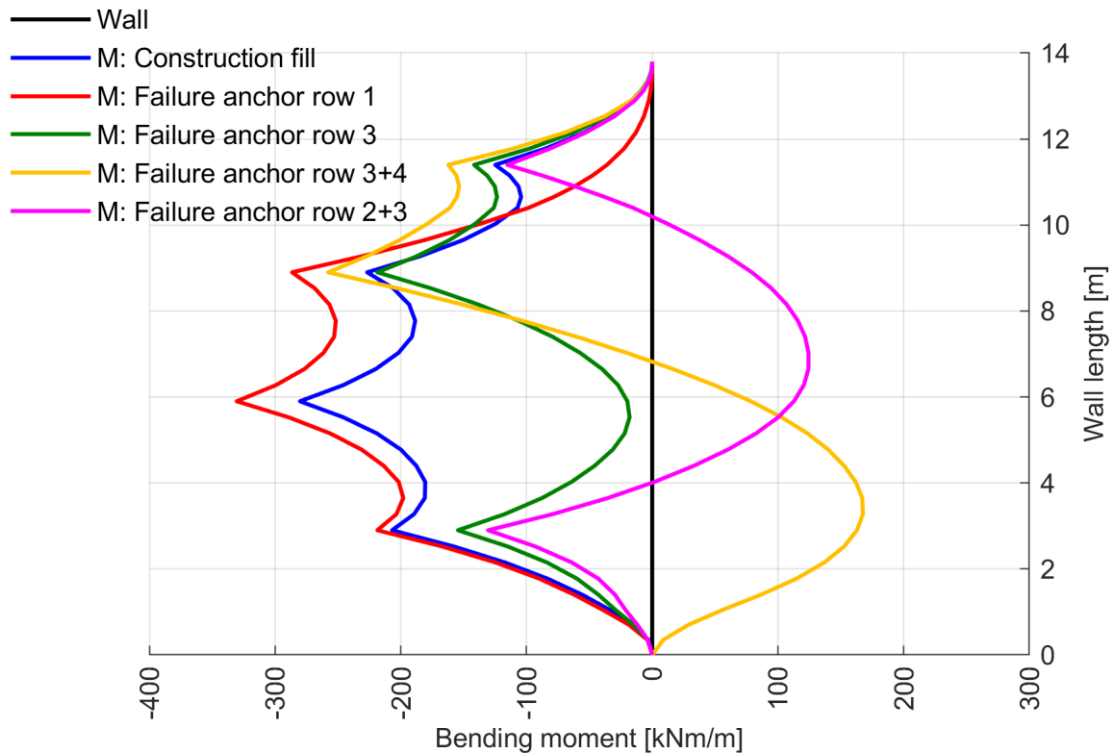


Fig. 194: $BMs M_{actual}$ after Construction fill and Failure cases for $c = 0.1$ kPa; HSS model; EBs with linear skin resistance

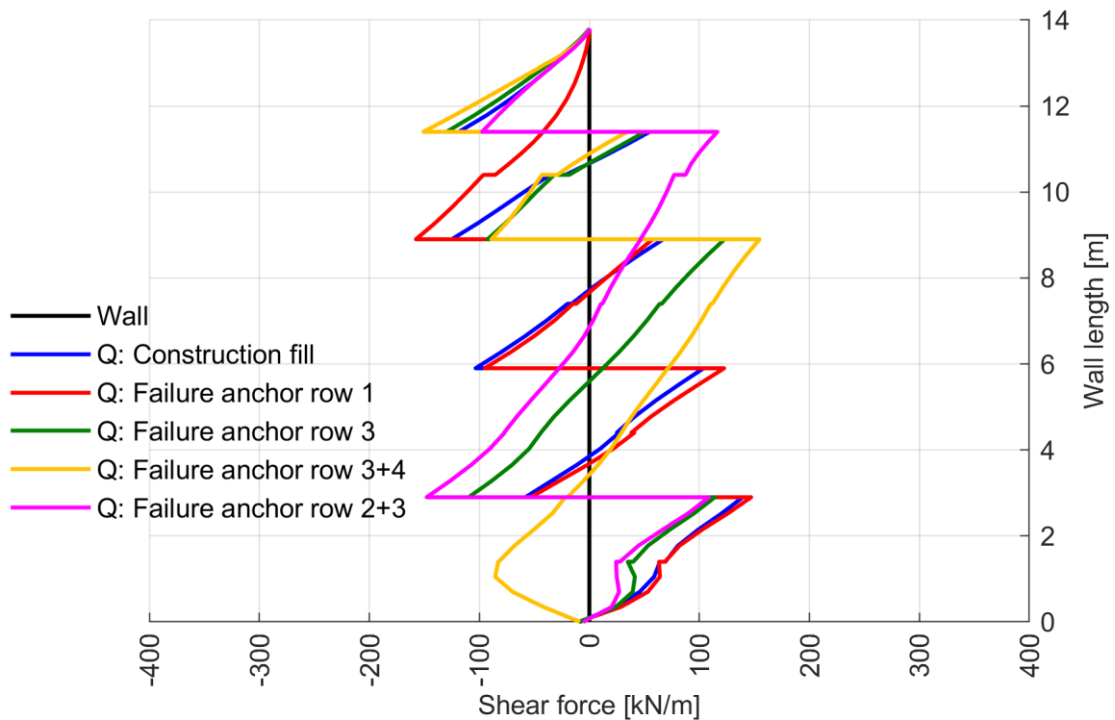


Fig. 195: $SFs Q_{actual}$ after Construction fill and Failure cases for $c = 0.1$ kPa; HSS model; EBs with linear skin resistance

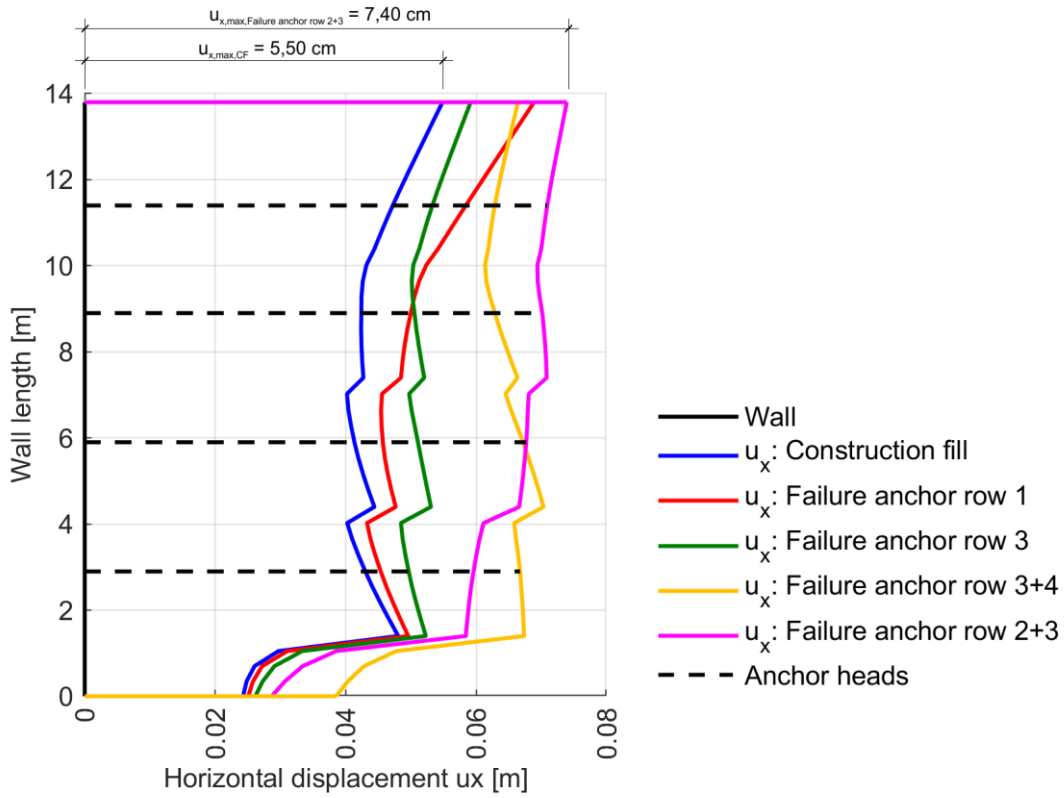


Fig. 196: Horizontal displacements u_x after Construction fill and Failure cases for $c = 0.1$ kPa; *HSS* model; *EBs* with linear skin resistance

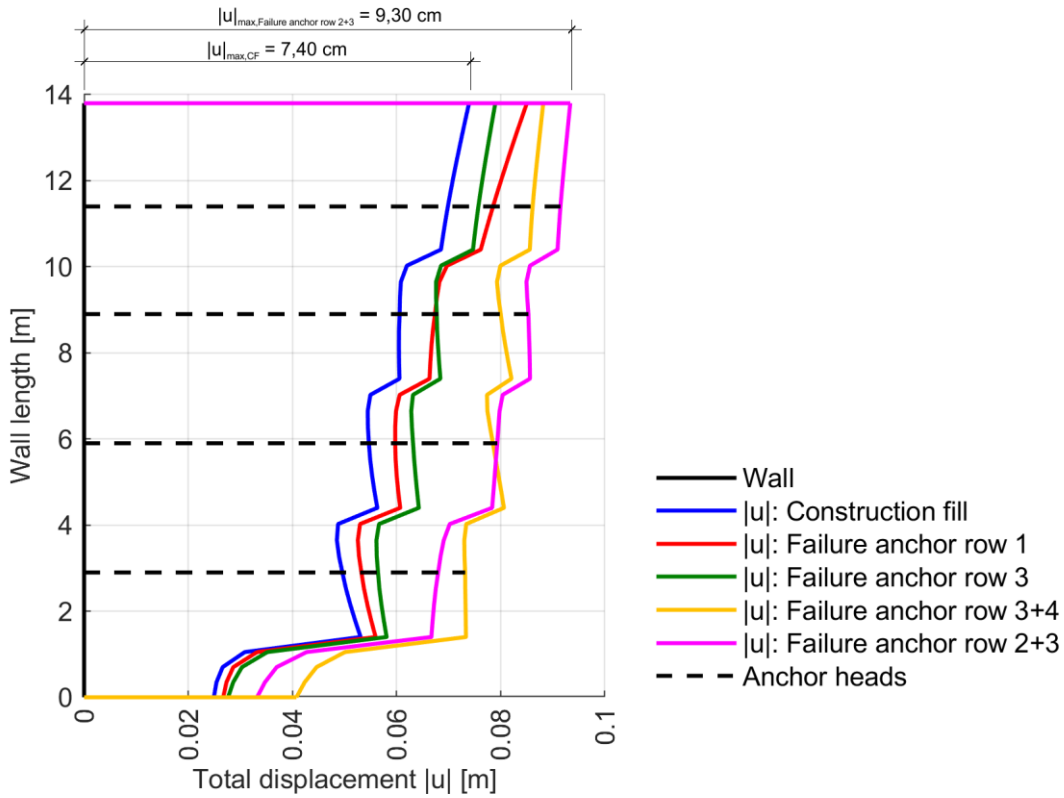


Fig. 197: Total displacements $|u|$ after Construction fill and Failure cases for $c = 0.1$ kPa; *HSS* model; *EBs* with linear skin resistance

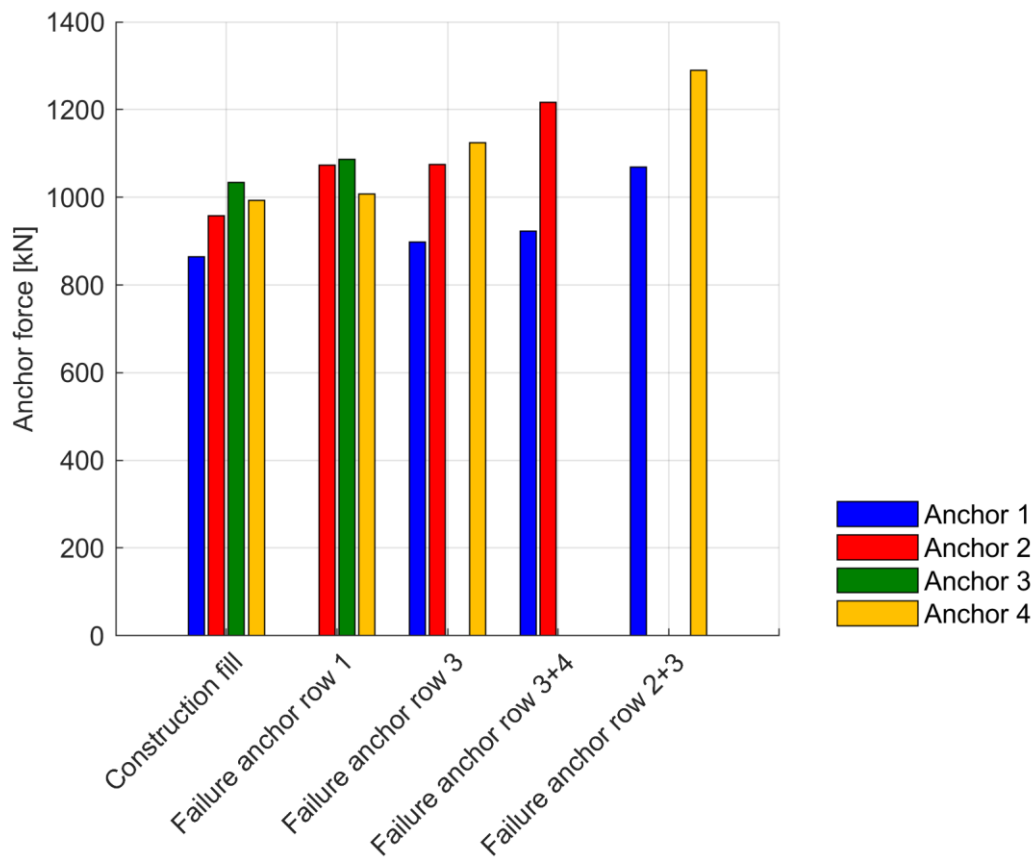


Fig. 198: Anchor forces after Construction fill and Failure cases for $c = 0.1$ kPa; *HSS* model; *EBs* with linear skin resistance

8.6 MC_R_{inter}=1_Geogrid_AnchorPre-stressed in 3D

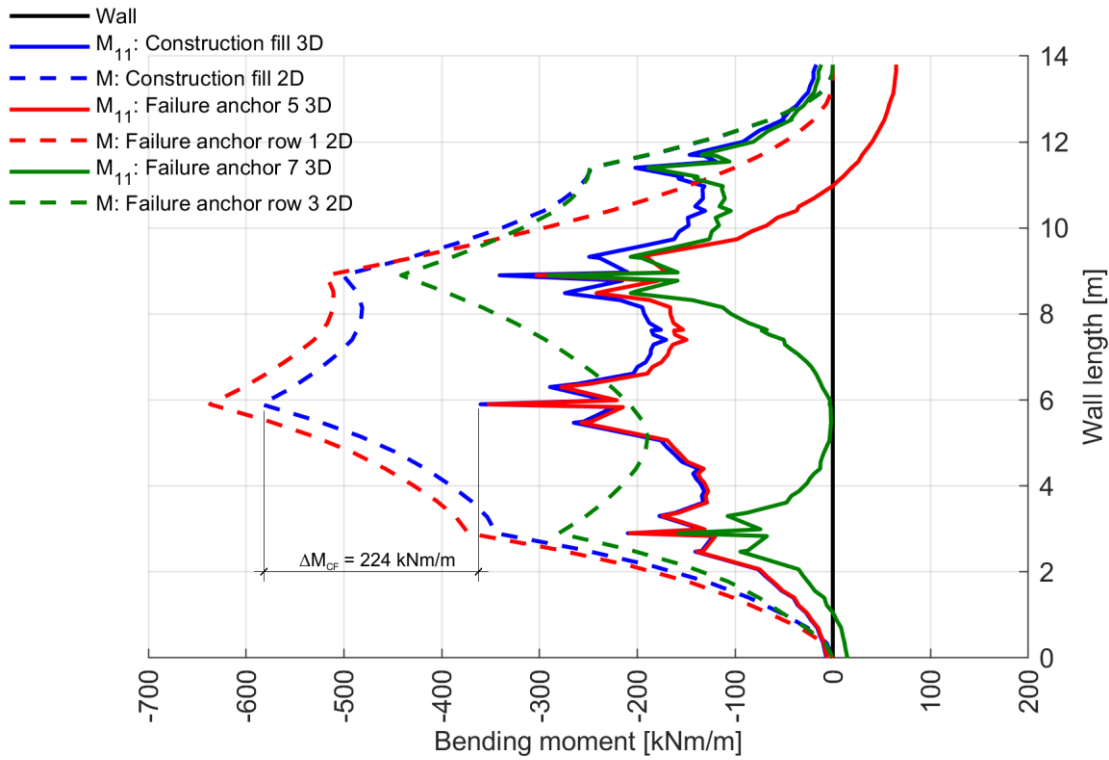


Fig. 199: *BMs* $M_{11,actual}$ after Construction fill and single anchor failure cases for $c = 0.1$ kPa; 2D vs. 3D at $y = 7.50$ m

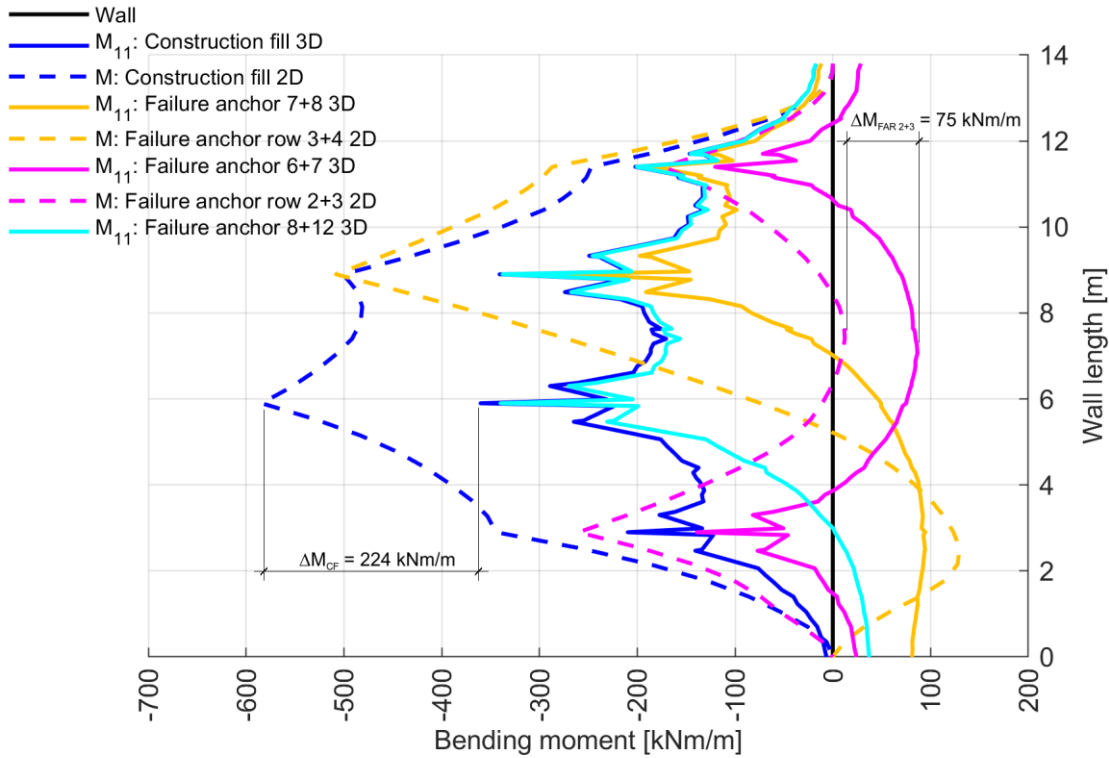


Fig. 200: *BMs* $M_{11,actual}$ after Construction fill and double anchor failure cases for $c = 0.1$ kPa; 2D vs. 3D at $y = 7.50$ m

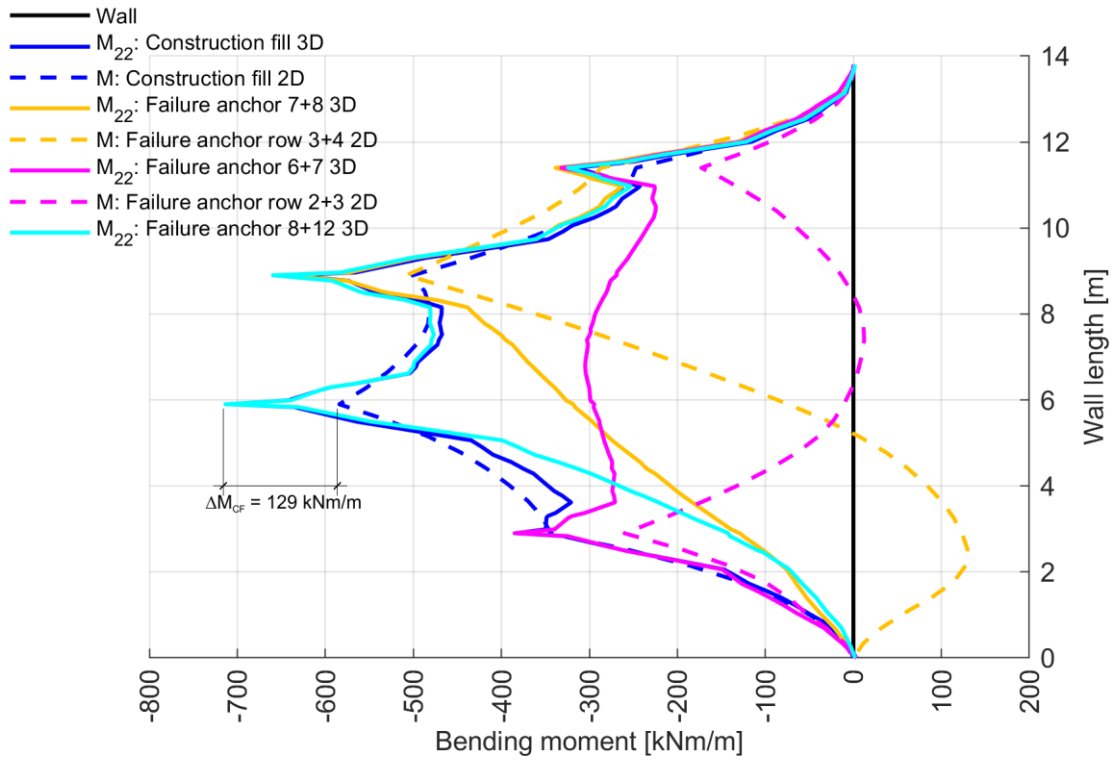


Fig. 201: $BM_s M_{22,actual}$ after Construction fill and double anchor failure cases for $c = 0.1 \text{ kPa}$; 2D vs. 3D at $y = 7.50 \text{ m}$

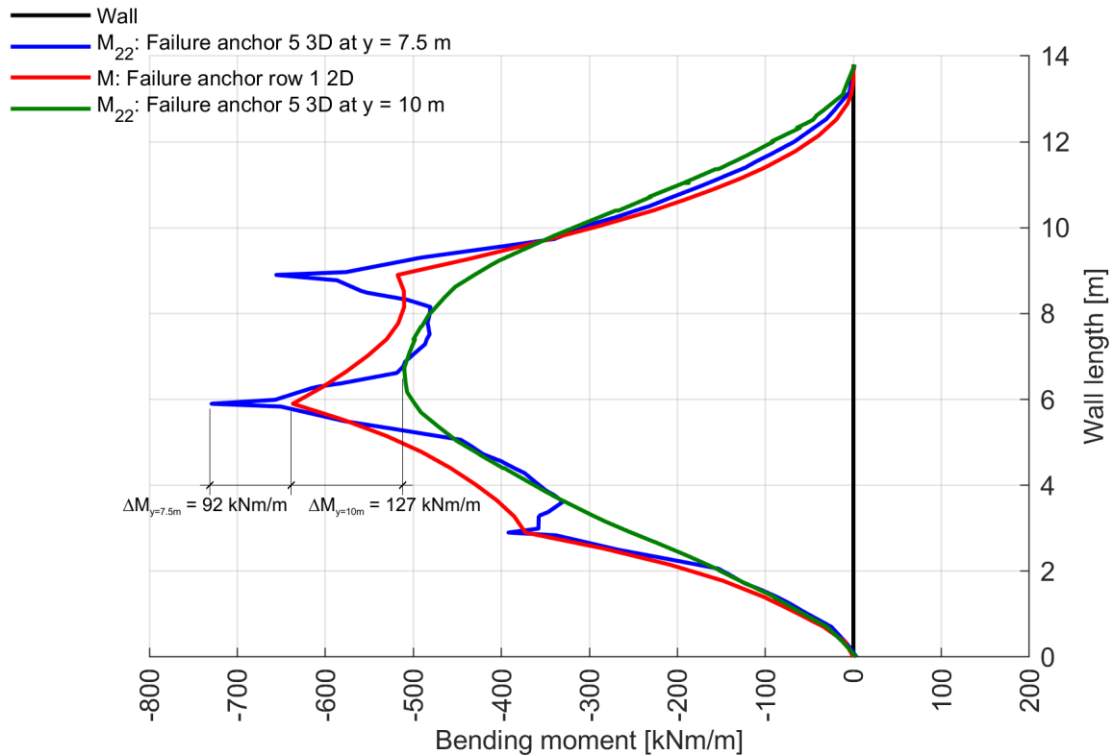


Fig. 202: $BM_s M_{22,actual}$ after Failure anchor 5 for $c = 0.1 \text{ kPa}$; 2D vs. 3D at $y = 7.50/10 \text{ m}$

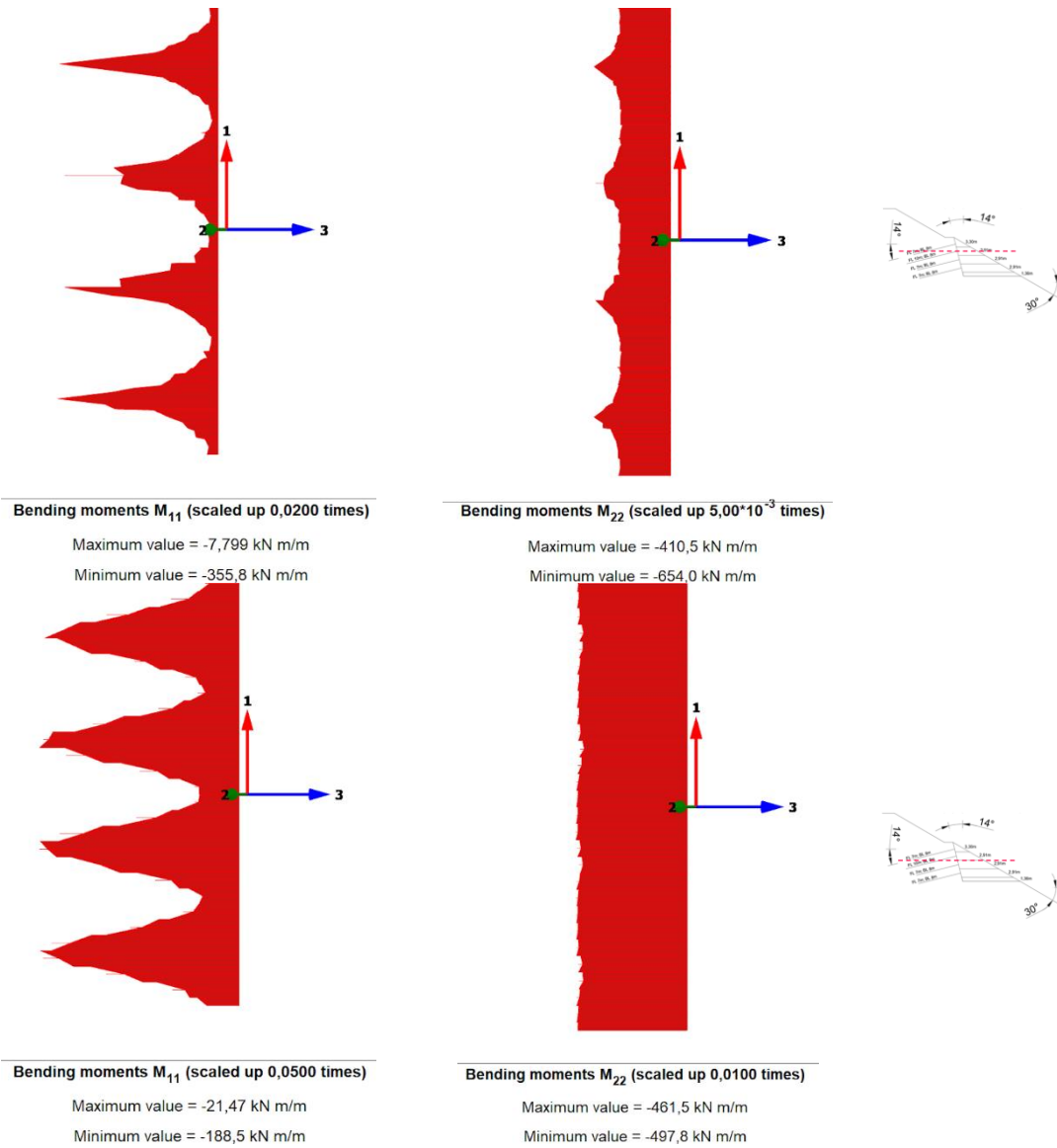


Fig. 203: Top view of $BMs M_{11,actual}/M_{22,actual}$ after Construction fill for $c = 0.1$ kPa; top: Horizontal cross section at level of anchor row 2; bottom: Horizontal cross section between anchor row 2 and anchor row 3

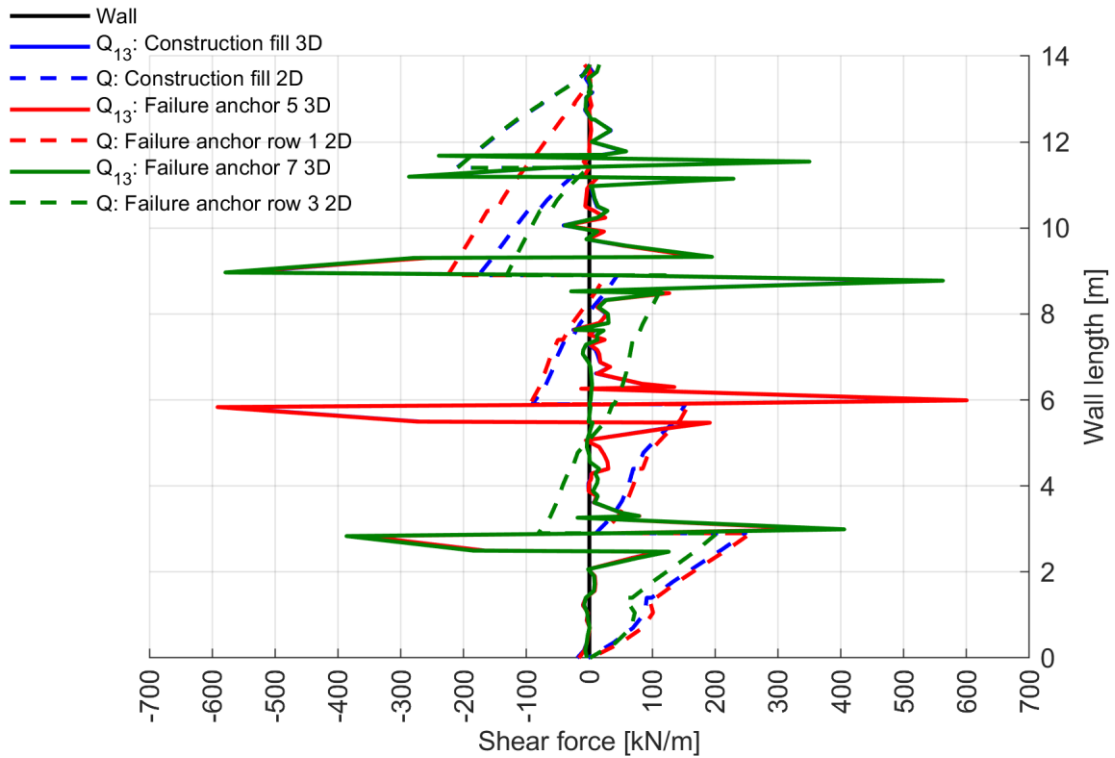


Fig. 204: $SFs Q_{13,actual}$ after Construction fill and single anchor failure cases for $c = 0.1$ kPa; 2D vs. 3D at $y = 7.50$ m

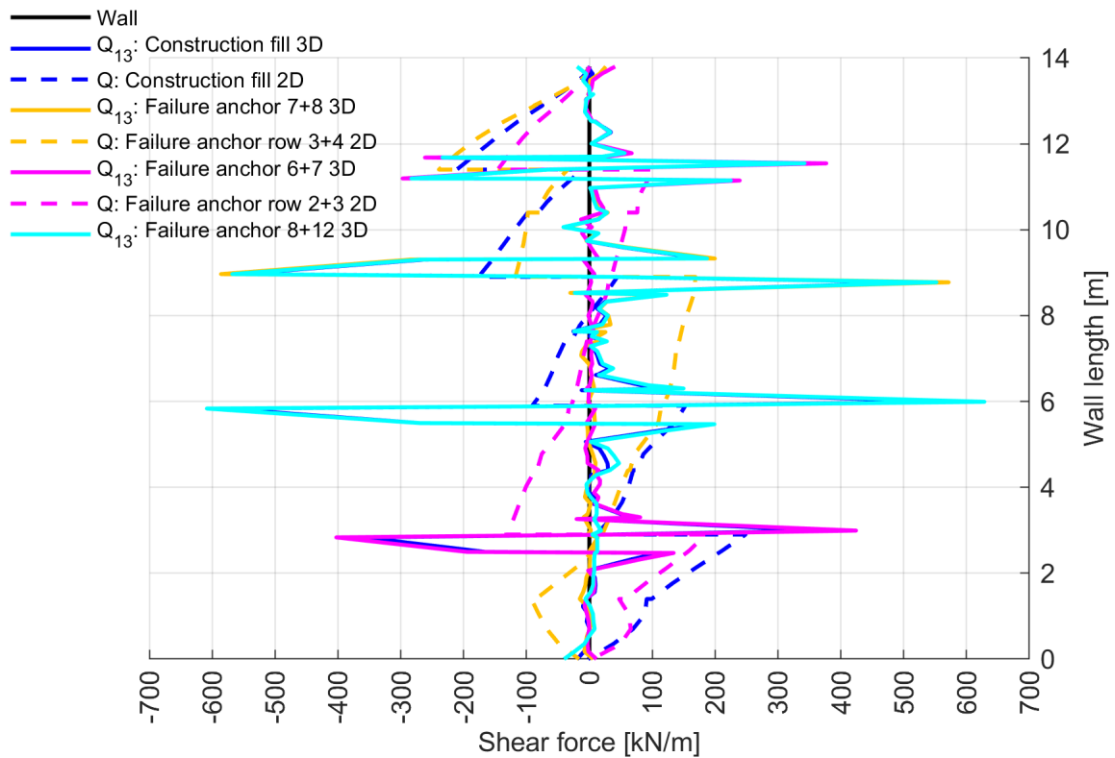


Fig. 205: $SFs Q_{13,actual}$ after Construction fill and double anchor failure cases for $c = 0.1$ kPa; 2D vs. 3D at $y = 7.50$ m

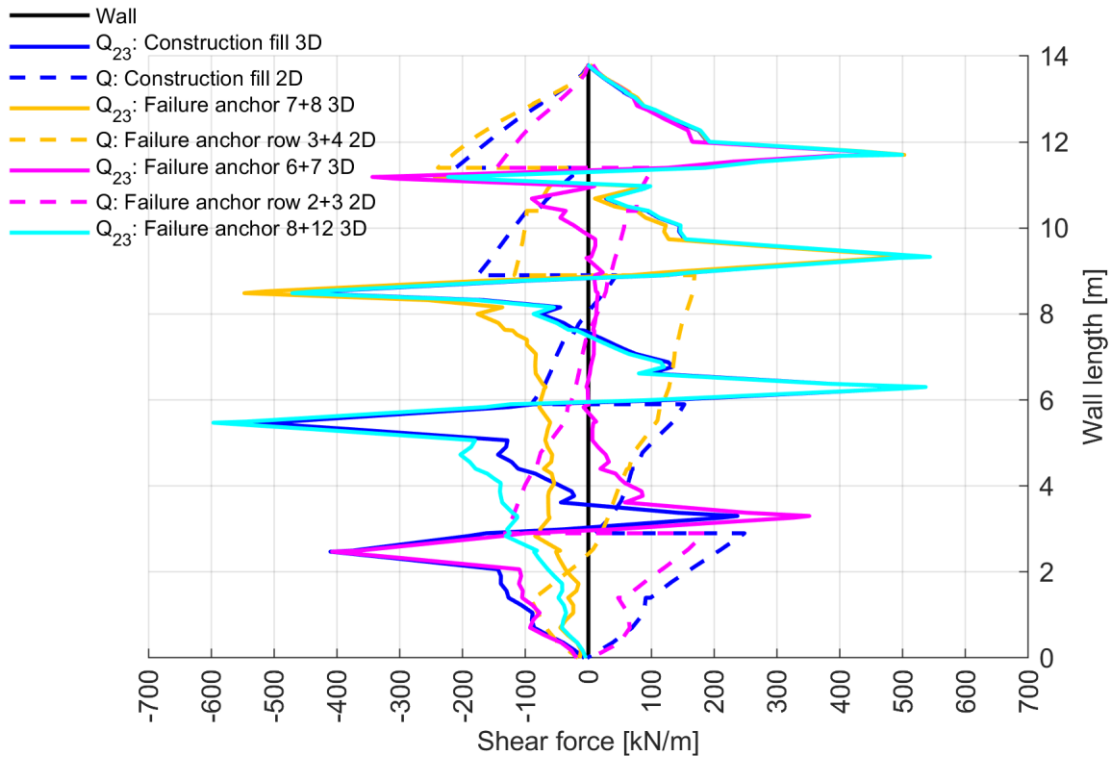


Fig. 206: $SFs Q_{23,actual}$ after Construction fill and double anchor failure cases for $c = 0.1 \text{ kPa}$; 2D vs. 3D at $y = 7.50 \text{ m}$

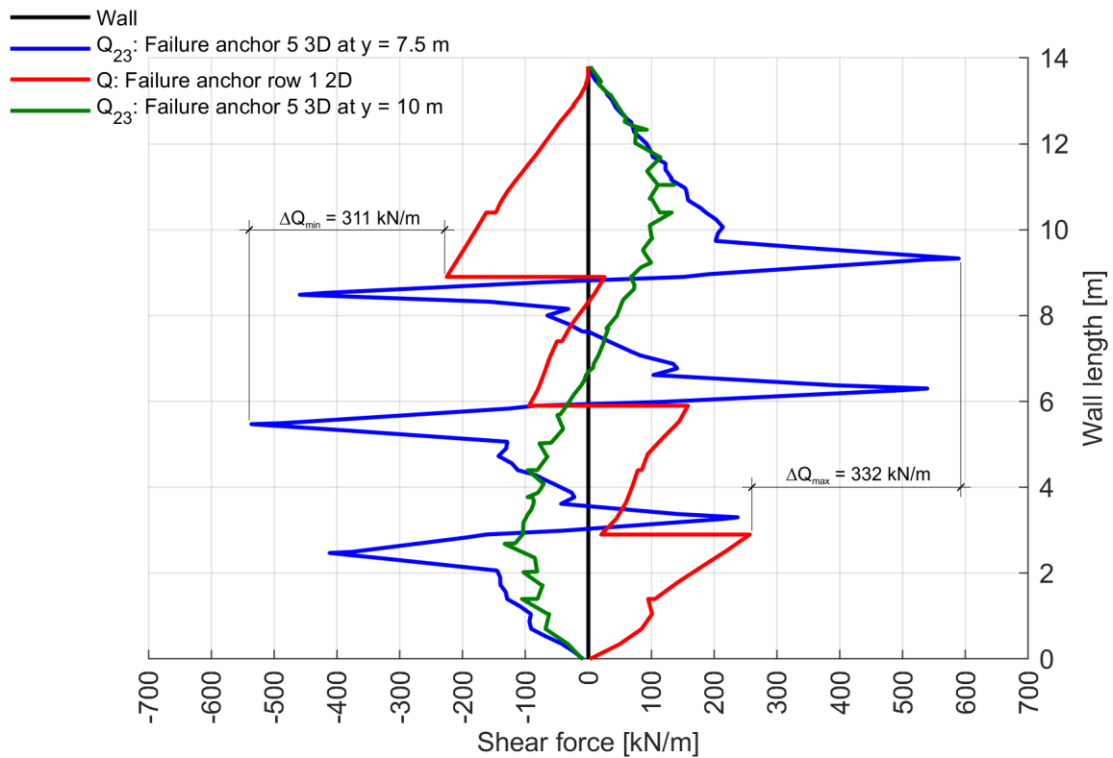


Fig. 207: $SFs Q_{23,actual}$ after Failure anchor 5 for $c = 0.1 \text{ kPa}$; 2D vs. 3D at $y = 7.50/10 \text{ m}$

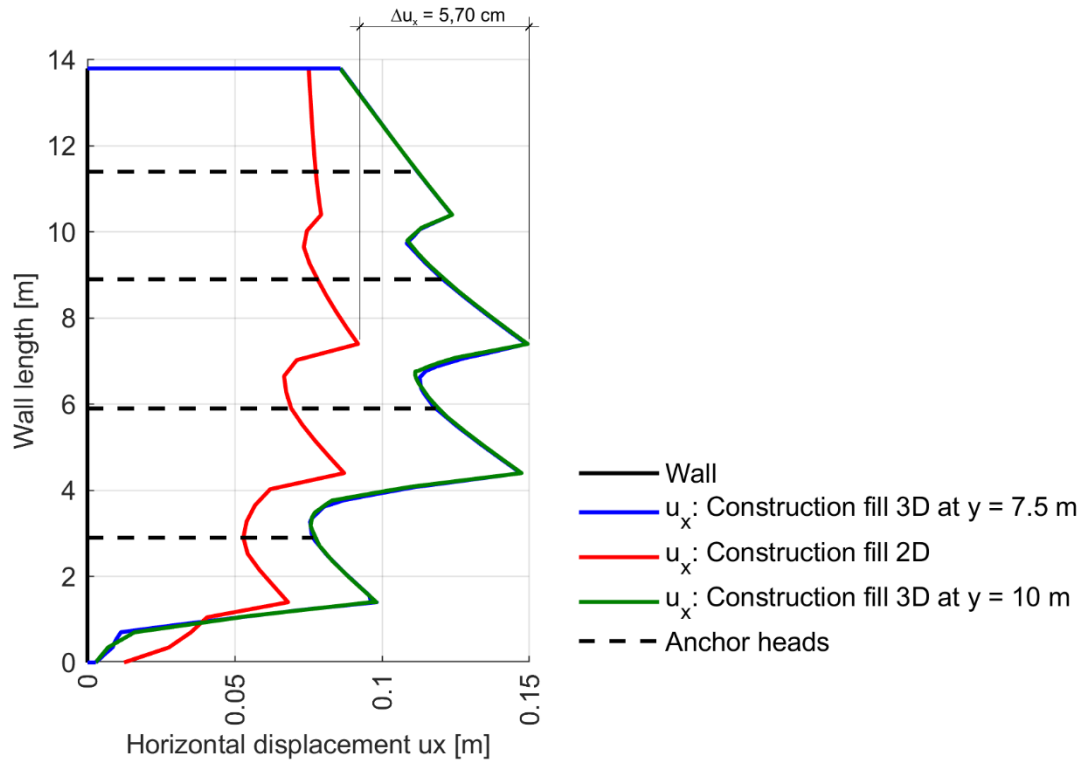


Fig. 208: Horizontal displacements u_x after Construction fill for $c = 0.1$ kPa; 2D vs. 3D at $y = 7.50/10$ m

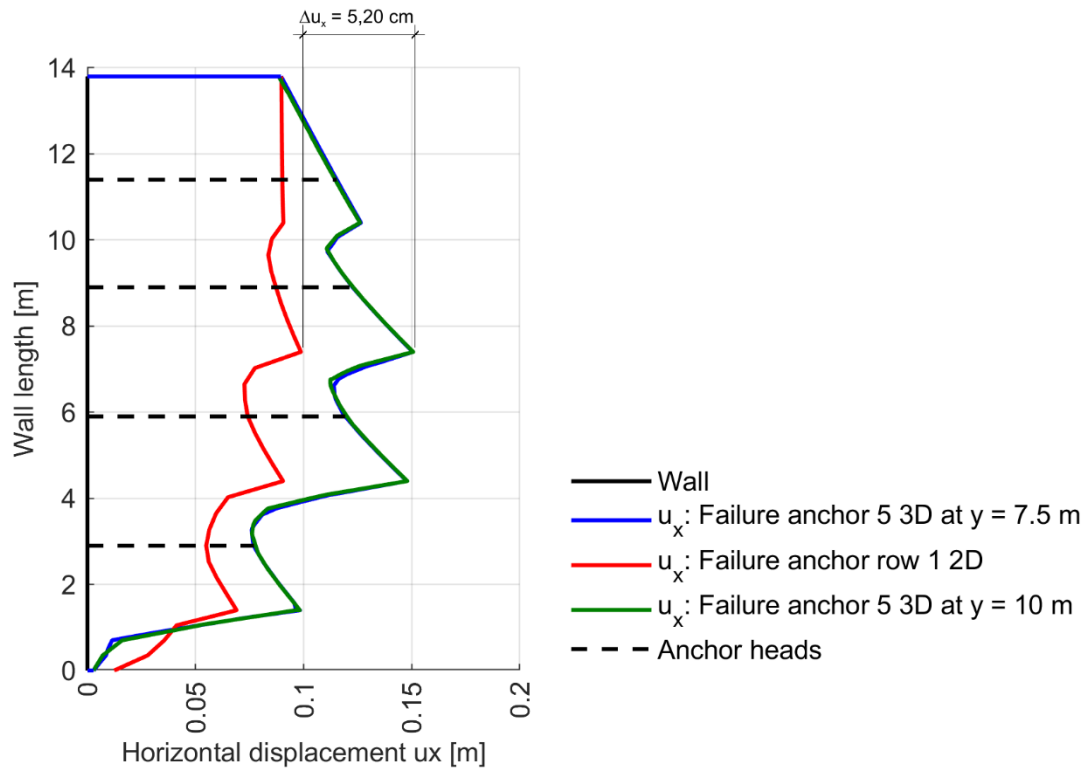


Fig. 209: Horizontal displacements u_x after Failure anchor 5 for $c = 0.1$ kPa; 2D vs. 3D at $y = 7.50/10$ m

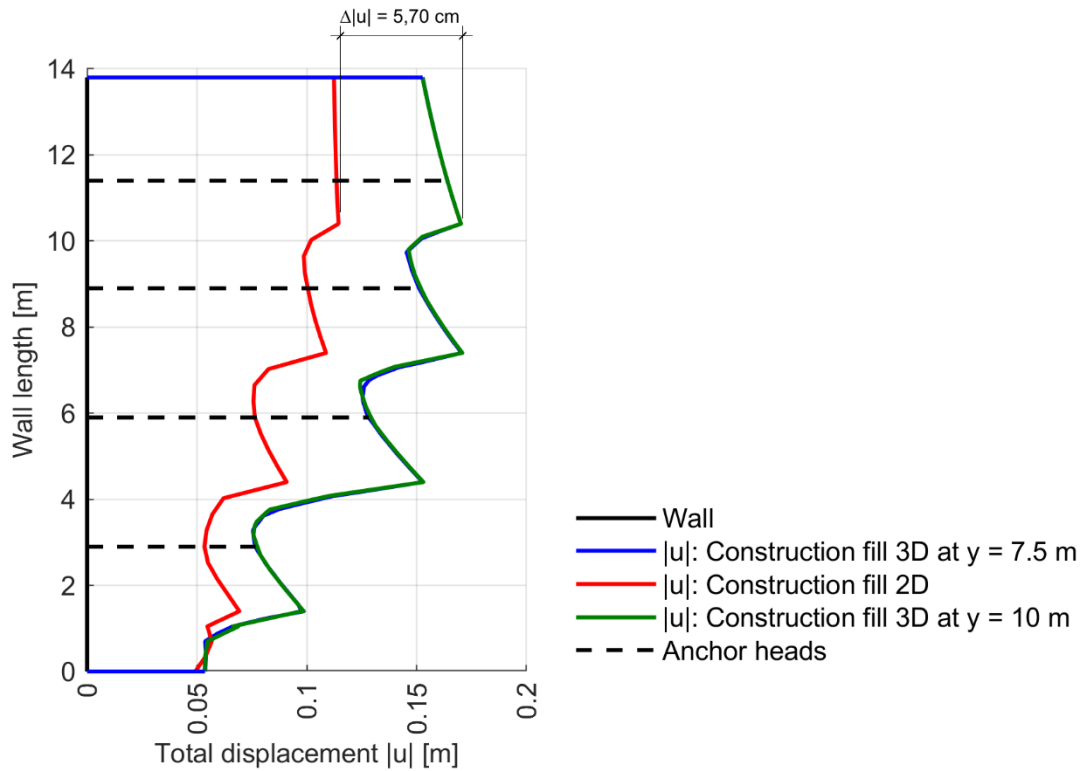


Fig. 210: Total displacements $|u|$ after Construction fill for $c = 0.1$ kPa; 2D vs. 3D at $y = 7.50/10$ m

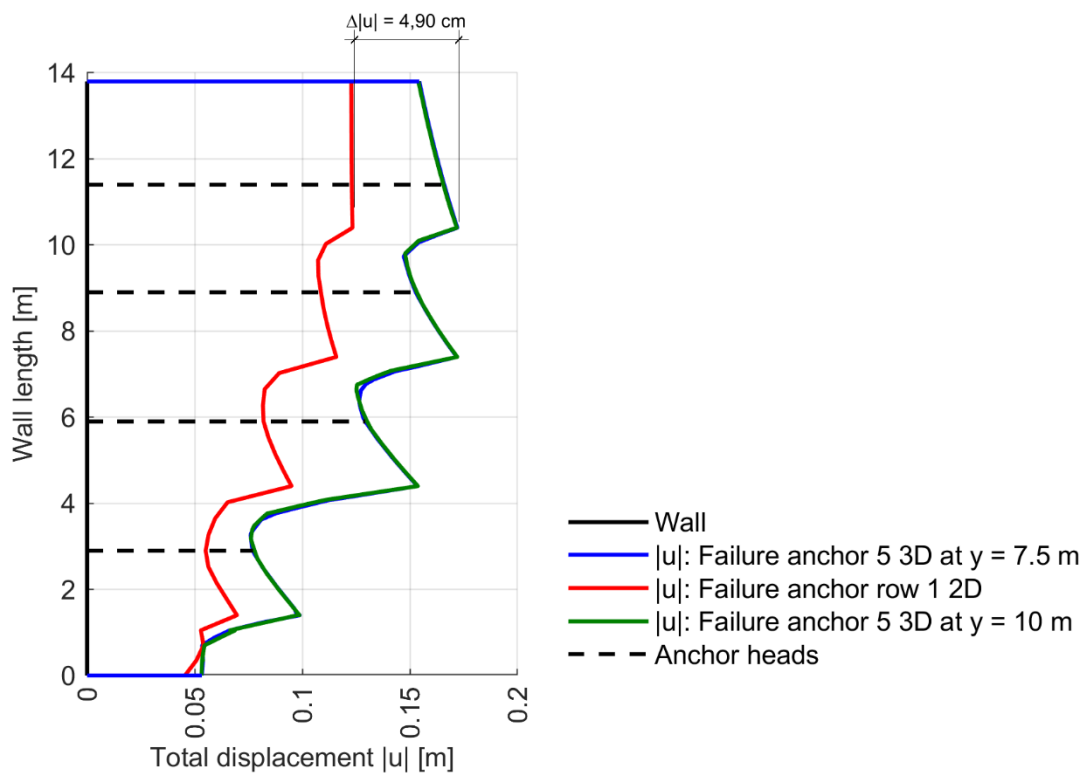


Fig. 211: Total displacements $|u|$ after Failure anchor 5 for $c = 0.1$ kPa; 2D vs. 3D at $y = 7.50/10$ m

8.7 $MC_{R_{inter}=0.9_EB_Constant_Anchor}$ Pre-stressed in 3D

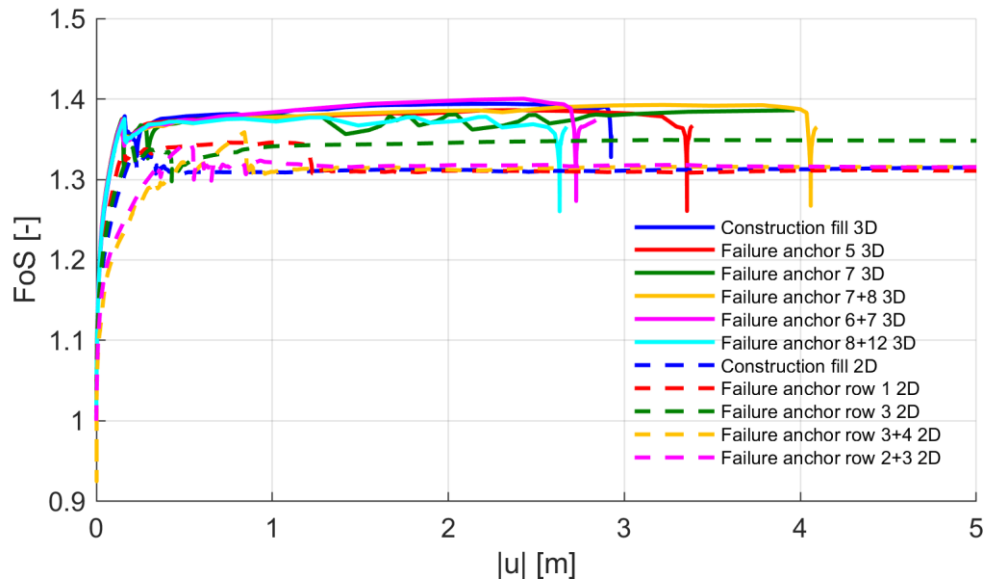


Fig. 212: FoS after φ - c reduction Construction fill and Failure cases for $c = 0.1$ kPa; EBs with constant skin resistance; 2D vs. 3D

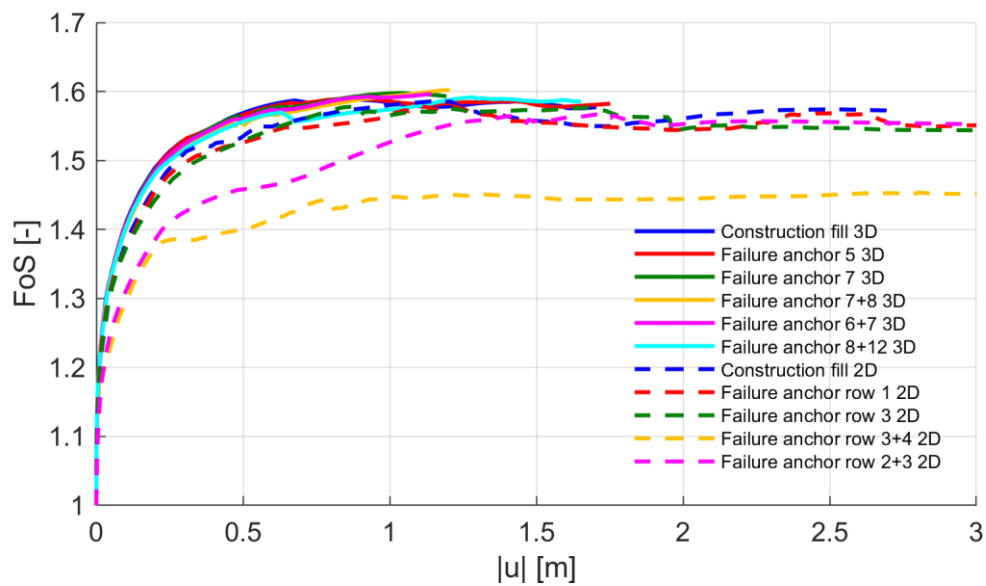


Fig. 213: FoS after φ - c reduction Construction fill and Failure cases for $c = 5$ kPa; EBs with constant skin resistance; 2D vs. 3D

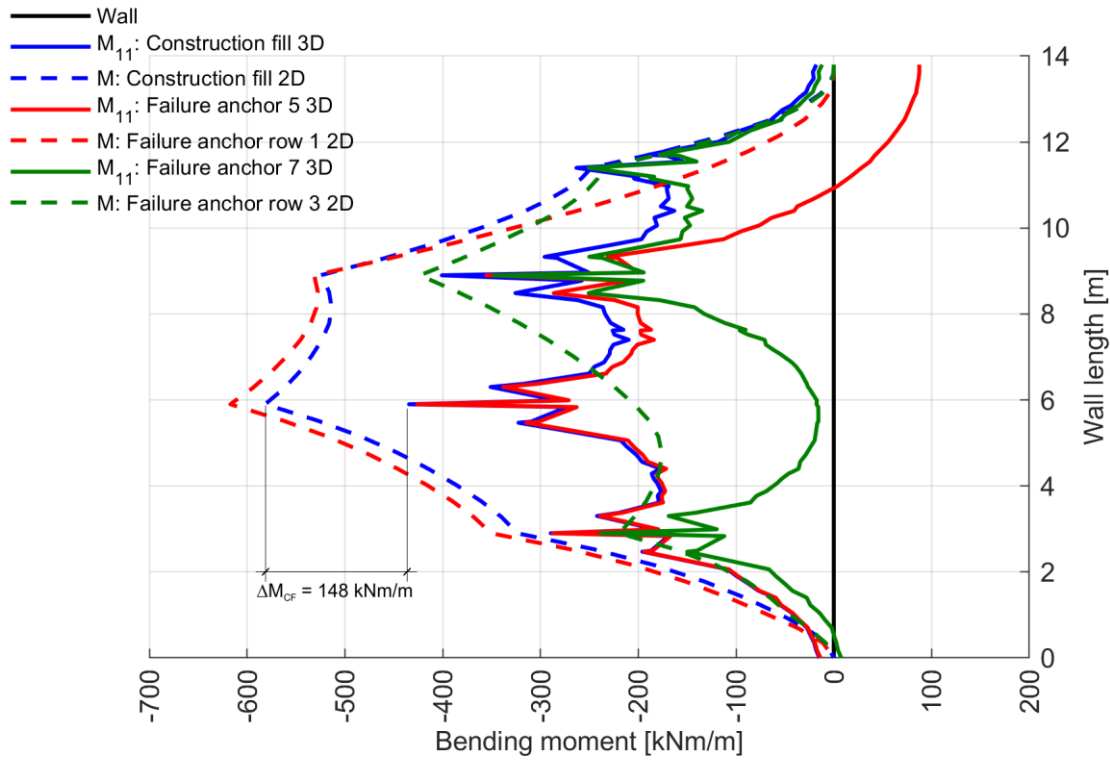


Fig. 214: $BM_s M_{11,actual}$ after Construction fill and single anchor failure cases for $c = 0.1 \text{ kPa}$; EBs with constant skin resistance; 2D vs. 3D at $y = 7.50 \text{ m}$

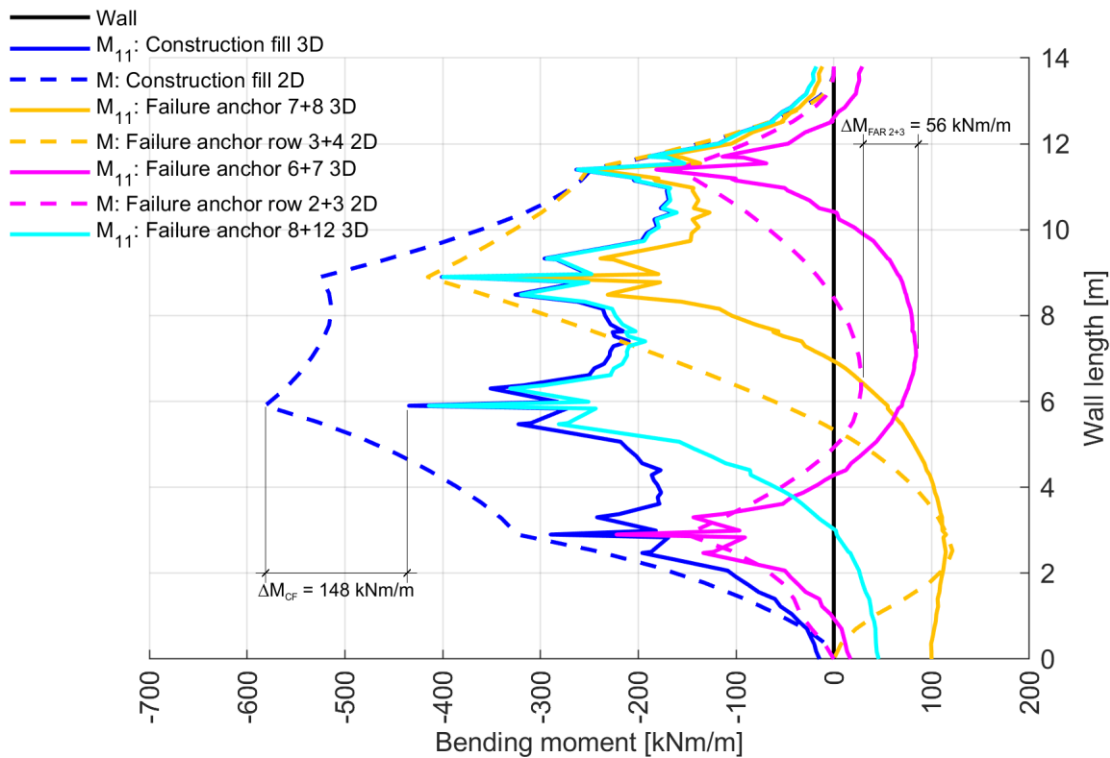


Fig. 215: $BM_s M_{11,actual}$ after Construction fill and double anchor failure cases for $c = 0.1 \text{ kPa}$; EBs with constant skin resistance; 2D vs. 3D at $y = 7.50 \text{ m}$

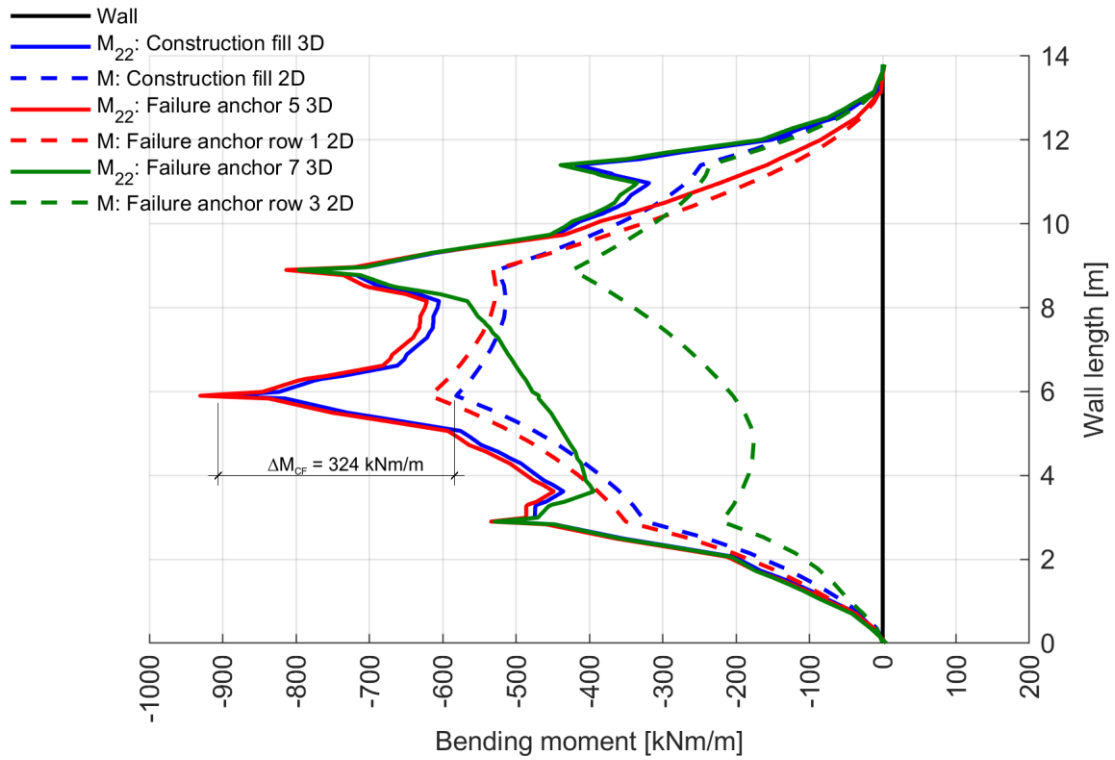


Fig. 216: $BM_s M_{22,actual}$ after Construction fill and single anchor failure cases for $c = 0.1$ kPa; EBs with constant skin resistance; 2D vs. 3D at $y = 7.50$ m

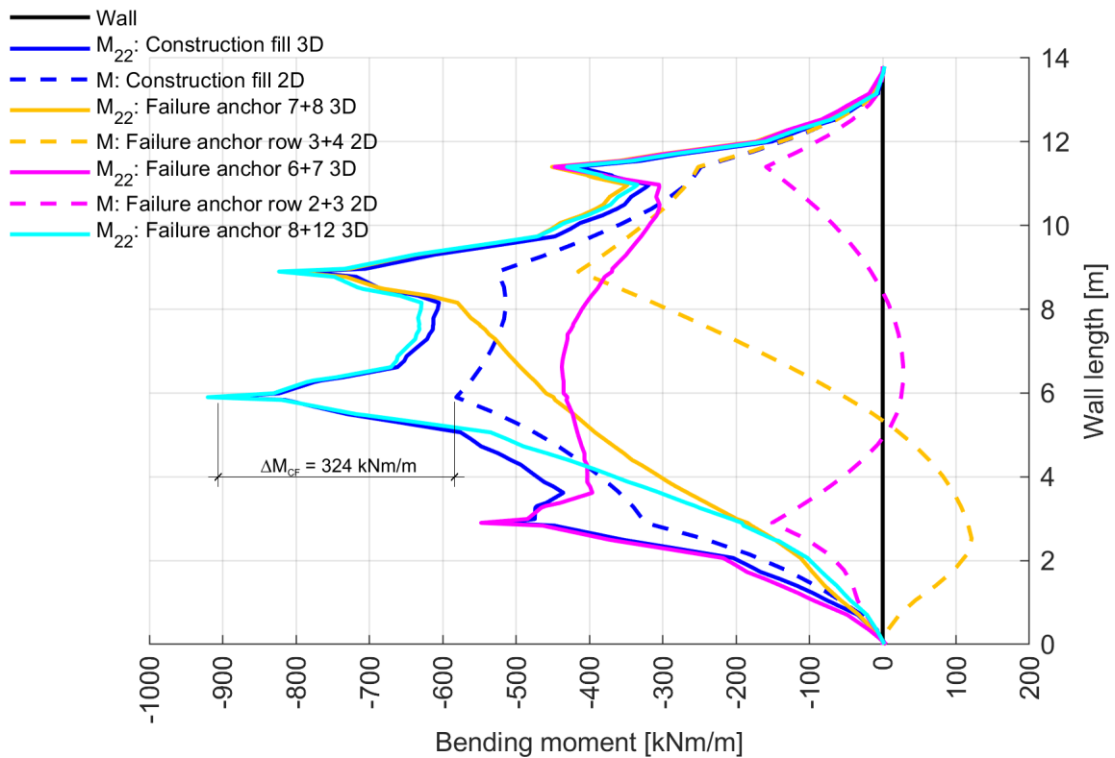


Fig. 217: $BM_s M_{22,actual}$ after Construction fill and double anchor failure cases for $c = 0.1$ kPa; EBs with constant skin resistance; 2D vs. 3D at $y = 7.50$ m

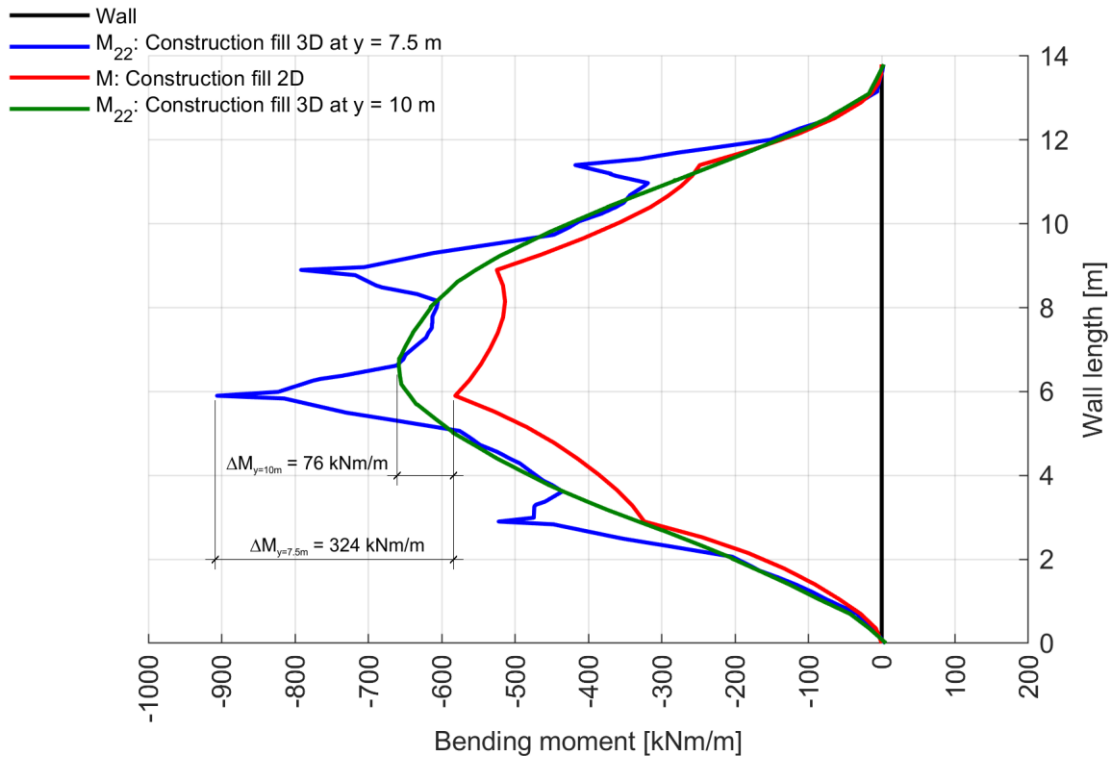


Fig. 218: $BM_s M_{22,actual}$ after Construction fill for $c = 0.1$ kPa; EBs with constant skin resistance; 2D vs. 3D at $y = 7.50/10$ m

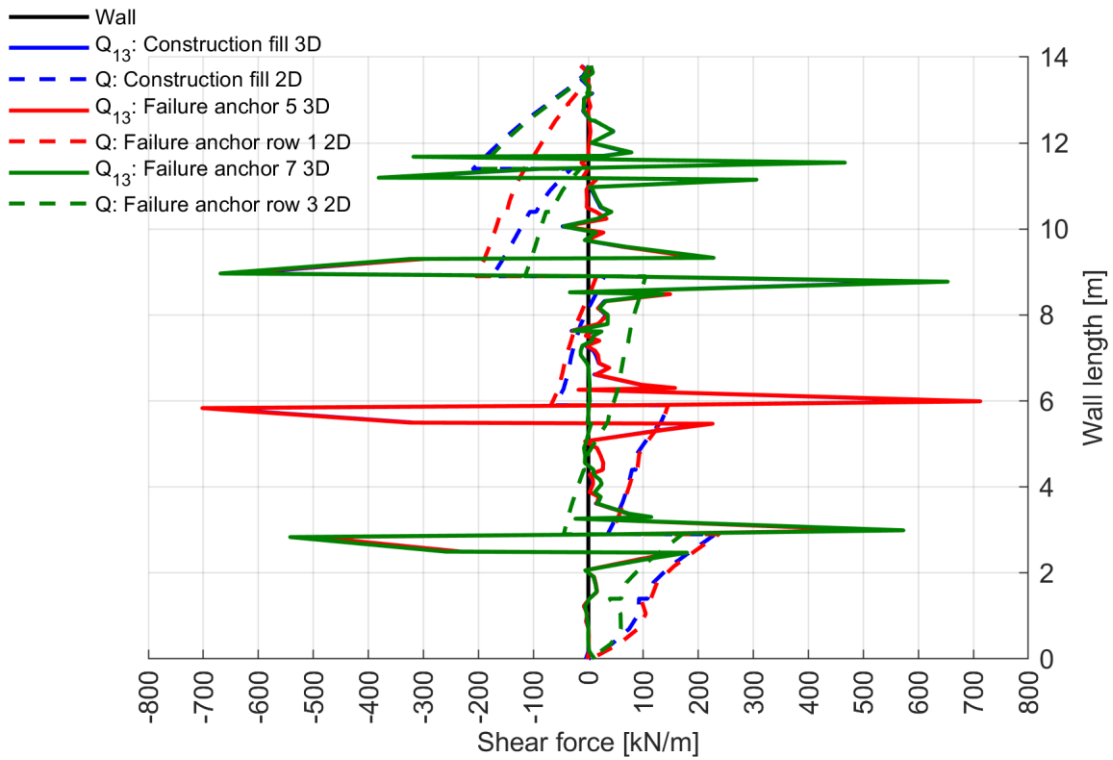


Fig. 219: $SFs Q_{13,actual}$ after Construction fill and single anchor failure cases for $c = 0.1$ kPa; EBs with constant skin resistance; 2D vs. 3D at $y = 7.50$ m

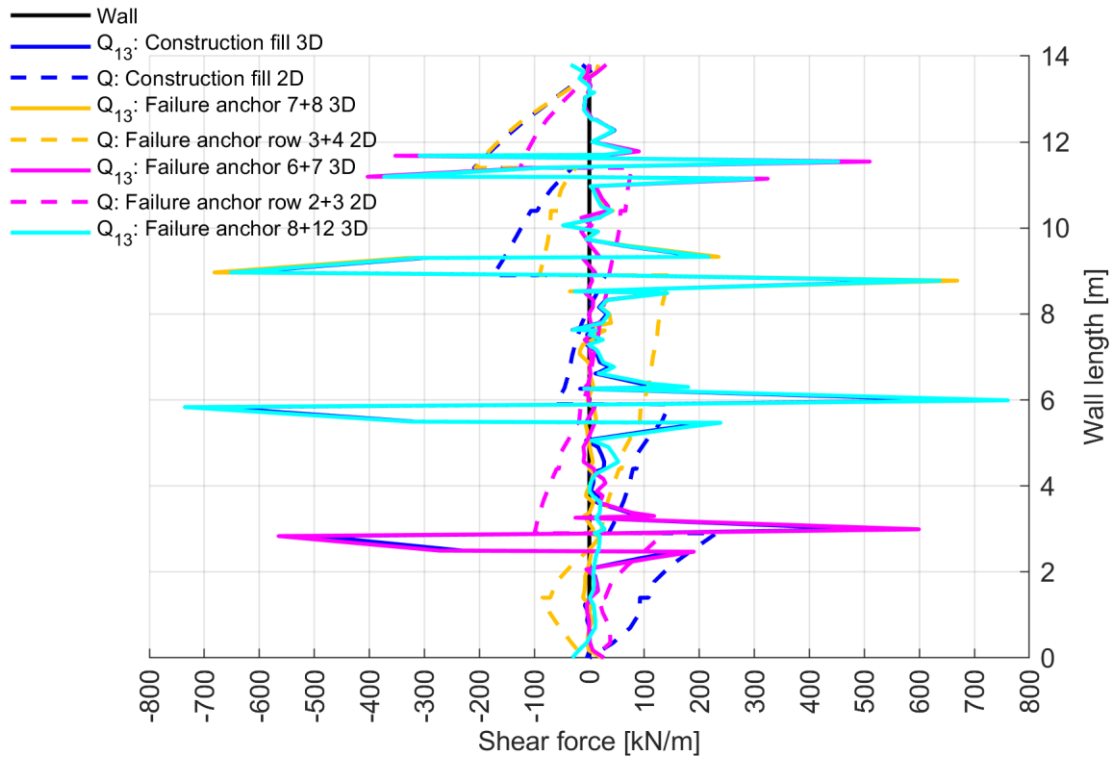


Fig. 220: $SFs Q_{13,actual}$ after Construction fill and double anchor failure cases for $c = 0.1$ kPa; EBs with constant skin resistance; 2D vs. 3D at $y = 7.50$ m

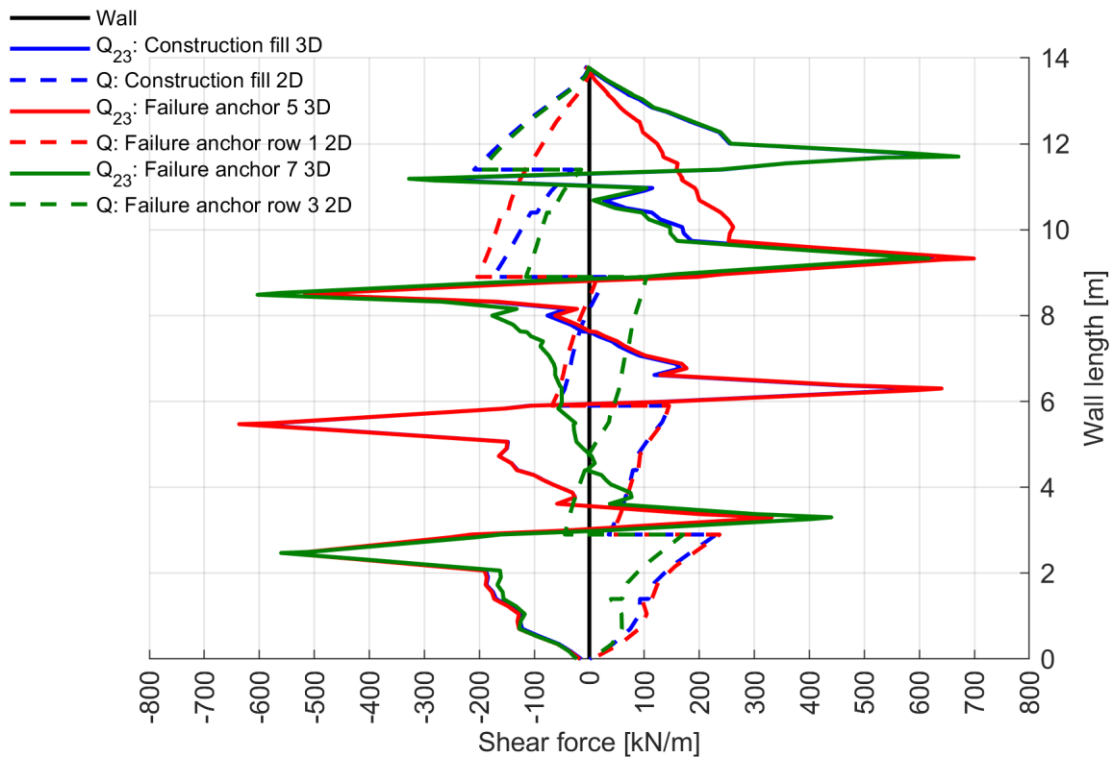


Fig. 221: $SFs Q_{23,actual}$ after Construction fill and single anchor failure cases for $c = 0.1$ kPa; EBs with constant skin resistance; 2D vs. 3D at $y = 7.50$ m

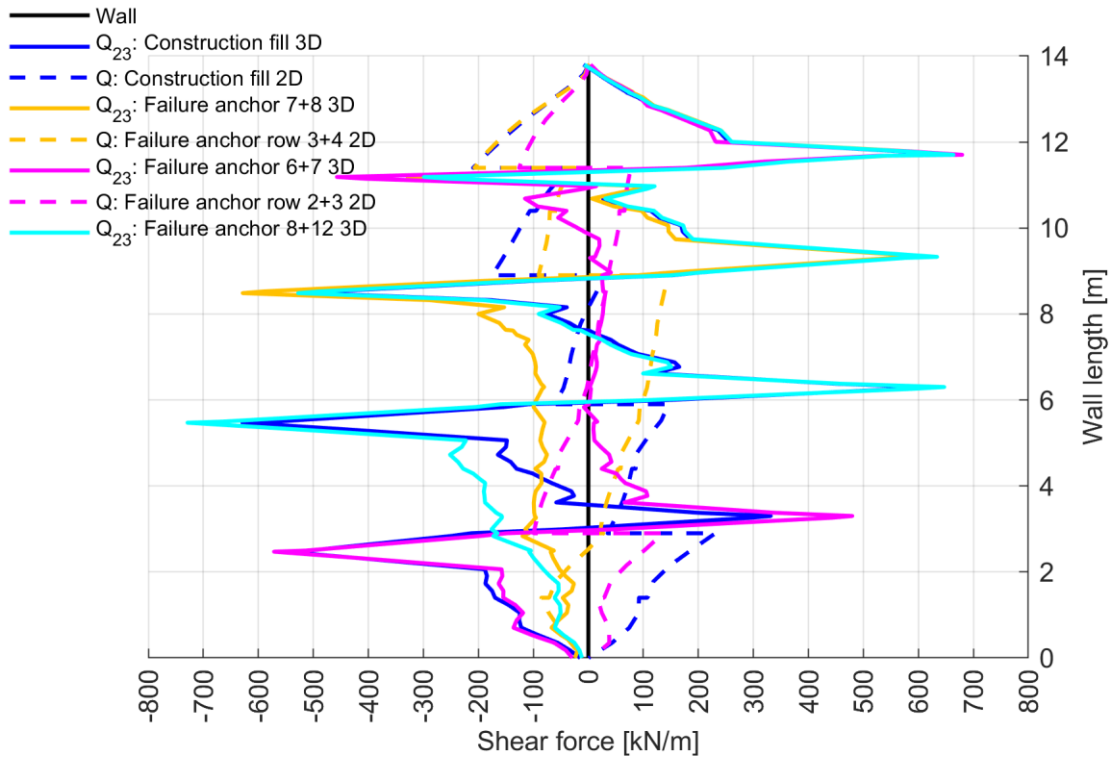


Fig. 222: $SFs Q_{23,actual}$ after Construction fill and double anchor failure cases for $c = 0.1 \text{ kPa}$; EBs with constant skin resistance; 2D vs. 3D at $y = 7.50 \text{ m}$

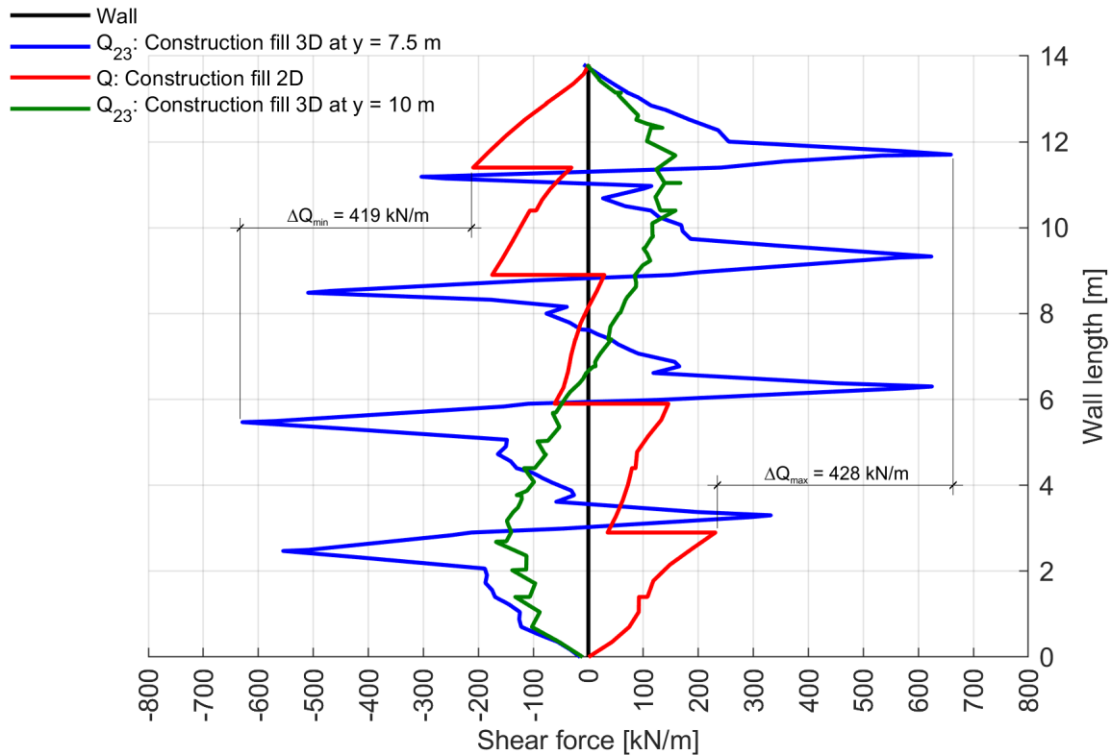


Fig. 223: $SFs Q_{23,actual}$ after Construction fill for $c = 0.1 \text{ kPa}$; EBs with constant skin resistance; 2D vs. 3D at $y = 7.50/10 \text{ m}$

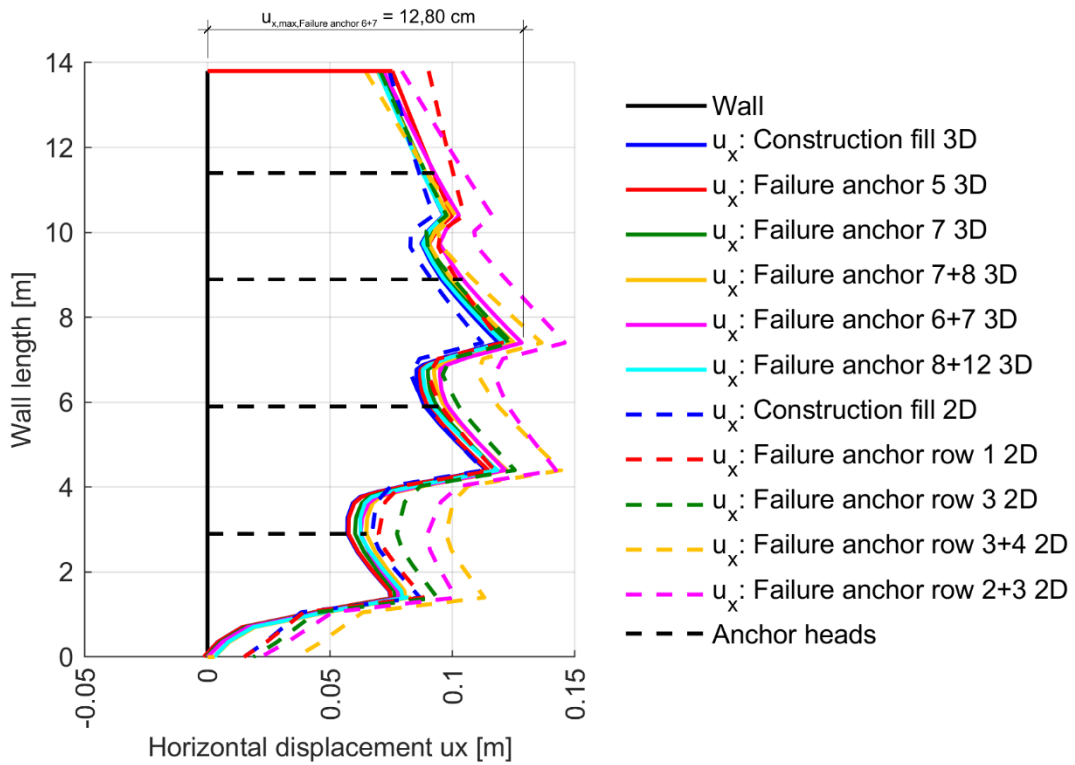


Fig. 224: Horizontal displacements u_x after Construction fill and Failure cases for $c = 0.1$ kPa; EBs with constant skin resistance; 2D vs. 3D at $y = 7.50$ m

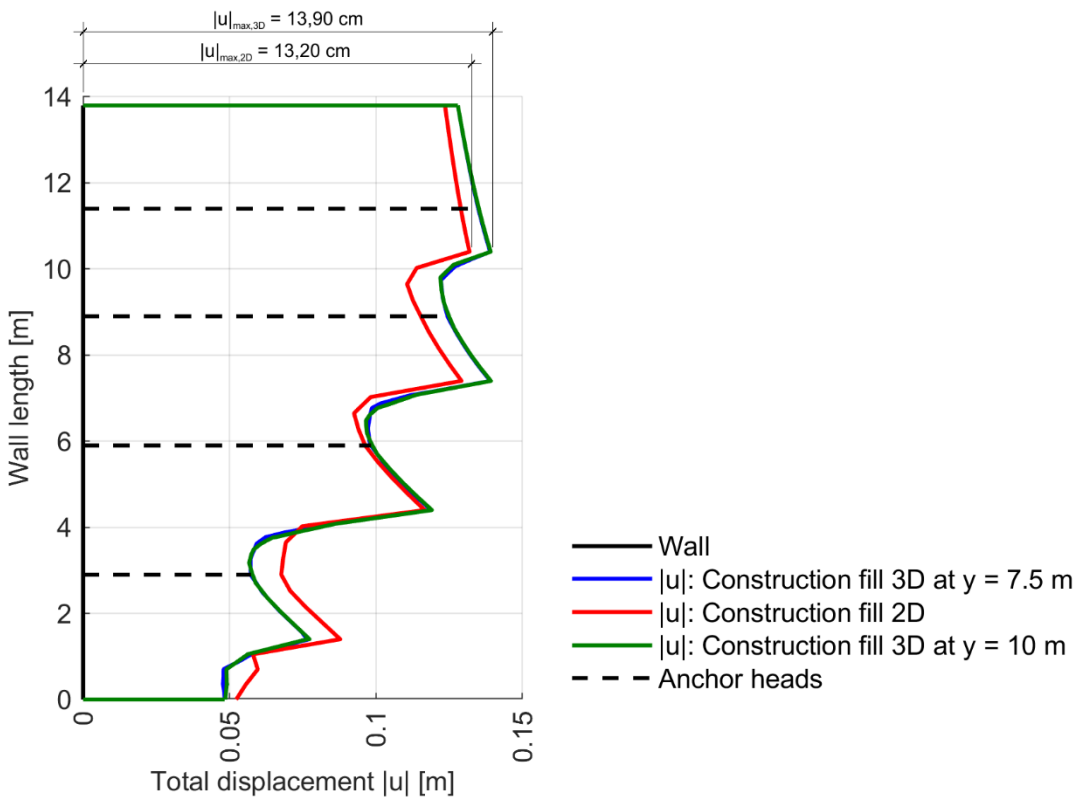


Fig. 225: Horizontal displacements u_x after Construction fill for $c = 0.1$ kPa; EBs with constant skin resistance; 2D vs. 3D at $y = 7.50/10$ m

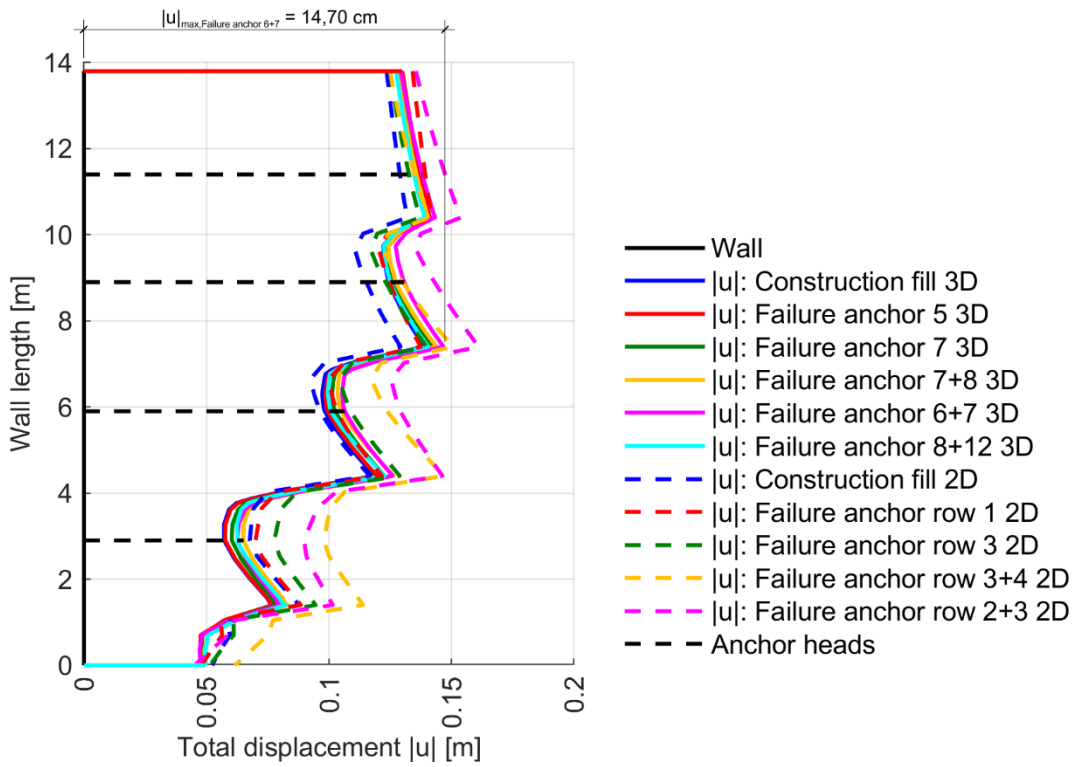


Fig. 226: Total displacements $|u|$ after Construction fill and Failure cases for $c = 0.1$ kPa; EBs with constant skin resistance; 2D vs. 3D at $y = 7.50$ m

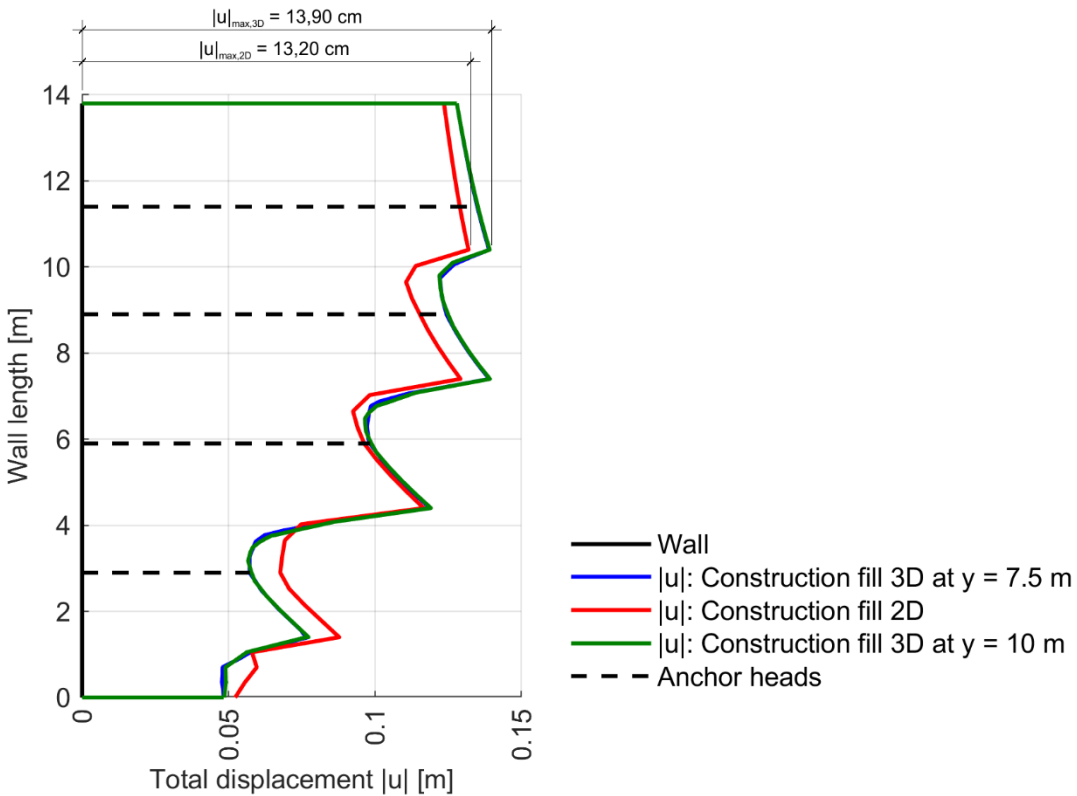


Fig. 227: Total displacements $|u|$ after Construction fill for $c = 0.1$ kPa; EBs with constant skin resistance; 2D vs. 3D at $y = 7.50/10$ m

8.8 $MC_{R_{inter}=0.9_EB_Linear_Anchor}$ Pre-stressed in 3D

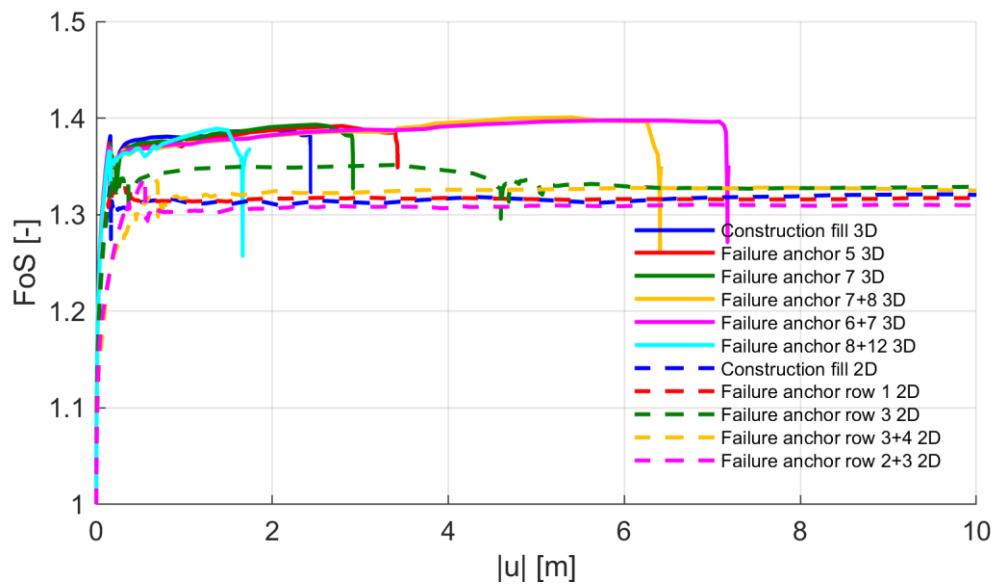


Fig. 228: FoS after φ - c reduction Construction fill and Failure cases for $c = 0.1$ kPa; EBs with linear skin resistance; 2D vs. 3D

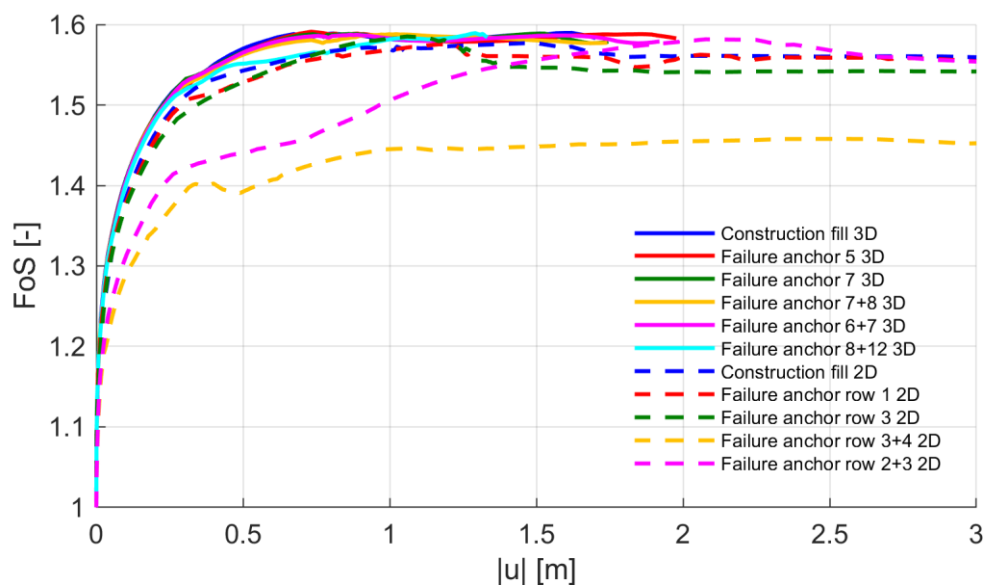


Fig. 229: FoS after φ - c reduction Construction fill and Failure cases for $c = 5$ kPa; EBs with linear skin resistance; 2D vs. 3D

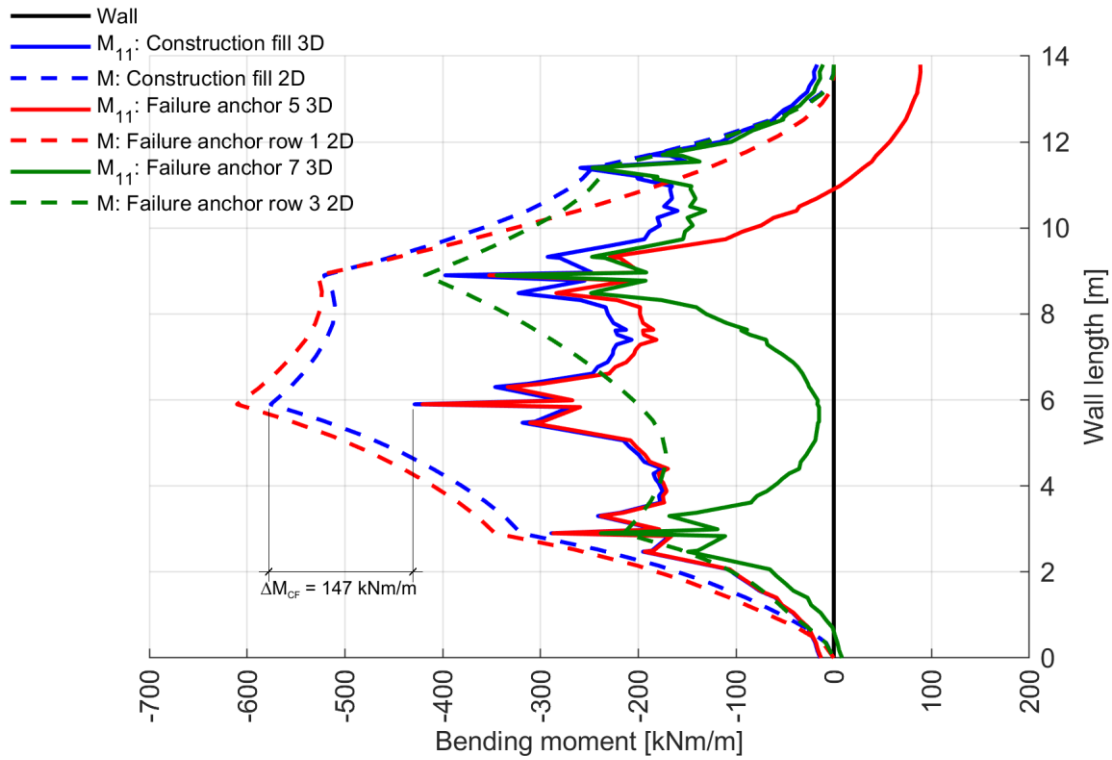


Fig. 230: $BM_s M_{11,actual}$ after Construction fill and single anchor failure cases for $c = 0.1 \text{ kPa}$; EBs with linear skin resistance; 2D vs. 3D at $y = 7.50 \text{ m}$

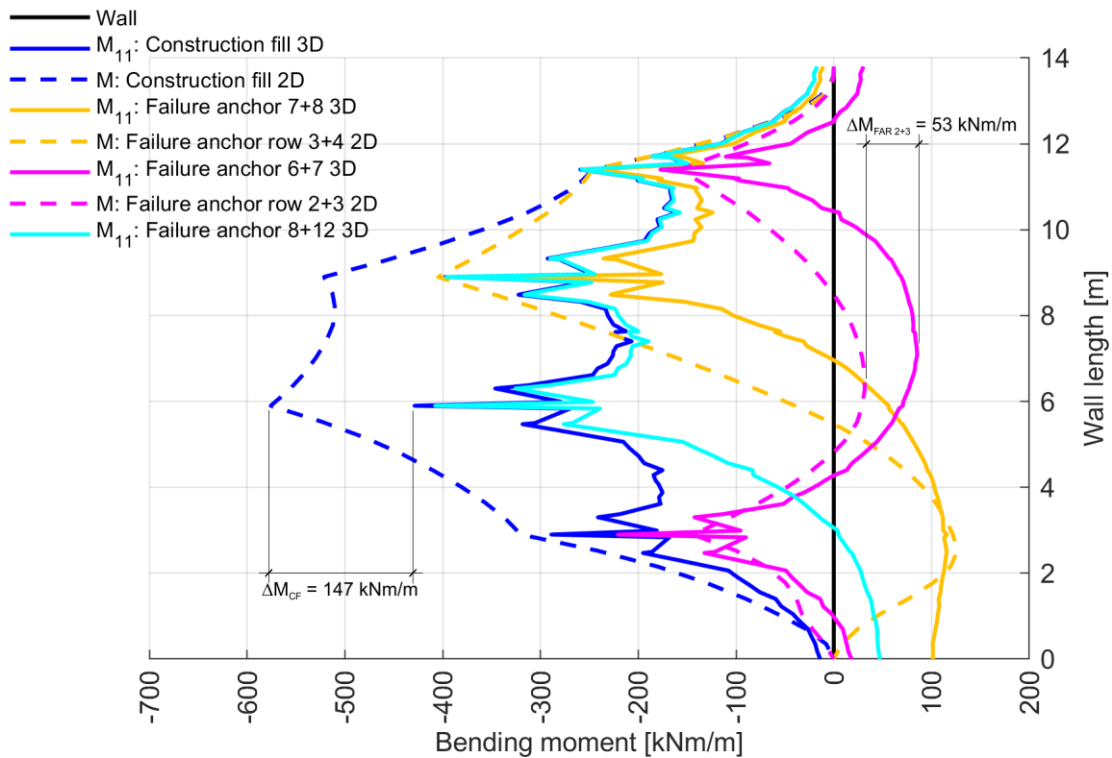


Fig. 231: $BM_s M_{11,actual}$ after Construction fill and double anchor failure cases for $c = 0.1 \text{ kPa}$; EBs with linear skin resistance; 2D vs. 3D at $y = 7.50 \text{ m}$

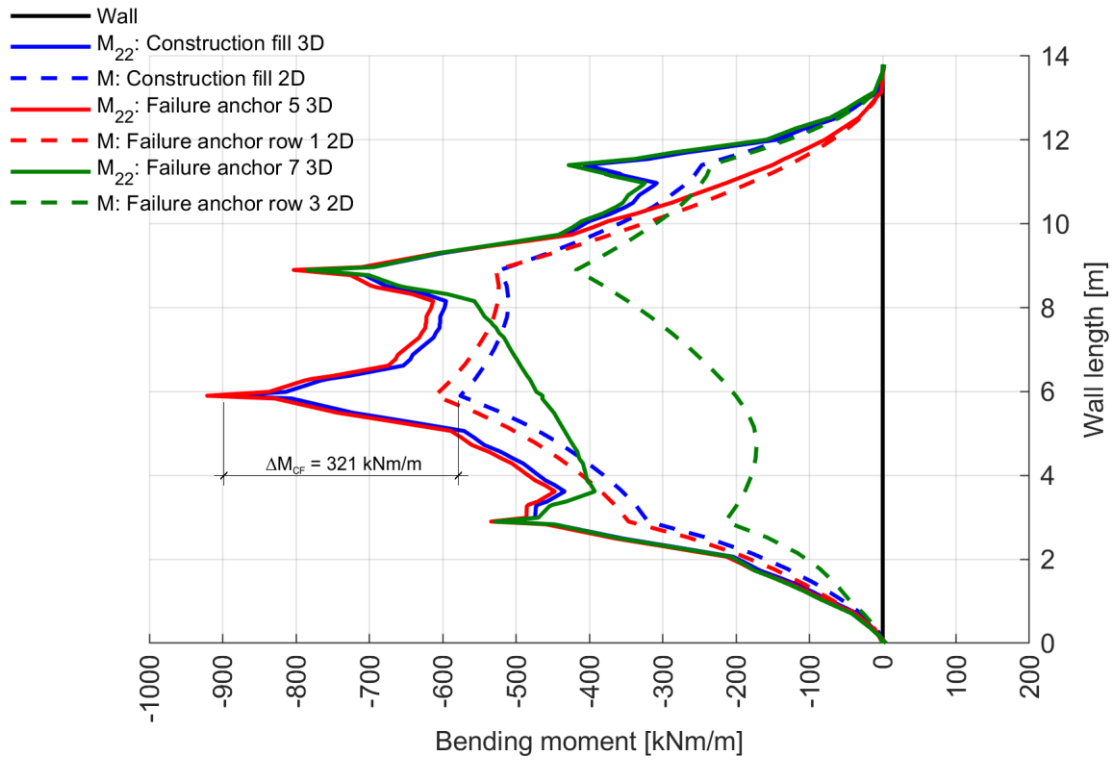


Fig. 232: $BMs M_{22,actual}$ after Construction fill and single anchor failure cases for $c = 0.1 \text{ kPa}$; EBs with linear skin resistance; 2D vs. 3D at $y = 7.50 \text{ m}$

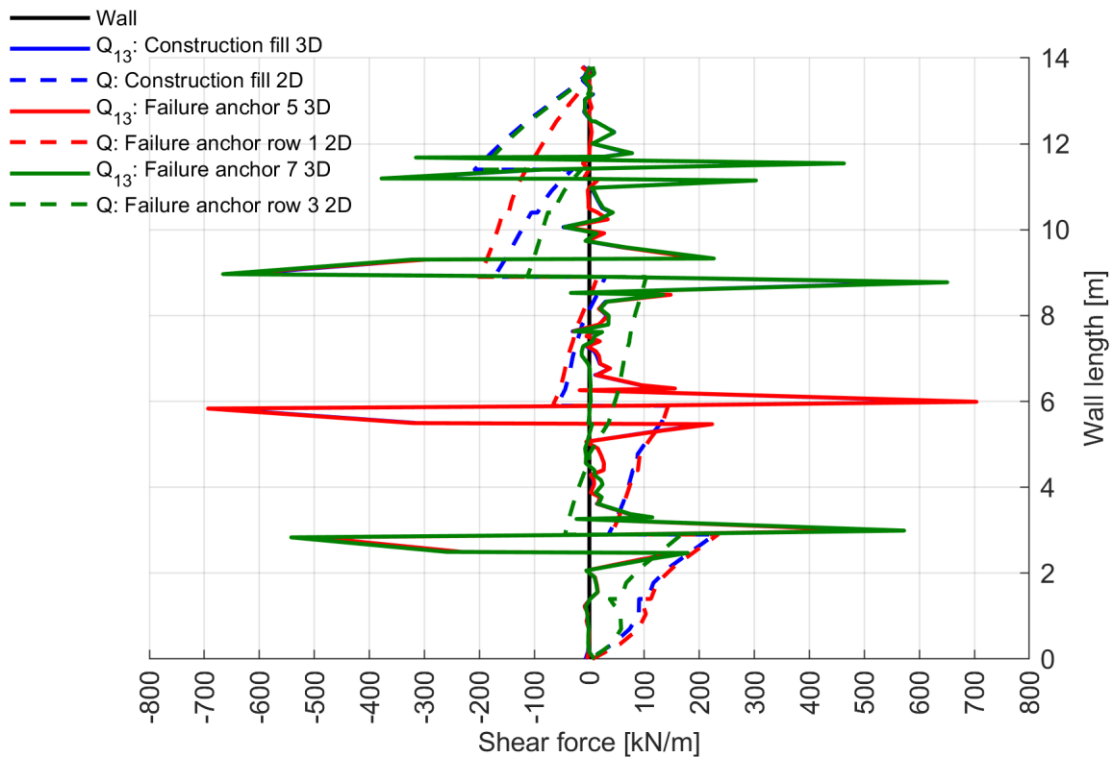


Fig. 233: $SFs Q_{13,actual}$ after Construction fill and single anchor failure cases for $c = 0.1 \text{ kPa}$; EBs with linear skin resistance; 2D vs. 3D at $y = 7.50 \text{ m}$

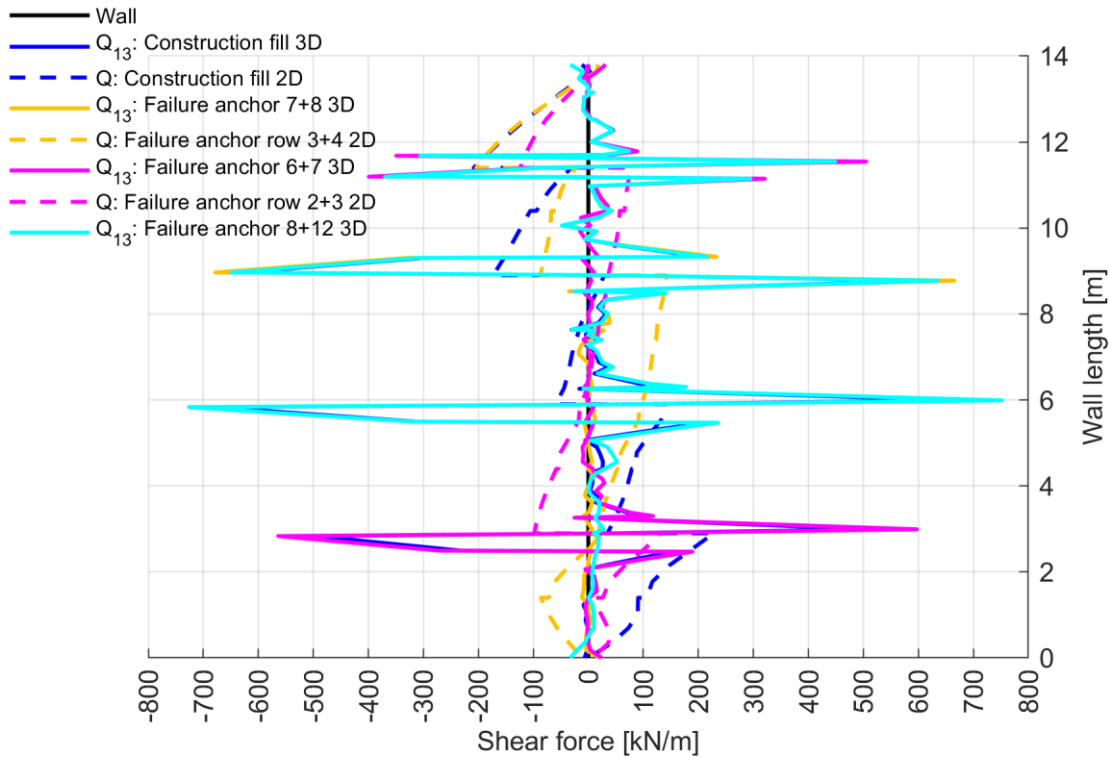


Fig. 234: $SFs Q_{13,actual}$ after Construction fill and double anchor failure cases for $c = 0.1 \text{ kPa}$; EBs with linear skin resistance; 2D vs. 3D at $y = 7.50 \text{ m}$

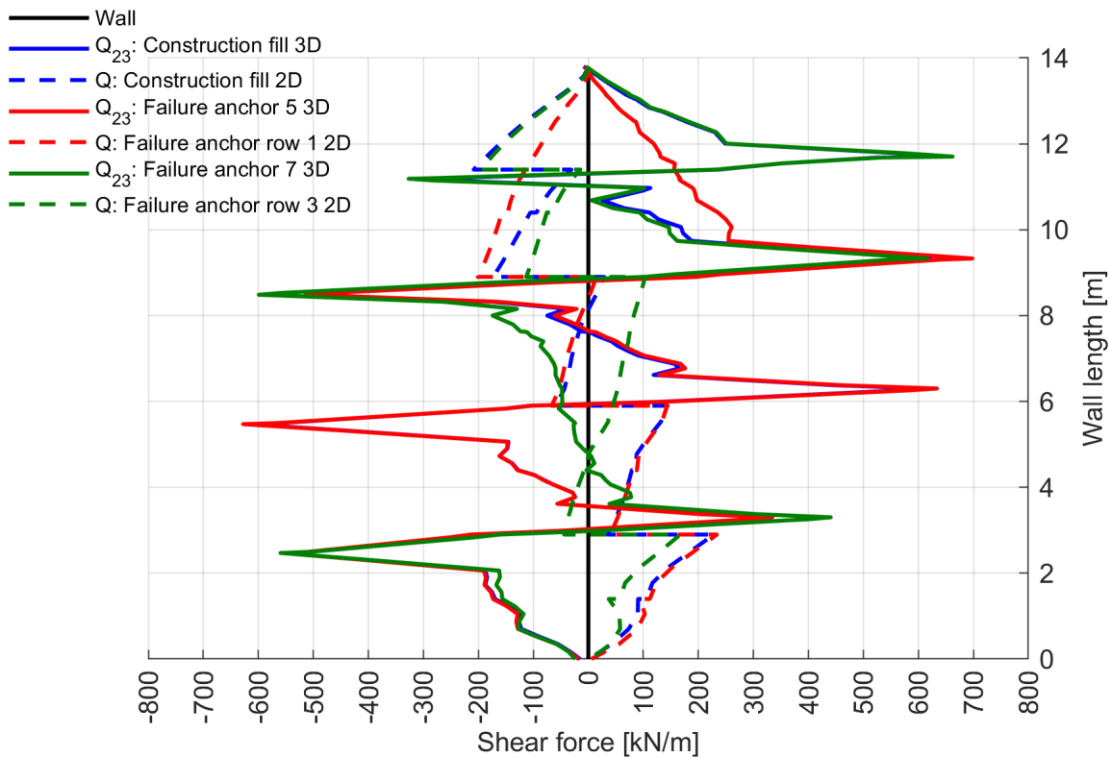


Fig. 235: $SFs Q_{23,actual}$ after Construction fill and single anchor failure cases for $c = 0.1 \text{ kPa}$; EBs with linear skin resistance; 2D vs. 3D at $y = 7.50 \text{ m}$

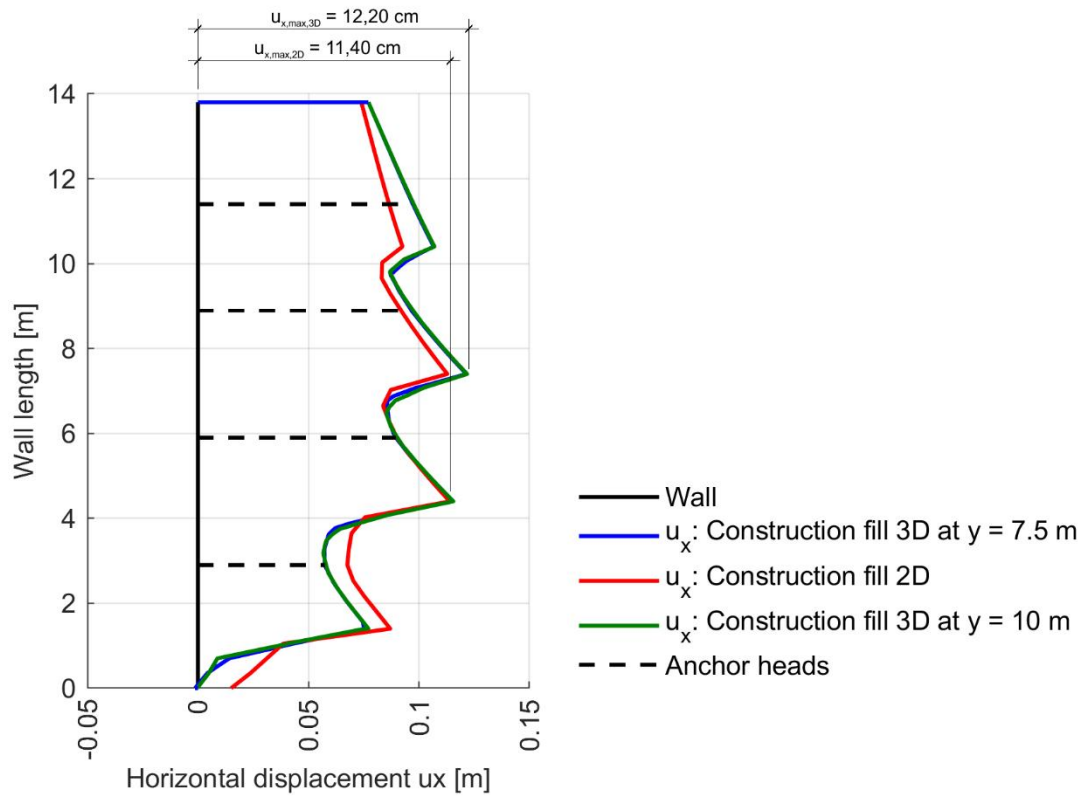


Fig. 236: Horizontal displacements u_x after Construction fill for $c = 0.1 \text{ kPa}$; *EBs* with linear skin resistance; 2D vs. 3D at $y = 7.50/10 \text{ m}$

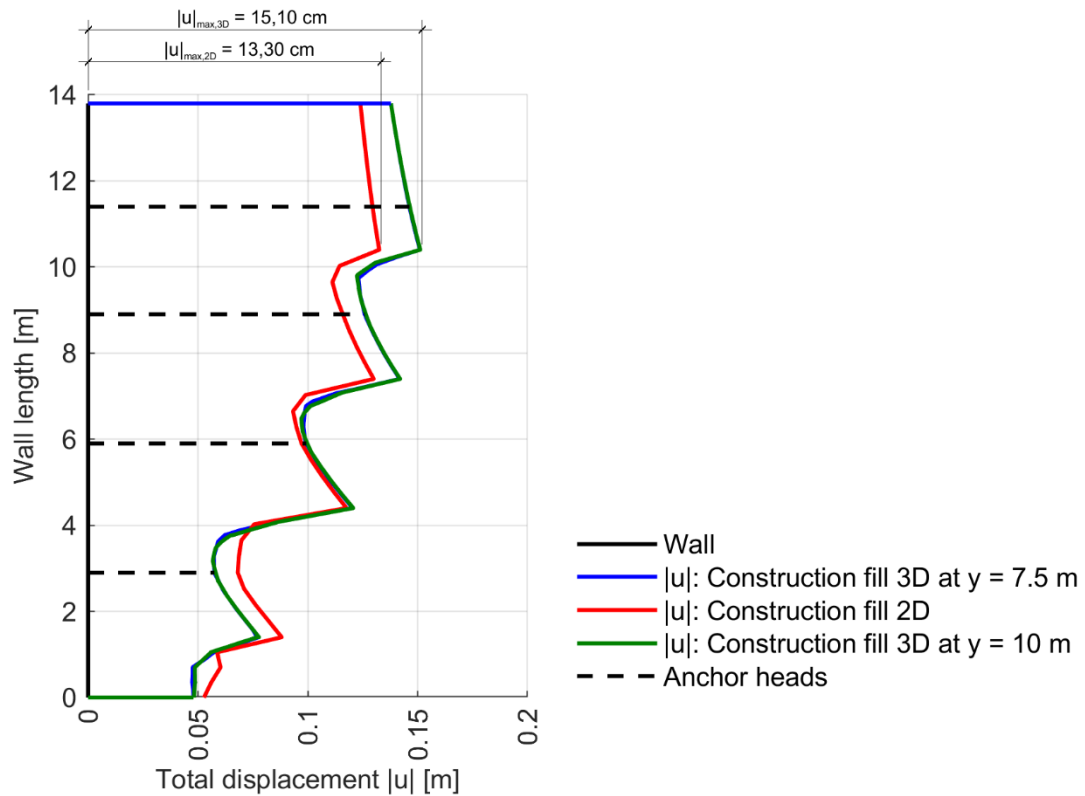
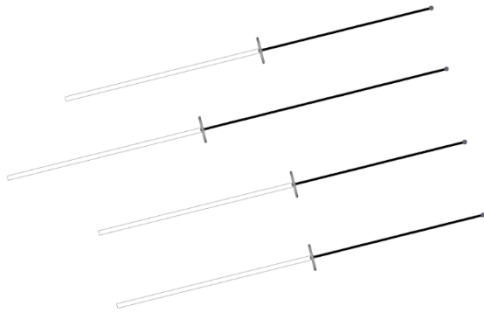


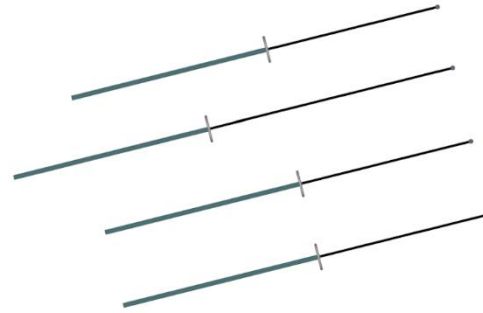
Fig. 237: Total displacements $|u|$ after Construction fill for $c = 0.1 \text{ kPa}$; *EBs* with linear skin resistance; 2D vs. 3D at $y = 7.50/10 \text{ m}$

8.9 $MC_{R_{inter}=1}$ _VolumeElements_AnchorPre-stressed in 3D

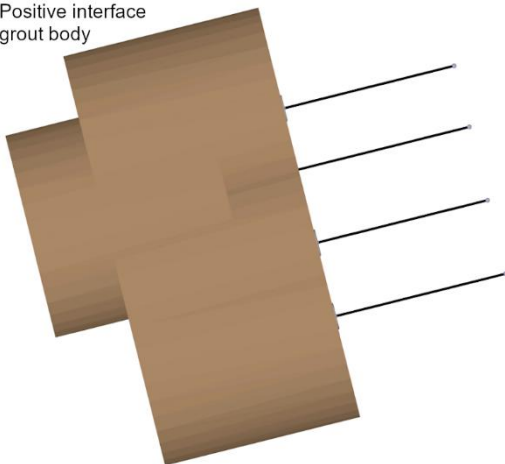
Tendon modelled as node-to-node anchor



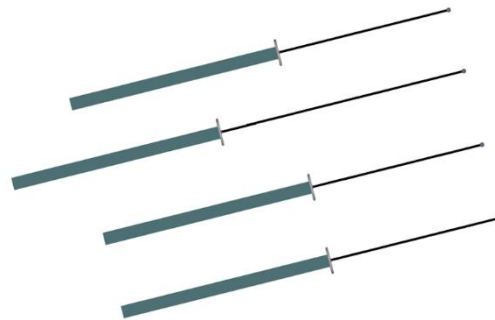
Grout body: Length = 8 m; Diameter = 0.178 m



Positive interface
grout body



Inner volume for mesh refinement:
Length = 8.50 m; Diameter = 0.50 m



Outer volume for mesh refinement:
Length = 9 m; Diameter = 1 m

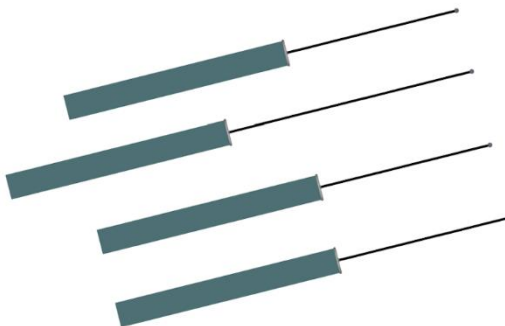


Fig. 238: Modelling sequence for grout body discretised by means of *Ves*

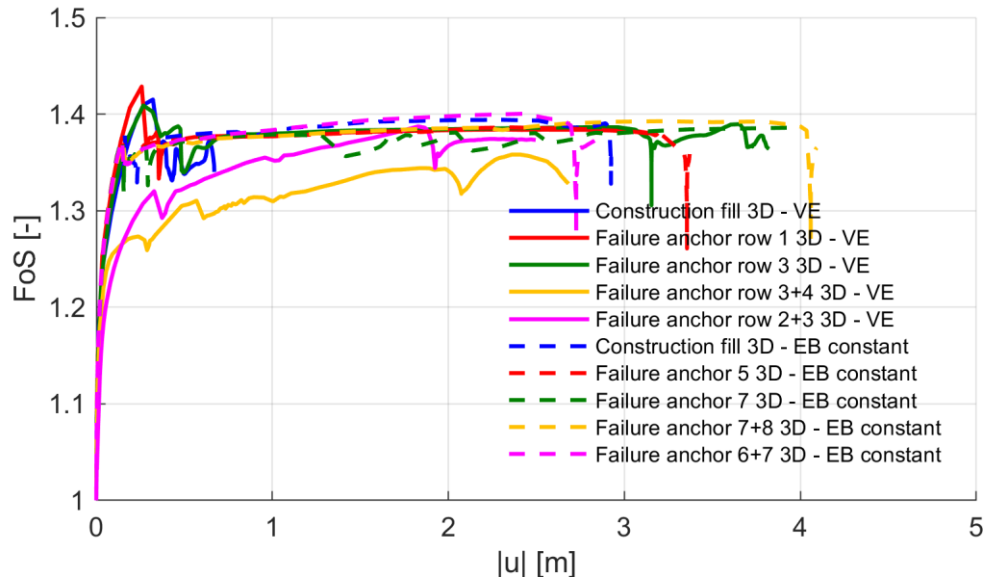


Fig. 239: FoS after φ - c reduction Construction fill and Failure cases for $c = 0.1$ kPa; VEs 3D vs. EBs with constant skin resistance 3D

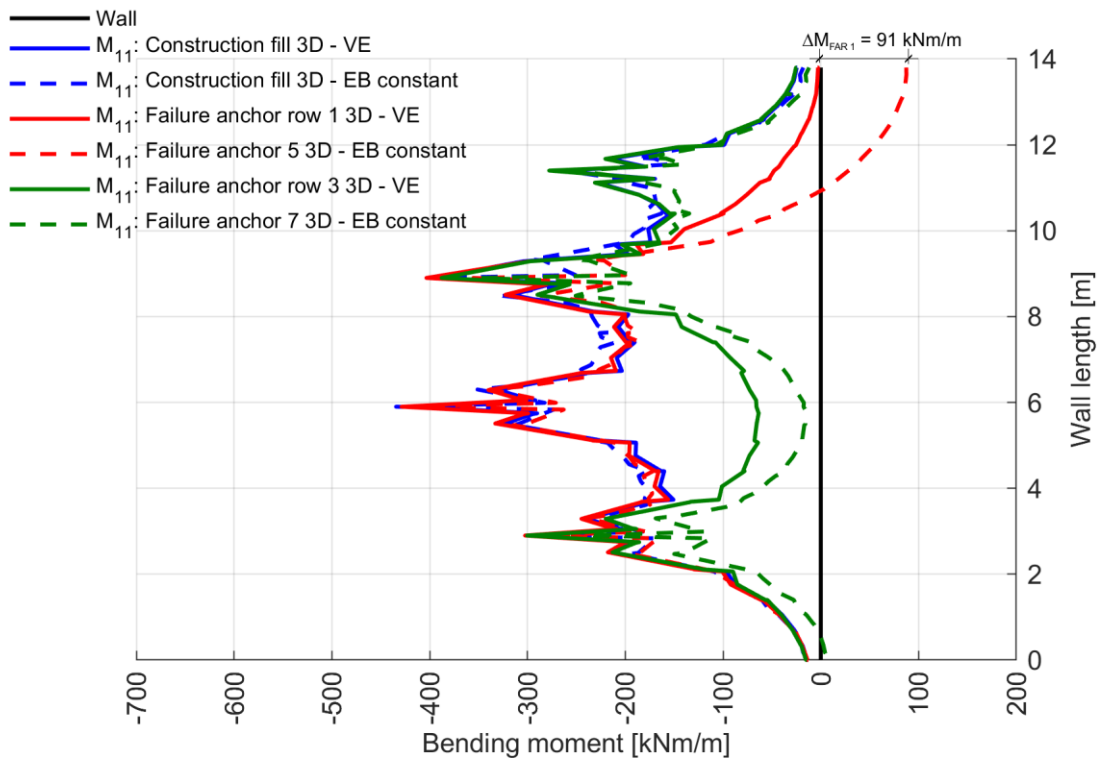


Fig. 240: BMs $M_{11,actual}$ after Construction fill and single anchor failure cases for $c = 0.1$ kPa; VEs 3D at $y = 2.50$ m vs. EBs with constant skin resistance 3D at $y = 7.50$ m

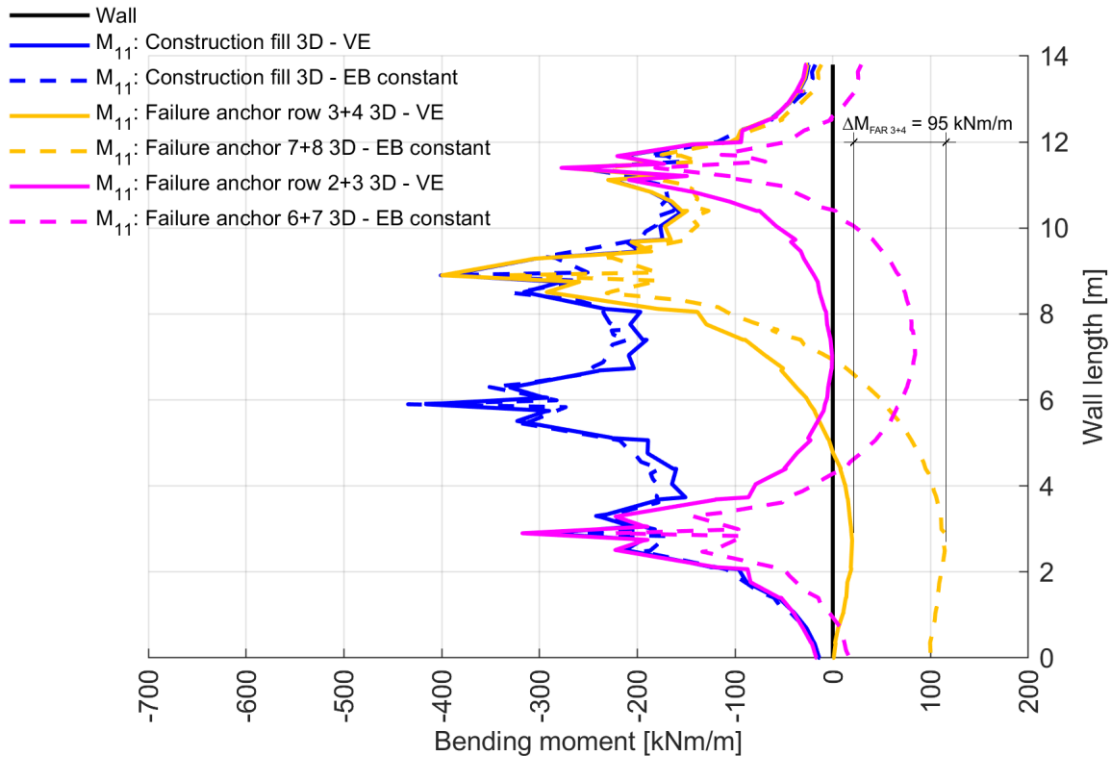


Fig. 241: $BM_s M_{11,actual}$ after Construction fill and double anchor failure cases for $c = 0.1$ kPa; VEs 3D at $y = 2.50$ m vs. EBs with constant skin resistance 3D at $y = 7.50$ m

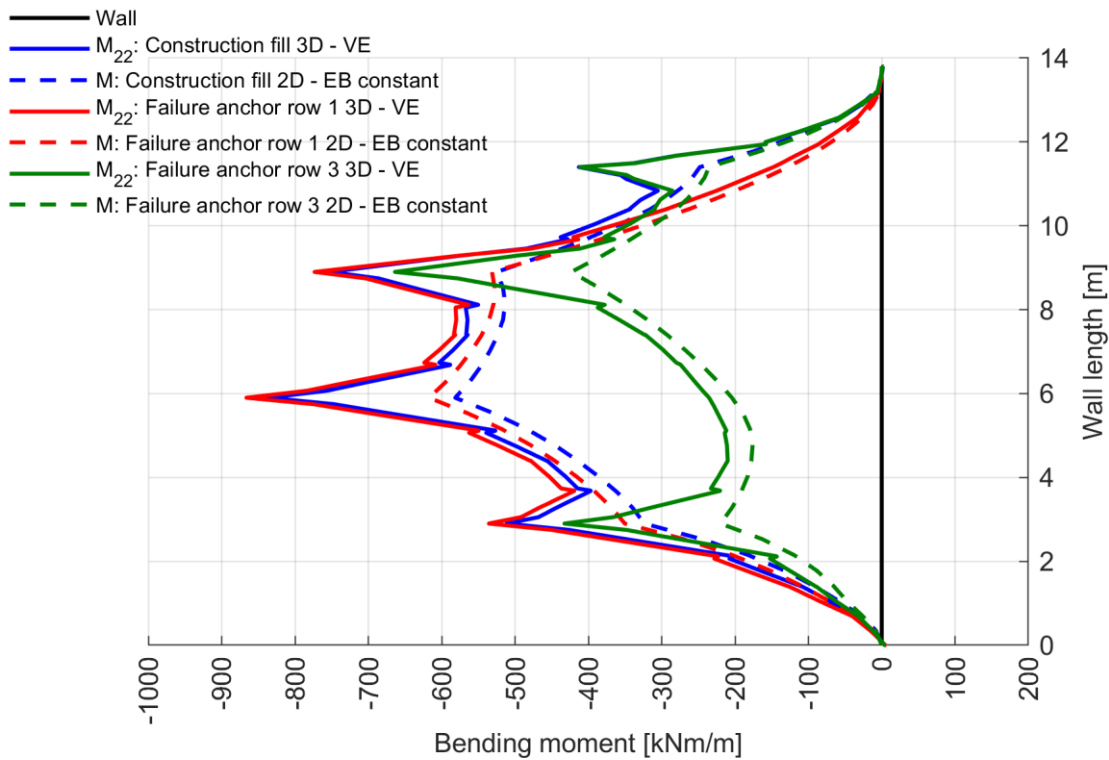


Fig. 242: $BM_s M_{22,actual}$ after Construction fill and single anchor failure cases for $c = 0.1$ kPa; VEs 3D at $y = 2.50$ m vs. EBs with constant skin resistance 2D

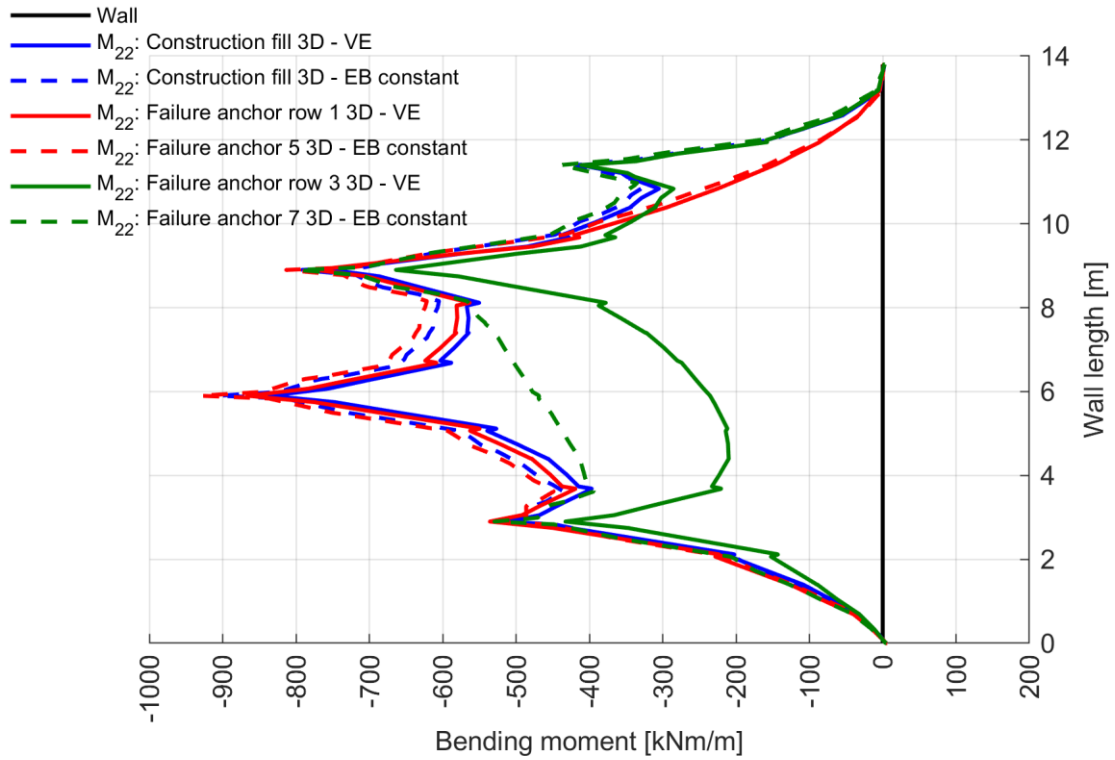


Fig. 243: $BMs M_{22,actual}$ after Construction fill and single anchor failure cases for $c = 0.1$ kPa; VEs 3D at $y = 2.50$ m vs. EBs with constant skin resistance 3D at $y = 7.50$ m

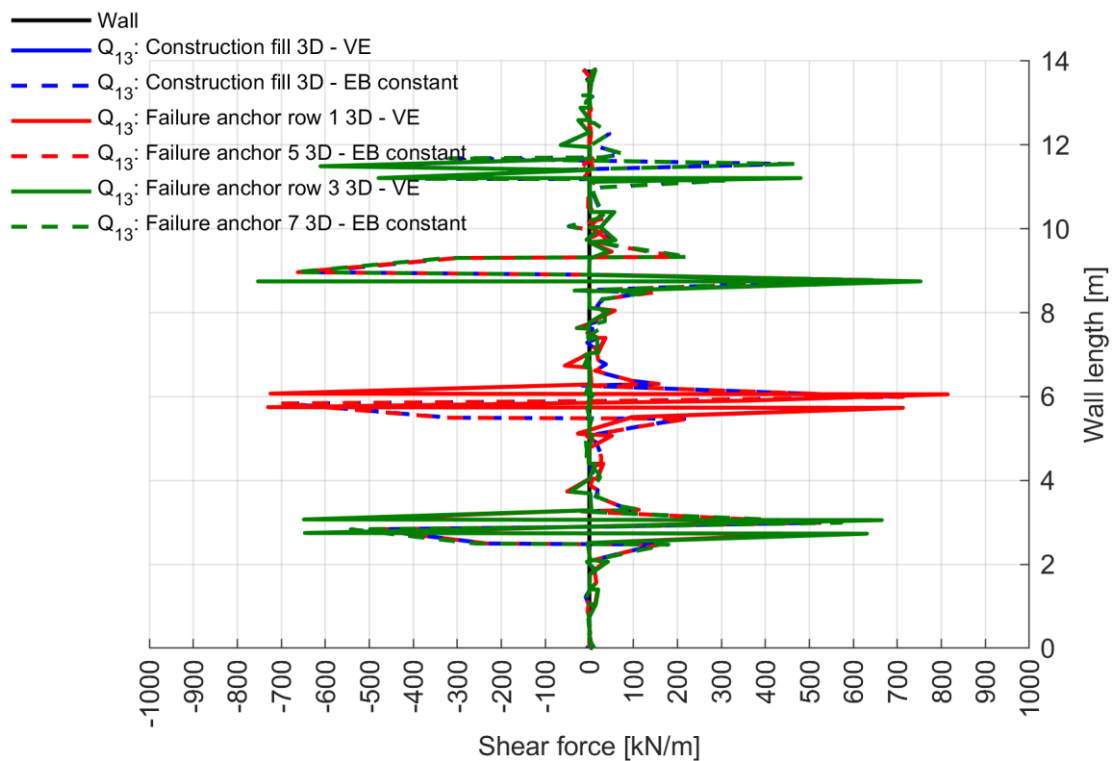


Fig. 244: $SFs Q_{13,actual}$ after Construction fill and single anchor failure cases for $c = 0.1$ kPa; VEs 3D at $y = 2.50$ m vs. EBs with constant skin resistance 3D at $y = 7.50$ m

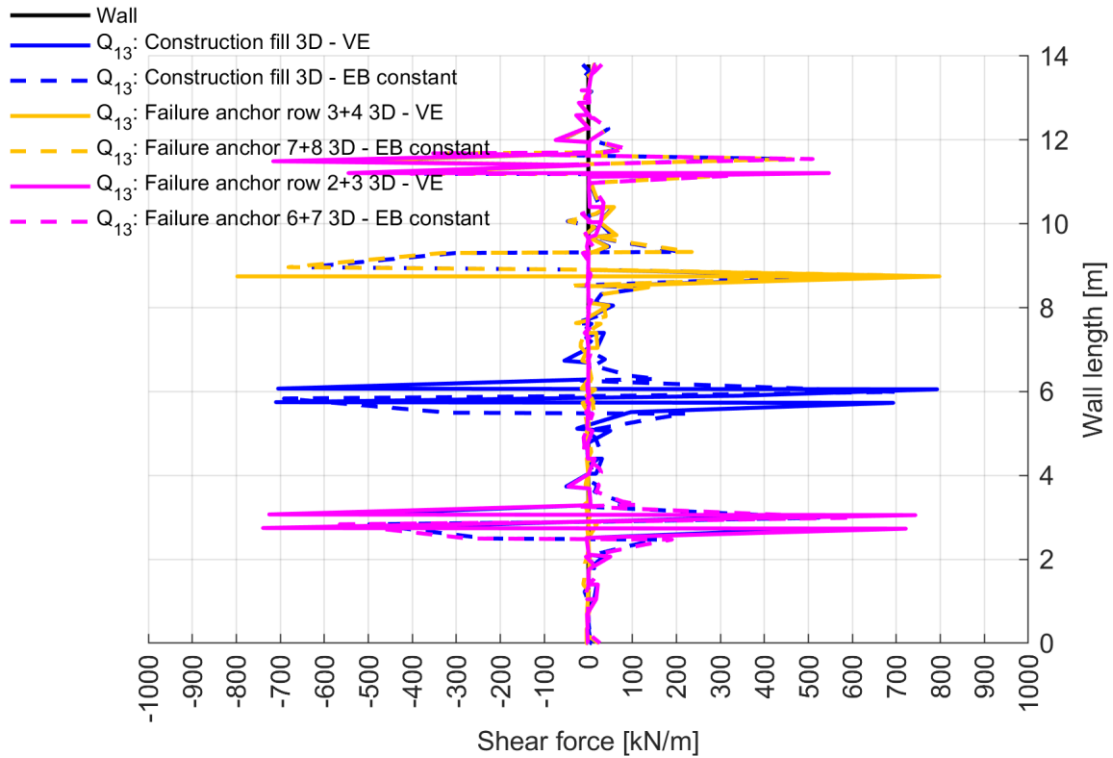


Fig. 245: $SFs Q_{13,actual}$ after Construction fill and double anchor failure cases for $c = 0.1 \text{ kPa}$; VEs 3D at $y = 2.50 \text{ m}$ vs. EBs with constant skin resistance 3D at $y = 7.50 \text{ m}$

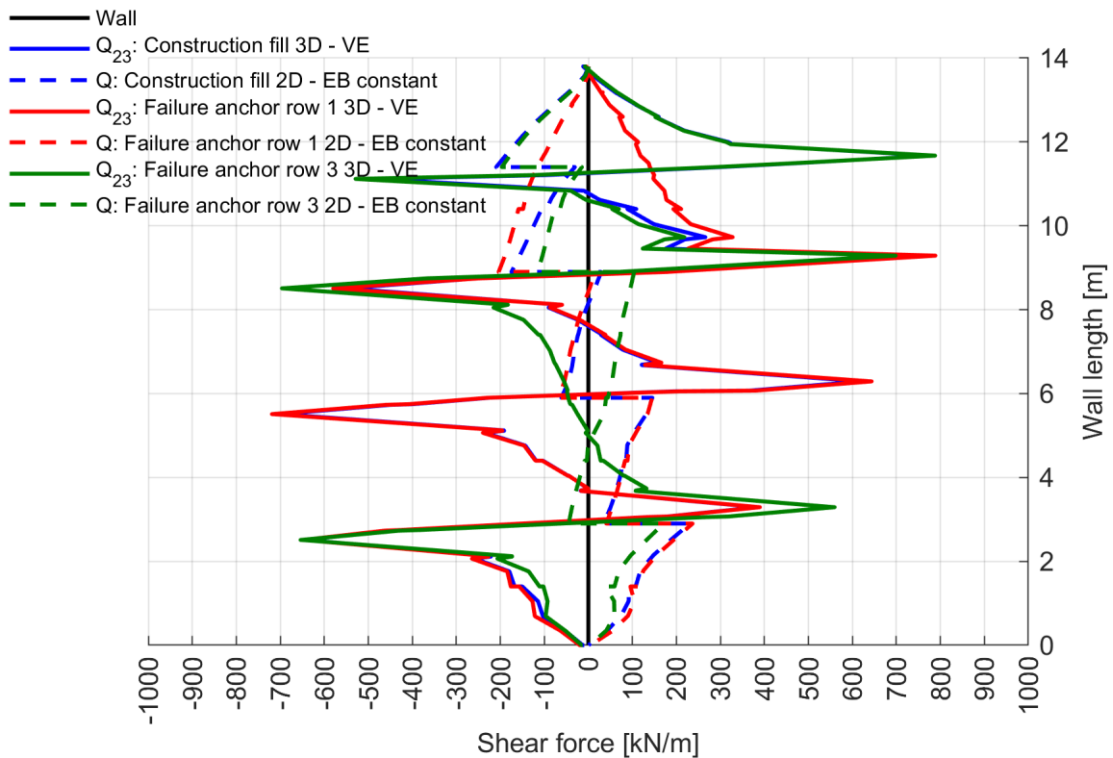


Fig. 246: $SFs Q_{23,actual}$ after Construction fill and single anchor failure cases for $c = 0.1 \text{ kPa}$; VEs 3D at $y = 2.50 \text{ m}$ vs. EBs with constant skin resistance 2D

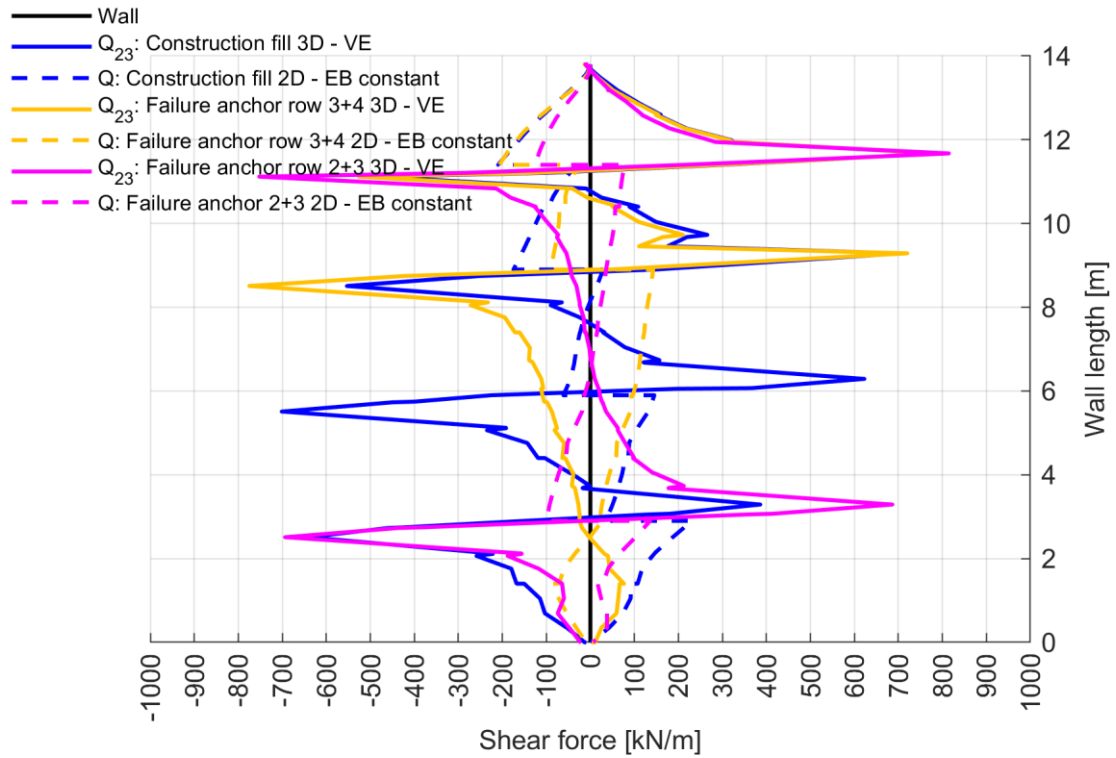


Fig. 247: $SFs Q_{23,actual}$ after Construction fill and double anchor failure cases for $c = 0.1$ kPa; VEs 3D at $y = 2.50$ m vs. EBs with constant skin resistance 2D

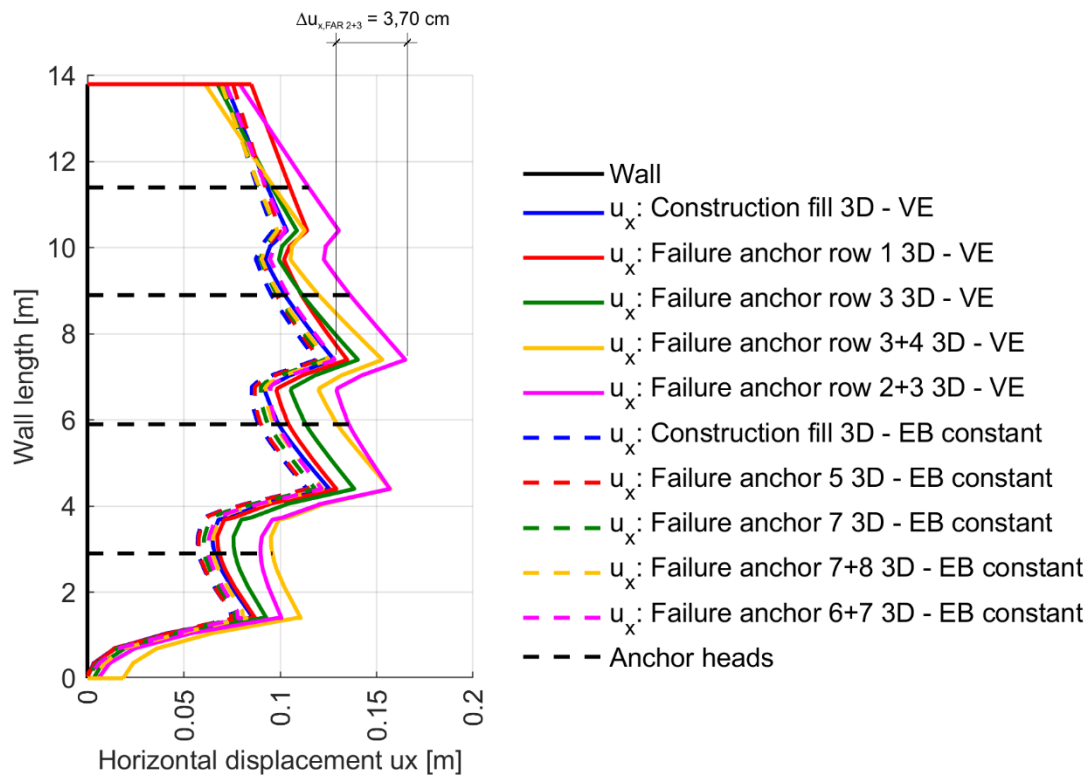


Fig. 248: Horizontal displacements u_x after Construction fill and Failure cases for $c = 0.1$ kPa; VEs 3D at $y = 2.50$ m vs. EBs with constant skin resistance 3D at $y = 7.50$ m

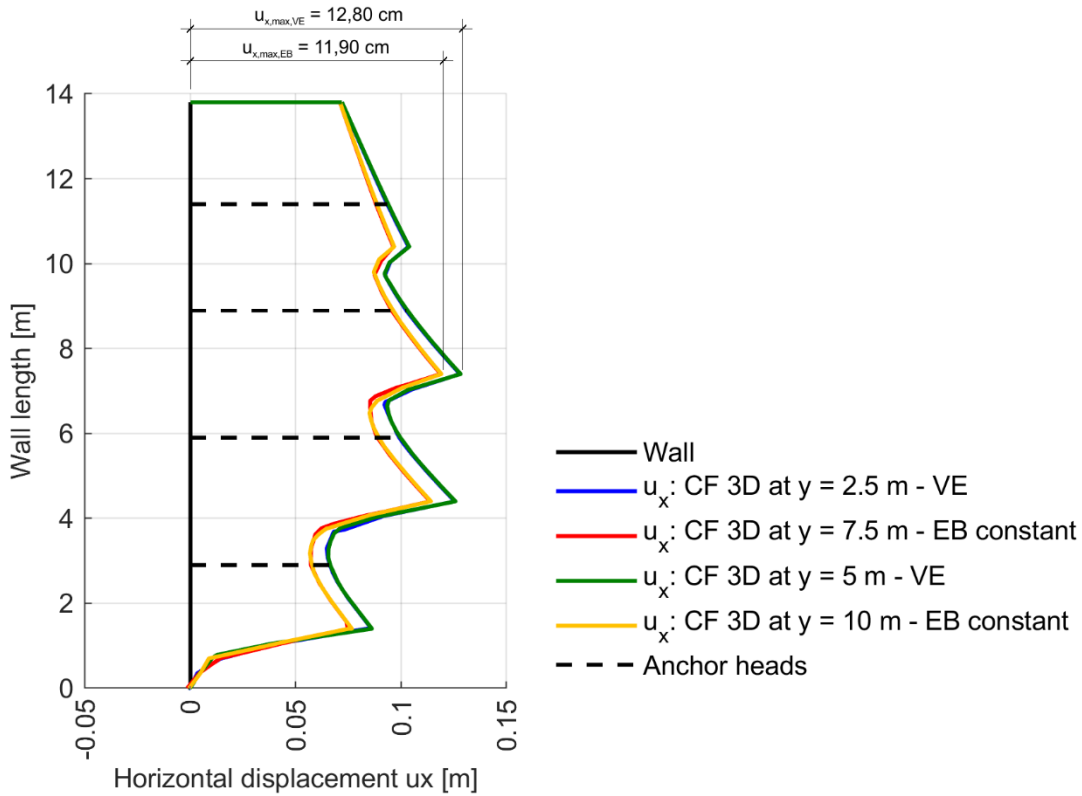


Fig. 249: Horizontal displacements u_x after Construction fill for $c = 0.1$ kPa; VEs 3D at $y = 2.5/5$ m vs. EBs with constant skin resistance 3D at $y = 7.5/10$ m

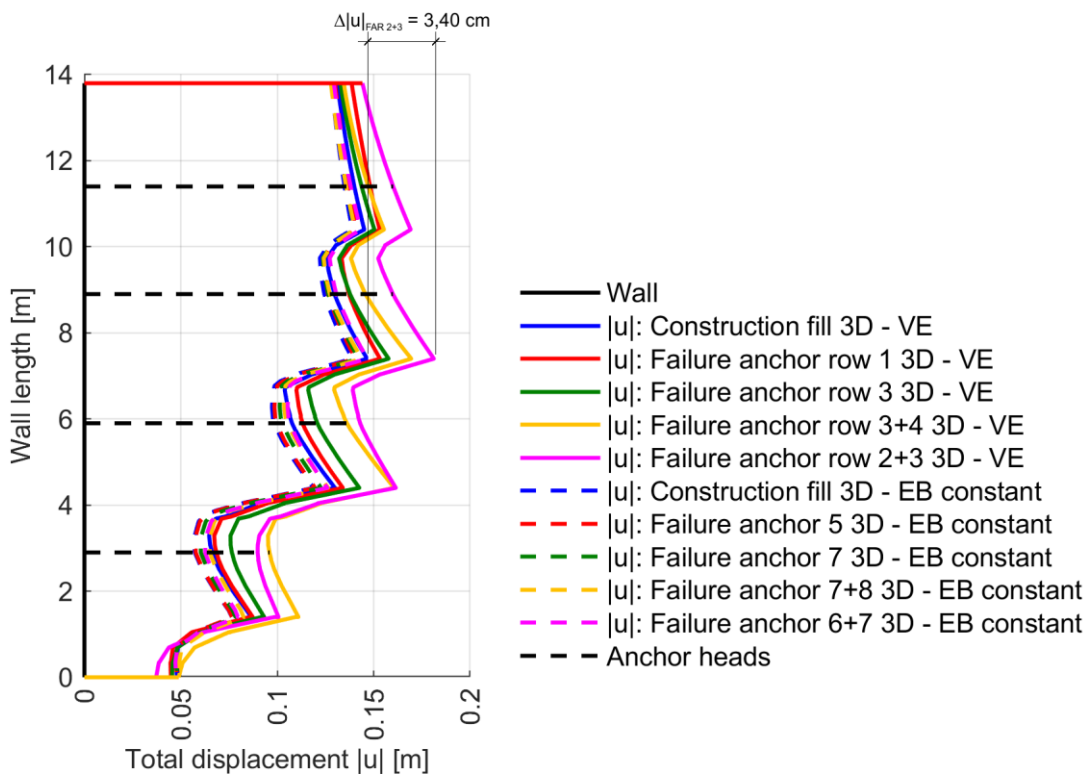


Fig. 250: Total displacements $|u|$ after Construction fill and Failure cases for $c = 0.1$ kPa; VEs 3D at $y = 2.50$ m vs. EBs with constant skin resistance 3D at $y = 7.50$ m

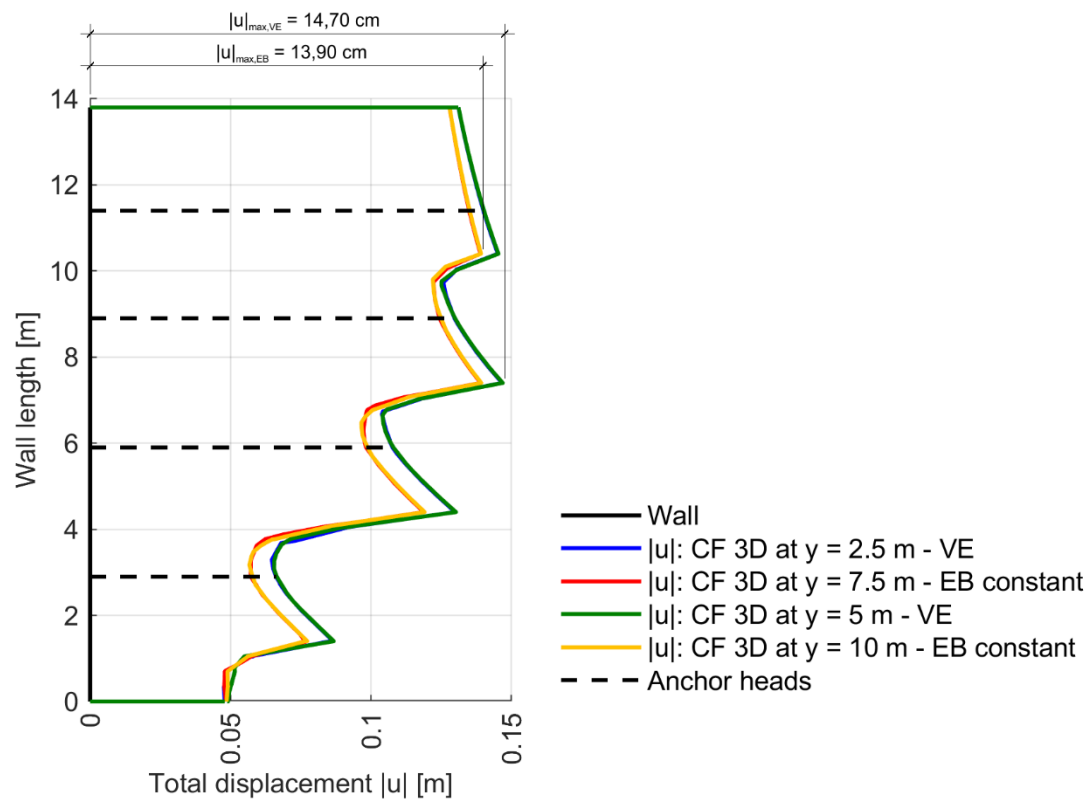


Fig. 251: Total displacements $|u|$ after Construction fill for $c = 0.1$ kPa; VEs 3D at $y = 2.50/5$ m vs. EBs with constant skin resistance 3D at $y = 7.50/10$ m

8.10 $MC_{R_{inter}=1_Geogrid_AnchorNon-Pre-stressed}$

8.10.1 Tendon in 3D modelled with plate elements

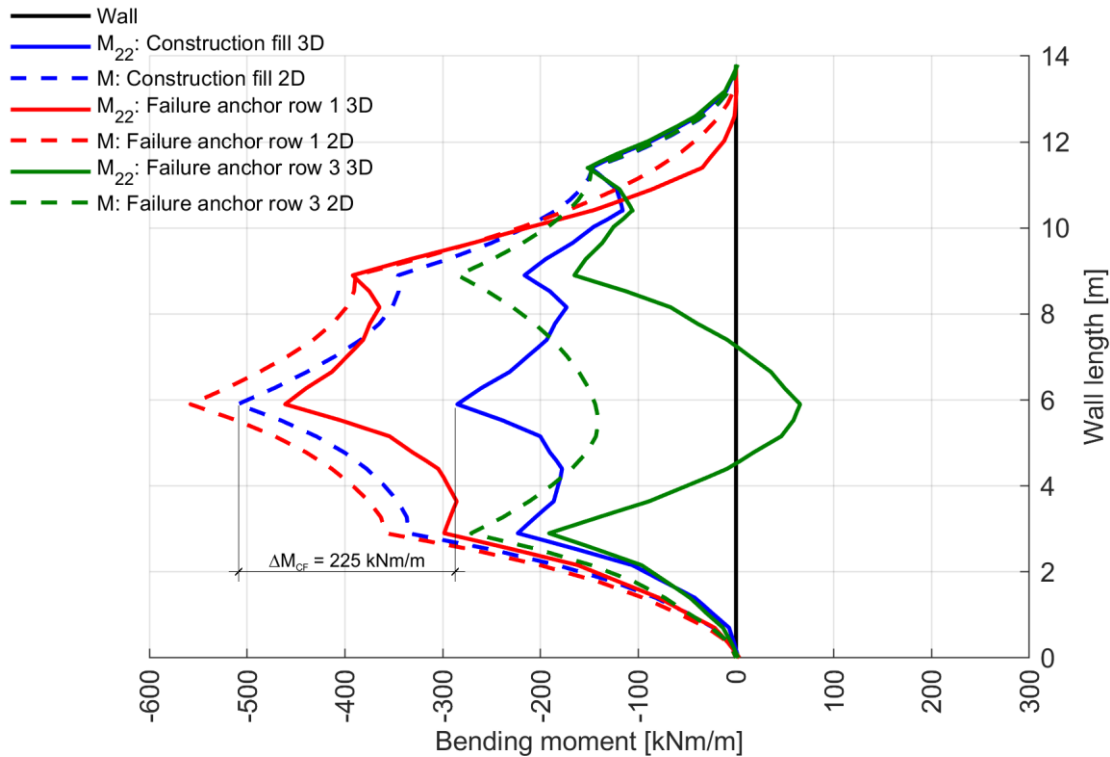


Fig. 252: $BMs M_{22,actual}$ after Construction fill and single row failure cases for $c = 0.1 \text{ kPa}$; 2D vs. 3D (Plate) at $y = 7.50 \text{ m}$

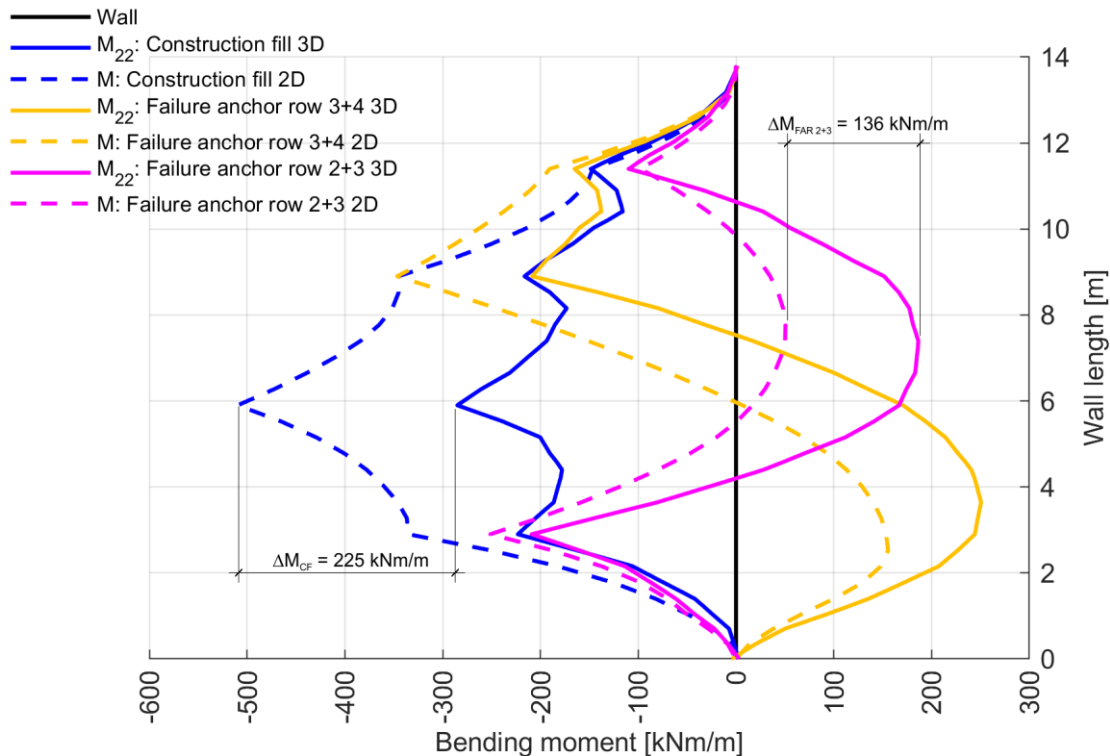


Fig. 253: $BMs M_{22,actual}$ after Construction fill and double row failure cases for $c = 0.1 \text{ kPa}$; 2D vs. 3D (Plate) at $y = 7.50 \text{ m}$

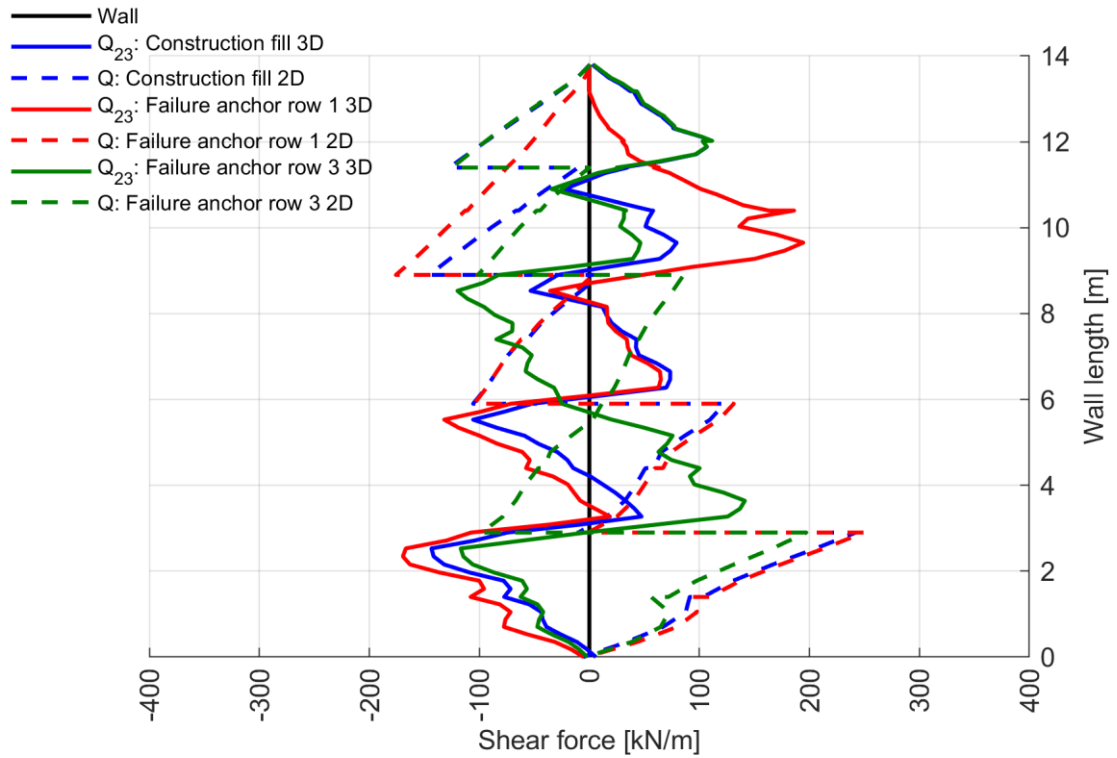


Fig. 254: $SFs Q_{23,actual}$ after Construction fill and single row failure cases for $c = 0.1$ kPa; 2D vs. 3D (Plate) at $y = 7.50$ m

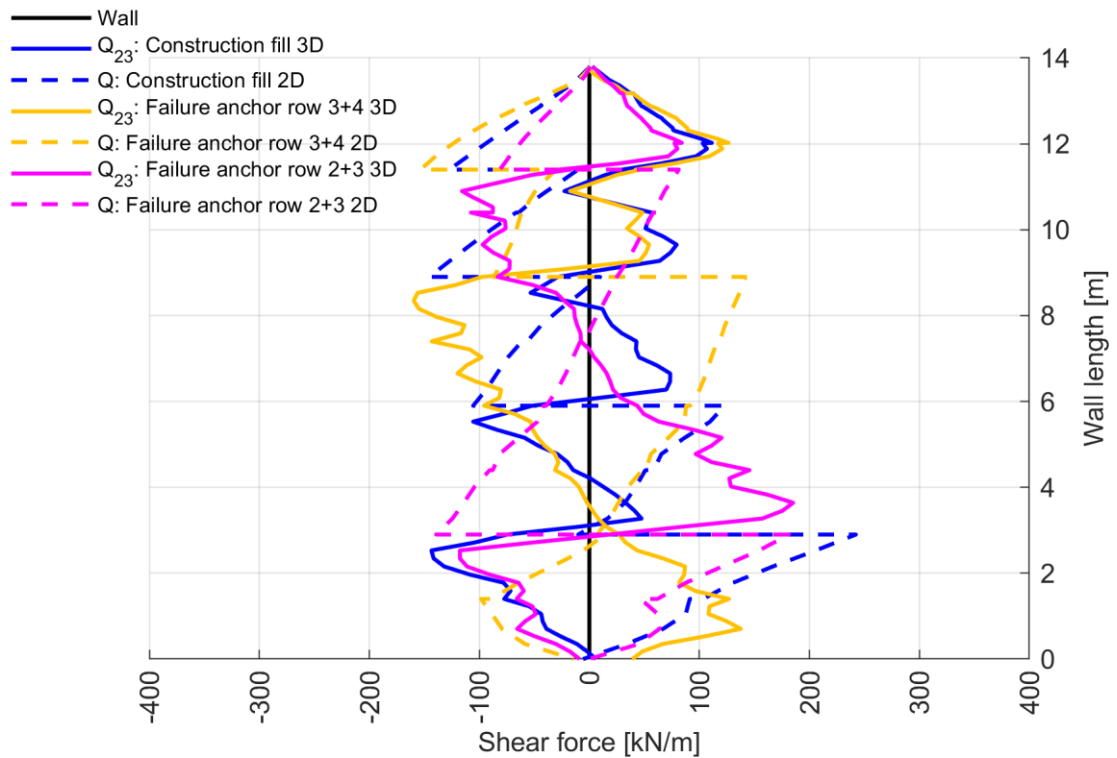


Fig. 255: $SFs Q_{23,actual}$ after Construction fill and double row failure cases for $c = 0.1$ kPa; 2D vs. 3D (Plate) at $y = 7.50$ m

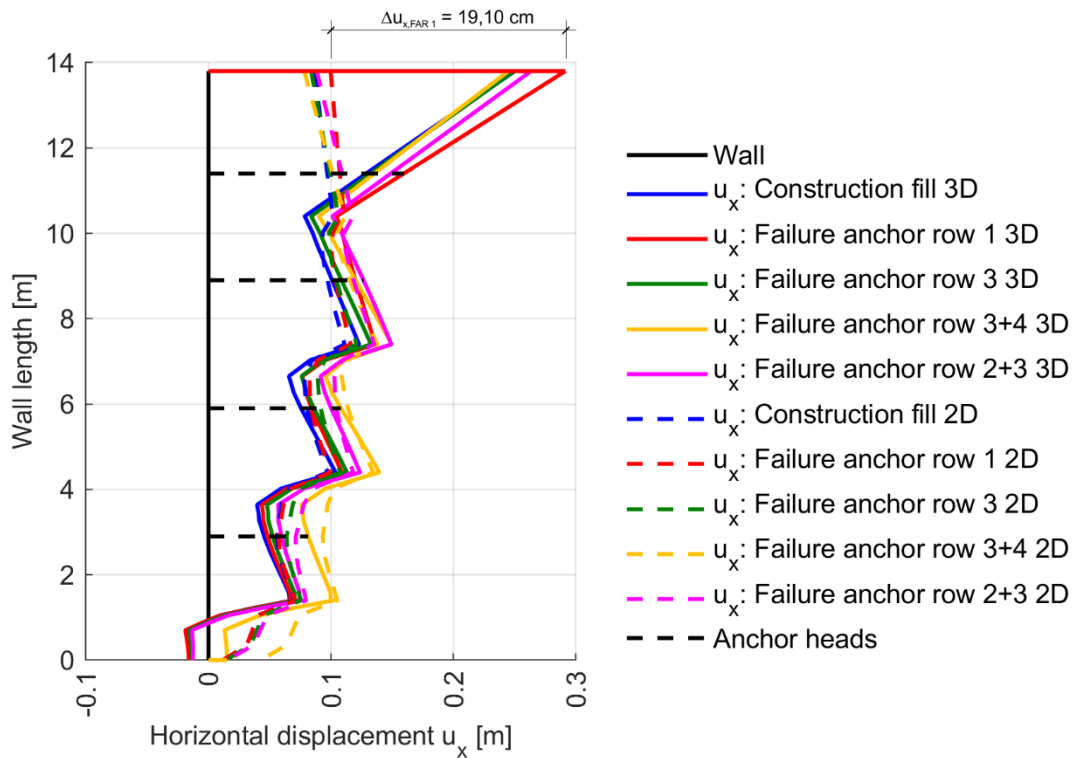


Fig. 256: Horizontal displacements u_x after Construction fill and Failure cases for $c = 0.1 \text{ kPa}$; 2D vs. 3D (Plate) at $y = 7.50 \text{ m}$

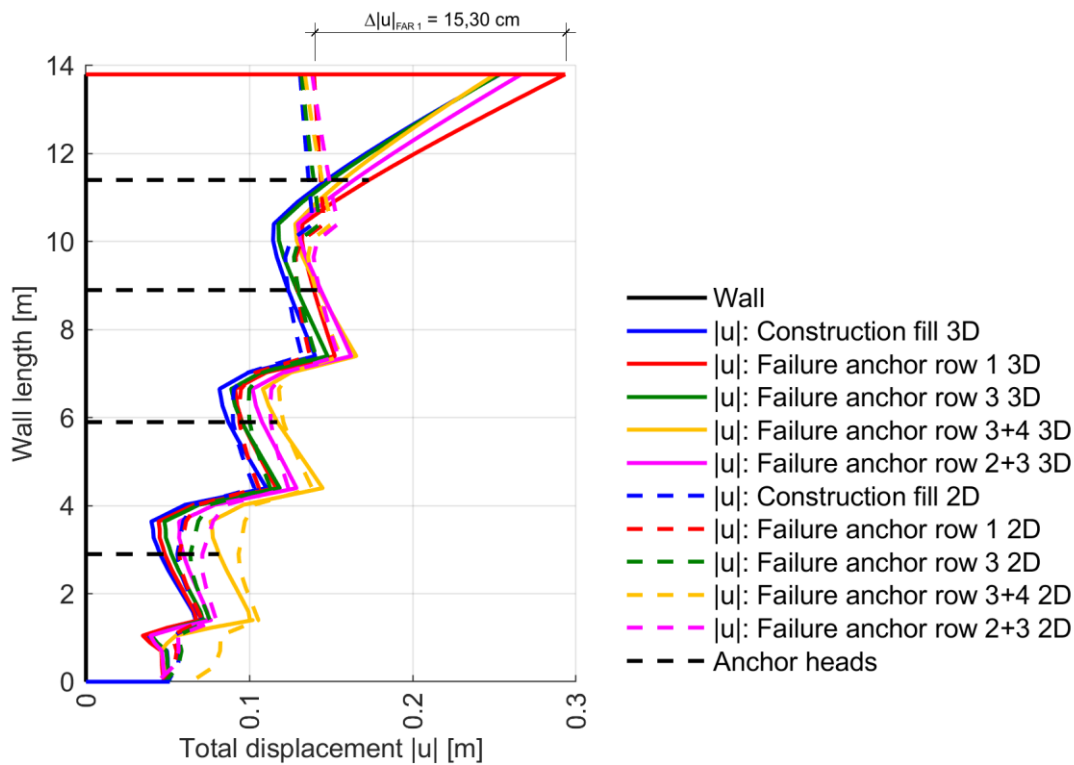


Fig. 257: Total displacements $|u|$ after Construction fill and Failure cases for $c = 0.1 \text{ kPa}$; 2D vs. 3D (Plate) at $y = 7.50 \text{ m}$

8.10.2 Tendon in 2D/3D modelled with plate elements

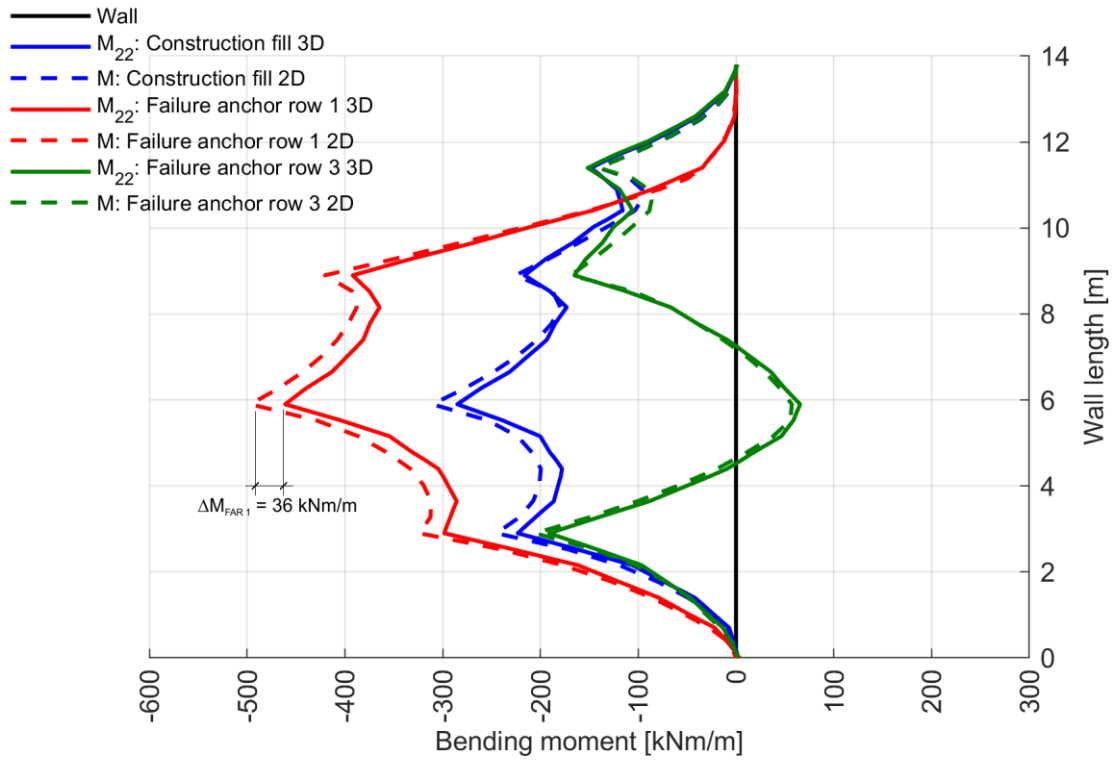


Fig. 258: $BM_s M_{22,actual}$ after Construction fill and single row failure cases for $c = 0.1$ kPa; 2D (Plate) vs. 3D (Plate) at $y = 7.50$ m

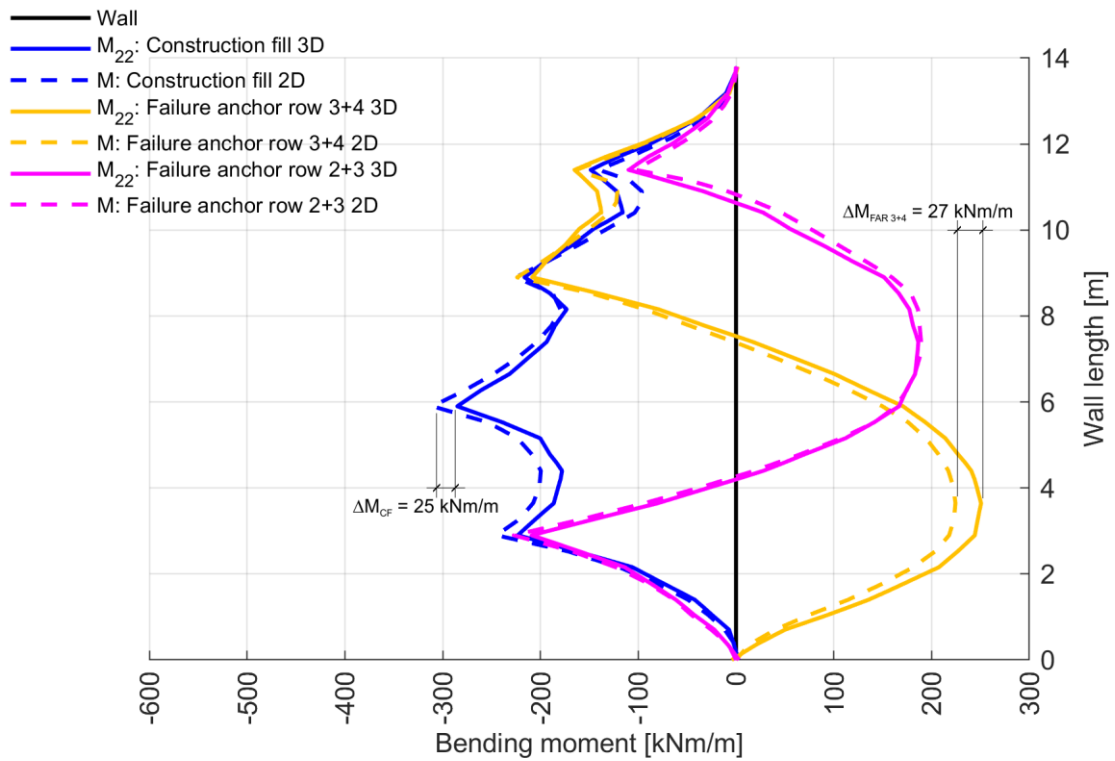


Fig. 259: $BM_s M_{22,actual}$ after Construction fill and double row failure cases for $c = 0.1$ kPa; 2D (Plate) vs. 3D (Plate) at $y = 7.50$ m

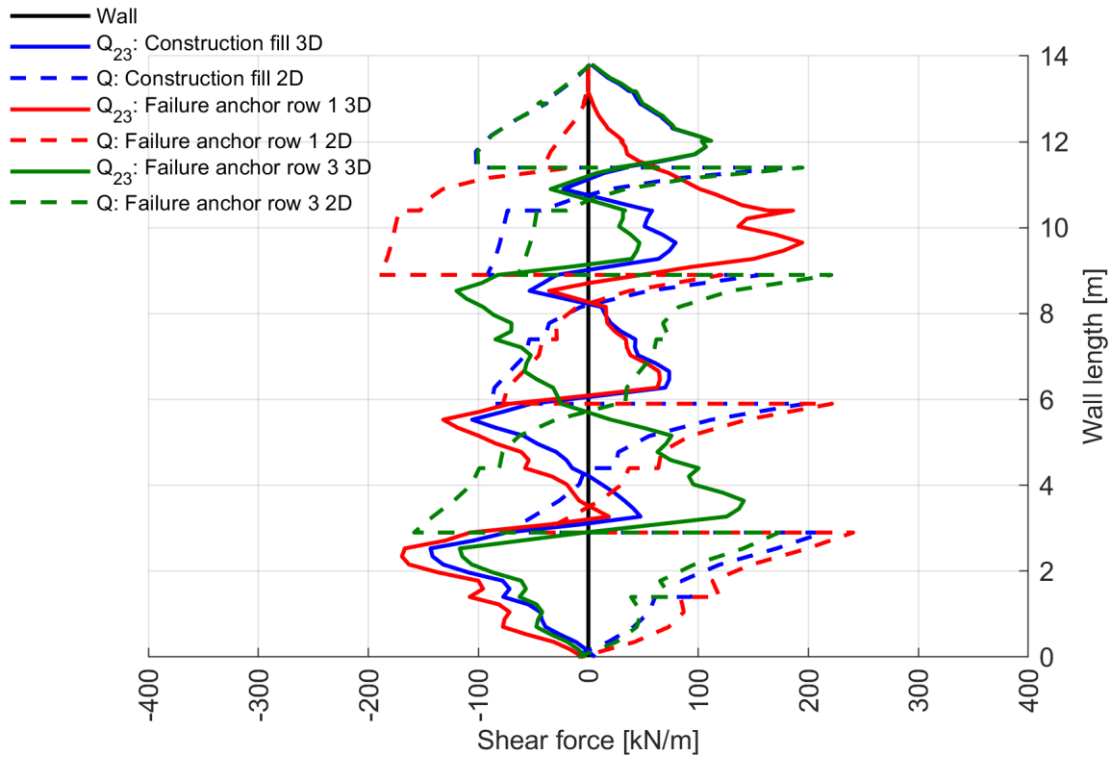


Fig. 260: $SFs Q_{23,actual}$ after Construction fill and single row failure cases for $c = 0.1$ kPa; 2D (Plate) vs. 3D (Plate) at $y = 7.50$ m

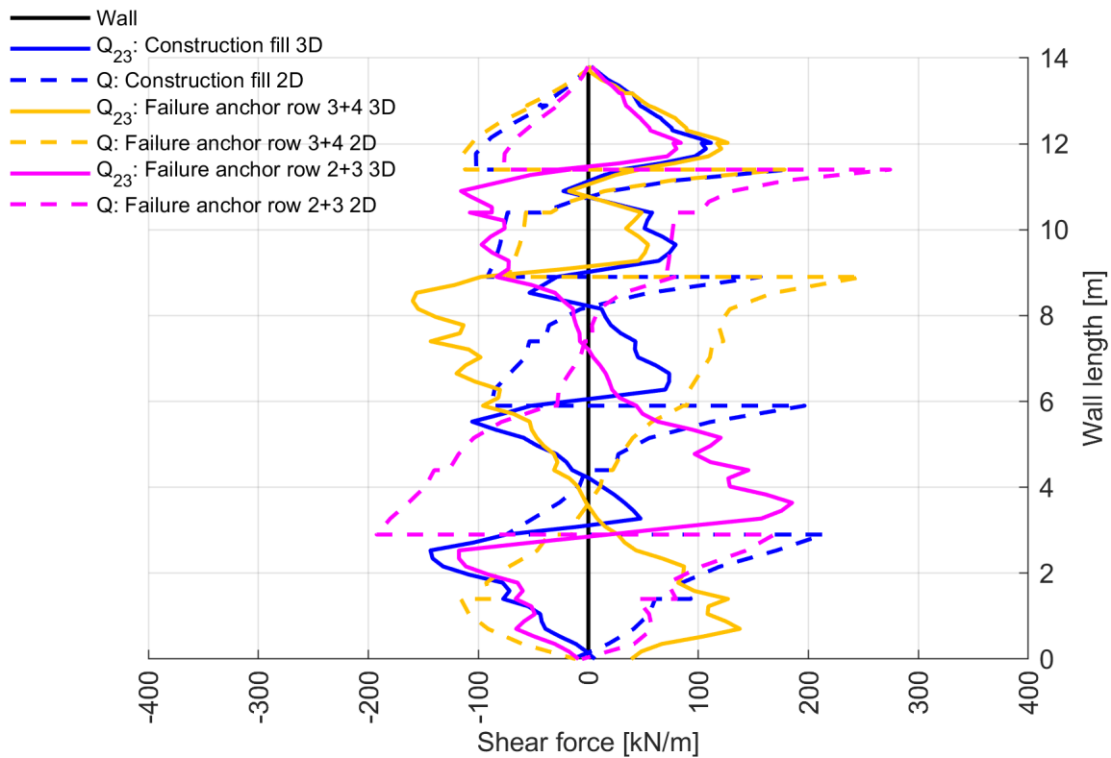


Fig. 261: $SFs Q_{23,actual}$ after Construction fill and double row failure cases for $c = 0.1$ kPa; 2D (Plate) vs. 3D (Plate) at $y = 7.50$ m

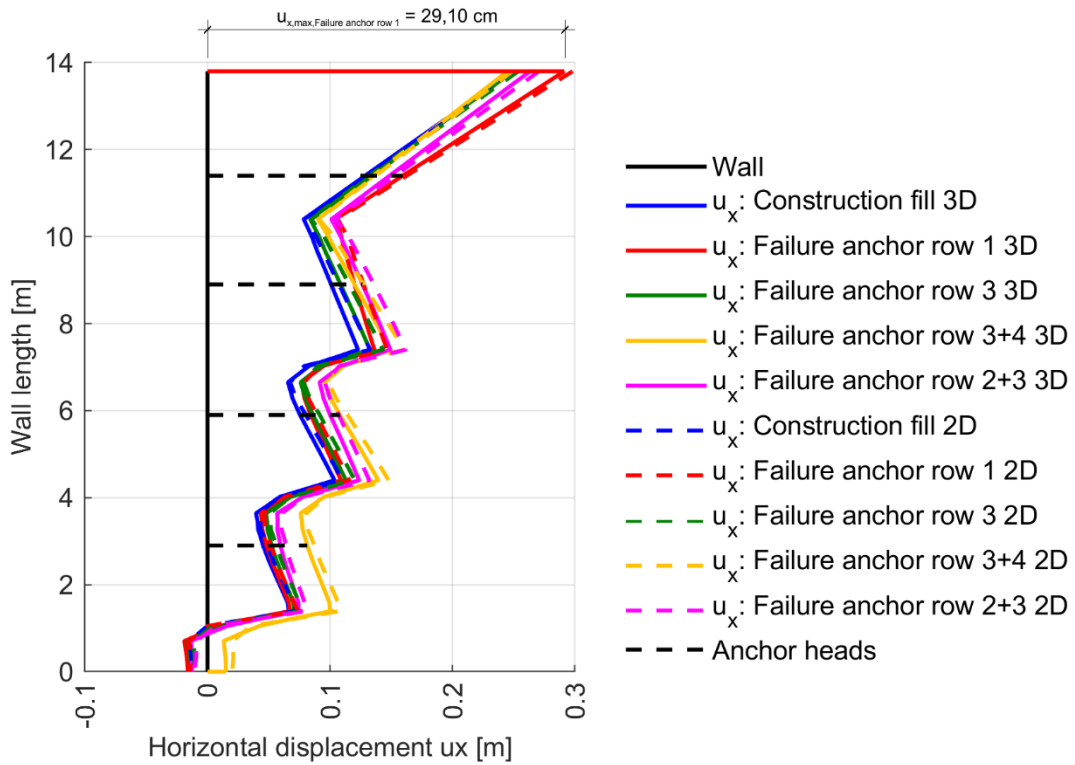


Fig. 262: Horizontal displacements u_x after Construction fill and Failure cases for $c = 0.1$ kPa; 2D (Plate) vs. 3D (Plate) at $y = 7.50$ m

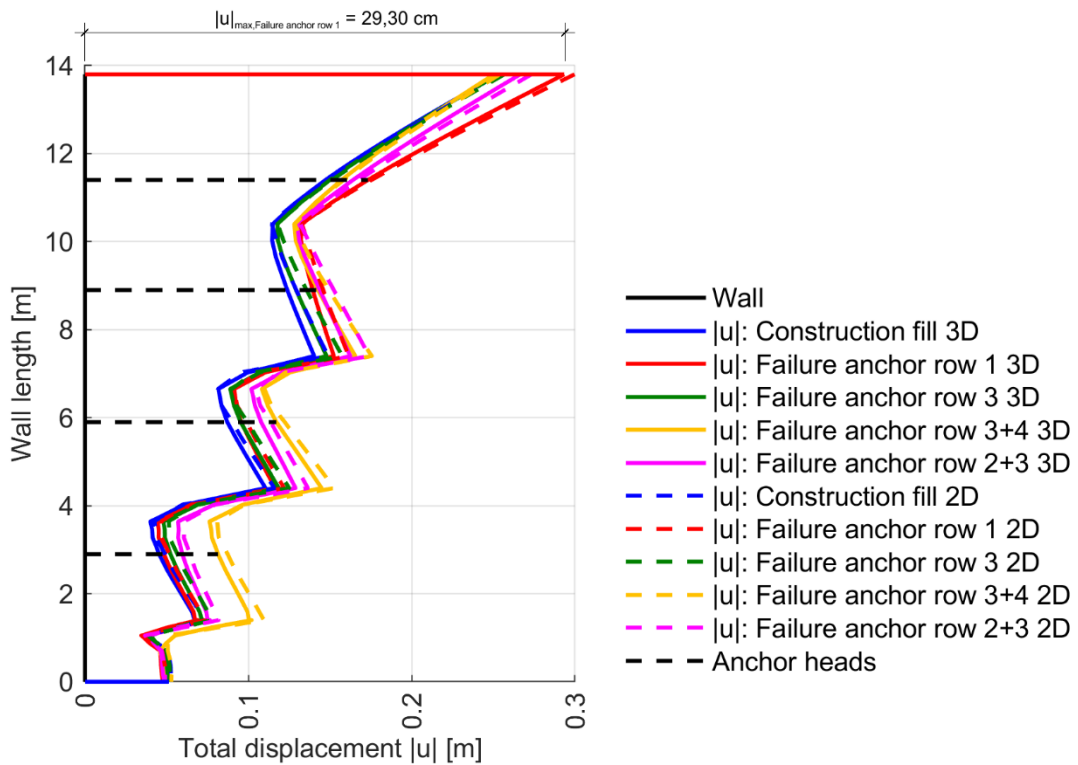


Fig. 263: Total displacements $|u|$ after Construction fill and Failure cases for $c = 0.1$ kPa; 2D (Plate) vs. 3D (Plate) at $y = 7.50$ m

8.10.3 Tendon in 3D modelled with plate and geogrid elements

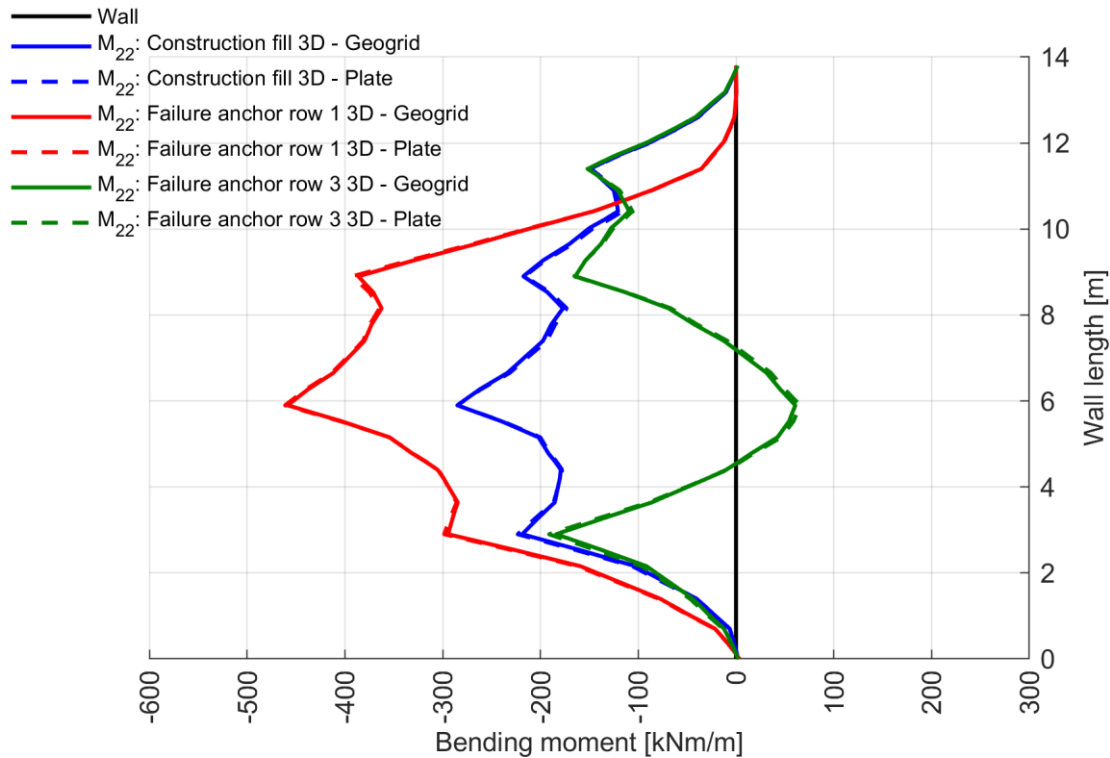


Fig. 264: $BM_s M_{22,actual}$ after Construction fill and single row failure cases for $c = 0.1 \text{ kPa}$; 3D (Plate) at 7.50 m vs. 3D (Geogrid) at $y = 7.50 \text{ m}$

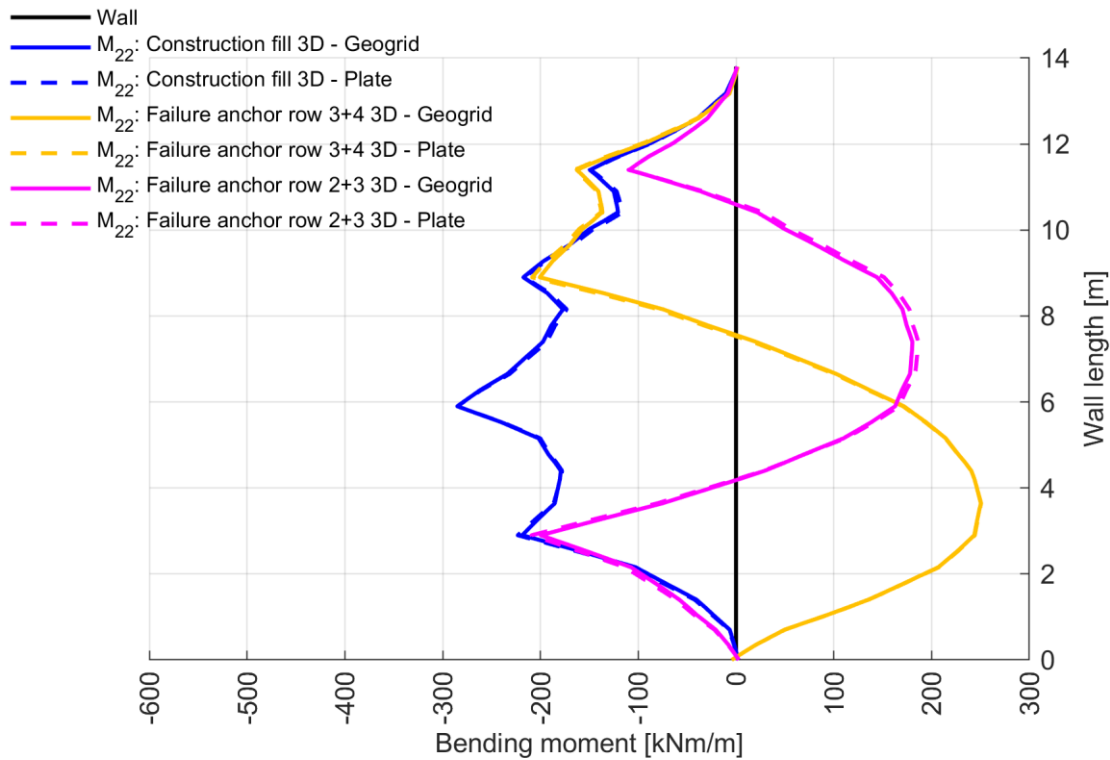


Fig. 265: $BM_s M_{22,actual}$ after Construction fill and double row failure cases for $c = 0.1 \text{ kPa}$; 3D (Plate) at 7.50 m vs. 3D (Geogrid) at $y = 7.50 \text{ m}$

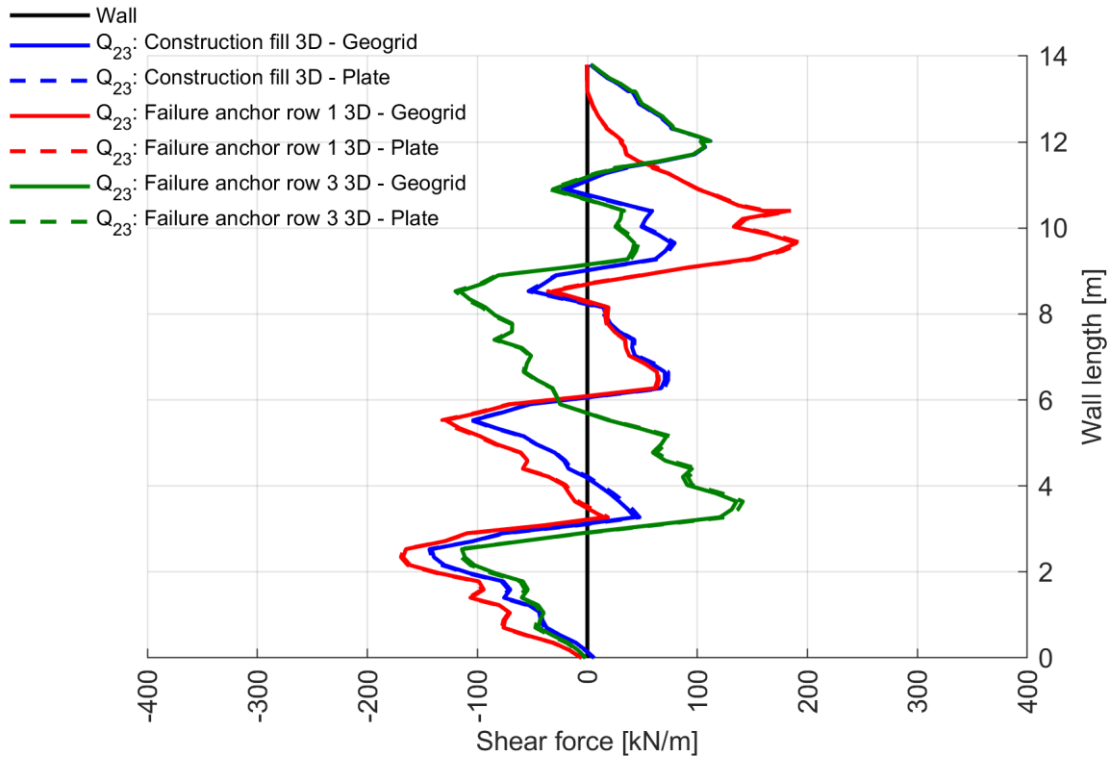


Fig. 266: $SFs Q_{23,actual}$ after Construction fill and single row failure cases for $c = 0.1 \text{ kPa}$; 3D (Plate) at 7.50 m vs. 3D (Geogrid) at $y = 7.50 \text{ m}$

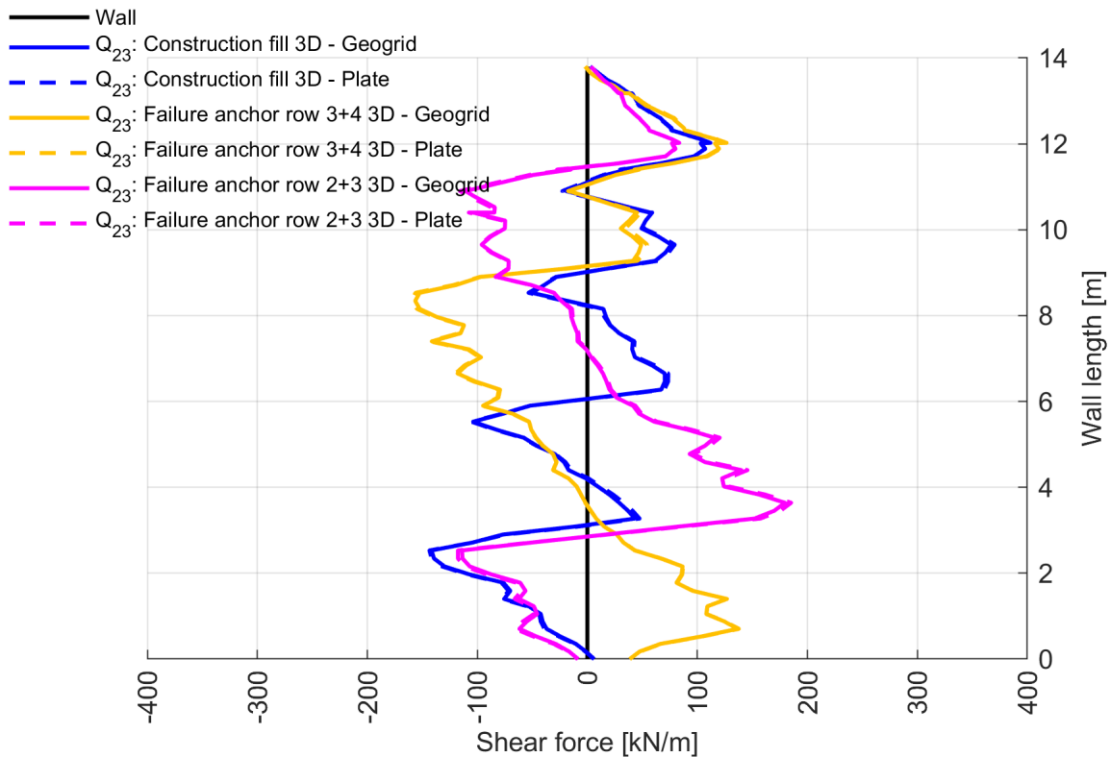


Fig. 267: $SFs Q_{23,actual}$ after Construction fill and double row failure cases for $c = 0.1 \text{ kPa}$; 3D (Plate) at 7.50 m vs. 3D (Geogrid) at $y = 7.50 \text{ m}$

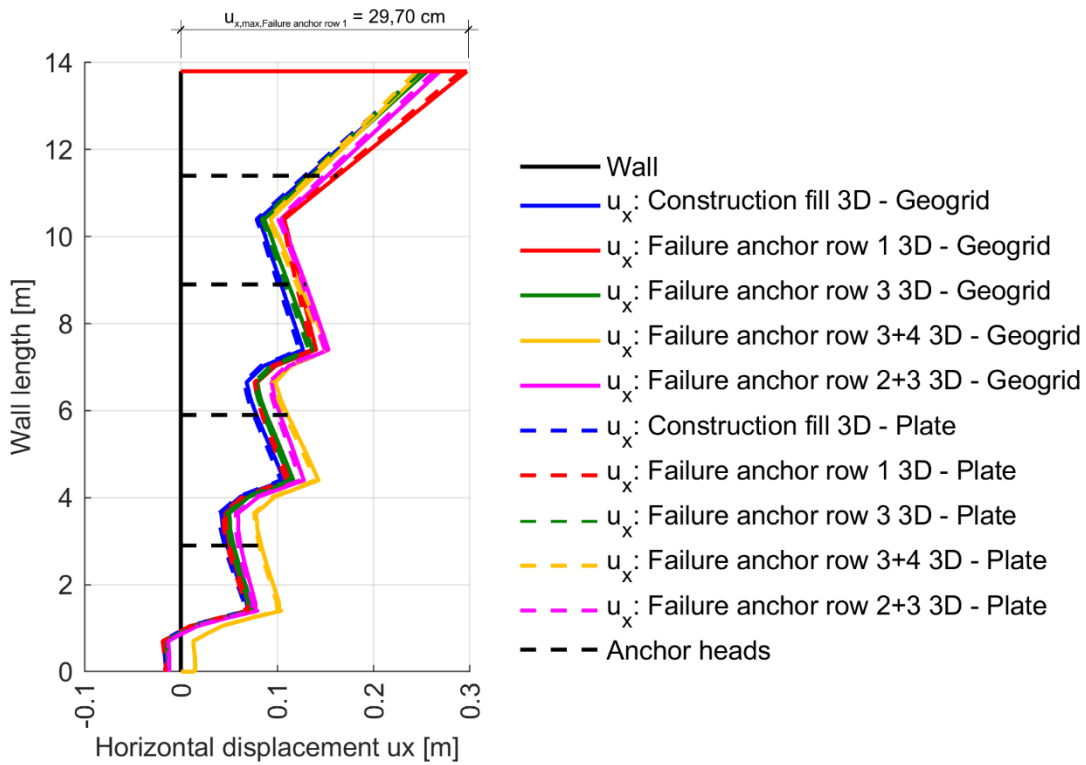


Fig. 268: Horizontal displacements u_x after Construction fill and Failure cases for $c = 0.1\ kPa$; 3D (Plate) at 7.50 m vs. 3D (Geogrid) at $y = 7.50\ m$

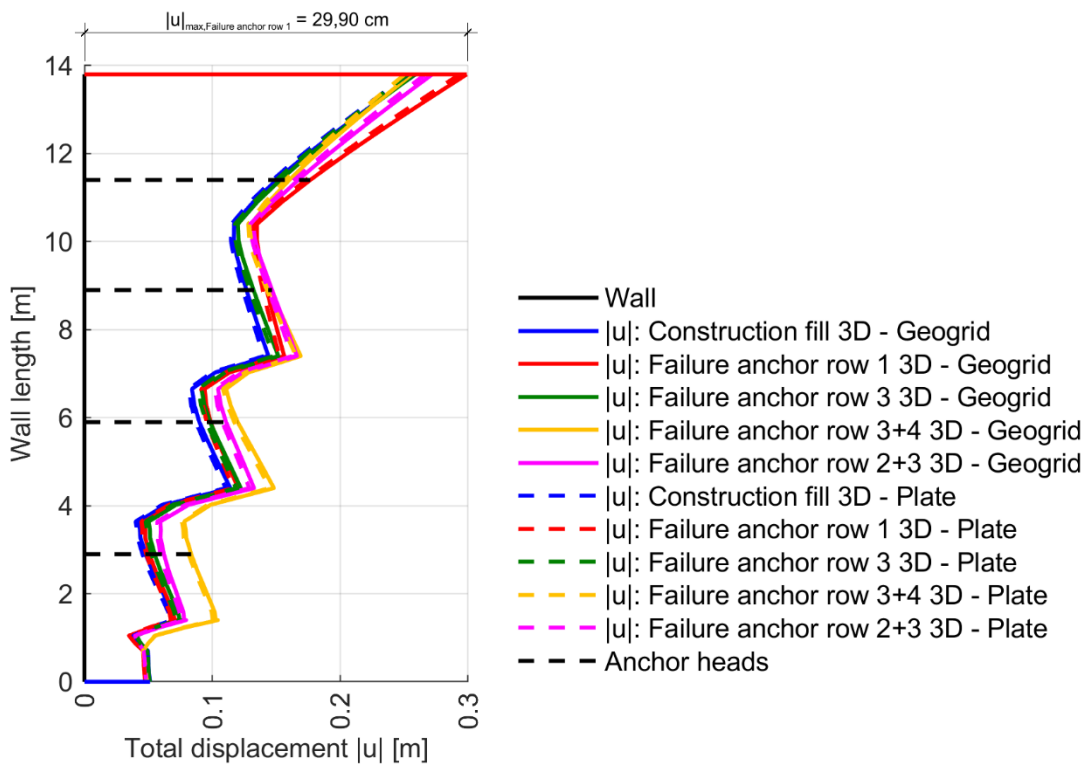


Fig. 269: Total displacements $|u|$ after Construction fill and Failure cases for $c = 0.1\ kPa$; 3D (Plate) at 7.50 m vs. 3D (Geogrid) at $y = 7.50\ m$